Dissertation

submitted to the

Combined Faculty of Mathematics, Engineering and Natural Sciences
of Heidelberg University, Germany

for the degree of

Doctor of Natural Sciences

Put forward by

Zhiqiu Huang (黄稚秋)

Born in: Shanghai/ People's Republic of China

(出生地:中华人民共和国上海市崇明县城桥镇)

Oral examination: 23.05.2024

Gamma-ray Bursts and Implications for Particle Acceleration at Ultra-relativistic Shocks

Referees: Dr. Brian Reville
Prof. Dr. Mattias Bartelmann

Zusammenfassung

Aktuelle Beobachtungen des Nachleuchtens von Gammastrahlenblitzen im TeV Bereich ermöglichen neue Rückschlüsse über die Beschleuning von Teilchen an relativistichen Stoßwellen. Kinetische Simulationen erlauben uns die maximale Energie der beschleunigten Teilchen zu berechen und mit Beobachtungen des GRB 190829A zu vergleichen. Der Vergleich zwischen theoretischen Vorhersagen und Beobachtungen zeigt Diskrepanzen. Diese motivieren neue Simulationen mit Hilfe eines von uns entwickeltem Monte-Carlo Code zur Berechnung der Teilchenbeschleunigung an relativistischen Stoßwellen mit homgenem und nicht-homogenem Magnetfeld. In der homogenen B-Feld Konfiguration zeigen die Simulationen, dass es für die Beschleuningung der Teilchen hinreichend ist, wenn auf einer Seite der Stoßwelle die Teilchen häufig gestreut werden. Den Fall des nicht homogenen B-Feldes modellieren wir mit Hilfe einer zylindrischen Magnetfeldtopologie, die typisch ist für astrophysikalische Jets. Wir beobachten, dass die Krümmung des Magnetfeldes es Teilchen mit geeignter Ladung ermöglicht die Stowelle mehrfach zu durchqueren. Unter nicht Beachtung der Verluste hat dies zur Folge, dass die maximale Teilchenenergie nur durch die Größe des Systems beschränkt ist. Diese Ergebnisse fordern die Behauptung, dass ultra-relativistische Stowellen Teilchen nicht effizient beschleunigen können heraus und machen eine Neubewertung der Teilchenbeschleunigung an relativistischen Stoßwellen auf erforderlich. Dies lässt auf neue theoretische Ergebnisse für den Entstehungsort ultrarelativistischer kosmischer Strahlung hoffen.

Abstract

Recent TeV detections of gamma-ray burst afterglows offer new insights into particle acceleration at relativistic shocks. Kinetic simulations have improved our understanding of shock microphysics, enhancing models of particle acceleration relevant to afterglows. We explore scenarios for determining the maximum achievable energy, comparing our findings with data from the H.E.S.S. source, GRB 190829A. This comparison reveals a tension between observations and theoretical expectations. Motivated by this, we developed a Monte Carlo code to revisit acceleration theory for relativistic shocks in uniform and non-uniform magnetic field configurations. In uniform fields, we demonstrate that acceleration requires only strong scattering on one side of the shock. Analytic solutions confirm this conclusion. For non-uniform fields, we consider a cylindrical magnetic-field structure typical of astrophysical jets. We find that curvature drifts enable repeated shock-crossings for particles of favourable charge, and neglecting losses extends the maximum energy to the system's confinement limit. These results challenge the misconception that ultra-relativistic shocks cannot serve as effective accelerators, offering a fresh perspective on relativistic shock acceleration. The findings suggest new features on maximum achievable energy and spectral index, indicating the need to revisit current knowledge on relativistic shocks. This could open promising avenues for producing ultra-high energy cosmic rays.

Within the framework of this thesis, the following papers have already been published:

In Chapter 4:

- ***The implications of TeV detected GRB afterglows for acceleration at relativistic shocks***
  Zhi-Qiu Huang, John G. Kirk, Gwenael Giacinti and Brian Reville.
  DOI:10.3847/1538-4357/ac3f38
  The Astrophysical Journal 925, 182

  I deduced the analytical formulas for the characteristic radiation frequencies and wrote the code to calculate all of the main plots used in our paper. I finished the first version of the draft and modified it with other co-authors.

In Chapter 5:

- ***Prospects for ultra-high-energy particle acceleration at relativistic shocks***
  Zhi-Qiu Huang, Brian Reville, John G. Kirk and Gwenael Giacinti.
  DOI:10.1093/mnras/stac3589
  Monthly Notices of the Royal Astronomical Society 522, 4955

  I developed the Monto-Carlo test-particle code given by Brian Reville, which was previously aimed to calculate the particle trajectory in given magnetic and electric fields, to study the particle acceleration at relativistic shocks and plotted all of the figures in this paper. I also led the paper writing and modify papers with other co-authers.

In Chapter 6:

- ***Particle acceleration at ultrarelativistic, perpendicular shock fronts***
  John G. Kirk, Brian Reville and Zhi-Qiu Huang.
  DOI:10.1093/mnras/stad1356
  Monthly Notices of the Royal Astronomical Society 519, 1022

  Motivated by the simulation results from my modified code, John Kirk utilized another analytical method to study the particle acceleration at ultrarelativistic, perpendicular shock. Conclusions from both two methods consist with each other. In this paper, I double checked the figures from numerical simulations plotted by Brian Reville, and discussed with John Kirk, giving a better explanation on the mapping content.

Contents

Chapter 1

High energy astrophysics

In this thesis, we will focus on gamma-ray bursts and particle acceleration at relativistic shocks, both of which are research topics in high-energy astrophysics.

High-energy astrophysics explores the most potent astrophysical phenomena in our universe, such as gamma-ray bursts and supernova remnants. These energetic events typically release electromagnetic radiation in high-energy bands, along with neutrinos and cosmic rays. Consequently, this field encompasses X-ray astronomy, gamma-ray astronomy, neutrino astronomy, and astroparticle physics. These subjects are all quite heated topics nowadays. In this thesis, we mainly focus on gamma-ray bursts, as one of the promising candidates for high-energy cosmic rays, and the acceleration process at shocks, as a long-discussed mechanism to produce high-energy particles. Let's first start from a brief introduction on cosmic rays.

1.1 Cosmic Rays

In 1912, Victor Hess observed an increase in the ionization rate in the atmosphere as altitude rose during his balloon experiment. This discovery suggested that the matter ionizing Earth's atmosphere originates outside the earth. Initially, high-energy electromagnetic radiation was considered to explain this phenomenon and was consequently named cosmic rays. We now understand that these are actually high-energy particles with strong penetrability. In recognition of this significant discovery, Hess was awarded the Nobel Prize in Physics in 1936.

From the 1940s, scientists launched balloons equipped with cloud chambers and photographic plates into the stratosphere [e.g. 1, 2]. Through these experiments, they discovered that relativistic protons are the main component of cosmic rays. In fact, cosmic rays are composed of protons, helium, and other heavy nuclei, as well as a small number of electrons. Cosmic rays span a wide energy range from hundreds of MeV to more than 100 EeV, covering 11 orders of magnitude (see Fig. 1.1). Such a broad energy spectrum indicates different origins for cosmic rays with varying energy levels.

The cosmic ray spectrum can be described by a power-law distribution with an index of -2.7. Around 3 PeV, this spectrum softens, and the spectral index becomes $\sim$ -3.1 [e.g. 3]. This region is known as the 'knee.' At 4 EeV, the spectrum hardens, and the spectral index returns to -2.7 [e.g. 4, 5]. This region is now known as the 'ankle.' Currently, the most popular explanation is that cosmic rays with energy below the knee are produced by galactic sources, such as galactic supernova remnants, while cosmic rays with energy beyond the ankle have extragalactic origins, such as gamma-ray bursts and active galactic nuclei. The origin of cosmic rays between the knee and the ankle is still under debate. In the following we will briefly introduce these three promising candidates of cosmic rays.

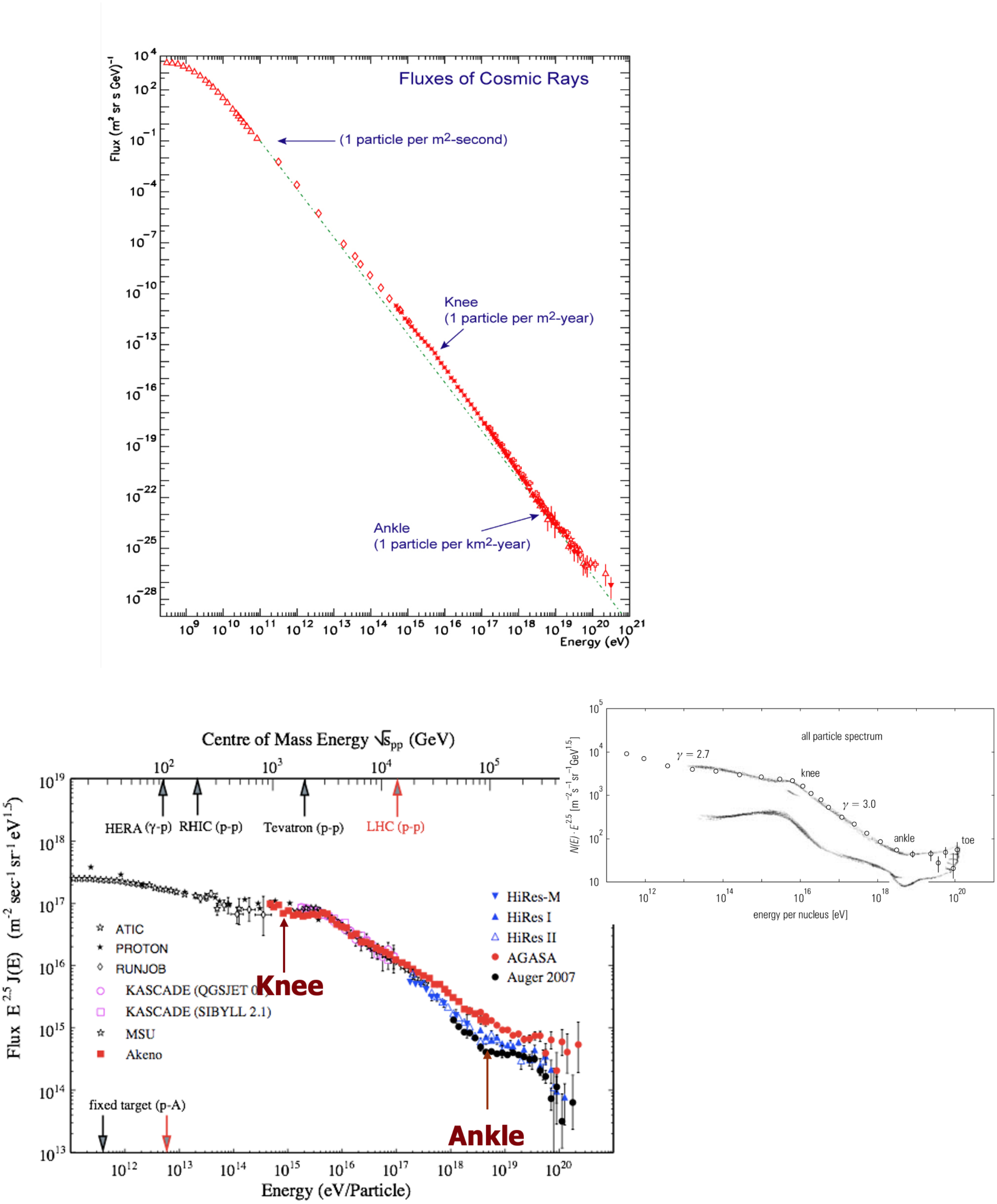

Figure 1.1: Cosmic ray spectrum in a wide energy band. The upper figure is taken from Cronin *et al.* [6]. The lower is taken from Blümer *et al.* [7] with some modification.

Figure 1.2: A composite image of the Crab Nebula from Hubble Space Telescope. Source link: `https://hubblesite.org/home`. Author: NASA, ESA, J. Hester and A. Loll (Arizona State University).

1.2 Supernova Remnants

When the nuclear fusion reaction in a main-sequence star ceases, there is no longer sufficient thermal pressure to counteract gravity, and the star begins to collapse. If the star is massive enough, an energetic explosion occurs in its envelope, resulting in a supernova (SN). During the burst, a non-relativistic shock can be produced and accelerate particles. The shock velocity can reach thousands of kilometers per second.

One of the most famous and well-studied SNe is SN 1054, which was recorded in great detail by Chinese, Arabian and Japanese astronomers. In 1731, a nebula was discovered at the position of this SN, now known as the Crab Nebula. This nebula is the remnant of the supernova explosion.

Based on their lightcurves and the absorption lines in their spectra, SNe can be divided into different categories. Depending on the presence of hydrogen lines, SNe are classified as Type I (without hydrogen lines) and Type II (with hydrogen lines) [8, 9]. Under these two main categories, SNe can be further subdivided based on their spectra. For example, Type Ia supernovae present strong ionized silicon absorption lines, while Type Ib/c has weak or no such absorption lines. Type Ib supernovae show strong neutral helium lines, which distinguish them from Type Ic.

The progenitors of different types of SNe are also different. Type Ia SNe are produced by accreting white dwarfs that reach the Chandrasekhar limit. Type Ib and Ic are originated from massive stars which have already lost their outer envelopes through strong stellar winds. The progenitors of Type II SNe are also massive stars with at least $9M_{\odot}$. Heavier elements can be burned inside and produce structures like an onion. Each shell is composed of different elements, and the elements become heavier as you go deeper into the star. At a certain stage, core collapse occurs, producing Type II SNe.

After the explosion, a supernova remnant (SNR) can be found near the location of its progenitor (Fig. 1.2). Stellar materials driven by the explosion can reach 10% the speed of light, being highly supersonic and triggering an expanding shock wave. This

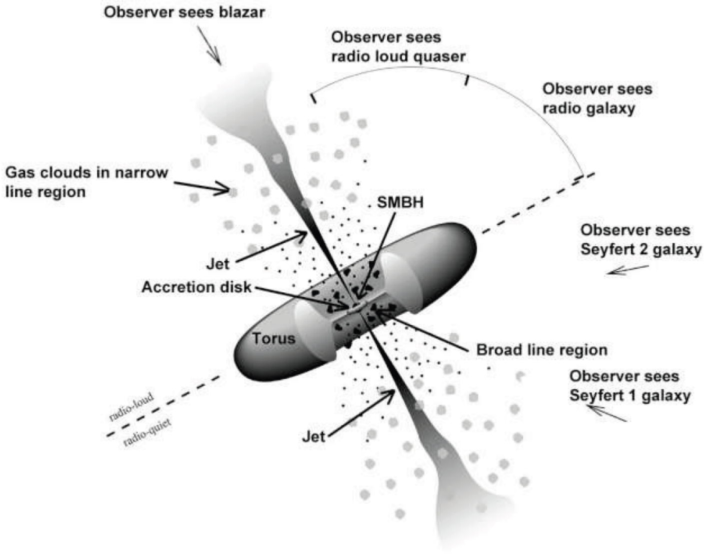

Figure 1.3: Schematic picture of the AGN unified model. This picture is adopted from Urry and Padovani [11].

shock wave sweeps up ambient medium and decelerates. This process can last hundreds or thousands of years. During this period, particles can be accelerated by the shock and become cosmic rays after escaping.

1.3 Active Galactic Nuclei

The luminosity from the central region of an active galactic nucleus (AGN) is much brighter than that from a normal galaxy, a phenomenon not explained by energy released through stellar nuclear fusion. This intense emission is believed to result from accretion processes around supermassive black holes at the galactic center. During accretion, a relativistic jet is generated and propogates along the rotational axis of the accretion disc. The electromagnetic spectra emitted by AGN span radio, microwave, infrared, optical, UV, X-ray, and gamma-ray bands.

In addition to exhibiting much luminous central regions compared to normal galaxies, AGN display rapid variability in luminosity, with periods ranging from a year to several days or even just a few hours. Emission lines from atoms and ions are also observed. Additionally, AGN can produce more photons in high energy bands, i.e., X-ray and gamma-ray as well as in the radio band.

Based on spectral features, AGN can be divided into several subclasses. Since the first discovery of quasars in the 1960s, many other subclasses have also been detected, such as Seyferts and blazars. It is well-argued that all of these subclasses can be explained by a unified model, in which distinct classes of AGN are actually variations of the same basic structure but viewed from different orientations [10, 11], as seen in Fig. 1.3.

Depending on the radio luminosity, it is convenient to categorize AGN into radio-loud and radio-quiet objects. The former has emissions predominantly contributed by the jet and the lobe, while the latter only has emissions from the accretion disc. Radio-loud AGN can then be further divided into radio-loud quasars, blazars, BL LAC objects and radio galaxies. Radio-quiet AGN include Seyfert galaxies and radio-quiet quasars.

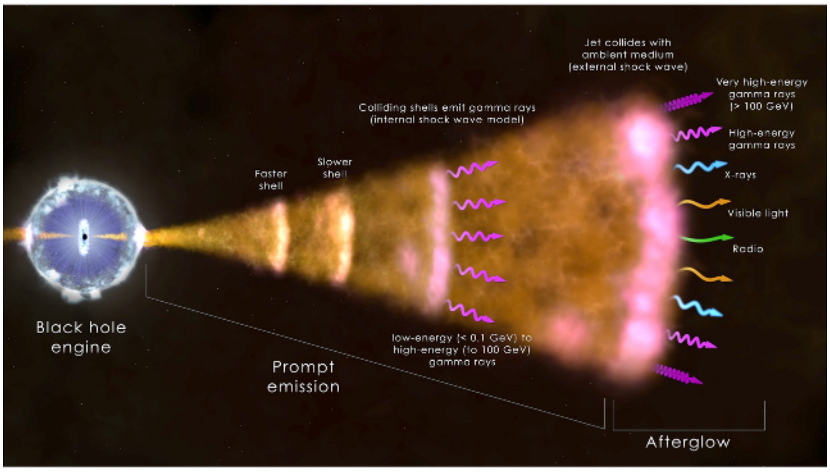

Figure 1.4: A schematic picture of GRBs from NASA. Source link: `https://earthsky.org/upl/2019/11/gamma-ray-burst-mechanism-lg.jpg`. Author: NASA/Goddard Space Flight Center/ICRAR.

1.4 Gamma-ray Bursts

Gamma-ray bursts (GRBs) are among the most catastrophic phenomena in our universe. Following Zhang [12], GRBs possess two main properties by definition. First, in the temporal domain, the term "burst" denotes a release of energy within a short time period, ranging from milliseconds to thousands of seconds. Second, in the spectral domain, "gamma-ray" represents the energy range in the hard X-ray/ soft gamma-ray band, from tens of keV to several MeV. This bursty emission is known as the prompt emission.

Observations of GRBs were long limited to the prompt emission phase until 1997 when the first afterglow was detected [13]. Distinguished from the prompt emission, afterglow emissions have a much wider energy range as well as a longer duration detectable days, weeks, months or even years after the burst in radio, optical, X-ray and gamma-ray bands.

The typical isotropic equivalent luminosity of GRBs is $\sim 10^{53}$ erg/s, comparable to releasing the total energy emitted by the sun throughout its entire life within less than one second. Due to this immense energy production, GRBs are also considered as prospective candidates for ultra-high energy cosmic rays (UHECR), neutrinos and gravitational waves.

AS GRBs constitute one of the main topics in my thesis, more detailed introductions can be found in Chapter. 3.

1.5 Shocks

Power-law distributions in electromagnetic spectra are frequently observed in high energy phenomena including those we mentioned above, strongly suggesting the non-thermal distribution of accelerated particles in these sources. This indicates Fermi acceleration in shocks as a prominent particle acceleration mechanism.

Shocks have long been proposed as a likely source to accelerate high-energy particles. When an object moves through a local fluid, disturbances propagate outwards with the speed of sound and interact with the ambient medium. Eventually, the remaining

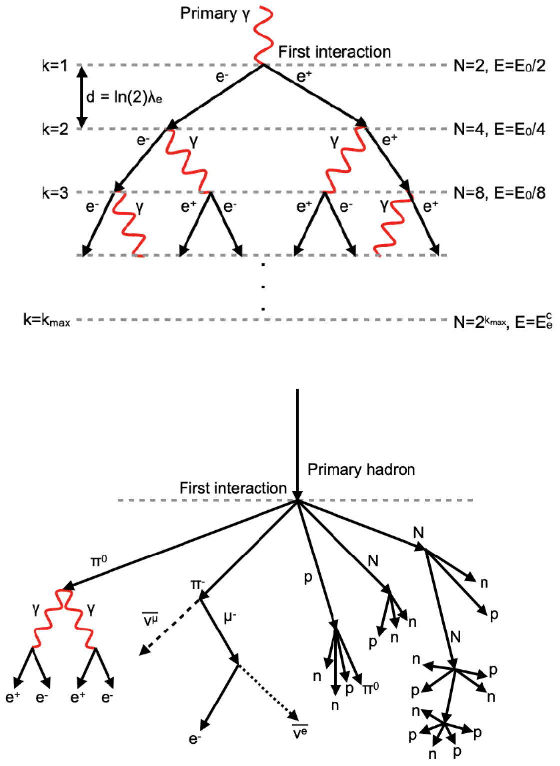

Figure 1.5: Schematic pictures of an electromagnetic shower and a hadronic shower. Upper: electromagnetic shower. Lower: hadronic shower. The original plots are taken from Ruiz Velasco [14].

fluid relaxes. However, if the object travels at a velocity greater than the sound speed, distributions triggered by this object are unable to propagate via sound waves and communicate to the rest of the fluid field. In this case, an abrupt discontinuity in the flow properties (pressure, density, etc.) would be generated, known as the shock. As one of the most promising sites to produce high-energy cosmic rays, we will give a round introduction on this phenomenon in the next chapter.

1.6 Imaging Atmospheric Cherenkov Technique

Before moving to the next chapter, I would like to introduce a quite important observational technique in high-energy astronomy. Due to the rapidly decreasing flux in high-energy bands for both photons and particles, we need telescopes with large effective areas to collect enough data, which is beyond the limitations for satellite-borne instruments. However, there exists another option.

Many ground-based instruments utilize Imaging Atmospheric Cherenkov Technique (IACT) to detect very-high-energy photons and charged particles. Penetrating the atmosphere, these photons as well as particles interact with air particles and produce a shower of secondary particles. Such a cascade is called as extensive air shower (EAS).

Depending on the primary hitting the atmosphere, two different showers can be generated. If the primary is a lepton or photon, it can produce an electromagnetic air shower by pair production and bremsstrahlung radiation. While for a primary hadron,

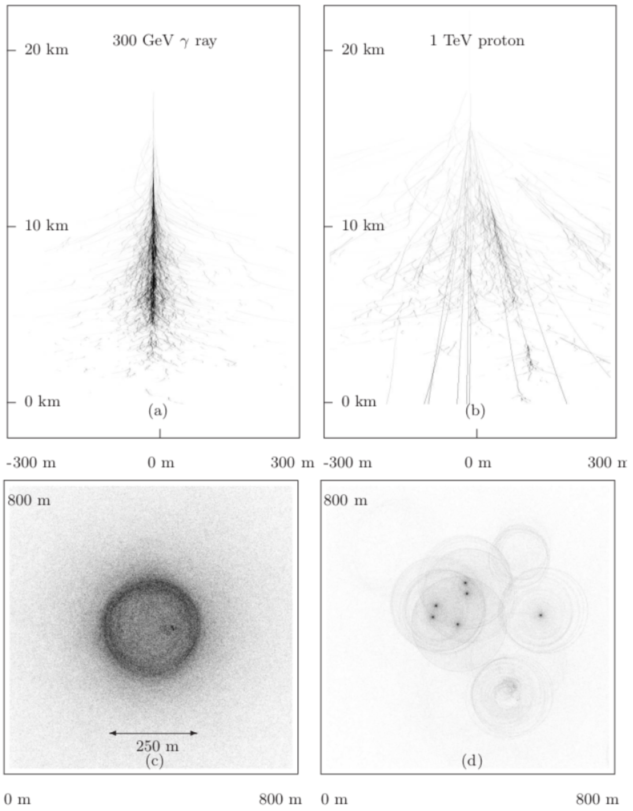

Figure 1.6: Comparison between gamma-ray and hadronic shower and Cherenkov emissions[15].

the corresponding air shower evolves differently and a hadronic shower occurs.

It is of significant importance for IACTs to distinguish photon-triggered showers and hadron-triggered showers. Here are some major differences. For electromagnetic shower, the lateral spread is smaller, inducing narrow showers. What's more, Hadronic showers exhibit a complex and variable structure due to the development of multiple electromagnetic sub-showers. Additionally, more muons are generated in hadronic showers by roughly two orders of magnitudes. An intuitive discrepancy between hadronic and electromagnetic shower can be seen in Fig. 1.6

Such a discrepancy provides an opportunity for us to distinguish these two kinds of showers through their emitted Cherenkov radiation. Cherenkov radiation is the emission of light when a charged particle moves through a dielectric medium at a speed greater than the speed of light in that medium. This phenomenon creates a faint blue glow, forming a cone of light with the charged particle at its center, as shown in Fig. 1.7.

Via IACTs, we can trace back to the directions of the incoming photons or hadrons according to the produced Cherenkov radiation. Since the projections of Cherenkov photons from showers, or the so-called light pools, distribute extensively on the ground. Ground-based telescopes are required for large detection areas to collect enough photons.

In gamma-ray imaging, the Cherenkov signal from an extensive air shower takes the form of a 3D ellipsoid, resulting in an elliptical image on the camera. The image position is contingent on the shower axis offset from the reflector axis. The major axis of the shower ellipse traces the path of the original gamma-ray, projecting onto both the sky and ground for estimating shower direction and impact point. The ellipse's length and width indicate the shower's longitudinal and lateral extent from a specific viewpoint.

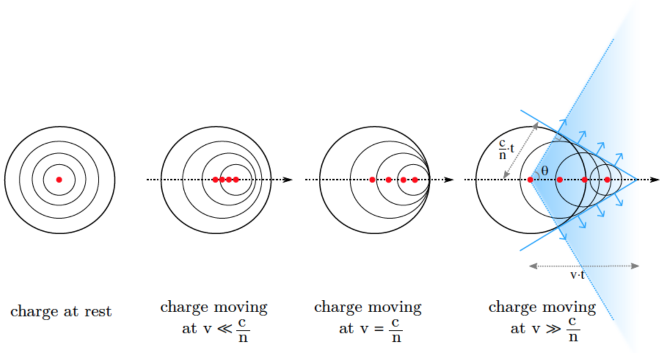

Figure 1.7: Origin of Cherenkov emissions [16].

Incorporating a second telescope into the light pool aids in mitigating uncertainties in direction and energy reconstruction.

Chapter 2

Shock, Fermi acceleration and radiation mechanisms

Shocks are a universal phenomena in astrophysics. Particles being accelerated to high energy through the Fermi mechanism at shocks are widely accepted as origins of electromagnetic emissions from various astrophysical objects. In the following sections, we will summarize the physics of shocks and Fermi acceleration.

2.1 Shock Dynamics

Before we study the physical properties across a shock, it is helpful to recall the theory of hydrodynamics, which can be used to study the evolution of a fluid.

2.1.1 Hydrodynamics

2.1.1.1 Non-relativistic Hydrodynamics

Neglecting the existence of magnetic fields, the equations to describe a single neutral fluid consist of three conservation laws for mass, momentum, and energy. In the non-relativistic regime, where the rest mass energy density is much larger than the kinetic energy density and the internal energy density, these three conservation equations can be written as:

$$\frac{\partial \rho}{\partial t} + \nabla \cdot (\rho \mathbf{u}) = 0; \tag{2.1}$$

$$\frac{\partial \mathbf{u}}{\partial t} + (\mathbf{u} \cdot \nabla)\, \mathbf{u} = -\frac{1}{\rho} \nabla p; \tag{2.2}$$

$$\frac{\partial \epsilon}{\partial t} + \nabla \cdot [(\epsilon + p)\, \mathbf{u}] = 0. \tag{2.3}$$

where ρ, p, are the mass density and pressure. $\epsilon = \frac{1}{2}\rho u^2 + e$ is the sum of the kinetic energy $\frac{1}{2}\rho u^2$ and the internal energy density e. $\mathbf{u}$ is the fluid velocity vector.

2.1.1.2 Relativistic Hydrodynamics

Without any energy source or external force, the mass conservation equation in the relativistic case can be formulated in the form as

$$\nabla_\mu (\rho u^\mu) = 0 \tag{2.4}$$

and energy and momentum conservation equations can be expressed as

$$\nabla_\mu T^{\mu\nu} = 0 \tag{2.5}$$

$T^{\mu\nu}$ is the energy-momentum tensor of the relativistic fluid.

The conservation equations can be written as

$$\frac{\partial}{\partial t}\begin{pmatrix} D \\ \boldsymbol{m} \\ E \end{pmatrix} + \nabla \cdot \begin{pmatrix} D\boldsymbol{u} \\ \boldsymbol{m}\boldsymbol{u} + p\mathbf{I} \\ \boldsymbol{m}c^2 \end{pmatrix} = 0 \tag{2.6}$$

in the laboratory frame, where $\boldsymbol{u}$, D, $\boldsymbol{m}$, E and p represents the fluid velocity, density, momentum density, total energy density and pressure, respectively [17].

Utilizing the Lorentz invariant thermodynamic quantities: the proper rest mass density ρ, the specific enthalpy h and the pressure p, the transformation to the local rest frame is

$$D = \gamma\rho, \tag{2.7}$$

$$\boldsymbol{m} = \rho h \gamma^2 \frac{\boldsymbol{u}}{c^2}, \tag{2.8}$$

$$E = \rho h \gamma^2 - p, \tag{2.9}$$

where γ is the Lorentz factor and c is the speed of light. The definition of he specific enthalpy h is given by

$$h = \frac{e+p}{\rho}. \tag{2.10}$$

Here e is the proper internal energy density.

2.1.1.3 Equation of State

To determine the jump conditions when crossing a shock front, we need to solve five conservation equations. However, the system above is not closed, as there are six variables and only five equations. One additional equation of state is required to close this system.

A widely accepted shortcut is to consider the fluid as an ideal gas. Introducing the so-called adiabatic index, the equation of state can be written as

$$p = (\hat{\gamma} - 1)e. \tag{2.11}$$

For a non-relativistic fluid, $\hat{\gamma} = 5/3$ and in the relativistic case, $\hat{\gamma} = 4/3$ considering monoatomic gas.

2.1.2 Hydrodynamic Shock Jump Conditions

Solving the hydrodynamic equations from the previous section allows us to determine the physical properties across the shock front, which are associated with the strength of the shock itself. These are known as the shock jump conditions or Rankine-Hugoniot conditions.

2.1.2.1 Jump Conditions in Non-relativistic Shocks

The fluid is separated by the shock front into two parts: the unperturbed region, or upstream and the perturbed region, or downstream. Three conservation laws need to be satisfied when crossing the shock front, and these can be written in the rest frame of the shock as

$$\rho_- u_- = \rho_+ u_+ \tag{2.12}$$
$$\rho_- u_-^2 + p_- = \rho_+ u_+^2 + p_+ \tag{2.13}$$
$$(\frac{1}{2}\rho_- u_-^2 + p_- + e_-)u_- = (\frac{1}{2}\rho_+ u_+^2 + p_+ + e_+)u_+. \tag{2.14}$$

Physical parameters with − and + are measured immediately upstream and downstream of the shock front.

Introducing the Mach number $M = \frac{u}{c_s} = \left(\frac{\rho u^2}{\hat{\gamma} p}\right)^{1/2}$, which reflects the strength of the shock, one can write the Rankine-Hugoniot conditions as:

$$\frac{\rho_+}{\rho_-} = \frac{(\hat{\gamma} + 1)M_-^2}{(\hat{\gamma} - 1)M_-^2 + 2}, \tag{2.15}$$
$$\frac{p_+}{p_-} = \frac{2\hat{\gamma} M_-^2 - \hat{\gamma} + 1}{\hat{\gamma} + 1}, \tag{2.16}$$
$$\frac{T_+}{T_-} = \frac{(2\hat{\gamma} M_-^2 - \hat{\gamma} + 1)[(\hat{\gamma} - 1)M_-^2 + 2]}{(\hat{\gamma} + 1)^2 M_-^2}. \tag{2.17}$$

The medium in the both upstream and downstream is considered to be in thermal equilibrium and T represents the corresponding temperature.

For non-relativistic shocks with a large Mach number $M \gg 1$, we have $\frac{\rho_+}{\rho_-} \simeq 4$, $\frac{p_+}{p_-} \simeq \frac{5}{4}M_-^2$ and $\frac{T_+}{T_-} \simeq \frac{5}{16}M_-^2$. One can see that the upper limit for the compression ratio by a strong non-relativistic shock is 4.

2.1.2.2 Jump Conditions in Relativistic Shocks

Following a similar method used in the non-relativistic case, the three relativistic Rankine-Hugoniot conditions in the shock rest frame can be described as

$$\gamma_- \rho_- u_- = \gamma_+ \rho_+ u_+ \tag{2.18}$$
$$\gamma_-^2 h_- u_-^2 + p_- = \gamma_+^2 h_+ u_+^2 + p_+ \tag{2.19}$$
$$\gamma_-^2 h_- u_- = \gamma_+^2 h_+ u_+ \tag{2.20}$$

where γ_- and γ_+ are the Lorentz factors in upstream and downstream.

If the medium upstream is cold ($e_- = p_- = 0$), which is a common condition for GRBs, we have the following solutions

$$\frac{\rho_+}{\rho_-} = \frac{\hat{\gamma}\gamma_{\rm rel} + 1}{\hat{\gamma} - 1}, \tag{2.21}$$
$$h_+/\rho_+ = \hat{\gamma}(\gamma_{\rm rel} - 1) + 1, \tag{2.22}$$
$$\gamma_-^2 = \frac{(h_+/\rho_+)^2(\gamma_{\rm rel} + 1)}{\hat{\gamma}(2 - \hat{\gamma})(\gamma_{\rm rel} - 1) + 2}, \tag{2.23}$$

here $\gamma_{\rm rel}$ represents the relative Lorentz factor between upstream and downstream.

For an ultra-relativistic shock with $\gamma_- \gg 1$, we obtain

$$u_+ = \hat{\gamma} - 1 = \frac{1}{3}, \tag{2.24}$$

$$\gamma_{\rm rel} = \gamma_-/\sqrt{2}, \tag{2.25}$$

$$\frac{\rho_+}{\rho_-} = 4\gamma_{\rm rel} \tag{2.26}$$

2.1.3 Relativistic Magnetohydrodynamics

The situation becomes more complicated when an electromagnetic field is taken into consideration. In ideal relativistic magnetohydrodynamics (MHD), the plasma is assumed to be a perfect conductor so that the electric field vanishes in the local fluid frame. In this case, the electromagnetic (EM) field can just be specified by the magnetic field.

Due to the existence of the magnetic field, the energy-momentum tensor includes two components, and should be rewritten as

$$T^{\mu\nu} = T^{\mu\nu}_{\rm fluid} + T^{\mu\nu}_{\rm EM} \tag{2.27}$$

$T^{\mu\nu}_{\rm fluid}$ is the fluid component,

$$T^{\mu\nu} = hu^\mu u^\nu + pg^{\mu\nu} \tag{2.28}$$

and $T^{\mu\nu}_{\rm EM}$ denotes the EM component,

$$T^{\mu\nu}_{\rm EM} = \frac{1}{4\pi}\left(F^\mu_\lambda F^{\lambda\nu} - \frac{1}{4}g^{\mu\nu}F^{\lambda\delta}F_{\lambda\delta}\right) \tag{2.29}$$

where

$$F^{\mu\nu} = \begin{pmatrix} 0 & E_x & E_y & E_z \\ -E_x & 0 & B_z & -B_y \\ -E_y & -B_z & 0 & B_x \\ -E_z & B_y & -B_x & 0 \end{pmatrix} \tag{2.30}$$

is the EM field tensor. $\mathbf{B} = (B_x, B_y, B_z)$ is the magnetic field and $\mathbf{E}$ is the electric field measured in the frame where the fluid's velocity is $\boldsymbol{\beta} = \mathbf{u}/c$. To constrain the electric field vanishing in the fluid rest frame, the generalised Ohm's law is augmented $\mathbf{E} = -\boldsymbol{\beta}\times\mathbf{B}$. Inserting the EM field tensor into the EM energy-momentum component, finally we get

$$T^{\mu\nu}_{\rm EM} = \frac{B^2}{4\pi}u^\mu u^\nu + \frac{B^2}{8\pi}g^{\mu\nu} - \frac{B^\mu B^\nu}{4\pi}. \tag{2.31}$$

The ideal MHD can be described as

- Mass conservation:

$$\nabla_\mu(\rho u^\mu) = 0; \tag{2.32}$$

- Energy-momentum conservation:

$$\nabla_\mu T^{\mu\nu} = 0; \tag{2.33}$$

- Maxwell's equations:

$$\nabla_\nu F^{\mu\nu} = 4\pi J^\mu; \tag{2.34}$$

$$\nabla_\lambda F_{\mu\nu} + \nabla_\mu F_{\nu\lambda} + \nabla_\nu F_{\lambda\mu} = 0 \tag{2.35}$$

J^μ here is the 4-current.

In MHD there exist three wave modes, the Alfvén mode, the fast and the slow magnetosonic modes, whose velocity can be denoted by $v_{\rm A}$, $v_{\rm fast}$ and $v_{\rm slow}$.

Two kinds of shock can exist. For the slow-mode shock,

$$v_{\mathrm{A}-} > v_- > v_{\mathrm{slow}-} \quad v_{\mathrm{A}+} > v_{\mathrm{slow}+} > v_+ \tag{2.36}$$

and for the fast-mode case,

$$v_- > v_{\mathrm{fast}-} > v_{\mathrm{A}-} \quad v_{\mathrm{fast}+} > v_+ > v_{\mathrm{A}+} \tag{2.37}$$

The slow-mode shock decreases the strength of the magnetic field across the shock, while the fast-mode one increases the strength.

2.1.3.1 MHD Waves

The existence of the magnetic field can break the isotropy in the fluid, which makes the propagation of waves more complicated. Recall the ideal MHD equation [12],

$$\begin{gathered}
\frac{\partial(\gamma\rho)}{\partial t} + \nabla\cdot(\gamma\rho\beta) = 0 \\
\frac{\partial}{\partial t}\left(\gamma^2 h\mathbf{u} + \frac{\mathbf{E}\times\mathbf{B}}{4\pi}\right) + \nabla\cdot\left[\gamma^2 h\mathbf{u}\otimes\mathbf{u} + \left(p + \frac{E^2+B^2}{8\pi}\right)\mathbf{I} - \frac{\mathbf{E}\otimes\mathbf{E}+\mathbf{B}\otimes\mathbf{B}}{4\pi}\right] = 0 \\
\frac{\partial}{\partial t}\left(\gamma^2 h - p - \gamma\rho + \frac{B^2+E^2}{8\pi}\right) + \nabla\cdot\left[\left(\gamma^2 h - \gamma\rho\right)\mathbf{u} + \frac{1}{4\pi}\mathbf{E}\times\mathbf{B}\right] = 0 \\
\frac{\partial\mathbf{B}}{\partial t} + c\nabla\times\mathbf{E} = 0 \\
\nabla\times\mathbf{B} = \frac{1}{c}\frac{\partial\mathbf{E}}{\partial t} + \frac{4\pi}{c}\mathbf{J} \\
\nabla\cdot\mathbf{B} = 0 \\
\nabla\cdot\mathbf{E} = 4\pi\rho_e \\
\mathbf{E} = -\frac{\boldsymbol{u}}{c}\times\mathbf{B}
\end{gathered} \tag{2.38}$$

where $\otimes$ represents the symbol of tensor product.

Now we assume the magnetic field $\mathbf{B} = B\hat{\mathbf{e}}_{\mathbf{z}}$, the wave propagation vector $\mathbf{k} = k_\perp\hat{\mathbf{e}}_x + k_{||}\hat{\mathbf{e}}_z$ ($k_\perp = k\sin\theta$ and $k_{||} = k\cos\theta$) and the perturbation vector $\xi = \xi_x\hat{\mathbf{e}}_x + \xi_y\hat{\mathbf{e}}_y + \xi_z\hat{\mathbf{e}}_z$. In a non-relativistic MHD fluid, the MHD wave propagation equation is

$$\begin{aligned}
\left[\omega^2 - (\hat{\mathbf{k}}\cdot\hat{\mathbf{b}})^2 v_{\mathrm{A}}^2\right]\xi =& \left[\left(v_s^2 + v_{\mathrm{A}}^2\right)(\hat{\mathbf{k}}\cdot\boldsymbol{\xi}) - v_{\mathrm{A}}^2(\xi\cdot\hat{\mathbf{b}})(\hat{\mathbf{k}}\cdot\hat{\mathbf{b}})\right]\hat{\mathbf{k}} \\
& - v_{\mathrm{A}}^2(\hat{\mathbf{k}}\cdot\boldsymbol{\xi})(\hat{\mathbf{k}}\cdot\hat{\mathbf{b}})\hat{\mathbf{b}},
\end{aligned} \tag{2.39}$$

where $v_s = \sqrt{\hat{\gamma}p/\rho_0}$ is the sound speed and $v_{\mathrm{A}} \equiv \frac{B_0}{\sqrt{4\pi\rho_0}}$. Disentangled along three dimensions, we have

$$\begin{aligned}
&\left(v_{\mathrm{A}}^2 k^2 + v_s^2 k_\perp^2\right)\xi_x + v_s^2 k_{||}k_\perp\xi_z = \omega^2\xi_x \\
&v_{\mathrm{A}}^2 k_{||}^2\xi_y = \omega^2\xi_y \\
&v_s^2 k_{||}k_\perp\xi_x + v_s^2 k_{||}^2\xi_z = \omega^2\xi_z
\end{aligned} \tag{2.40}$$

The y-component gives us the dispersion relation

$$\omega^2 = v_{\mathrm{A}}^2 k^2 \cos^2\theta. \tag{2.41}$$

Combing the other two equations we have

$$\omega^4 - \left(v_{\mathrm{A}}^2 + v_s^2\right) k^2 \omega^2 + v_{\mathrm{A}}^2 v_s^2 k^4 \cos^2\theta = 0, \tag{2.42}$$

which gives solutions

$$v^2 = \frac{v_{\mathrm{A}}^2 + v_s^2 \pm \sqrt{(v_{\mathrm{A}}^2 + v_s^2)^2 - 4v_{\mathrm{A}}^2 v_s^2 \cos^2\theta}}{2}. \tag{2.43}$$

Here we get the speed for fast and slow magnetsonic waves, which depend on the direction of the magnetic field and propagation.

2.1.3.2 Jump Conditions in Special Cases: Perpendicular Shocks

If the magnetic field in one side of the shock is perpendicular to the shock normal, it is the same on the other side. Note that in the shock rest frame, there is an associated electric field E upstream generated by Ohm's law, which should equal that downstream. Besides, the contribution to the internal energy and pressure should also be included. Thus, the relativistic shock jump conditions should be modified as:

$$n_- u_- = n_+ u_+, \tag{2.44}$$

$$E = u_- B_- = u_+ B_+, \tag{2.45}$$

$$\gamma_- \frac{h_-}{n_-} + \frac{E\gamma_- B_-}{4\pi n_- u_-} = \gamma_+ \frac{h_+}{n_+} + \frac{E\gamma_+ B_+}{4\pi n_+ u_+}, \tag{2.46}$$

$$u_- \frac{h_-}{n_-} + \frac{p_-}{n_- u_-} + \frac{(\gamma_- B_-)^2}{8\pi n_- u_-} = u_+ \frac{h_+}{n_+} + \frac{p_+}{n_+ u_+} + \frac{(\gamma_+ B_+)^2}{8\pi n_+ u_+} \tag{2.47}$$

Considering a cold upstream, we introduce the magnetization parameter in the upstream σ:

$$\sigma \equiv \sigma_- = \frac{B_-^2}{4\pi\rho_-} \tag{2.48}$$

For an ultra-relativistic case with $\hat{\gamma} = 4/3$, the downstream Lorentz factor γ_+ satisfies

$$\gamma_+^2 = \frac{8\sigma^2 + 10\sigma + 1 + (2\sigma + 1)\sqrt{16\sigma^2 + 16\sigma + 1}}{16(\sigma + 1)} \tag{2.49}$$

2.1.3.3 Jump Conditions in Special Cases: Parallel Shocks

If the plasma velocity is parallel to the magnetic field and the shock normal on both sides of the shock, $B_- = B_+$, we can get a purely hydrodynamic jump condition in the downstream:

$$v_- \to 1, \quad v_+ \to 1/3, \quad \gamma_+ \to 3\sqrt{2}/4, \tag{2.50}$$

$$\gamma_{\mathrm{rel}} \to \gamma_-/\sqrt{2}, \quad h_+/\rho_+ \to 2\sqrt{2}\gamma_-/3, \quad R = \rho_+/\rho_- \to 2\sqrt{2}\gamma_-. \tag{2.51}$$

However, a perpendicular component for a small range of magnetisation values is still possible to be generated, known as a 'switch-on' shock. It happens in the condition that

$v_{A-} < v_-$ and $v_{A+} > v_+$, which implies

$$\sqrt{1+\sigma^2} < \gamma_- < \sqrt{3}\sigma. \tag{2.52}$$

This condition requires a plasma where the energy density of the magnetic field significantly surpasses that of the rest mass, alongside a shock front normal closely aligning with the upstream magnetic field.

2.2 Particle Acceleration in the Non-Relativistic Case

After the discovery of cosmic rays, the mechanism that can accelerate particles to such high energies has been studied extensively. The first significant step in the theory of particle acceleration was taken by Enrico Fermi in 1949 [18]. He proposed that cosmic rays are generated and accelerated in the interstellar medium (ISM). These particles interact with randomized magnetic fields occupying the ISM space. Consider particles colliding with a moving magnetized cloud. Depending on the relative motion between particles and the cloud, particles can gain (head-on) or lose energy (tail-on) after collisions. Averaging over many collisions, the energy gain of particles is

$$\frac{\Delta E}{E} \propto \left(\frac{v}{c}\right)^2, \tag{2.53}$$

and clearly this acceleration mechanism is second order.

2.2.1 Second Order Fermi Acceleration

Assume a magnetized cloud moving along the x-axis with a velocity V. A particle with an initial energy E_1 and a velocity v_1 enters the cloud. θ_1 is the angle between v_1 and x-axis.

The probability of particles colliding with the cloud with the angle θ_1 can be expressed as

$$P(\theta_1) = \frac{1}{2}\left(\frac{v_1 - V\cos\theta_1}{v_1}\right) \tag{2.54}$$

which is proportional to the relative velocity between the particle and the cloud.

The particle energy measured in the cloud rest frame $E_1^{'}$ can be obtained by Lorentz transformation

$$E_1^{'} = \Gamma E_1 \left(1 - \frac{V}{c}\cos\theta_1\right) \tag{2.55}$$

Inside the cloud, the particle energy is conserved between each collisions, and the final energy when this particle leave the cloud $E_2^{'}$ should equal to $E_1^{'}$. Transforming back outside the cloud,

$$E_2 = \Gamma E_2^{'} \left(1 + \frac{V}{c}\cos\theta_2^{'}\right). \tag{2.56}$$

The energy gain of a relativistic particle per cycle is

$$\frac{\Delta E}{E_1} = \Gamma^2 \left(1 - \frac{V}{c}\cos\theta_1\right)\left(1 + \frac{V}{c}\cos\theta_2^{'}\right) - 1. \tag{2.57}$$

Note that the average value on $\cos\theta_1$ is

$$\langle\cos\theta_1\rangle = \int_0^{\pi} \cos\theta_1 P(\theta_1) d\cos\theta_1 \tag{2.58}$$

$$= -\frac{V}{3v_1} \tag{2.59}$$

and

$$\left\langle \cos\theta_2' \right\rangle = 0 \tag{2.60}$$

since the scattering inside the cloud is completely random.

Therefore, for non-relativistic magnetized cloud ($\Gamma = 1$), the average energy gain is

$$\left\langle \frac{\Delta E}{E_1} \right\rangle \simeq \frac{1}{3}\left(\frac{V}{v_1}\right)^2 \tag{2.61}$$

For second order Fermi acceleration, two main difficulties arise in explaining astrophysical observations. First, as mentioned earlier, this acceleration mechanism is inefficient. Second, the resulting spectrum is not universal and proves challenging to fit to observational data.

2.2.2 First Order Fermi Acceleration

In second order Fermi acceleration, the energy gain during a head-on collision is of the order V/c. However, the discrepancy between the probabilities of head-on and tail-on collisions is also of the same order, which reduces the acceleration efficiency.

Assuming particles consistently experience head-on collisions and avoid tail-on collisions, the acceleration process becomes more efficient and of first order. This type of mechanism is referred to as first order Fermi acceleration. A typical case is diffusive shock acceleration (DSA).

Typically, there exists magnetic turbulence preceding and following a shock, which can interact with particles and alter their directions of motion. Consider a particle upstream crosses the shock front and moves to downstream. Subsequently, this particle may be scattered by turbulence and return back to upstream. As seen in the downstream frame, the particle experiences a head-on collision and gains energy. Therefore, this process exhibits characteristics of first-order acceleration.

To get the spectral properties, in the following we study this acceleration mechanism through two methods.

2.2.2.1 Microscopic Approach

For simplicity, we consider the non-relativistic case. A particle upstream with momentum p_- crosses the shock front with a pitch angle μ_- ($1 \geq \mu_- > -u_-/v_-$) and moves to downstream. Its momentum measured in the downstream frame is [19]

$$p_+ = p_-\left(1 + \mu_-\frac{\Delta u}{v_-}\right) \tag{2.62}$$

where $\Delta u = u_- - u_+$. u_- and u_+ are the fluid velocity upstream and downstream, respectively (Detailed deduction in Appendix. A). This particle is then scattered and change its pith angle, while the momentum magnitude is conserved. If it can recrosses the shock later, with a pitch angle μ_+ ($-1 \leq \mu_+ < -u_+/v_+$), its momentum measured in the upstream frame is

$$\bar{p}_- = p_+ \left(1 - \mu_+ \frac{\Delta u}{v_+}\right) \tag{2.63}$$

Assuming an isotropic distribution, the probability of a particle crossing the shock is proportional to the relative velocity between the shock front and itself $|\mu v + u|$. The average gained momentum in one shock crossing cycle is then

$$\left\langle \frac{\Delta p}{p_-} \right\rangle = \frac{\int_{-u_-/v_-}^{1} d\mu_- \, |\mu_- v_- + u_-| \int_{-1}^{-u_+/v_+} d\mu_+ \, |\mu_+ v_+ + u_+| \left(\frac{\bar{p}_- - p_-}{p_-}\right)}{\int_{-u_-/v_-}^{1} d\mu_- \, |\mu_- v_- + u_-| \int_{-1}^{-u_+/v_+} d\mu_+ \, |\mu_+ v_+ + u_+|}. \tag{2.64}$$

Considering a relativistic particle with $v \gg u$, we get

$$\begin{aligned} \Delta p &= p_- \left(1 + \mu_- \frac{\Delta u}{v}\right)\left(1 - \mu_+ \frac{\Delta u}{v}\right) - p_- \\ &= p_- \left(\mu_- - \mu_+\right) \frac{\Delta u}{v} \end{aligned} \tag{2.65}$$

Ignoring terms of order u/v, the average gained momentum is

$$\begin{aligned} \left\langle \frac{\Delta p}{p_-} \right\rangle &= \frac{\Delta u \int_0^1 d\mu_- \int_{-1}^0 d\mu_+ \, |\mu_- \mu_+| \left(\mu_- - \mu_+\right)}{v \int_0^1 d\mu_- \int_{-1}^0 d\mu_+ \, |\mu_- \mu_+|} \\ &= \frac{\Delta u \int_0^1 d\mu_- \int_{-1}^0 |\mu_-| \left(\mu_-/2 + 1/3\right)}{v/4} \\ &= \frac{4\Delta u}{3v}. \end{aligned} \tag{2.66}$$

Not all of the particles downstream can recross the shock front. Some of them can be swept to far downstream and escape. The flux of particles moving from upstream to downstream is

$$\begin{aligned} \dot{n}_{\text{cross}} &= 2\pi p_+^2 \int_{-u_+/v_+}^{1} |\mu_+ v_+ + u_+| \, f_+\left(p_+\right) d\mu_+ \\ &\simeq 2\pi p_+^2 v f_+\left(p_+\right) \int_0^1 |\mu_+| \, d\mu_+ \\ &= 2\pi p_+^2 v f_+\left(p_+\right)/2 \\ &= v\mathcal{N}_+/4 \end{aligned} \tag{2.67}$$

where $\mathcal{N}_+$ is the particle number. The flux of escaping particles equals $\dot{n}_{\text{cross}}$ minus the flux that return back to upstream,

$$\begin{aligned} \dot{n}_{\text{esc}} &= \dot{n}_{\text{cross}} - 2\pi p_+^2 \int_{-1}^{-u_+/v_+} |\mu_+ v_+ + u_+| \, f_+\left(p_+\right) d\mu_+ \\ &= 2\pi p_+^2 \int_{-1}^{1} \left(\mu_+ v_+ + u_+\right) f_+\left(p_+\right) d\mu_+ \\ &= \mathcal{N}_+ u_+. \end{aligned} \tag{2.68}$$

Hence the escape probability is

$$P_{\text{esc}} = \frac{\dot{n}_{\text{esc}}}{\dot{n}_{\text{cross}}} = \frac{4u_+}{v}. \tag{2.69}$$

In a steady state, the flux of particles with momentum larger than $p + \Delta p$ must equal the flux of such particles that recross the shock

$$\int_{p+\Delta p}^{\infty} dp' \dot{n}_{\mathrm{cross}}(p') = (1 - P_{\mathrm{esc}}) \int_{p}^{\infty} dk \dot{n}_{\mathrm{cross}}(p'). \tag{2.70}$$

Since $\Delta p/p \simeq \Delta u/v$, much smaller than unity in the non-relativistic case, the equation above can be simplified as

$$\left\langle \frac{\Delta p}{p} \right\rangle p\mathcal{N}_+ = P_{\mathrm{esc}} \int_{p}^{\infty} dp' \mathcal{N}_+(p'). \tag{2.71}$$

If $\left\langle \frac{\Delta p}{p} \right\rangle$ is independent of p, we can get the final solution

$$\mathcal{N}_+ = Ap^{-1-P_{\mathrm{esc}}/\langle \Delta p/p \rangle} \tag{2.72}$$

$$= Ap^{2-3u_-/\Delta u}. \tag{2.73}$$

Thus the phase space distribution f is

$$f \propto p^{-3u_-/\Delta u}. \tag{2.74}$$

For a strong non-relativistic strong, the compression ratio $r = u_-/u_+ = 4$, thus

$$f \propto p^{-4}. \tag{2.75}$$

Similar deductions and discussions on microscopic approach can been found in Bell [20, 21].

2.2.2.2 Macroscopic Approach

Another method to get the spectral properties accelerated by a shock is to solve the particle transport equation [22–24]. In a one-dimensional non-relativistic shock propagating along the x-axis, the particle distribution near the shock front in the non-relativistic case is nearly isotropic, allowing us to use

$$f = f_0 - \lambda \frac{\partial f_0}{\partial x} \mu \tag{2.76}$$

where f_0 is the isotropic part and λ is the mean free path of the interaction between particles and the wave.

the particle transport equation can be written as,

$$\frac{\partial f_0}{\partial t} + u \frac{\partial f_0}{\partial x} = \frac{\partial}{\partial x} \left(D \frac{\partial f_0}{\partial x} \right) + \frac{1}{3} \frac{du}{dx} p \frac{\partial f_0}{\partial p} + Q \tag{2.77}$$

where $D = \frac{1}{3}\lambda v \mu$ is the diffusion coefficient. The second term on the left side is the advection term. On the right side of the equation, the three terms denote diffusion, adiabatic expansion and extra sources or sinks.

Considering a time-steady condition without external sources, the transport equation can be simplified as

$$u \frac{\partial f_0}{\partial x} - \frac{\partial}{\partial x} \left(D \frac{\partial f_0}{\partial x} \right) = 0. \tag{2.78}$$

In each half plane (upstream and downstream), the solution has the form of

$$f_i = A_i(p_i) + B_i e^{\int_0^x \frac{u_i dx'}{D_i}} \tag{2.79}$$

To solve this transport equation, we need to impose several boundary conditions. Far downstream $x \to \infty$, the particle distribution should be finite $f_+ < \infty$, hence we have $B_+ = 0$. For far upstream $x \to -\infty$, $\lim_{x \to \infty} f_-(x, p) = A_-(p)$. Assuming particles produced at the shock, $A_- = 0$. Now the solution should be

$$f_0(x, p) = \begin{cases} A_+(p), x > 0 \\ \\ B_- e^{\int_0^x \frac{u_- dx'}{D_-}}, x < 0 \end{cases} \tag{2.80}$$

Note $p_+ = p_- \left(1 + \frac{\Delta u}{v}\mu\right)$ considering transform between downstream and upstream, and insert Eq. 2.80 into Eq. 2.76, we have

$$f = \begin{cases} A_+ \left(p_- + \frac{\Delta u}{v} p_- \mu\right), x = 0^+ \\ \\ B_-(p_-) \left(1 - \frac{3u_1\mu}{v}\right), x = 0^- \end{cases} \tag{2.81}$$

Taking a Taylor expansion,

$$f = \begin{cases} A_+ + \frac{\Delta u}{v} \mu p_- \frac{\partial A_+}{\partial p}, x = 0^+ \\ \\ B_- - B_- \frac{3u_-}{v} \mu, x = 0^- \end{cases} \tag{2.82}$$

This solution should be continuous at the shock for all μ, hence

$$A_+ = B_- \tag{2.83}$$

$$\frac{\Delta u}{v} p \frac{\partial A_+}{\partial p} = -B_- \frac{3u_-}{v}. \tag{2.84}$$

Finally we have

$$A_+ \propto p^{-s} \tag{2.85}$$

where $s = \frac{3u_-}{\Delta u}$.

2.2.3 Pitch-Angle Scattering of Particles by Alfvén Waves

Let us first recall the motion of charged particles in a uniform magnetic field along the z axis. The equation of motion is

$$m \frac{d\boldsymbol{v}}{dt} = e \frac{\boldsymbol{v} \times \boldsymbol{B_0}}{c} \tag{2.86}$$

where m and e represent the mass and charge of the particle. B_0 is the strength of the magnetic fields.

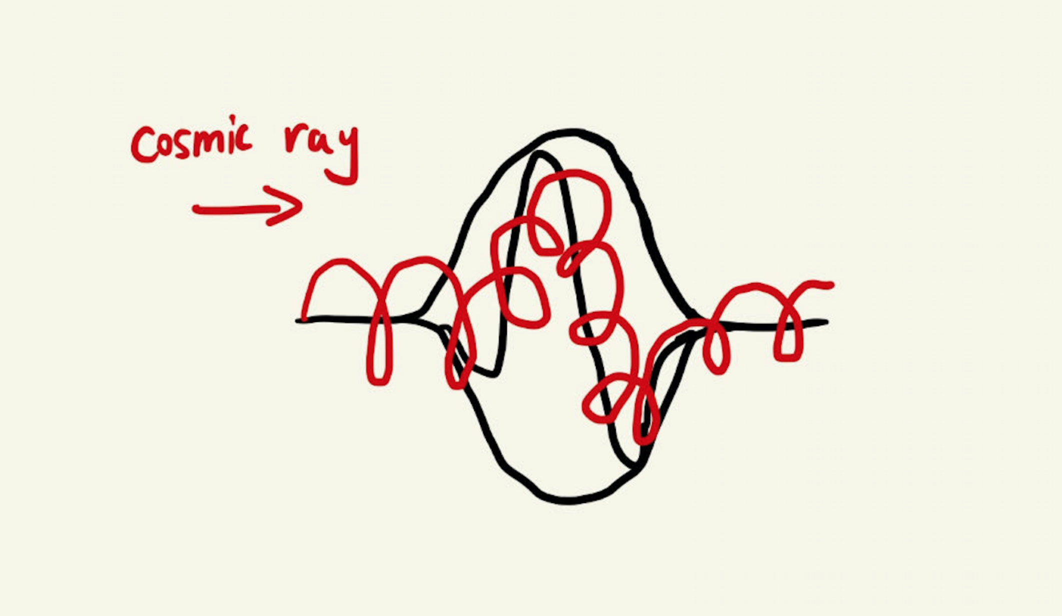

Figure 2.1: Interaction between a particle and a wave packet. The original figure is adapted from Kulsrud [25].

In the Cartesian coordinate the solution can be written as

$$v_x = v_\perp \sin(\Omega t + \phi) \tag{2.87}$$
$$v_y = v_\perp \cos(\Omega t + \phi)$$
$$v_z = v_\parallel \tag{2.88}$$

where $v_\perp, v_\parallel$ and ϕ are constant. $\Omega = eB_0/mc$ is the gyro-frequency of the particle.

The position of the particle is then $\boldsymbol{r} = \int \boldsymbol{v} dt$

$$x = -\frac{v_\perp}{\Omega}\cos(\Omega t + \phi) + X_0 \tag{2.89}$$
$$y = \frac{v_\perp}{\Omega}\sin(\Omega t + \phi) + Y_0$$
$$z = v_\parallel t = Z_0$$

Charged particles would rotate along the magnetic line and do gyro-motion.

Consider an interaction between one charged particle and linearly polarized Alfvén wave packets which results in a random diffusion in the pitch angle (see Fig. 2.1) [25].

Assume that the length of a single wave packet is L within one period and the Alfvén wave is polarized in the x direction. We choose a coordinate frame in which this wave packet is at rest. A charged particle moves from the left with a velocity $v_z > 0$ along the z direction, so the z position of the particle is $z_0 + v_z t$. The perturbed magnetic field in the Alfvén wave behaves sinusoidally as

$$\delta B_\perp = \hat{x}\delta B \sin\left(kz - \omega t\right). \tag{2.90}$$

The particle would rotate along the regular field B_0 with a frequency Ω, and its velocity in the y direction is:

$$v_y = v_\perp \sin\left(\Omega t + \phi\right) \tag{2.91}$$

where ϕ represents the random phase between the particle and the wave. The z component of the Lorentz force at the particle is

$$\begin{aligned} (v \times B)_z = & \quad -ev_\perp \delta B_\perp \\ = & \quad -ev_\perp \delta B_x \sin\left(kz_0 + kv_z t\right) \sin\left(\Omega t + \phi\right) \\ = & \quad \frac{1}{2} ev_\perp \delta B_x \{\cos\left[(kv_z - \omega + \Omega)t + (kz_0 + \phi)\right] \\ & \quad - \cos\left[(kv_z - \omega - \Omega)t + (kz_0 - \phi)\right]\} \end{aligned} \tag{2.92}$$

Integrating over a time interval, the first term can average out due to the high frequency in t, while the second term may not average out because of its lower frequency if

$$k_z v_z - \omega - \Omega \approx 0 \tag{2.93}$$

In this condition, the change in the z component of momentum is

$$\begin{aligned} \Delta p_z \quad & = e \int dt \left(\frac{v \times B}{c}\right)_z \\ & = \frac{1}{2} \frac{ev_\perp \delta B}{c} \frac{2\pi}{kv_z} \cos(kz_0 - \phi) \\ & \approx \pi \frac{ev_\perp \delta B}{c\Omega} \cos\phi' \\ & = \pi \frac{e\gamma v_\perp}{c} \frac{\delta B mc}{eB} \cos\phi' \\ & = \pi p_\perp \sin\theta \left(\frac{\delta B}{B}\right) \cos\phi'. \end{aligned} \tag{2.94}$$

Here we adopt the length of the wave packet as $L = 2\pi/k$ and the relative phase $\phi' = kz_0 - \phi$. τ is the time for the particle to cross the wave packet. Assume that τ equals to the wave period $\tau = 2\pi/(kv_z - \omega) = 2\pi/k(v_z - v_\mathrm{A})$. Since in most cases $v_\mathrm{A} \ll v_z$, we have $\tau \approx 2\pi/kv_z$.

The particle energy keeps constant since there is no electric field in the rest frame of the wave packet. This interaction only changes the pitch angle. Using $p_z = p\cos\theta$, we have

$$\delta(p\cos\theta) \quad = -p\sin\theta\delta\theta = \pi p \sin\theta \left(\frac{\delta B}{B}\right) \cos\phi' \tag{2.95}$$

$$\delta\theta \quad = -\pi \frac{\delta B}{B} \cos\phi' \tag{2.96}$$

whether $\delta\theta$ increases or decreases depends on the initial relative phase ϕ' of the interaction.

Suppose that wave packets locate tightly one after another with random phases. In a time t, a particle can interact with these wave packets t/τ times. After several interactions, the square of the total change is

$$\left\langle (\Delta\theta)^2 \right\rangle = \sum \left\langle (\delta\theta)^2 \right\rangle = \frac{t}{\tau} \frac{\pi^2}{2} \left\langle \left(\frac{\delta B}{B}\right)^2 \right\rangle \tag{2.97}$$

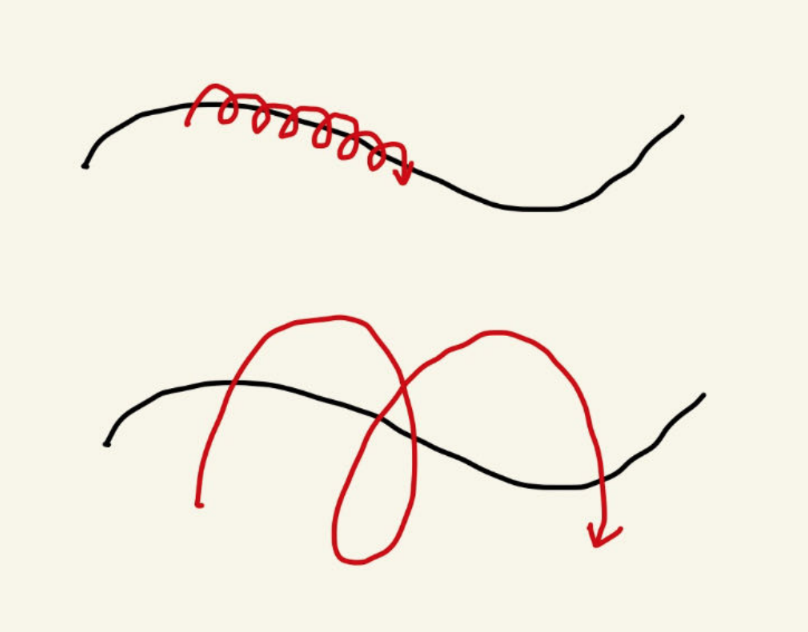

Figure 2.2: Negligible pitch-angle scattering unless $\lambda \approx r_L$. The original figure is adapted from Kulsrud [25].

where $\langle(\cos^2\phi)\rangle = \frac{1}{2}$.

So the diffusion rate can be calculated as

$$\frac{\left\langle (\Delta\theta)^2 \right\rangle}{2t} = \frac{\pi}{8}\Omega \left\langle \left(\frac{\delta B}{B}\right)^2 \right\rangle \tag{2.98}$$

For particles moving from right with $v_z < 0$, the resonant condition becomes $kv_z - \omega + \Omega = 0$. We can see that the pitch-angle scattering is identical for left-moving and right-moving particles for linearly polarized Alfvén waves. The consequence of such a linearly polarized wave is equivalent to a combination of a right circularly polarized and a left circularly polarized wave.

In the above we choose the Alfvén wave with its wavelength $\lambda/2\pi \approx v/\Omega \approx r_L$, the gyro-radius of the particle. For waves with much longer wavelengths, a particle would travel along the field line and its pitch angle doesn't change after crossing the wave packet. For waves with much smaller wavelengths, the influence on the particle caused by rapidly oscillating field is also negligible (see Fig. 2.2).

Another remarkable point is as follows. Assume that the wave packet has a length of n wavelengths, so $\left\langle (\Delta\theta)^2 \right\rangle$ enhances by a factor of n^2 and τ also increases by n. The corresponding diffusion rate is then

$$\frac{\left\langle (\Delta\theta)^2 \right\rangle}{2t} = n\frac{\pi}{8}\Omega \left\langle \left(\frac{\delta B}{B}\right)^2 \right\rangle \tag{2.99}$$

For a smooth turbulence spectrum

$$\left(\frac{\delta B}{B}\right)^2 = \Delta k I(k) \tag{2.100}$$

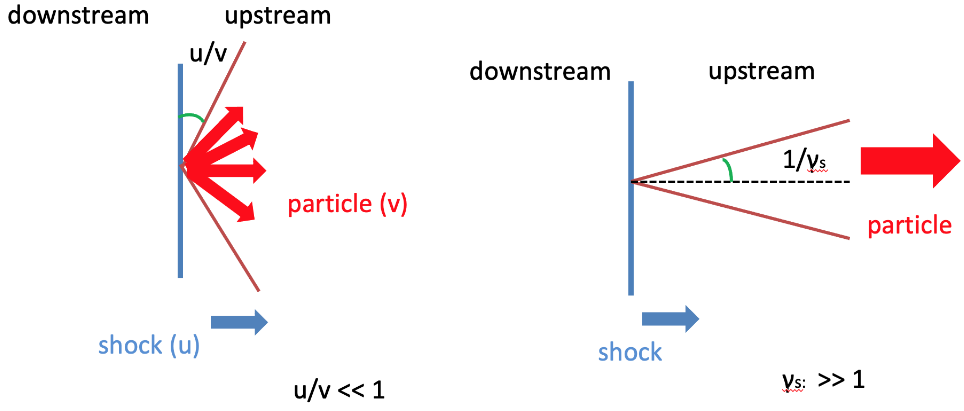

Figure 2.3: Schematic pictures of the particle distribution at both the non-relativistic and the relativistic shock.

where Δk is inversely related to the length of the wave packet $\Delta k = k/n = 1/nr_L$. Hence the diffusion coefficient is independent of n and only relies on $I(k)$ at the resonant wave number $k = 1/r_L$

$$D_\theta = \frac{\left\langle (\Delta\theta)^2 \right\rangle}{2t} = \frac{\pi}{8}\Omega I \tag{2.101}$$

2.3 Particle Acceleration in the Relativistic Case

2.3.1 Comparison between non-relativistic and relativistic shocks

Depending on its velocity, a shock can be classified into the non-relativistic and relativistic cases. The differences in velocity leads to substantial discrepancies in the physical properties of the shock.

In a non-relativistic shock, the particle velocity v is significantly larger than the shock velocity u. As a consequence, particles downstream can easily outrun the shock and move to upstream. Particles far downstream still have the possibility to return back to upstream and undergo acceleration again. The particle distribution near the shock front in a non-relativistic case is nearly isotropic, and the spatial diffusion equation can be solved to obtain the particle distribution. However, the particle can only gain a small fraction of energy compared to its initial energy after completing a crossing cycle.

However, the situation in the relativistic case is notably different. In this scenario, the shock velocity becomes comparable to the particle velocity. Thus, for particles capable of moving to upstream, their trajectories downstream must be close to the shock compared to their gyro-radius in the shock rest frame. When crossing the shock from downstream to upstream, these particles are confined within a cone with a small opening angle $1/\gamma_\mathrm{s}$ as seen in the upstream rest frame, an effect of relativistic beaming (the right panel in Fig. 2.3). Obviously, the particle distribution at a relativistic shock is highly anisotropic, therefore the diffusion approximation for the spatial transport is no longer feasible.

2.3.2 Energy Gain at Relativistic Shocks

Because of the kinematical properties and the anisotropic angular distribution of particles near the shock, the energy gain during one crossing cycle in the relativistic case differs significantly from that in the non-relativistic case. To estimate the energy ratio

Table 2.1: Physical quantities in URF, DRF and SRF for the ultra-relativistic shock. This table is adopted from Achterberg *et al.* [26].

Quantity	**URF**	**DRF**	**SRF**
Shock speed	$\beta_{\mathrm{s}} \approx 1 - \frac{1}{2\Gamma_{\mathrm{s}}^2}$	$\bar{\beta}_{\mathrm{s}} \approx \frac{1}{3}$	0
Upstream fluid speed	0	$\bar{\beta}_{\mathrm{u}} \approx -\left(1 - \frac{1}{\Gamma_{\mathrm{s}}^2}\right)$	$\widetilde{\beta_{\mathrm{u}}} = -\beta_{\mathrm{s}}$
Downstream fluid speed	$\beta_{\mathrm{rel}} \approx 1 - \frac{1}{\Gamma_{\mathrm{s}}^2}$	0	$\widetilde{\beta_{\mathrm{d}}} \approx -\frac{1}{3}$
Particle energy	$E = \Gamma_{\mathrm{rel}}\ (1 + \beta_{\mathrm{rel}}\bar{\mu})\ \bar{E}$	$\bar{E} = \Gamma_{\mathrm{rel}}\ (1 - \beta_{\mathrm{rel}}\mu)\ E$	$\widetilde{E}$
Cosine flight direction	$\mu = \frac{\bar{\mu} + \beta_{\mathrm{rel}}}{1 + \beta_{\mathrm{rel}}\bar{\mu}}$	$\bar{\mu} = \frac{\mu - \beta_{\mathrm{rel}}}{1 - \beta_{\mathrm{rel}}\mu}$	$\widetilde{\mu}$
Edge of loss cone	$\sin\theta_{\mathrm{c}} = 1/\Gamma_{\mathrm{s}}$	$\bar{\mu} = \bar{\beta}_{\mathrm{s}} \approx \frac{1}{3}$	$\widetilde{\mu} = 0$

before and after one cycle, we need to do Lorentz transformations for various physical quantities between different frames of reference: the upstream rest frame (URF), downstream rest frame (DRF) and shock rest frame (SRF), as listed in Table 2.1.

Consider a particle moving from upstream to downstream and back, with an initial energy E_{i} and a final energy E_{f}. Direction cosine $\mu_{\to\mathrm{d}}$ and $\mu_{\to\mathrm{u}}$ represents the angles for particles crossing the shock into downstream and upstream. Here we assume the scattering in both the upstream and the downstream flow is elastic so the particle energy in URF and DSF remains constant. In URF, the gained energy ratio can be expressed as

$$\frac{E_{\mathrm{f}}}{E_{\mathrm{i}}} = \frac{1 - \beta_{\mathrm{rel}}\mu_{\to\mathrm{d}}}{1 - \beta_{\mathrm{rel}}\mu_{\to\mathrm{u}}}, \tag{2.102}$$

or

$$\frac{E_{\mathrm{f}}}{E_{\mathrm{i}}} = \frac{1}{2}\Gamma_{\mathrm{s}}^2 \left(1 - \beta_{\mathrm{rel}}\mu_{\to\mathrm{d}}\right)\left(1 + \beta_{\mathrm{rel}}\bar{\mu}_{\to\mathrm{u}}\right). \tag{2.103}$$

Similarly, for an observer in the downstream frame, this energy ratio equals to

$$\frac{\bar{E}_{\mathrm{f}}}{\bar{E}_{\mathrm{i}}} = \frac{1 + \beta_{\mathrm{rel}}\bar{\mu}_{\to\mathrm{u}}}{1 + \beta_{\mathrm{rel}}\bar{\mu}_{\to\mathrm{d}}} = \frac{1 - \beta_{\mathrm{rel}}\mu_{\to\mathrm{d}}}{1 - \beta_{\mathrm{rel}}\mu_{\to\mathrm{u}}}. \tag{2.104}$$

2.3.2.1 First Shock Cross

Usually we consider a cold upstream medium. Particles upstream are initially at rest so that $E_{\mathrm{i}} \approx mc^2$, where m is the rest mass of a particle. After the first cycle returning back to upstream, the particle energy becomes

$$E_{\mathrm{f}} \approx \frac{1}{2}\Gamma_{\mathrm{s}}^2 \left(1 + \beta_{\mathrm{rel}}\bar{\mu}_{\to\mathrm{u}}\right) mc^2. \tag{2.105}$$

For particles that can return back upstream, their velocity along the shock normal must exceed the shock velocity. Hence in DRF, $\frac{1}{3} < \bar{\mu}_{\to\mathrm{u}} \leqslant 1$, and we have

$$\frac{2}{3}\Gamma_\mathrm{s}^2 < \frac{E_\mathrm{f}}{E_\mathrm{i}} \leqslant \Gamma_\mathrm{s}^2 \tag{2.106}$$

for the energy gain after the first crossing cycle.

2.3.2.2 Constraints on the Energy Gain

Now we consider particles that have already finished complete shock crossing cycle more than once. When crossing the shock into upstream, particles must satisfy

$$\mu > \beta_\mathrm{s}, \quad \bar{\mu} > \bar{\beta}_\mathrm{s} \approx \frac{1}{3}. \tag{2.107}$$

These particles are constrained in a cone with an opening angle θ_c, which follows

$$\sin\theta_\mathrm{c} = \sqrt{1-\beta_\mathrm{s}^2} = \frac{1}{\Gamma_\mathrm{s}}. \tag{2.108}$$

In a ultra-relativistic shock with $\Gamma_\mathrm{s} \gg 1$, we have $\sin\theta_\mathrm{c} \approx \theta_\mathrm{c}$ and therefore

$$\theta_{\to\mathrm{u}} < \theta_\mathrm{c} \approx \frac{1}{\Gamma_\mathrm{s}}. \tag{2.109}$$

This is the constraint for particles that just entered the upstream medium. To return back downstream, the directions of particle motion should be changed, i.e., $\theta_{\to\mathrm{d}} > \theta_\mathrm{c}$, either by upstream deflection or scattering.

Achterberg *et al.* [26] proves that particles can only be changed an angle $|\theta| \sim \theta_\mathrm{c}$ before overtaken again by the shock. These particles are thus confined in a cone with an opening angle $\sim 2/\Gamma_\mathrm{s} \ll 1$.

Using the small angle approximation $\mu = 1 - \frac{1}{2}\theta^2$, the gained energy ratio becomes [27]

$$\frac{E_\mathrm{f}}{E_\mathrm{i}} \approx \frac{2+\Gamma_\mathrm{s}^2\theta_{\to\mathrm{d}}^2}{2+\Gamma_\mathrm{s}^2\theta_{\to\mathrm{u}}^2}. \tag{2.110}$$

Note that based on the range of $\theta_{\to\mathrm{d}}$ and $\theta_{\to\mathrm{u}}$, this ratio is always larger than unity, so particles can always gain energy through one shock crossing cycle. The average value of this ratio should be around 2. In one word, the particle energy can increase by a factor of ~ 2 per cycle, while by a factor of $\sim \Gamma_\mathrm{s}^2$ during the first cycle.

2.3.3 Eigenfunction Method

As mentioned in Section 2.2 (see Eq 2.64), for particles moving from downstream to upstream, there exists an angle $\mu = -u_-/v$ in the shock rest frame, within which the particle cannot catch up the shock. In the non-relativistic case, the particle velocity is much larger than the shock velocity and hence $\mid u_-/v \mid \sim 0$. As a result, we can simply assume an almost isotropic particle distribution near the shock front. However, when the shock also becomes relativistic, $\mid u_-/v \mid \sim 1$, the particle distribution would be highly anisotropic. Due to this deviation from the non-relativistic case, the characteristics of the produced particle spectrum also differ from what we discussed in the previous chapter.

The transport equation in the relativistic case is given by [28]

$$\begin{aligned}\Gamma(1+u\mu v)\left(\frac{\partial f}{\partial t}-\Gamma^2\frac{\partial u}{\partial t}E\frac{\partial f}{\partial p_x}\right)+ \\ \Gamma(u+\mu v)\left(\frac{\partial f}{\partial x}-\Gamma^2\frac{\partial u}{\partial z}E\frac{\partial f}{\partial p_x}\right)=\mathcal{C}(f)+\mathcal{S}\end{aligned} \tag{2.111}$$

here $\mathcal{C}(f)$ is the collisional operator.

In the shock rest frame, fluid velocities upstream and downstream are constant. Assuming a time-stationary condition without any kind of particle injections and sinks $\mathcal{S}=0$, Eq. 2.111 reads

$$\Gamma(u+v\mu)\frac{\partial f}{\partial x} = \mathcal{C}(f), \tag{2.112}$$

For high-energy particles with $v\sim 1$, if we only consider diffusion in pitch angle,

$$\Gamma(u+\mu)\frac{\partial f}{\partial x} = \frac{\partial}{\partial \mu}D_{\mu\mu}\frac{\partial f}{\partial \mu}, \tag{2.113}$$

Like the case of a non-relativistic shock, the particle distribution f should match on both sides of the shock front in the shock rest frame

$$f_-(p_-,\mu_-,0) = f_+(p_+,\mu_+,0) \tag{2.114}$$

Separating the variables in the particle distribution, f can be written as

$$f(p,\mu,z) = \sum_i a_i p^{-s}X_i(x)Q_i(\mu). \tag{2.115}$$

Inserting this expression into the transport equation, we have

$$\Gamma(u+\mu)\frac{dX_i}{dx}Q_i = (\overline{\mathcal{D}}Q_i)X_i \tag{2.116}$$

where $\overline{\mathcal{D}}$ is defined as

$$\overline{\mathcal{D}}R = \frac{d}{d\mu}\left[D(\mu)(1-\mu^2)\frac{dR}{d\mu}\right]. \tag{2.117}$$

Hence we can get

$$\begin{aligned}\Gamma\frac{1}{X_i}\frac{dX_i}{dx} &= \frac{1}{Q_i(u+\mu)}\overline{\mathcal{D}}Q_i = \Lambda_i \\ X_i(x) &= \exp\left(\frac{\Lambda_i x}{\Gamma}\right)\end{aligned} \tag{2.118}$$

Also we have

$$\frac{d}{d\mu}\left(D(\mu)(1-\mu^2)\frac{dQ_i}{d\mu}\right) = \Lambda_i(u+\mu)Q_i \tag{2.119}$$

Q_i are eigenfunctions associated with Λ_i which satisfy

$$\int_{-1}^{1}Q_iQ_j(u+\mu)d\mu = 0 \quad \text{if } i\neq j \tag{2.120}$$

and we get

$$\Lambda_{-i-1} < \Lambda_{-i} < \Lambda_0 = 0 < \Lambda_i < \Lambda_{i+1} \tag{2.121}$$

Now we have

$$f(p,\mu,x) \;=\; \sum_i a_i p^{-s} \exp\left(\frac{\Lambda_i x}{\Gamma}\right) Q_i(\mu) \tag{2.122}$$

To avoid infinity, note that in the upstream for all terms such that $\Lambda_i \leqslant 0$ and in the downstream for all terms such that $\Lambda_i \geqslant 0$, $a_i = 0$ is required.

The matching condition at the shock front is now

$$\sum_{i>0} a_i^- p_-^{-s} Q_i^-(\mu_-) \;=\; \sum_{i\leqslant 0} a_i^+ p_+^{-s} Q_i^+(\mu_+) \tag{2.123}$$

Using the Lorentz transformation between p_- and p_+,

$$\sum_{i>0} a_i^- (\Gamma_{\mathrm{rel}}(1+u_{\mathrm{rel}}\mu_-))^s Q_i^-(\mu_-) \;=\; \sum_{i\leqslant 0} a_i^+ Q_i^+(\mu_+). \tag{2.124}$$

where $u_{\mathrm{rel}} = (u_- - u_+)/(1-u_-u_+)$ is the relative velocity between upstream and downstream flows and Γ_{rel} is the corresponding relative Lorentz factor.

When $u_- \to 1$, it would be difficult to find the eigenfunctions. In [29], they proposed an analytical approximation to solve this problem. Introducing $y = (1+\mu)/(1-u)$ and taking the Taylor expansion for the diffusion coefficient $D_{\mu\mu} \approx d(1+\mu)$, where $d = \frac{dD_{\mu\mu}}{d\mu}$ at $\mu = -1$, the transport equation becomes

$$y\frac{d^2Q_i}{dy^2} + \frac{dQ_i}{dy} \;=\; \Lambda_i \frac{(1\,-\,u)^2}{d}(y\,-\,1)Q_i. \tag{2.125}$$

When $y \to \infty$, $Q_i \sim \exp\left(-(1-u)\sqrt{\Lambda_i/d}y\right)$, so the solutions should be in the form of

$$Q_i \;=\; \exp\left(-(1-u)\sqrt{\Lambda_i/d}y\right)\sum_n^N c_n y^n. \tag{2.126}$$

Now we can get the recurrence relation (detailed deductions seen in Appendix B)

$$c_{n+1} \;=\; \frac{k(2n\,+\,1\,-\,k)c_n}{(n\,+\,1)^2} \tag{2.127}$$

here $k = (1-u)\sqrt{\Lambda_i/d}$. To avoid an infinite series of y, c_{N+1} must vanish $(2(N+1)+1-k=0)$, implying $k = 2N+1$. The ordered positive eigenvalues are

$$\Lambda_i \;=\; \frac{d(2i\,-\,1)^2}{(1\,-\,u)^2} \tag{2.128}$$

The recurrence relation can be rewritted as

$$c_{n+1} \;=\; \frac{2(2N\,+\,1)(n\,-\,N)c_n}{(n\,+\,1)^2}. \tag{2.129}$$

The first positive upstream eigenfunction is good enough to describe the distribution, which allows us to get

$$f_-(p_-,\mu_-,z) \;=\; p_-^{-s}\exp\left(-\frac{1\,+\,\mu_-}{1\,-\,u_-}\right)\exp\left(\frac{dz}{(1\,-\,u_-)^2\Gamma_-}\right). \tag{2.130}$$

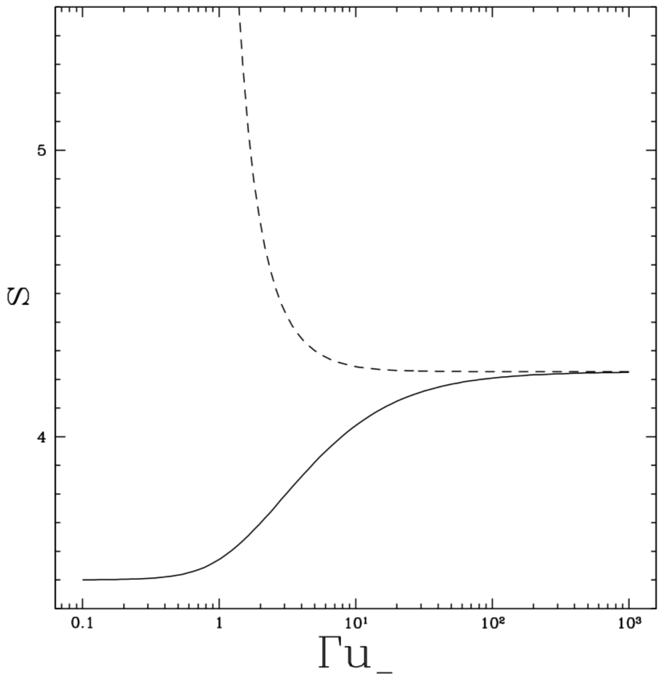

Figure 2.4: The evolution of the spectral index s with the upstream four velocity $\Gamma_- u_-$, the solid line for a gas with a fixed adiabatic index 4/3 and the dashed line for a relativistic gas $u_- u{+}{+} = 1/3$. In bith cases, $s = 4.23$ when $u_- \rightarrow 1$. This plot is taken from Kirk *et al.* [30].

for $z < 0$.

The particle distribution at the shock front in the shock rest frame is thus

$$f(p_{\mathrm{sh}}, \mu_{\mathrm{sh}}, 0) = p_{\mathrm{sh}}^{-s}(1 - \mu_{\mathrm{sh}} u_-)^{-s} \exp\left(-\frac{1 + \mu_{\mathrm{sh}}}{1 - u_- \mu_{\mathrm{sh}}}\right). \tag{2.131}$$

Let's recall Eq. 2.120 at $x = 0$ and insert $Q_i^-(\mu^-)$, $Q_j^+(\mu^+)$ as well as the Lorentz transformations from upstream to downstream. Then we have

$$S_{ij} = \int_{-1}^{1} d\mu_+ (u_+ + \mu_+)(1 + u_{\mathrm{rel}} \mu_-)^s Q_i^-(\mu_-) Q_j^+(\mu_+). \tag{2.132}$$

The spectral index s can be found from $|S_{ij}| = 0$.

Some corresponding results can be seen in Fig. 2.4 and Fig. 2.5.

2.3.4 Particle-in-Cell Simulations

Besides the analytical method we mentioned, numerical simulations are also a powerful tool to study particle acceleration at relativistic shocks. Many corresponding works are done during the last few years using the kinetic particle-in-cell (PIC) method [e.g. 31–33].

Sironi *et al.* [34] studied the physical properties near the shock front from gamma-ray bursts. For weakly magnetized relativistic shocks, they are efficient particle accelerators under the condition that the magnetization parameter $\sigma \lesssim 10^{-3}$ for electron-positron plasmas and $\sigma \lesssim 5 \times 10^{-5}$ for electron-ion plasmas.

In weakly magnetized shocks, the growth of non-linear magnetic turbulence near the shock front is driven by Weibel instability [e.g. 31, 34]. If the characteristic scales of

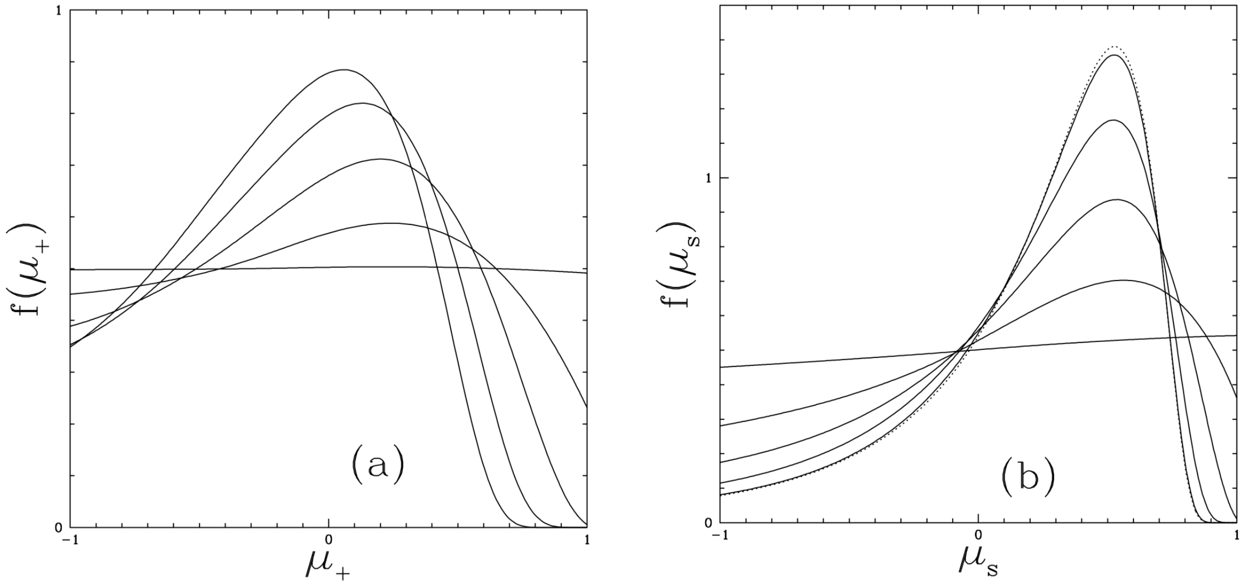

Figure 2.5: Angular distributions (a) in the downstream frame and (b) in the shock rest frame. Solid curves represent different values of the upstream four velocity: $\Gamma_{-}u_{-} = 0.1, 0.5, 1, 2, 10$. The dotted line in (b) is derived from Eq. 2.131 using $\Gamma_{-}u_{-} \rightarrow \infty$ and $s = 4.23$. This plot is adopted from Kirk *et al.* [30].

these turbulence structures are smaller than the gyroradius of a particle, they can cause non-resonant scattering.

Fig. 2.6 demonstrates how the turbulent structures triggered by Weibel instability evolves with σ. As the value of σ increases, Weibel filaments around the shock front becomes narrower until entirely dominant by the shock-compressed background magnetic field (see from up to down in the left panel of Fig. 2.6). The magnetized parameters of shocks from gamma-ray bursts are typically around 10^{-8}, indicating that these shocks are also mediated by Weibel instability and the characteristic scale of turbulent structures is $\sim 20c/\omega_p$, where ω_p is the plasma frequency of the fluid.

2.3.5 Maximum achievable energy accelerated at relativistic shocks

2.3.5.1 Hillas Limit

When discussing the maximum particle energy accelerated at relativistic shocks, the Hillas limit or Hillas condition is often considered. For particles to be accelerated, they must be constrained by the magnetic field inside the sources. In 1984 Hillas proposed that an astrophysical object can accelerate particles until the gyro-radius of the particle becomes comparable to the size of the source [35]. Particles with higher energy would rapidly escape from this object and hence the acceleration process stops. As a result, the theoretically maximum accelerated energy is

$$E_{\text{max}} = Z\beta eBR \simeq 10^{21} Z \frac{\beta}{1} \frac{B}{1\text{G}} \frac{R}{1\text{pc}} \text{eV} \tag{2.133}$$

where Z is the atomic number of the particle, e is the charge of an electron, B is the magnetic field in the object and R is the size of the source. Fig. 2.7 plots the characteristic magnetic fields and spatial sizes of astrophysical objects on the R-B plane. The blue and red lines represent the conditions that can accelerate particles with $Z = 1$ and $Z = 26$

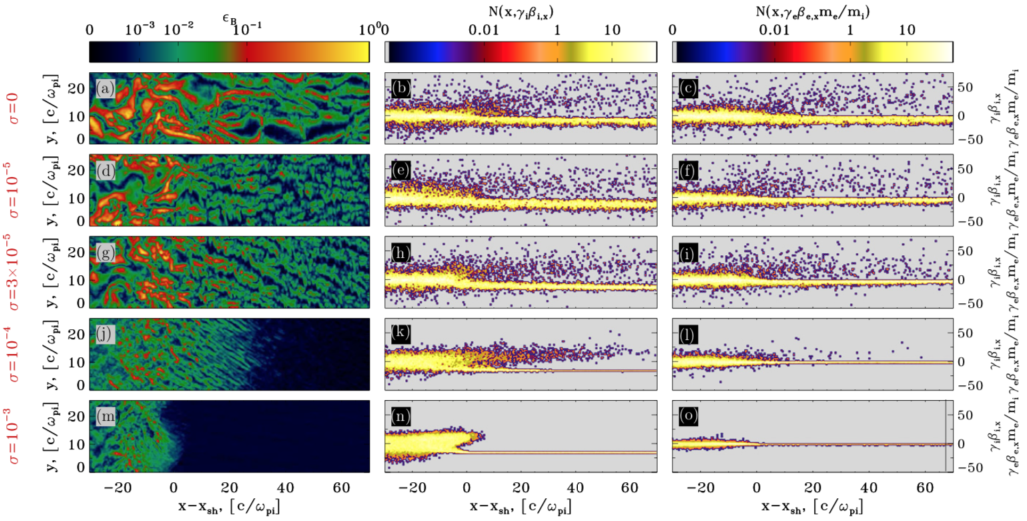

Figure 2.6: 2D PIC simulations of perpendicular electron-ion shocks from Sironi *et al.* [34]. The left panels demonstrate the evolution of the turbulent structures with the the magnetization parameter σ.

to 10^{20} eV. Only objects locating upper these two lines can accelerate particle beyond 10^{20} eV. From this plot, we can see that the physical conditions to accelerated UHECRs are extremely strict. Only limit kinds of sources can satisfy these conditions.

2.3.5.2 Magnetized Limit

The Hillas limit is just an idealized theoretical upper limit for the maximum accelerated energy. However, in reality, various mechanisms exist to quench particle acceleration at relativistic shocks. As a prerequisite, It is helpful to understand the particle motion near a relativistic shock. Particle trajectories are mainly influenced by two mechanisms, as shown in Fig. 2.8. Due to the presence of the regular magnetic field, charged particles undergo regular deflection or gyro-motion. Besides, particles also interact with small-scale magnetic turbulence. When particles collide with turbulence, they are scattered by a small angle while doing ballistic motions between each scattering. After several scatterings, a significant change in the direction of particle motion can be accumulated.

For particles to undergo acceleration, they must repeatedly cross the shock front. Particles upstream can always return back to downstream, either through regular deflection or scattering. In contrast, particles downstream cannot effectively return back to upstream, lacking cross-field diffusion. Therefore, a widely-held belief is that the acceleration efficiency at perpendicular relativistic shocks is determined by the physical conditions downstream.

In most cases, the regular magnetic field downstream is typically perpendicular to the shock normal because of shock compression. If particle motions are dominant by regular deflection, they will be constrained to move along the magnetic line, washed away from the shock front and can hardly be accelerated anymore (as proposed in [e.g. 26, 37]. To return back to upstream, these particles should be scattered and become isotropic immediately. Balancing the corresponding isotropization timescale and the gyro-timescale, we obtain an upper limit known as the magnetized limit.

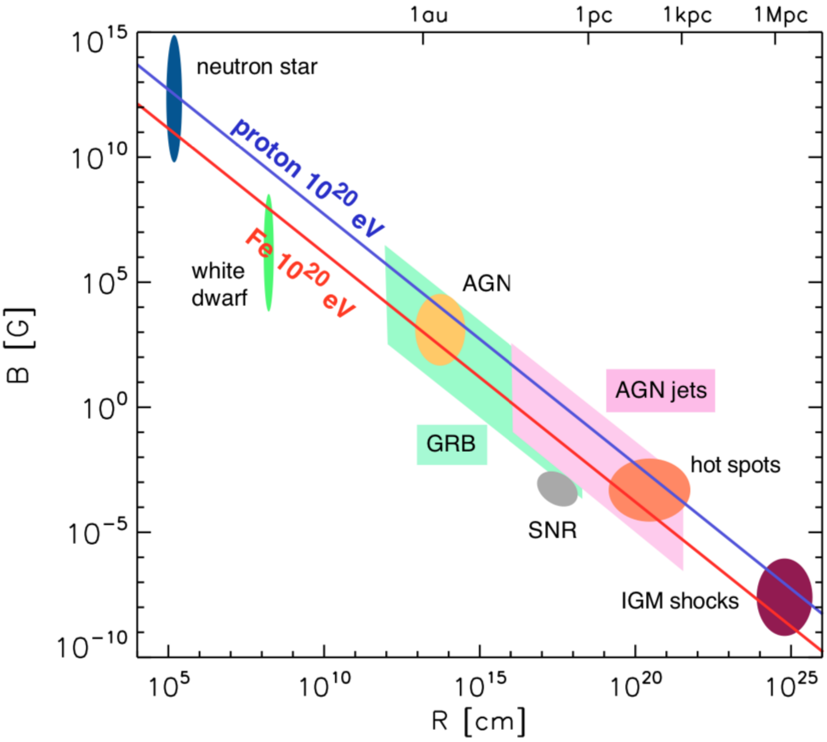

Figure 2.7: Various astrophysical objects on the Hillas diagram. The red and blue lines represent the conditions that sources can accelerate iron and protons to 10^{20} eV, respectively. This plot is taken from Kotera and Olinto [36].

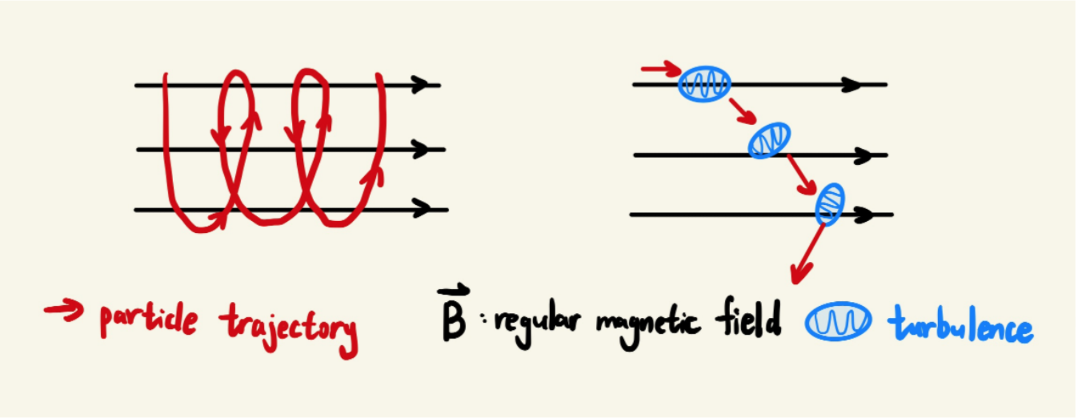

Figure 2.8: Schematic plot of particle motions near a relativistic shock. Left panel: regular deflection or gyro-motion by the regular magnetic field. Right panel: small-angle scattering by small-scale turbulence.

2.3.5.3 Loss Limit

As mentioned above, turbulence drives the particle distribution towards isotropy. However, this process force particles to lose their energies and cool down. If the energy lost during one shock crossing cycle exceed the gained energy, the acceleration process will saturate, which also sets a constraint on the maximum achievable energy, called as the loss limit [38]. For high-energy electrons, the energy losses are dominant by two radiation mechanisms: synchrotron radiation and inverse Compton scattering.

2.4 Synchrotron Radiation

At the end of this chapter, I would like to introduce the two main radiation processes for high-energy electrons.

Consider a uniform magnetic field with a magnificence B. A particle with charge q, mass m and Lorentz factor γ would do gyro-motion with an incident angle α along the magnetic line and emit synchrotron radiation.

Following Rybicki and Lightman [39], the synchrotron spectrum has the form of

$$P(\nu,\gamma) = \frac{\sqrt{3}q^3 B\sin\alpha}{mc^2} F\left(\frac{\nu}{\nu_{\rm ch}}\right), \tag{2.134}$$

where $P(\nu,\gamma) = dE/dtd\nu$ is the radiation power per unit frequency, and $\nu_{\rm ch}$ is the characteristic photon frequency

$$\nu_{\rm ch} = \frac{\omega_{\rm ch}}{2\pi} = \frac{3}{4\pi}\gamma^2\frac{qB_\perp}{mc}. \tag{2.135}$$

Here $B_\perp = B\sin\alpha$ is the perpendicular field strength.

The function $F(x) \equiv x\int_x^\infty K_{5/3}(\xi)d\xi$ reaches its maximal value 0.92 at $x = 0.29$.

The total emission power from one particle can be obtained by integrating over ν

$$P(\gamma) = 2\sigma_{\rm T}c\gamma^2\beta_\perp^2 U_B, \tag{2.136}$$

where $\beta_\perp = v\sin\alpha/c$ is the dimensionless velocity perpendicular to the magnetic field and $U_B = B^2/8\pi$ is the energy density of the field and $\sigma_{\rm T} = \frac{8\pi}{c}\left(\frac{q^2}{mc^2}\right)^2$ is the Thomson cross section. For electrons, this cross section is

$$\sigma_{\rm T,e} \equiv \frac{8\pi}{c}\left(\frac{e^2}{m_e c^2}\right)^2 \simeq 6.65\times 10^{-25}{\rm cm}^2. \tag{2.137}$$

If the magnetic field is randomized, the emission power becomes

$$P(\gamma) = \frac{4}{3}\sigma_{\rm T}c\gamma^2\beta^2 U_B, \tag{2.138}$$

since $\langle\beta_\perp^2\rangle = 2\beta^2/3$.

Although the emission spectrum per frequency from a single particle is continuous, most power is concentrated near $\sim 0.29\nu_{\rm ch}$. Hence in many cases, we consider emissions from a single particle with a δ-function form for simplicity.

In astrophysics, we usually observe emissions from a population of electrons rather

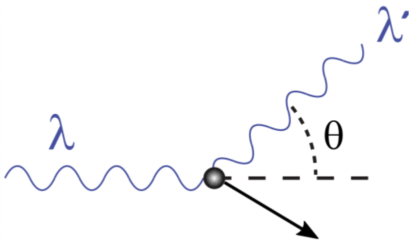

Figure 2.9: Compton scattering in the electron rest frame.

than a single one. These particles are often distributed in a form of a power law

$$N(\gamma)d\gamma = C\gamma^{-p}d\gamma, \tag{2.139}$$

with a range from the minimal and maximal Lorentz factors $\gamma_{\rm m}$ and $\gamma_{\rm M}$.

Integrating over all of these electrons, we have

$$F_\nu \propto \int_{\gamma_{\rm min}}^{\gamma_{\rm M}} P(\nu,\gamma)\gamma^{-p}d\gamma. \tag{2.140}$$

And the final synchrotron radiation spectrum has three parts

$$F_\nu \propto \begin{cases} \nu^{1/3}, & \nu < \nu_{\rm m} \\ \nu^{-(p-1)/2}, & \nu_{\rm m} < \nu < \nu_{\rm M} \\ \nu^{1/2}e^{-(\nu/\nu_{\rm M})}, & \nu > \nu_{\rm M} \end{cases} \tag{2.141}$$

2.5 Inverse Compton Scattering

2.5.1 Scattering Process

Consider a photon with energy $\epsilon^{'}$ collide with an electron in the electron rest frame (Fig. 2.9). After the collision, this photon would be scattered and change its direction of motion by an angle θ. Conservation of momentum and energy provides us the relation for the photon energy after scattering,

$$\epsilon_1^{'} = \frac{\epsilon^{'}}{1+\epsilon^{'}(1-\cos\theta)}. \tag{2.142}$$

Here all energies are normalised to mc^2

If the incident photon energy is much smaller than the rest energy of the electron $\epsilon \ll m_{\rm e}c^2$, $\epsilon_1 \approx \epsilon$. The photon just change its direction of motion and its energy doesn't change after the interaction, which is known as Compton scattering.

Now we consider a collision between a high energy electron ($v \sim c$) collide with a photon in the observer frame K. Transform to the electron rest frame $K^{'}$ (Fig. 2.10), the photon energy $\epsilon^{'}$ becomes

$$\epsilon^{'} = \epsilon\gamma(1-\beta\cos\theta) \tag{2.143}$$

Use Eq. 2.142 and then transform back to the K frame, the photon energy after

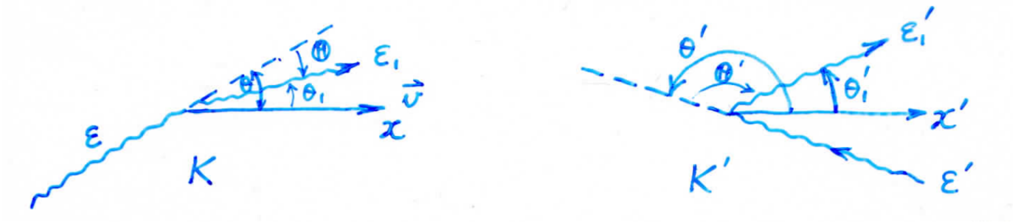

Figure 2.10: Inverse Compton scattering process in the observer frame K and the electron rest frame $K^{'}$.

scattering is

$$\epsilon_1 = \frac{\epsilon\gamma^2(1-\beta\cos\theta)(1+\beta\cos\theta_1^{'})}{1+\epsilon\gamma(1-\beta\cos\theta)(1-\cos\theta_{sc}^{'})}. \tag{2.144}$$

If $\gamma\epsilon \ll 1$, which means the incident photon energy $\epsilon^{'}$ is much smaller than the electron rest energy in the $K^{'}$ frame, we get the inverse Compton scattering in the Thomson limit. In this case, the final scattered photon energy $\epsilon_1 \sim \gamma^2\epsilon$. The photon energy can greatly boost through this process, and hence inverse Compton scattering is an efficient radiation process to produce high energy emissions.

2.5.2 Radiation Spectrum

Now we try to find the photon production rate by an electron. It is easy to study in the electron rest frame. Integrating over all incoming angles and energies [40, 41]

$$\frac{dN_{\gamma,e}}{dt^{'}d\epsilon_1^{'}d\Omega_1^{'}} = \int d\epsilon^{'}d\Omega^{'}cn_{\gamma}^{'}\frac{d\sigma_{\mathrm{KN}}}{d\epsilon_1^{'}d\Omega_1^{'}} \tag{2.145}$$

where

$$\begin{aligned}\frac{d\sigma_{\mathrm{KN}}}{d\varepsilon_1^{'}d\Omega_1^{'}} &= \tfrac{3\sigma_T}{16\pi}\left(\tfrac{\varepsilon_1^{'}}{\varepsilon^{'}}\right)^2\left(\tfrac{\varepsilon_1^{'}}{\varepsilon^{'}}+\tfrac{\varepsilon^{'}}{\varepsilon_1^{'}}-\sin^2\theta_{\mathrm{sc}}^{'}\right)\delta\left(\varepsilon_1^{'}-\tfrac{\varepsilon^{'}}{1+\varepsilon^{'}(1-\cos\theta_{sc}^{'})}\right) \qquad (2.146)\\ &= \tfrac{3\sigma_T}{16\pi}\tfrac{1+\cos^2\theta_{sc}^{'}}{[1+\varepsilon^{'}(1-\cos\theta_{sc}^{'})]^2}\left[1+\tfrac{\epsilon^{'2}(1-\cos\theta_{sc}^{'})^2}{(1+\cos^2\theta_{sc}^{'})[1+\varepsilon^{'}(1-\cos\theta_{sc}^{'})]}\right]\delta\left(\varepsilon_1^{'}-\tfrac{\varepsilon^{'}}{1+\varepsilon^{'}(1-\cos\theta_{sc}^{'})}\right)\end{aligned}$$

For an isotropic photon background in the observer frame, we can finally get

$$\frac{dN_{\gamma,e}}{dtd\epsilon_1} = \frac{3}{4}\frac{\sigma_{\mathrm{T}}cN}{\gamma^2\epsilon}F(x)S(x;1/4\gamma^2,1) \tag{2.147}$$

where

$$x = \frac{\epsilon_1}{4\gamma^2\epsilon(1-\epsilon_1/\gamma)}, \tag{2.148}$$

and

$$F(x) = 2x\ln(x)+1+x-2x^2+\frac{1}{2}\frac{(\Gamma_\epsilon x)^2}{1+\Gamma_\epsilon}(1-x) \tag{2.149}$$

with $\Gamma_\epsilon = 4\gamma\epsilon$

Note that $S(x;a,b)$ is the top-hat function

$$S(x;a,b) = \begin{cases} 1, & a<x<b \\ 0, & \text{otherwise} \end{cases} \tag{2.150}$$

In the Thomson limit when $x \approx \epsilon_1/4\gamma^2\epsilon$, the energy loss rate of a particle in an isotropic photon background is

$$P(\gamma) = \frac{4}{3}\sigma_{\mathrm{T}} c \gamma^2 U_R. \tag{2.151}$$

Chapter 3

Gamma-ray bursts

After acquiring a comprehensive understanding of relativistic shocks in the previous chapter, we now know how power-law distributions of particles are generally produced in high-energy astrophysical objects. Particles accelerated by gamma-ray burst (GRB) blast waves, usually electrons, radiate photons, generating multi-wavelength emissions detected by human-made instruments. In this chapter, we will delve into detailed discussions on GRBs to gain a better understanding of the physics behind GRB radiations.

3.1 History of GRB detections

The discovery of GRBs was quite dramatic. A series of satellites named *Vela* was launched in the 1960s by the United States to monitor nuclear experiments from the Soviet Union. In 1967, the first GRB was discovered as an unexpected find. Initially, these signals were considered to be originated from the earth. However after detailed analysis, scientists realized that these events should come from the universe.

Following this first detection, several gamma-ray detectors, like *UHURU*, *Ginga* and *Apollo 16* were launched and observed hundreds of GRBs. Unfortunately, due to the lack of accurate localization of GRBs, it was challenging to follow up and observe their electromagnetic counterparts. Since there were few constraints from observations, numerous models were proposed to explain GRB emissions, including the fireball model [42–44]. Determining the actual energy released by GRBs is crucial to test all these models, requiring information on the distance of these events. However, this was impossible at that time due to the poor localization capability of detectors. Two types of models were established based on their assumptions about the distance scale. One proposed the origin from our own galaxy while another favored a cosmological origin.

This problem wasn't solved until 1991, when the *Compton GRO* spacecraft was launched. BATSE was one of the instruments on board, aiming to detect GRBs. Although its localization error boxes were still large, we made several significant advancements in understanding the physics of GRBs. The angular distribution of detected GRBs was highly isotropic rather than concentrating in the galactic plane [45] (see Fig. 3.3). Besides, the intensity distribution at the faint part deviated from the prediction in Euclidean geometry [46]. Both of these pieces of evidence suggested a cosmological origin for GRBs.

Another important discovery from BATSE observations is that, GRBs can be divided into two categories based on the duration of their prompt emissions [47], as shown in Fig. 3.4. There are two peaks on this plot, one at around 0.2 second and another around 20 seconds, named short GRBs and long GRBs. The separation line between these two types is located at nearly 2 seconds.

A significant breakthrough was achieved in 1997, when the *BeppoSAX* satellite was launched. *BeppoSAX* carried a wide-field X-ray camera with more accurate localization capabilities than previous gamma-ray detectors, enabling the discovery of corresponding

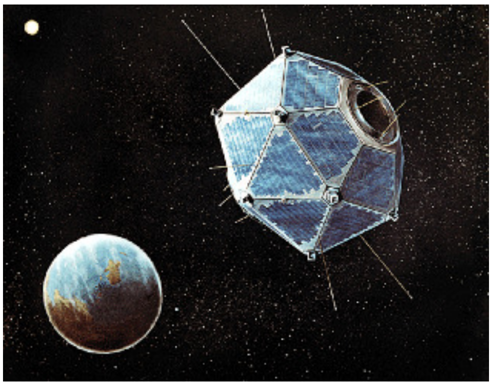

Figure 3.1: *Vela* satellite. Source link: `http://heasarc.gsfc.nasa.gov/docs/vela5b/vela5b_images.html`

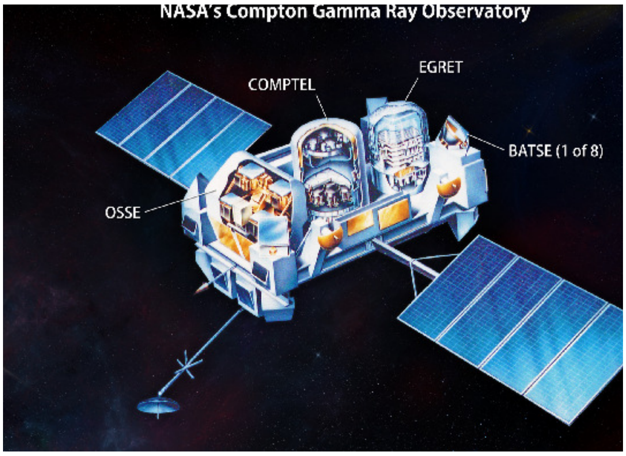

Figure 3.2: *Compton GRO*. Source link: `http://svs.gsfc.nasa.gov/12194`. Author: NASA/Goddard Space Flight Center.

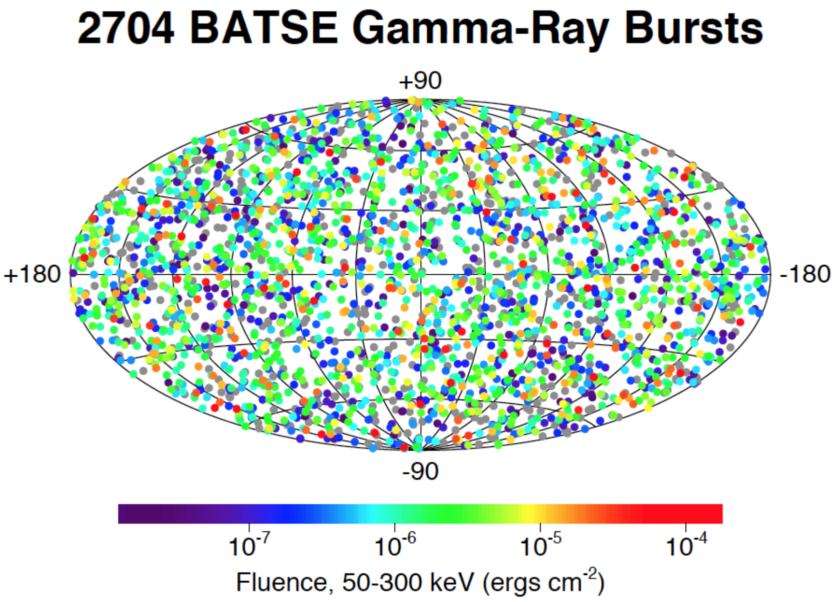

Figure 3.3: GRB skymap from BATSE. Source link: `http://cossc.gsfc.nasa.gov/docs/cgro/cgro/batse_src.html` Credit: CGRO BATSE Team

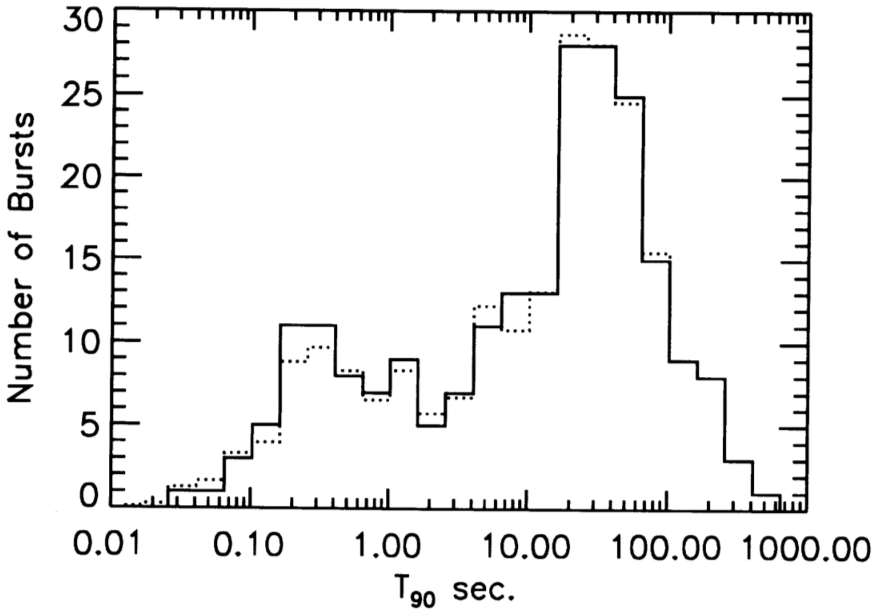

Figure 3.4: Duration distribution for GRBs from the first BATSE catalog. This picture is adopted from Kouveliotou *et al.* [47].

Figure 3.5: *Swift* and *Fermi* satellites. For the image of *Swift*, source link: `http://swift.sonoma.edu/resources/multimedia/images` Author: NASA E/PO, Sonoma State University/Aurore Simonnet. For the image of *Fermi*, source link: `https://science.nasa.gov/toolkits/spacecraft-icons` Author: NASA.

counterparts and the acquisition of distance information for GRBs. On February 28, 1997, the first X-ray afterglow was detected eight hours after the burst [13]. Later, the first optical afterglow was also observed by ground-based instruments [48]. The first radio afterglow was discovered [49] from GRB 970508. Just two months later, through observing its optical afterglow, the first redshift measurement from this event was made by the Keck II 10-meter telescope [50]. The redshift of this long GRB was $z = 0.835$, confirming the cosmological origin of long GRBs. The discoveries of afterglows were important milestones in this field. The abundant multi-wavelength data provided more constraints on GRB models and improved our understanding of GRB nature.

Another important discovery from the *BeppoSAX* era was the possible association between a long GRB 980425 and a Type Ib/c supernovae SN 1998bw [51, 52]. These two events happened within two days, but the distance between them was $1.6'$. In 2003, the detection of GRB 030329 by *HETE-2* and the observation of SN 2003dh revealed a more robust GRB-SN connection [53, 54]. These two bursts and their connection with SNe suggested the collapse of massive stars as the origin of long GRBs [55, 56].

In 2004, the *Swift* observatory was launched, which turned out to be another successful mission. *Swift* carries a Burst Alert Telescope (BAT; Barthelmy *et al.* [57]), an X-ray Telescope (XRT; Burrows *et al.* [58]) and a UV-Optical Telescope (UVOT; Roming *et al.* [59]). XRT and UVOT can quickly capture counterparts after bursts and hence made it possible to detect emissions at early stages. This advantage allowed *Swift* to successfully identify the host galaxies of several short GRBs and their locations in the host. These results are distinct from long GRBs, suggesting a different origin for these short events [60, 61]. Theoretically, short GRBs were widely believed to be produced by the mergers of two neutron stars (NS-NS) or a neutron star and a black hole. Observations by *Swift* also provided abundant early afterglow data in the X-ray band, including the discovery of X-ray flares following the prompt emission. At the same time, *Fermi* Gamma-Ray Space Telescope (FGST) was launched in June 2008, carrying a Large Area Telescope (LAT) and a Gamma-ray Burst Monitor (GBM). These two instruments cover a wide energy range, i.e., LAT: 20 MeV to 300 GeV and GBM: 8 keV to 40 MeV, making it possible to study both prompt emissions and afterglows over a broad band.

Instruments mentioned above detect the gamma-ray photons directly. However, the flux of gamma-ray photons in our universe drops rapidly. Therefore it is ineffective to collect data using space-borne instruments or satellites because of the limited collection

Figure 3.6: H.E.S.S, MAGIC, VERITAS and CTA. The photo of H.E.S.S was taken on the H.E.S.S. II Open Day 2012, author: Klepser, DESY, H.E.S.S. collaboration. Source link for MAGIC picture: https://www.mpg.de/593689/pressRelease20090415, credit: R. Wagner from Max Planck Institute for Physics. Source link for the photo of VERITAS: http://www.nsf.gov/news/news_images.jsp?cntn_id=115836&org=NSF, author: VERITAS collaboration. Source link for the CTA picture: https://www.eso.org/public/images/eso1841a/, author: M-A. Besel from CTA collaboration.

areas. To observe photons with much higher energy like TeV photons, ground-based telescopes are required. When high-energy photons propagate into the atmosphere, they will collide with atmospheric atoms and generate showers of secondary charged particles. These particles can travel with a velocity larger than the speed of light in the atmosphere and emit Cherenkov radiation.

The Imaging Atmospheric Cherenkov Technique, or IACT, works by imaging the flash of Cherenkov photons from air showers. Devices using this technique are called as the Air Cherenkov Telescopes, e.g., High Energy Stereoscopic System (H.E.S.S.), Major Atmospheric Gamma Imaging Cherenkov Telescopes (MAGIC) and Very Energetic Radiation Imaging Telescope Array System (VERITAS). These telescopes can detect gamma-ray photons in the energy range of tens of GeV to tens of TeV. The next-generation Cherenkov Telescope Array (CTA) is still under construction and is expected to be in operation soon.

A similar technique involves detecting Cherenkov radiation produced by high-energy particles striking water. In this case, large tanks or pools filled with water are utilized, as seen in projects like the Large High Altitude Air Shower Observatory (LHAASO) and the High Altitude Water Cherenkov Observatory (HAWC).

Figure 3.7: LHAASO and HAWC. The LHAASO picture is adopted from Cao [62]. The HAWC photo is taken from Pretz [63].

3.2 Classification of GRBs

As mentioned in Section 3.1, a popular classification of GRBs is based on the duration timescale of prompt emissions. Events with a duration of more than 2 seconds are defined as long GRBs while those lasting less than 2 seconds are classified as short GRBs. Statistically, the long-duration class is on average softer than the short-duration class.

3.2.1 Long GRBs

Most observed GRBs are long GRBs. Because these events constitute the majority of the population and tend to have the brightest afterglows, long GRBs have been observed in much greater detail than their short counterparts. Almost every well-studied long GRB has been linked to a galaxy with rapid star formation, and in many cases, to a core-collapse supernova, unambiguously associating long GRBs with the deaths of massive stars.

Most long GRBs are located in irregular, star-forming galaxies [64]. Long GRB host galaxies are usually metal-poor [e.g. 64–66], which is consistent with the prediction of the collapsar progenitor model [55]. Nonetheless, there are still some long GRBs found in relatively metal-rich galaxies. However, the spatial resolution at the redshifts of these GRBs is not good enough to determine the metallicity in the surrounding environment. It is still possible that long GRBs are exclusively born in the metal-poor environment, considering variations of metallicity in small scales [67]. Fruchter *et al.* [64] showed that long GRBs follow the areas with a very high specific star formation rate in their host galaxies, and most long GRBs locate in the core regions of the hosts, where specific star formation rate is the highest.

3.2.2 Short GRBs

Detections of afterglows from short GRBs show that these events are associated with regions of little or no star formation. This rules out a link to massive stars, confirming that short events are physically distinct from long events. In addition, there has been no association with supernovae. Theoretically, short GRBs are believed to be produced by mergers of compact objects, such as binary neutron star mergers and black hole-neutron star mergers.

During the merger, neutron-rich ejecta would be torn off from the surface of neutron stars, providing an idealized site for rapid neutron capture (r-process) and the synthesis of heavy elements. Since these produced heavy elements are unstable, they will decay and emit energy, powering a supernova-like transient [68, 69]. Since such a transient is much fainter than a normal supernova but roughly one thousand times brighter than a nova, this event is named 'macronova' [70] or 'kilonova' [69]. The peak luminosity of kilonovae would be in the infrared band because of the high opacity from lanthanide-kind elements in the ejecta [71, 72].

Most short GRBs reside in late-type galaxies, where the star formation rate is moderate. Compared with long GRB hosts, short GRB host galaxies are larger, with a relatively older stellar population [73] and higher metallicity [74]. Some short GRBs are found in elliptical and early-type galaxies [60, 61, 75]. The distribution of short GRBs covers both elliptical and spiral galaxies, suggesting that these events are not directly linked to deaths of massive stars but rather to the mergers of compact objects.

Before the merger of a binary system, two compact stars undergo supernova explosions,

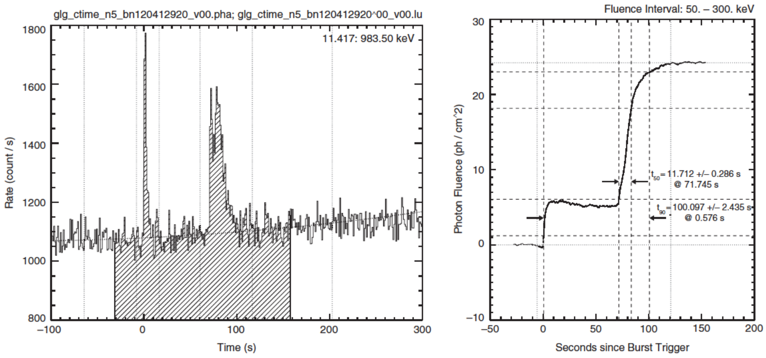

Figure 3.8: Illustration of T_{90} taken from von Kienlin *et al.* [85].

providing a kick velocity to this system. Hence, when these two stars collide with each other, the system has already moved far away from its original star-forming region. That's why short GRBs are typically far from the bright light of their hosts, and some of them are even hostless.

One of the most famous GRB detections was GRB 170817A. On August 17, 2017, a gravitational wave signal from a binary neutron star merger (GW170817) was detected at 12:41:04 UTC by LIGO/Virgo [76]. 1.74 second later, a short GRB was successively detected by *Fermi* and the *International Gamma-Ray Astrophysics Laboratory* (*INTEGRAL*) [77–79]. About 10 hours after the merger, a kilonova emission known as AT 2017gfo was also reported [e.g. 80–84].

This first joint detection of the gravitational wave event and its electromagnetic counterparts not only proves mergers of compact objects as the origins of short GRBs, but also represents the beginning of multi-messenger astronomy.

3.3 GRB Phenomenology

To understand the physics of GRBs, first we need to collect as much observational data as possible. The emissions from GRBs are usually divided into two phases: the prompt emission phase and the afterglow emission phase. In this section we will introduce some basic properties of these two phases.

3.3.1 Prompt Emission

The prompt emission phase is defined as the phase when a sudden luminous burst occurs in the sub-MeV band is detected by GRB detectors. The duration of this burst is usually measured using what we called T_{90}. The definition of T_{90} is the time interval between the moments when 5% and 95 % of the total fluence is collected by the instrument, as shown in Fig. 3.8.

However, there are several limitations to T_{90} measurements. First, it relies on the energy bandpass of the detector. For a certain GRB, an instrument with a lower bandpass could yield a longer T_{90} since the pulses are wider at lower energy. Besides, the detection of T_{90} is also dependent on the sensitivity of the instruments. The more sensitive a detector is, the lower its background noise level, and hence the longer T_{90} it can measure. Finally, there could be several emission episodes during the prompt phase, which poses challenges in T_{90} detections.

In physics, GRB prompt emissions and afterglows are differentiated based on the

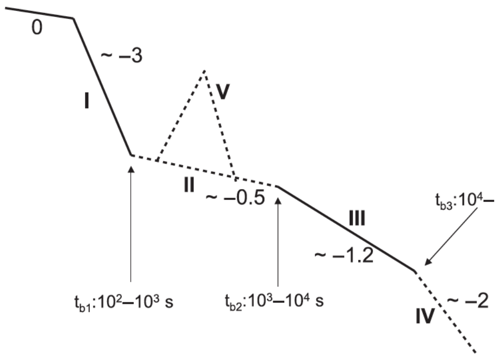

Figure 3.9: Canonical X-ray afterglow lightcurve [88] with five components. I. steep decay phase; II. shallow decay phase or plateau; III. normal decay phase; IV. post-jet-break phase; V. X-ray flare.

location of emitted gamma-ray photons. Prompt emissions are produced by the ejecta dissipating energy from an internal site, while afterglows are considered to be related to external shocks (e.g., forward shocks). It is sometimes difficult to distinguish prompt emissions from afterglows in practice.

Note that during the prompt phase, signals can be detected not only in sub-MeV but also in other wavelengths. Optical, X-ray and GeV components have already been observed during the prompt phase from several GRBs.

3.3.2 Afterglow

The afterglow is defined as the emission after the prompt phase, which was predicted before its discovery [86, 87]. Here is the basic argument: a GRB must deliver a large amount of energy in a small space volume, triggering a fireball propagating outwards relativistically. The ambient medium around the central engine would decelerate the ejecta and produce a relativistic forward shock penetrating into the circumburst medium as well as a reverse shock moving towards the ejecta. Particles like electrons and protons can be accelerated to very high energy by shocks and produce broad-band emissions through synchrotron radiation and inverse-Compton scattering with surrounding photon background. Such a kind of emission should keep fading with time as the shock slows down. As a result, the lightcurves at late time in all wavelengths are expected to decay as power laws

$$F_\nu(t,\nu) \propto t^{-\alpha}\nu^{-\beta}. \tag{3.1}$$

X-ray Afterglow A characteristic lightcurve in the X-ray band can be decomposed into five components, as shown in Fig. 3.9.

The first component, or the earliest decay segment in the afterglow phase is the steep decay phase. The typical temporal decay slope is quite steep, $\alpha \sim 3$ to ~ 10. This phase is usually connected to the end of the prompt emission smoothly, suggesting this phase as a natural tail of the prompt phase [89]. However, afterwards it breaks to a softer decay phase which is considered to have an external shock origin, indicating that prompt emissions and afterglows are generated from different emission sites. Hence, the prompt emission must be produced from internal sites.

After the first rapid decay phase, the X-ray lightcurve enters the shallow decay phase, with $\alpha \sim 0$ to ~ 0.7. If α is close to 0, then there is a plateau in the lightcurve. In the following normal decay phase, the decay slope is approximately $\alpha \sim 1$. Even later, when

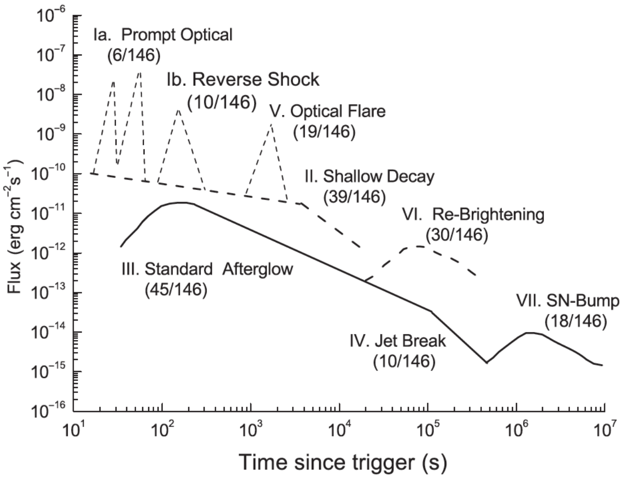

Figure 3.10: Schematic picture for optical afterglow lightcurves [90].

the external shock transitions from relativistic to non-relativistic, there would be a jet break effect, resulting in a decay slope of ~ -2 in the post-jet-break phase.

X-ray flares have been detected in a large fraction of GRBs, showing rapid rise and steep decay in the lightcurves. The origins of X-ray flares, as well as plateaus, are believed to produced by the long-lasting central engine.

Optical Afterglow The optical afterglow emissions at late time typically exhibit a single power-law decay with $\alpha \sim 1$. If this event is bright enough, one may also observe a jet break at a later time with $\alpha \sim 2$. The early-time optical afterglow lightcurves show more complicated features (see Fig. 3.10), which can be separated into multiple components. Besides the typical emissions from standard afterglow (III), jet break (IV) and supernova bump (VII), one can also observe prompt optical flares following the gamma-ray prompt emission (Ia), early optical flash produced by reverse shocks (Ib), shallow decay phase (II), optical flares (V) or re-brightening phase (VI).

Radio Afterglow Radio afterglows have been detected in 30% of GRBs, exhibiting an early rising phase and peaking at 8.5 GHz around three to six days after the burst. The peak can be explained by the transition between the typical synchrotron frequency and the the self-absorption frequency in the standard forward shock model. Early radio flares have also been observed in some samples, with a peak at 1 day after the trigger. For example, a radio flare was detected from GRB 130427A, peaking around 1.5 days, as shown in Fig. 3.11.

Gamma-ray Afterglow At high energies, the number of photons reduces rapidly. To gather enough signals, gamma-ray detectors need large effective areas, which becomes a challenge for space-borne instuments Hence, only a small fraction of GRBs were detected with high-energy afterglow emissions. In most cases, these high-energy photons are observed from bright GRBs or GRBs with quite early-time detections.

Theoretically, these gamma-ray emissions are produced through a different radiation process than other energy bands. Accelerated electrons can hardly produce such high-energy photons through synchrotron process. A widely-accepted explanation is that, these gamma-ray photons should be produced through SSC process. Emitted synchrotron photons can be scattered by electrons and gain energy. However, the Klein-Nishina effect should be considered especially for TeV photons, which results in a rapid decrease on the high-energy afterglow spectra.

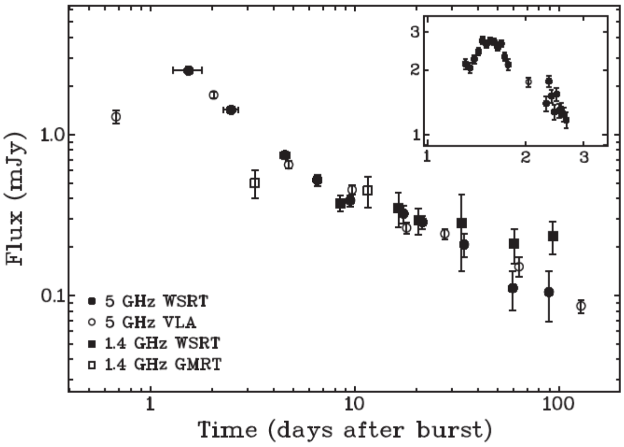

Figure 3.11: Radio afterglow from GRB 130427A [91].

Recently, several GRBs with TeV photons have been detected, including GRB 190114C detected by MAGIC Collaboration [92], as well as GRB 180720B [93] and GRB190829A [94] detected by H.E.S.S Collaboration. Fig. 3.12 shows the high-energy afterglow detections from GRB 190114C at a short time interval after the trigger. Moreover, LHAASO reported the detection of gamma-ray photons up to $\sim$ 10 TeV from GRB 221009A [95]. All of these observational data confirmed the presence of very-high-energy emissions from GRB afterglows, provided critical tests on the standard afterglow model and even hinted some new physics [e.g. 96–98].

3.4 Standard Model for GRB afterglows

Thanks to the abundant observational data during the afterglow phase, we have gained a deep understanding on the nature of GRB afterglow emissions. The most widely accepted model is the standard single-zone synchrotron self-Compton model. A relativistic shock is generated after the burst and propagate outwards. During the propagation, the shock penetrates into the ambient medium, sweeps up matter and decelerates. Particles like electrons can be accelerated to very high energy during this process and interact with the ambient magnetic field or the external photon background, producing synchrotron radiation or external inverse-Compton (EC) radiation. In most cases, the energy density of the external photon background is much smaller than the magnetic field, so we usually neglect the EC component on the afterglow spectrum, while the influence from synchrotron radiation photons is quite important. These synchrotron photons can collide with accelerated electrons and be scattered to much higher energy, and this process is known as the synchrotron self-Compton process (SSC). Based on the standard SSC model, there are two components on the afterglow spectrum: the synchrotron component and the SSC component [99] (The synchrotron component was first studied by Sari *et al.* [100]).

In this single-zone SSC model, accelerated electrons are assumed to concentrate in a thin shell near the shock front. The particle distribution and other physical parameters are considered to be homogenous in this shell. Fig. 3.13 shows all of the parameters we need in the single-zone SSC model, including the isotropic energy of the shock E, the energy fractions that transfer into the electrons and the magnetic field $\epsilon_{\rm e}$, $\epsilon_{\rm B}$, the

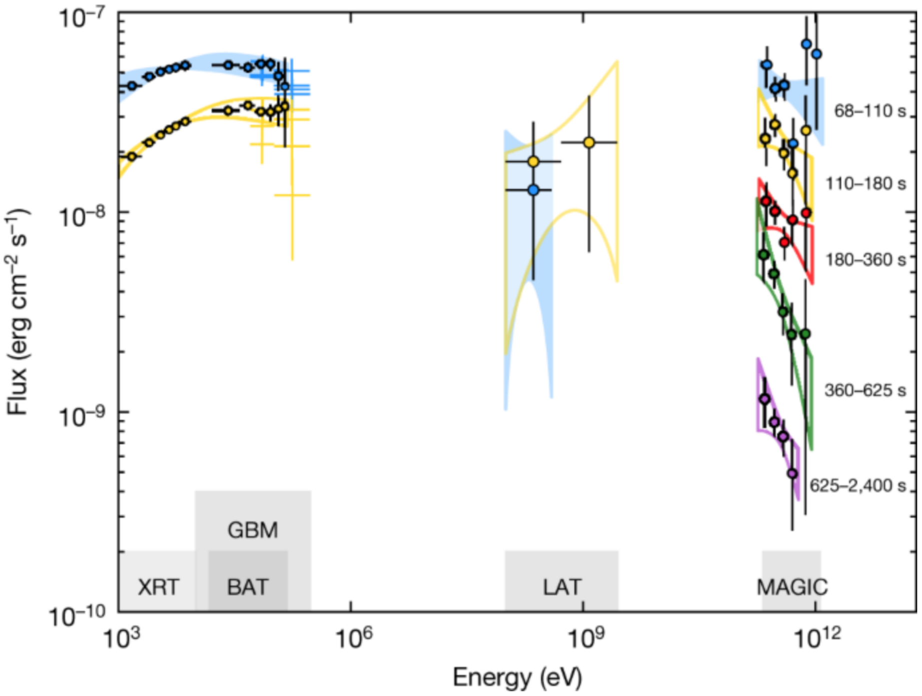

Figure 3.12: GeV and TeV afterglow emissions from GRB 190114C from 68 - 2400 s [92].

spectral index of the accelerated spectrum p and the number density of the surrounding medium n.

3.4.1 Evolution of the Shock

To get the afterglow spectrum, first we need to know the time evolution of the relativistic shock. In Blandford and McKee [101], the fluid dynamics of the shock was well studied, and the corresponding evolution of the shock is now known as the Blandford-McKee solution.

Consider a spherical shock propagating into the surrounding medium, where the density evolve with the radius as $n = n_0 R^{-k}$. In the adiabatic case, the total energy of the shock is given by [101]

$$E = 16\pi n m_{\rm p} c^2 R^3 \Gamma^2 / (17 - 4k), \tag{3.2}$$

where Γ is the Lorentz factor of the shocked fluid, R is the radius of the shock front, n is the density of the external medium at the shock front, $m_{\rm p}$ is the mass of a proton and c is the speed of light.

During the propagation, the shock would emit photons continuously. The time interval δt that we observed two photons emitted from R and $R + \delta R$ is $\sim (1 + z)\delta R/2\Gamma_s^2 c$ [102], where $\Gamma_s = \sqrt{2}\Gamma$ is the Lorentz factor of the shock front. Integrating this expression over time, we have

$$\begin{aligned} t &= \int dt \sim \int (1 + z) dR/2\Gamma_s^2 c \\ &= \frac{1 + z}{2(4 - k)} \frac{R}{\Gamma_s^2 c} \\ &= \frac{1 + z}{4(4 - k)} \frac{R}{\Gamma^2 c} \end{aligned} \tag{3.3}$$

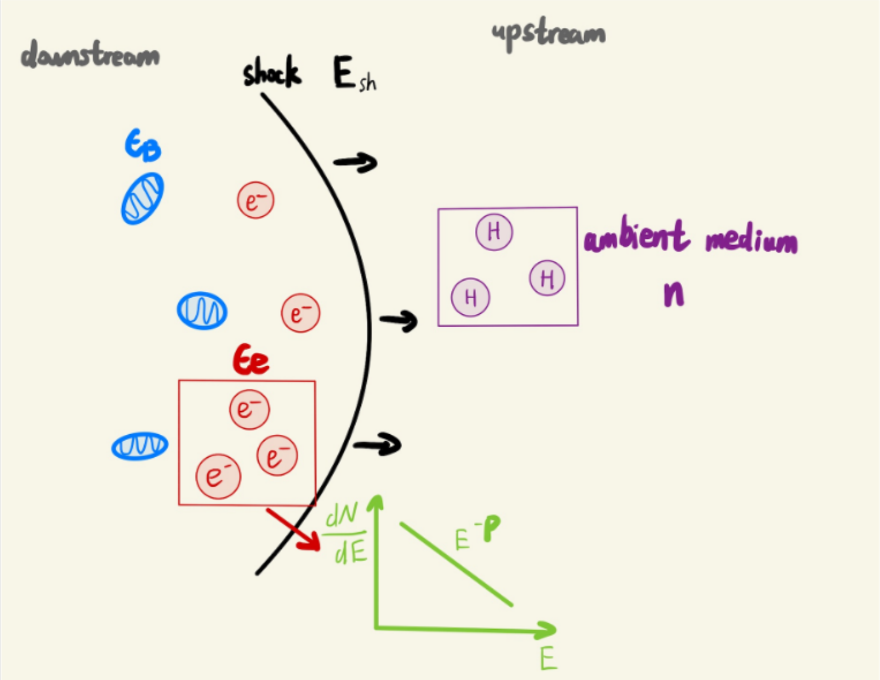

Figure 3.13: Schematic picture of the standard single-zone SSC model.

From Eq. 3.2 and Eq. 3.3, we can derive the expressions for R and Γ, which reads

$$R = \left[\frac{17Et}{\pi n_0 m_{\rm p} c(1+z)}\right]^{1/4} \tag{3.4}$$

$$\Gamma = \left[\frac{17(1+z)^3 E}{65536\pi n_0 m_{\rm p} c^5 t^3}\right]^{1/8} \tag{3.5}$$

for a constant density profile ($k = 0$), and

$$R = \left[\frac{9Et}{2\pi n_0 m_{\rm p} c(1+z)}\right]^{1/2} \tag{3.6}$$

$$\Gamma = \left[\frac{9(1+z)E}{128\pi n_0 m_{\rm p} c^3 t}\right]^{1/4} \tag{3.7}$$

for the wind density profile ($k = 2$).

3.4.2 Evolution of the Electron Spectrum

During the propagation, the shock would sweep out the external medium and accelerate particles into a non-thermal distribution. The spectrum of these injected electrons can be described by a power law $N_{\rm inj}(\gamma^{'}) \propto \gamma^{'-p}$ between a minimum Lorentz factor $\gamma^{'}_{\rm min}$ and a maximum Lorentz factor $\gamma^{'}_{\rm max}$ with an exponential cutoff. In this paper, quantities denoted with a prime are measured in the shocked fluid frame.

Assuming $p > 2$ and $\gamma^{'}_{\rm max} \gg \gamma^{'}_{\rm min}$, we have

$$\gamma^{'}_{\rm min} \approx \frac{\epsilon_{\rm e}}{\eta_{\rm e}} \left(\frac{p-2}{p-1}\right) \frac{m_{\rm p}}{m_{\rm e}} \Gamma \tag{3.8}$$

where $\epsilon_{\rm e}$ is the fraction of the shock energy transferred into electrons and $m_{\rm e}$ is the mass of an electron, and $\eta_{\rm e}$ is the fraction of electrons to be accelerated.

Accelerated electrons will lose energy through three radiation processes: synchrotron, synchrotron-self Compton (SSC) and external Compton (EC) emissions. The radiation power are

$$P^{'}_{\rm syn} = \frac{4}{3}\sigma_{\rm T} c \gamma^{'2} U^{'}_{\rm B}, \tag{3.9}$$

$$P^{'}_{\rm SSC} = \frac{4}{3}\sigma_{\rm T} c \gamma^{'2} U^{'}_{\rm syn}, \tag{3.10}$$

$$P^{'}_{\rm EC} = \frac{4}{3}\sigma_{\rm T} c \gamma^{'2} U^{'}_{\rm ext}. \tag{3.11}$$

where $U^{'}_{\rm B}$, $U^{'}_{\rm syn}$, $U^{'}_{\rm ext} \equiv \frac{4}{3}\Gamma^2 U_{\rm ext}$ are the energy densities of the magnetic field, the synchrotron radiation and the external photon background in the shocked fluid frame, respectively. We assume that a constant fraction $\epsilon_{\rm B}$ of the shock energy is carried by the magnetic field. The strength of the magnetic field $B^{'}$ can be described by

$$B^{'} = (32\pi m_{\rm p} \epsilon_{\rm B} n)^{1/2} \Gamma c. \tag{3.12}$$

The expansion time of the shock in the downstream frame is given by

$$\int d\tau^{'}_{\rm exp} \sim \int dR/\Gamma_s c \tag{3.13}$$

$$\tau^{'}_{\rm exp} = \frac{\sqrt{2}}{5-k} \frac{R}{\Gamma c} \tag{3.14}$$

while the characteristic cooling timescale of an electron is

$$\tau^{'}_{\rm c} \approx \frac{\gamma^{'} m_{\rm e} c^2}{P^{'}_{\rm syn} + P^{'}_{\rm SSC} + P^{'}_{\rm EC}} = \frac{\gamma^{'} m_{\rm e} c^2}{P^{'}_{\rm syn}(1 + x + y)} \tag{3.15}$$

Balancing these two timescales, we obtain the expression for the characteristic cooling Lorentz factor

$$\gamma^{'}_{\rm c} = \frac{3(5 - k)\Gamma m_{\rm e} c^2}{4\sqrt{2}\sigma_{\rm T} R (U^{'}_{B} + U^{'}_{\rm syn} + U^{'}_{\rm ext})} \tag{3.16}$$

$$= \frac{\gamma^{'\rm syn}_{\rm c}}{1 + x + y} \tag{3.17}$$

where $\gamma^{'\rm syn}_{\rm c} = \frac{3(5-k)\Gamma m_{\rm e} c^2}{4\sqrt{2}\sigma_{\rm T} R U^{'}_{B}}$ is the characteristic Lorentz factor when only considering energy losses through synchrotron radiation, x and y represent the ratios of luminosities through different radiation processes[99, 103].

$$y \equiv \frac{U^{'}_{\rm ext}}{U^{'}_{\rm B}} = \frac{\Gamma^2 U_{\rm ext}}{U^{'}_{\rm B}} \tag{3.18}$$

$$x \equiv \frac{U'_{\rm syn}}{U'_{\rm B}} = \frac{\eta \epsilon_{\rm e}}{\epsilon_{\rm B}(1+x+y)} \tag{3.19}$$

where η is the fraction of the electron energy radiated through synchrotron, SSC and EC processes. If $\gamma'_{\rm min} > \gamma'_c$, all of the initially injected electrons lose almost all of their energy through radiation, and hence $\eta = 1$. We call it as the fast cooling case. While for $\gamma'_c > \gamma'_{\rm min}$, only electrons with Lorentz factor greater than γ'_c cool down and this situation is called as the slow cooling case. The expression for η can can be summarized as

$$\eta = \begin{cases} 1, & \gamma'_{\rm min} > \gamma'_c \\ \left(\frac{\gamma'_c}{\gamma'_{\rm min}}\right)^{2-p}, & \gamma'_c > \gamma'_{\rm min} \end{cases} \tag{3.20}$$

Note that we don't consider the Klein-Nishina effect here. Eq. 3.20 is only valid in the Thomson regime.

Combine Eq. 3.19 and Eq. 3.20, we have

$$\begin{array}{ll} x(1+x+y) = \frac{\epsilon_{\rm e}}{\epsilon_{\rm B}}, & \gamma'_{\rm min} > \gamma'_{\rm c} \\ x(1+x+y)^{3-p} = \frac{\epsilon_{\rm e}}{\epsilon_{\rm B}}\left(\frac{\gamma'_c}{\gamma'_{\rm min}}\right)^{2-p}, & \gamma'_{\rm c} > \gamma'_{\rm min} \end{array} \tag{3.21}$$

If $\gamma'_{\rm c} > \gamma'_{\rm min}$, the electron spectrum is in the slow cooling region. Electrons with Lorentz factor around $\gamma'_{\rm min}$ are not affected by energy losses. In this case, the electron distribution can be written as,

$$N(\gamma') \propto \begin{cases} \gamma'^{-p}, & \gamma'_{\rm min} < \gamma' < \gamma'_{\rm c} \\ \gamma'^{-p-1}, & \gamma' > \gamma'_{\rm c} \end{cases} \tag{3.22}$$

Otherwise, (i.e. $\gamma'_{\rm c} < \gamma'_{\rm min}$), the electron spectrum is in the fast cooling region.

$$N(\gamma') \propto \begin{cases} \gamma'^{-2}, & \gamma'_{\rm c} < \gamma' < \gamma'_{\rm min} \\ \gamma'^{-p-1}, & \gamma' > \gamma'_{\rm min} \end{cases} \tag{3.23}$$

3.4.3 Synchrotron Component

The majority of the afterglow emissions, from radio, optical and X-ray bands, are produced through synchrotron radiation. Accelerated electrons interact with the shocked magnetic field and emit synchrotron photons. Observations in these energy bands were detected much earlier than those in gamma-ray bands, and the first theoretical explanations were also proposed earlier. The detailed calculations on the synchrotron spectrum has been discussed in Sari *et al.* [100].

The characteristic synchrotron frequency we observed is

$$\nu_{\rm syn} = \Gamma \gamma'^2 \frac{eB}{2\pi m_{\rm e} c}/(1+z) \tag{3.24}$$

where e is the charge of an electron.

And the peak spectral power, which is independent with γ', can be described as

$$P_{\nu,\max} \approx \frac{\Gamma^2 P'_{\rm syn}}{\nu_{\rm syn}(1 + z)} = \frac{m_{\rm e}c^2\sigma_{\rm T}}{3e}\Gamma B \tag{3.25}$$

In the case of fast cooling, the synchrotron spectrum is

$$F_\nu^{\rm syn} = \begin{cases} (\nu/\nu_{\rm c})^{1/3} F_{\nu,\max}, & \nu_{\rm c} > \nu \\ (\nu/\nu_{\rm c})^{-1/2} F_{\nu,\max}, & \nu_{\min} > \nu > \nu_{\rm c} \\ (\nu_{\min}/\nu_{\rm c})^{-1/2} (\nu/\nu_{\min})^{-p/2} \exp(-\nu/\nu_{\max}) F_{\nu,\max}, & \nu > \nu_{\min} \end{cases} \tag{3.26}$$

and in the case of slow cooling, we have

$$F_\nu^{\rm syn} = \begin{cases} (\nu/\nu_{\min})^{1/3} F_{\nu,\max}, & \nu_{\min} > \nu \\ (\nu/\nu_{\min})^{-(p-1)/2} F_{\nu\,\max}, & \nu_{\rm c} > \nu > \nu_{\min} \\ (\nu_{\rm c}/\nu_{\min})^{-(p-1)/2} (\nu/\nu_{\rm c})^{-p/2} \exp(-\nu/\nu_{\max}) F_{\nu,\max}, & \nu > \nu_{\rm c} \end{cases} \tag{3.27}$$

where $\nu_{\min} = \nu_{\rm syn}(\gamma'_{\min})$, $\nu_{\rm c} = \nu_{\rm syn}(\gamma'_{\rm c})$, $\nu_{\max} = \nu_{\rm syn}(\gamma'_{\max})$ and $F_{\nu,\max} = N_{\rm e}P_{\nu,\max}/4\pi D^2$ is the peak flux observed at the distance D. Here $N_{\rm e}$ is the total number of the accelerated electrons. Because of the relativistic beaming effect, only radiation emitted by electrons moving towards the observer within a small solid angle $d\Omega \sim 1/\Gamma^2$ can be detected. In the case with a constant external density profile, $N_{\rm e} = 4\pi R^3 n_0 d\Omega/3$ and in the wind density profile $N_{\rm e} = \eta_{\rm e}4\pi R n_0 d\Omega$. Meanwhile, the radiation power of these upcoming electrons also boost by a factor of Γ^2 due to the Doppler effect, hence the combined influence on $F_{\nu,\max}$ from these two effects is offset.

3.4.4 SSC Component

Due to the limit on the maximum electron energy accelerated at relativistic shocks, it is hard to produce gamma-ray photons (GeV or even TeV) through synchrotron radiation. Hence, some other radiation mechanism should come into play. Because of the high energy density of the produced synchrotron emissions, these photons can be scattered by accelerated electrons and boost their energy. The spectrum from such a SSC process was firstly discussed in Sari and Esin [99]. In the fast cooling regime,

$$F_\nu^{\rm SSC} \simeq \frac{\sigma_T N_{\rm e}}{4\pi R^2} F_{\nu,\max} x_0 \times \begin{cases} \frac{5}{6}\left(\frac{\nu_{\rm a}}{\nu_c}\right)^{1/3}\left(\frac{\nu}{\nu_{\rm a}^{\rm SSC}}\right), \nu < \nu_{\rm a}^{\rm SSC} \\ \frac{9}{10}\left(\frac{\nu}{\nu_{\rm c}^{\rm SSC}}\right)^{1/3}, \nu_{\rm a}^{\rm SSC} < \nu < \nu_{\rm c}^{\rm SSC} \\ \frac{1}{3}\left(\frac{\nu}{\nu_{\rm c}^{\rm SSC}}\right)^{-1/2}\left[\frac{28}{15} - \ln\left(\frac{\nu}{\nu_{\rm c}^{\rm SSC}}\right)\right], \nu_{\rm c}^{\rm SSC} < \nu < \sqrt{\nu_{\rm c}^{\rm SSC}\nu_{\min}^{\rm SSC}} \\ \frac{1}{3}\left(\frac{\nu}{\nu_{\rm c}^{\rm SSC}}\right)^{-1/2}\left[2\frac{(p+5)}{(p+2)(p-1)} - \frac{2(p-1)}{3(p+2)} + \ln\left(\frac{\nu_{\min}^{\rm SSC}}{\nu}\right)\right], \sqrt{\nu_{\rm c}^{\rm SSC}\nu_{\min}^{\rm SSC}} < \nu < \nu_{\min}^{\rm SSC} \\ \frac{1}{(p+2)}\left(\frac{\nu}{\nu_{\min}^{\rm SSC}}\right)^{-p/2}\left(\frac{\nu_{\rm c}}{\nu_m}\right)\left[\frac{2}{3}\frac{(p+5)}{(p-1)} - \frac{2}{3}\frac{(p-1)}{(p+2)} + \ln\left(\frac{\nu}{\nu_{\min}^{\rm SSC}}\right)\right], \nu > \nu_{\min}^{\rm SSC} \end{cases} \tag{3.28}$$

And in the slow cooling regime,

$$F_\nu^{\mathrm{SSC}} \simeq \frac{\sigma_T N_{\mathrm{e}}}{4\pi R^2} F_{\nu,\max} x_0 \times \begin{cases} \frac{5}{2}\frac{(p-1)}{(p+1)}\left(\frac{\nu_{\mathrm{a}}}{\nu_{\min}}\right)^{1/3}\left(\frac{\nu}{\nu_{\mathrm{a}}^{\mathrm{IC}}}\right), \nu < \nu_{\mathrm{a}}^{\mathrm{SSC}} \\ \frac{3}{2}\frac{(p-1)}{(p-1/3)}\left(\frac{\nu}{\nu_{\min}^{\mathrm{IC}}}\right)^{1/3}, \nu_{\mathrm{a}}^{\mathrm{SSC}} < \nu < \nu_{\min}^{\mathrm{SSC}} \\ \frac{(p-1)}{(p+1)}\left(\frac{\nu}{\nu_{\min}^{\mathrm{SSC}}}\right)^{(1-p)/2}\left[\frac{4(p+1/3)}{(p+1)(p-1/3)} + \ln\left(\frac{\nu}{\nu_{\min}^{\mathrm{SSC}}}\right)\right], \nu_{\min}^{\mathrm{SSC}} < v < \sqrt{\nu_{\min}^{\mathrm{SSC}}\nu_{\mathrm{c}}^{\mathrm{SSC}}} \\ \frac{(p-1)}{(p+1)}\left(\frac{\nu}{\nu_{\min}^{\mathrm{SSC}}}\right)^{(1-p)/2}\left[2\frac{(2p+3)}{(p+2)} - \frac{2}{(p+1)(p+2)} + \ln\left(\frac{\nu_{\mathrm{c}}^{\mathrm{SSC}}}{\nu}\right)\right], \sqrt{\nu_{\min}^{\mathrm{SSC}}\nu_{\mathrm{c}}^{\mathrm{SSC}}} < \nu < \nu_{\mathrm{c}}^{\mathrm{SS}} \\ \frac{(p-1)}{(p+1)}\left(\frac{\nu}{\nu_{\min}^{\mathrm{SSC}}}\right)^{-p/2}\left(\frac{\nu_{\mathrm{c}}}{\nu_{\min}}\right)\left[2\frac{(2p+3)}{(p+2)} + \frac{2}{(p+2)^2} + \frac{(p+1)}{(p+2)}\ln\left(\frac{\nu}{\nu_{\mathrm{c}}^{\mathrm{SSC}}}\right)\right], \nu > \nu_{\mathrm{c}}^{\mathrm{SSC}} \end{cases} \tag{3.29}$$

where $x_0 = 0.5$. The break frequencies are defined as $\nu_{\mathrm{a}}^{\mathrm{SSC}} = 4\gamma_{\min}^{\prime 2}\nu_{\mathrm{a}} x_0$, $\nu_{\min}^{\mathrm{SSC}} = 4\gamma_{\min}^{\prime 2}\nu_{\min} x_0$ and $\nu_{\mathrm{c}}^{\mathrm{SSC}} = 4\gamma_{\mathrm{c}}^{\prime 2}\nu_{\mathrm{c}} x_0$.

Note $\gamma_{\max}^{'}$ is not taken into account in above expressions. For more exact calculations, we need to substitute the upper limit of integration in the electron spectrum by $\gamma_{\max}^{'}$ (for details see Zhang *et al.* [103]).

3.4.5 EC Component

Long GRBs are widely considered to be located at star-forming regions, where a dense external photon background may exist. In Zhang *et al.* [103], they take this EC scattering into consideration, assuming an external monochromic photon field with a characteristic energy $\epsilon_0 = h\nu_0$.

The characteristic frequency of the observed photons is

$$\nu^{\mathrm{EC}}(\gamma^{'}) \approx \frac{4}{3}\Gamma^2 \gamma^{\prime 2}\nu_0/(1+z) \tag{3.30}$$

where ν_0 is the frequency of the monochromic external photons.

The total spectrum in the fast cooling regime is

$$F_\nu^{\mathrm{EC}} = F_{\nu,\max}^{\mathrm{EC}} \begin{cases} \left(\nu/\nu_{\mathrm{c}}^{\mathrm{EC}}\right), & \nu < \nu_{\mathrm{c}}^{\mathrm{EC}} \\ \left(\nu/\nu_{\mathrm{c}}^{\mathrm{EC}}\right)^{-1/2}, & \nu_{\mathrm{c}}^{\mathrm{EC}} < \nu < \nu_{\min}^{\mathrm{EC}} \\ \left(\nu_{\min}^{\mathrm{EC}}/\nu_{\mathrm{c}}^{\mathrm{EC}}\right)^{-1/2}\left(\nu/\nu_{\min}^{\mathrm{EC}}\right)^{-p/2}\exp(-\nu/\nu_{\max}^{\mathrm{EC}}), & \nu > \nu_{\min}^{\mathrm{EC}} \end{cases} \tag{3.31}$$

and in the slow cooling regime,

$$F_\nu^{\mathrm{EC}} = F_{\nu,\max}^{\mathrm{EC}} \begin{cases} \left(\nu/\nu_{\min}^{\mathrm{EC}}\right), & \nu < \nu_{\min}^{\mathrm{EC}} \\ \left(\nu/\nu_{\min}^{\mathrm{EC}}\right)^{-(p-1)/2}, & \nu_{\min}^{\mathrm{EC}} < \nu < \nu_{\mathrm{c}}^{\mathrm{EC}} \\ \left(\nu_{\mathrm{c}}^{\mathrm{EC}}/\nu_{\min}^{\mathrm{EC}}\right)^{-(p-1)/2}\left(\nu/\nu_{\mathrm{c}}^{\mathrm{EC}}\right)^{-p/2}\exp(-\nu/\nu_{\max}^{\mathrm{EC}}), & \nu > \nu_{\mathrm{c}}^{\mathrm{EC}} \end{cases} \tag{3.32}$$

where $\nu_{\min}^{\mathrm{EC}} = \nu^{\mathrm{EC}}(\gamma_{\min}^{'})$, $\nu_{\mathrm{c}}^{\mathrm{EC}} = \nu^{\mathrm{EC}}(\gamma_{\mathrm{c}}^{'})$, $\nu_{\max}^{\mathrm{EC}} = \nu^{\mathrm{EC}}(\gamma_{\max}^{'})$, and F_ν^{EC} is the peak flux,

$$F_{\nu,\max}^{\mathrm{EC}} \equiv \frac{\eta N_{\mathrm{e}} \Gamma P_{\nu',\max}^{\prime \mathrm{EC}}}{4\pi D^2}(1+z) \tag{3.33}$$

$P_{\nu',\max}^{\prime \mathrm{EC}} = \frac{\sigma_{\mathrm{T}} c(\Gamma U_{\mathrm{ext}})}{\nu_0}$ is the peak spectral power in the shocked fluid frame.

Note that the realistic EC component could be more complicated, depending on the detailed spectra of the external photon backgrounds. In most cases, this EC component is neglected due to the weak energy density of the external radiation background.

Chapter 4

The implications of TeV GRB afterglows for acceleration at relativistic shocks

Gamma-ray burst afterglows have been detected in multi-wavelength bands for several decades. Nowadays we have already accumulated abundant observational data from radio, infrared, optical, X-ray to GeV bands. Thanks to these plentiful information, scientists built up a standard single-zone synchrotron self-Compton (SSC) model to explain the afterglow data. For a long time, this model can explain the observational data quite well.

In the last few years photons in TeV bands have been detected by MAGIC and H.E.S.S from three GRB events. Moreover, on October 9th, 2022, over 5000 very-high-energy photons up to ~ 10 TeV were captured by LHAASO. These breakthrough in gamma-ray domain provide provides new methods to test the standard SSC model as well as new hints on particle acceleration at relativistic shocks.

In this chapter we try to constrain the maximum electron energy accelerated at GRB relativistic shocks using the late-time TeV afterglow detections of GRB 190829A. Adopting characteristic afterglow parameters, this maximum energy would be fixed by the magnetized limit, too low to explain the X-ray data. Such a conclusion motivates us to do further studies on particle acceleration at relativistic shocks, which will be introduced in the following two chapters. Besides, because of the Klein-Nishina effect, the fitted spectra derived from the single-zone SSC model should be quite soft in TeV bands, conflicting with data measurements in other works. Such a conclusion seriously challenges the external shock model for GRB afterglows.

The Astrophysical Journal, 925:182 (7pp), 2022 February 1 https://doi.org/10.3847/1538-4357/ac3f38

The Implications of TeV-detected GRB Afterglows for Acceleration at Relativistic Shocks

Zhi-Qiu Huang[1], John G. Kirk[1], Gwenael Giacinti[1,2,3], and Brian Reville[1]
[1] Max-Planck-Institut für Kernphysik, Postfach 10 39 80, D-69029 Heidelberg, Germany
[2] Tsung-Dao Lee Institute, Shanghai Jiao Tong University, Shanghai 200240, People's Republic of China
[3] School of Physics and Astronomy, Shanghai Jiao Tong University, Shanghai 200240, People's Republic of China

Received 2021 September 28; revised 2021 November 29; accepted 2021 November 30; published 2022 February 3

Abstract

Motivated by the detection of very-high-energy (VHE) gamma rays deep in the afterglow emission of a gamma-ray burst (GRB), we revisit predictions of the maximum energy to which electrons can be accelerated at a relativistic blast wave. Acceleration at the weakly magnetized forward shock of a blast wave can be limited by either the rapid damping of turbulence generated behind the shock, the effect of a large-scale ambient magnetic field, or radiation losses. Within the confines of a standard, single-zone, synchrotron self-Compton (SSC) model, we show that observations of GRB 190829A rule out a rapid damping of the downstream turbulence. Furthermore, simultaneous fits to the X-ray and TeV gamma-ray emission of this object are not possible unless the limit on acceleration imposed by the ambient magnetic field is comparable to or weaker than that imposed by radiation losses. This requires the dominant length scale of the turbulence behind the shock to be larger than that implied by particle-in-cell simulations. However, even then, Klein–Nishina effects prevent production of the hard VHE gamma-ray spectrum suggested by observations. Thus, TeV observations of GRB afterglows, though still very sparse, are already in tension with the SSC emission scenario.

Unified Astronomy Thesaurus concepts: High energy astrophysics (739); Gamma-ray bursts (629)

1. Introduction

The spectral evolution of the afterglows of gamma-ray bursts (GRBs) provides crucial information on their properties, as well as those of the surrounding medium (Mészáros 2002; Piran 2004; Kumar & Zhang 2015). To date, these data have predominantly been modeled under the assumption that the radiating particles are accelerated at or close behind the relativistic shock front that the GRB drives into its surroundings, although an alternative scenario in which electrons are injected via postburst activity in the central engine has its attractions (Kirk et al. 2021). When predicting the spectra and the characteristic frequencies of afterglow radiation, theoretical uncertainties have generally been parameterized by three essential quantities: the power-law index (p) of the accelerated particles and the ratio of the energy density in the accelerated electrons (ϵ_e) and magnetic field (ϵ_B) to that of the shocked fluid. The external shock acceleration model has long been the preferred scenario due not only to the relative simplicity of the model but also because the inferred injection spectra are broadly consistent with predictions from shock acceleration theory (e.g., Kirk et al. 2000).

Since the afterglow is observed mainly in the radio, optical, and X-ray bands, there has been relatively little interest in predicting the maximum energy to which particles can be accelerated. However, recent observations of afterglow radiation in very-high-energy (VHE) γ rays by the H.E.S.S. and MAGIC collaborations (Abdalla et al. 2019, 2021; Acciari et al. 2019) have prompted us to reconsider this question.

In a previous paper, Kirk & Reville (2010, hereafter KR), we estimated the maximum energy to which particles can be accelerated and the frequency of the photons they radiate without considering in detail the dynamics of the shock. For ultrarelativistic shocks, we found that the maximum synchrotron photon energy falls well below the synchrotron burn-off limit (see also Derishev 2007; Lemoine 2013; Sironi et al. 2013; Asano et al. 2020). Here we compute the characteristic frequencies of the synchrotron and related synchrotron self-Compton (SSC) radiation from a GRB afterglow under the assumption of self-similar evolution of the shock front (Blandford & McKee 1976) and develop a simple single-zone ("thin shell") model to determine the spectrum and light curves. We revise expectations regarding different limitations on the maximum electron energy and critically assess their applicability in light of TeV γ-ray observations.

The outline of the paper is as follows. In the next section, we provide an overview of maximum-energy predictions for shock-accelerated electrons at weakly magnetized ultrarelativistic shocks. In Section 3, the predicted photon spectra of a self-similar blast wave are presented and compared to recent GRB detections by the H.E.S.S. experiment. The implications of our results for the shock acceleration model and the potential of future observations to sharpen these conclusions are discussed in Section 4.

2. The Maximum Energy of Accelerated Electrons

The Lorentz factor of the decelerating outer shock in the self-similar model of Blandford & McKee (1976) satisfies $\Gamma_{\rm sh} \propto t^{-m/2}$, the two principal cases of interest being shock propagation into a uniform medium ($m = 3$) or a wind profile ($m = 1$). Here t is time measured in the rest frame of the explosion's progenitor. To compare radiation signatures with observations, relevant parameters should be expressed in terms of the "observer time", $t_{\rm obs} = (1 + z)(t - \boldsymbol{n} \cdot \boldsymbol{r}/c)$, with z the redshift of the source, $\boldsymbol{r}$ the position vector of the emitting plasma relative to the site of the explosion, and $\boldsymbol{n}$ the observer's direction. Since the radial velocity of the plasma is highly relativistic, those parts of the shock moving close to the direction of the observer make the dominant contribution, and the problem can be simplified by defining $t_{\rm obs}$ as the time at which a photon emitted at the point on the shock front closest

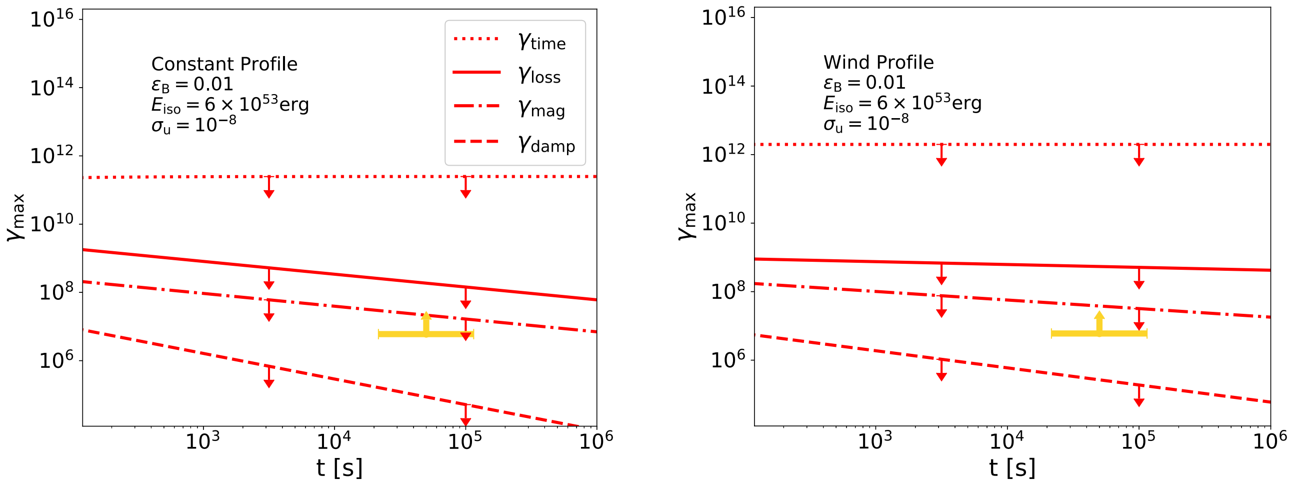

Figure 1. Maximum electron energy as a function of observer time for different external profiles. Left panel: constant-density profile. Right panel: wind density profile. From bottom to top, we identify four different limits: damping limited (dashed), magnetization limit (dashed–dotted), radiation loss limited (solid), and time limited (dotted). The maximum detected photon energy serves as a lower limit on the maximum electron energy in the source and is shown in yellow for the late-time VHE emission of GRB 190829A. The damping limit is shown for $L_{\rm damp} \approx \sigma_u^{-1/2} c/\omega_{\rm p}$ (see text), and the loss and magnetization limits for $\ell_{\rm w} = 10$.

to Earth reaches the observer, $t_{\rm obs} \approx (1+z)t/[2(m+1)\Gamma_{\rm sh}^2]$ (this simplification can, of course, be relaxed; e.g., Panaitescu & Mészáros 1998; Chevalier & Li 2000).

We consider the adiabatic expansion of a blast wave of total energy E into (a) a uniform medium of number density n ($m = 3$) and (b) a medium with number density $n = A/r^2$ ($m = 1$). In terms of observer time and to lowest order in $\Gamma_{\rm sh}^{-2}$, the shock Lorentz factor decelerates as

$$\Gamma_{\rm sh} = \begin{cases} \left[\dfrac{17(1+z)^3 E}{4096 \pi n m_{\rm p} c^5}\right]^{1/8} t_{\rm obs}^{-3/8} & \text{case (a)} \\ \left[\dfrac{9(1+z)E}{32\pi A m_{\rm p} c^3}\right]^{1/4} t_{\rm obs}^{-1/4} & \text{case (b),} \end{cases} \tag{1}$$

where $m_{\rm p}$ is the proton mass, and we consider only a pure electron–proton external medium. We will assume the electron acceleration time is short compared to the dynamical time of the shock (verified in Figure 1), such that the maximum energy due to losses or other effects can be determined based on the instantaneous shock conditions.

Predictions for the maximum electron energy in a decelerating blast wave follow from the improved understanding of the microphysics of ultrarelativistic weakly magnetized ($\sigma_{\rm u} \ll 1$) shocks provided by kinetic plasma simulations. Here $\sigma_{\rm u} = B_1^2/4\pi n_1 m_p c^2$ is the upstream magnetization parameter, where n_1 and B_1 are, respectively, the proper number density and magnetic field strength immediately upstream of the shock.

The key parameter used by KR to characterize the downstream turbulence is its "strength", a, that is, the ratio of the characteristic size λ of the intense magnetic field structures that mediate the shock transition (and persist downstream), to the length scale defined by the averaged turbulent magnetic field strength:

$$a = \lambda[eB/(m_{\rm e}c^2)]. \tag{2}$$

Here B is the rms magnetic field strength inside the structures, and $m_{\rm e}$ ($-e$) is the mass (charge) of the electron. Kinetic simulations indicate that the typical size of the structures is several plasma inertial lengths. Therefore, we define $\lambda = \ell_{\rm w} c/\omega_{\rm p}$, where $\omega_{\rm p}$ is the plasma frequency of the relativistic fluid, and follow Sironi et al. (2013) by setting $\ell_{\rm w} = 10$ in our modeling, though values as large as 30 are also quoted. The effective mass of the particles in the immediate postshock relativistic proton–electron fluid is determined by the pressure $p_2 = (2/3)\Gamma_{\rm sh}^2 n_1 m_{\rm p} c^2$ and the proper particle number density $n_2 = 2\sqrt{2}\,\Gamma_{\rm sh} n_1$, leading to $\omega_{\rm p} = \sqrt{\pi n_2^2 e^2 c^2/p_2}$ (Amano & Kirk 2013), where we have used the jump conditions for a cold upstream medium. Simulations of weakly magnetized relativistic shocks show the magnetization parameter associated with the self-generated field $\epsilon_{\rm B} = B^2/(24\pi p_2)$ peaks at the shock's position. Strong fluctuating fields extend upstream and downstream but plateau downstream at a level of 10^{-3}–10^{-2} (e.g., Keshet et al. 2009; Vanthieghem et al. 2020). The plateau value is important for the determination of the maximum electron energy.

In terms of the postshock magnetization parameter, one finds in the immediate downstream region of the self-similar expanding shock

$$a = \begin{cases} 2.6 \times 10^4 \ell_{\rm w} \epsilon_B^{1/2} E_{54}^{1/8} n_1^{-1/8} t_{10}^{-3/8} (1+z)^{3/8} & \text{case (a)} \\ 5.7 \times 10^4 \ell_{\rm w} \epsilon_B^{1/2} E_{54}^{1/4} A_{35}^{-1/4} t_{10}^{-1/4} (1+z)^{1/4} & \text{case (b),} \end{cases} \tag{3}$$

where $t_{10} = t_{\rm obs}/10$ hr, and $E_{54} = E/10^{54}$ erg. In case (b), the upstream density is determined by the (assumed) constant mass-loss rate of the progenitor and its asymptotic wind velocity. We use $A = A_{35} \times 10^{35}$ cm^{-1}, corresponding to a mass-loss rate of $\dot{M} = 10^{-5} M_\odot$ yr^{-1} and wind velocity $v_{\rm wind} = 3000$ km s^{-1}. From Equation (3), it is clear that $a \gg 1$, which implies that the electron emits synchrotron radiation (Landau & Lifshitz 1971) rather than "jitter" radiation, although low-frequency modifications due to repeated scatterings may nevertheless be present (Fleishman 2006; Reville & Kirk 2010).

The parameter a also determines the transport regime for accelerated electrons; those with Lorentz factor $\bar{\gamma}_{\rm e} < a$ (hereafter, a bar denotes quantities measured in the frame comoving with the plasma) are tied to magnetic field lines and undergo "helical" transport between scatterings. On the other hand, those with $\bar{\gamma}_e > a$ are deflected by only a small angle per fluctuation interaction and undergo "ballistic" transport between scatterings. In each case, the turbulence is expected to drive the particle distribution toward isotropy. However, in doing so, it causes the electrons to radiate. In relativistic shock acceleration theory, the isotropization rate is thought to be roughly equal to the rate of energy gain. In each transport regime, one can define a Lorentz factor $\bar{\gamma}_{\max}$ such that isotropization/energization is slower than radiation losses if $\bar{\gamma}_e > \bar{\gamma}_{\max}$. Generalizing the results found by KR to include cooling by inverse Compton scattering, one finds the maximum energy when limited by radiative losses

$$\bar{\gamma}_{\rm loss} = \begin{cases} a_{\rm crit} & a < a_{\rm crit} \\ a_{\rm crit}\sqrt{a_{\rm crit}/a} & a > a_{\rm crit} \end{cases}, \tag{4}$$

where

$$\begin{aligned} a_{\rm crit} &= \{3m_e \ell_w c^3/[2e^2\omega_p(1+x)]\}^{1/3} \\ &= \begin{cases} 4.1 \times 10^6 \ell_w^{1/3} n_1^{-1/6}(1+x)^{-1/3} & \text{case (a)} \\ 8.9 \times 10^6 E_{54}^{1/6} \ell_w^{1/3} A_{35}^{-1/3} & \\ \times\, t_{10}^{1/6}(1+z)^{-1/6}(1+x)^{-1/3} & \text{case (b).} \end{cases} \end{aligned} \tag{5}$$

Here $x = \dot{\gamma}_{\rm IC}/\dot{\gamma}_{\rm syn}$ is the ratio of the power emitted by a single electron as inverse Compton emission to that emitted as synchrotron radiation. If Compton scattering takes place in the Thomson regime, x is independent of the electron energy. Furthermore, neglecting the contribution of external photons, $x \approx \bar{U}_{\rm syn}/\bar{U}_B$, the ratio of the energy density of synchrotron photons to that of the magnetic field, measured in the comoving frame (see Section 3.3). Comparing Equations (3) and (5), we expect $a \ll a_{\rm crit}$, which implies that transport of the highest-energy electrons proceeds in the ballistic regime via small-angle scattering.

In this regime, the isotropization rate is (KR)

$$\nu_{\rm iso} \approx \langle \Delta\theta^2 \rangle \nu_{\rm sc} = \left(\frac{a}{\bar{\gamma}}\right)^2 \frac{c}{\lambda}. \tag{6}$$

Although isotropization is dominated by frequent interactions with small-scale fields, the rate at which this occurs decreases rapidly with increasing Lorentz factor. At sufficiently large energies, the effect on a particle trajectory becomes negligible compared to that of the magnetic field averaged over scales much larger than the scattering mean free path, $c/\nu_{\rm iso}$. This large-scale field downstream of the shock can be determined from the ambient magnetic field via the shock jump conditions, $\langle B_{2,\parallel}\rangle = \langle B_{1,\parallel}\rangle$ and $\langle B_{2,\perp}\rangle = 2\sqrt{2}\,\Gamma_{\rm sh}\langle B_{1,\perp}\rangle$, the average being taken over spatial scales $\gg \lambda$. Defining the mean downstream electron gyrofrequency $\omega_g = e\langle B_2\rangle/\bar{\gamma} m_e c$, electrons are said to be magnetized when $\omega_g > \nu_{\rm iso}$. Unless the upstream field is aligned with the shock normal to within $1/\Gamma_{\rm sh}$ (a situation we do not consider here), the downstream mean field is effectively perpendicular to the bulk flow direction. Achterberg et al. (2001) found that for acceleration to proceed in this case, the isotropization rate in the downstream frame should exceed the gyrofrequency in the average field if particles are to overtake the receding shock (see also Lemoine & Pelletier 2010). For a shock with an external magnetization parameter $\sigma_u = B_1^2/4\pi n_1 m_p c^2$, and as before, turbulent magnetic fluctuations concentrated at $\lambda = \ell_w c/\omega_p$, it follows that particles are magnetized downstream when their Lorentz factor exceeds

$$\bar{\gamma}_{\rm mag} = \ell_w \frac{m_p}{m_e} \epsilon_B \sigma_u^{-1/2}. \tag{7}$$

The maximum electron Lorentz factor is then determined by the more stringent of the two limits: $\bar{\gamma}_{\max} = {\rm Min}(\bar{\gamma}_{\rm loss}, \bar{\gamma}_{\rm mag})$. We note that additional large-scale magnetic field fluctuations related to upstream wave excitation (Reville & Bell 2014) or ambient turbulence may provide a channel to circumvent the magnetized energy limit, though this may introduce other spectral features (e.g., Niemiec et al. 2006).

In addition to the loss and magnetized limits, a third constraint on the maximum electron Lorentz factor arises if the magnetic field fluctuations generated at the shock damp away rapidly (see also Lemoine 2013). Defining $L_{\rm damp}$ as the characteristic length scale of this decay, it follows that the return probability for particles with a mean free path $c/\nu_{\rm sc} > L_{\rm damp}$ is significantly reduced. Simulations by Sironi et al. (2013), for example, display a symmetric rise and decay profile of ϵ_B about the shock, with a characteristic scale[4] $L_{\rm damp} \approx \sigma_u^{-1/2} c/\omega_p$. The maximum energy is therefore limited by this effect to

$$\bar{\gamma}_{\rm damp} \approx (\ell_w \epsilon_B m_p/m_e)^{1/2} \Gamma_{\rm sh} \sigma_u^{-1/4}, \tag{8}$$

which we refer to as the damping limit.

Figure 1 shows the three limits on the maximum electron Lorentz factor given by Equations (4), (7), and (8), taking instantaneous values of the shock parameters in the two scenarios considered. Standard GRB afterglow parameters are adopted here and in subsequent figures. The values are boosted to the upstream observer's frame for comparison to observations (neglecting redshift). The detection of late-time TeV emission from two GRBs places a firm lower limit on the maximum particle energy in the observer's frame, indicated in yellow in the figure. As a consistency check, we also indicate the maximum energy that might be expected from time-limited acceleration using the prescription of Achterberg et al. (2001),

$$\bar{\gamma}_{\rm time} = \bar{\gamma}(t_0) + \int_{t_0}^{t_{\rm obs}} {\rm d}t \frac{\bar{\gamma}(t)}{t_{\rm cyc}(\bar{\gamma}, t)}, \tag{9}$$

where $t_{\rm cyc}$ is the cycle time assuming ballistic scattering only in the downstream and the combined action of scattering and regular deflection in the upstream. We choose as an initial condition $\bar{\gamma}(t_0) = \Gamma_{\rm sh}(t_0)$, and since $\Gamma_{\rm sh}$ diverges as $t \to 0$, we select t_0 such that $\Gamma_{\rm sh}(t_0) = 300$. This equation is integrated numerically from t_0 to the observed time to give the time-limited acceleration upper limit in Figure 1. The fact that this limit substantially exceeds the others justifies our use of instantaneous flow parameters when evaluating the latter.

3. The Synchrotron Self-Compton Spectrum

3.1. Characteristic Frequencies

In the context of the rough estimates we seek here, synchrotron radiation can be treated as narrowband; i.e., electrons with a Lorentz factor $\bar{\gamma}_e$ radiate only photons close to a characteristic

---

[4] Approximately equal to the upstream gyroradius of shock-reflected particles as measured by a downstream observer.

frequency given by $\bar{\nu} = h_1 B \bar{\gamma}_e^2$, where $h_1 = 1.3 \times 10^6$ Hz G^{-1}. This frequency is independent of pitch angle, and the photons can be considered to be radiated isotropically in the comoving frame of the plasma. At the observer, these photons appear blueshifted by the Doppler factor $\mathcal{D} = \gamma_2(1 + \beta\bar{\mu})$, where $\gamma_2 = (1 - \beta^2)^{-1/2} = \Gamma_{\rm sh}/\sqrt{2}$ is the bulk Lorentz factor of the ultrarelativistic expanding plasma immediately downstream of the shock front, and $\bar{\mu}$ is the cosine of the angle between the photon momentum and the radius vector $\boldsymbol{r}$ as measured in the comoving frame. Also taking the cosmological redshift z into account, the highest-frequency photons that can be produced by shock acceleration emerge from the closest point to Earth on the shock (i.e., $\bar{\mu} = 1$, $\mathcal{D} \approx 2\gamma_2$),

$$\nu_{\rm max}^{\rm loss} = \mathcal{D} h_1 B a_{\rm crit}^2/(1 + z) = \begin{cases} 0.6 \ell_{\rm w}^{2/3} \epsilon_{\rm B,-2}^{1/2} n_1^{-1/12} E_{54}^{1/4} t_{10}^{-3/4} \\ \times (1 + z)^{-1/4} (1 + x)^{-2/3}\ \text{MeV} \quad \text{case (a)} \\ 1.2 \ell_{\rm w}^{2/3} \epsilon_{\rm B,-2}^{1/2} E_{54}^{1/3} A_{35}^{-1/6} t_{10}^{-2/3} \\ \times (1 + z)^{-1/3} (1 + x)^{-2/3}\ \text{MeV} \quad \text{case (b)}, \end{cases} \tag{10}$$

where $\epsilon_{\rm B} = 10^{-2} \epsilon_{\rm B,-2}$. Here we have assumed ballistic transport. If helical transport applies, i.e., $a > a_{\rm crit}$, the maximum synchrotron photon energy is $h\nu_{\rm max}^{\rm loss}/m_e c^2 = \mathcal{D}(1 + x)^{-1} \alpha_{\rm f}^{-1}$, where $\alpha_{\rm f}$ is the fine-structure constant. If, on the other hand, magnetization of the electrons limits their acceleration, Equation (7), then the synchrotron limit is

$$\nu_{\rm max}^{\rm mag} = \mathcal{D} h_1 B \ell_w^2 \left(\frac{m_{\rm p}}{m_{\rm e}}\right)^2 \epsilon_B^2 \sigma_u^{-1}/(1 + z) = \begin{cases} 1.1\, \ell_{\rm w}^2 \sigma_{-8}^{-1} \epsilon_{\rm B,-2}^{5/2} n_1^{1/4} (1 + z)^{-1/4} E_{54}^{1/4} t_{10}^{-3/4}\,\text{keV} & \text{case (a)} \\ 0.5\, \ell_{\rm w}^2 \sigma_{-8}^{-1} \epsilon_{\rm B,-2}^{5/2} A_{35}{}^{1/2} t_{10}^{-1}\ \text{keV} & \text{case (b)} \end{cases}, \tag{11}$$

where $\sigma_u = 10^{-8} \times \sigma_{-8}$. Note here the strong dependence on $\ell_{\rm w}$ and ϵ_B, in contrast to the cooling-limited maximum frequency. For example, if $\epsilon_B \ll 0.01$, the maximum synchrotron photons may not reach the X-ray band at late times.

We emphasize that in both cases, the synchrotron cutoff lies below the frequently quoted maximum value (synchrotron burn-off/Bohm limit) of $2\gamma_2 m_e c^2/\alpha_{\rm f} = 2\gamma_2 \times 68$ MeV, where $\alpha_{\rm f}$ is the fine-structure constant. Employing a multizone emission model to overcome the synchrotron burn-off limit (e.g., Kumar et al. 2012; Khangulyan et al. 2021) must also contend with the maximum-energy predictions for weakly magnetized shocks.

The lower bound on the Lorentz factor of accelerated electrons is conventionally fixed by the efficiency with which energy is extracted from the particles flowing into the shock via the equation

$$\bar{\gamma}_{\rm min} \left[\frac{1 - (\bar{\gamma}_{\rm min}/\bar{\gamma}_{\rm max})^{p-2}}{1 - (\bar{\gamma}_{\rm min}/\bar{\gamma}_{\rm max})^{p-1}}\right] = \left(\frac{p - 2}{p - 1}\right) \frac{m_{\rm p}}{m_{\rm e}} \epsilon_{\rm e} \gamma_2, \tag{12}$$

where p is the index of the injection spectrum assumed to be a power law with abrupt low- and high-energy cutoffs (see Derishev & Piran 2021, for alternative approaches). It is commonly assumed that $\bar{\gamma}_{\rm max} \gg \bar{\gamma}_{\rm min}$, in which case the term in square brackets can be set to unity. However, special care should be taken if p is close to 2, as suggested, for example, by Ajello et al. (2019). Although the corresponding correction to $\bar{\gamma}_{\rm min}$ is typically small, it has a significant impact on the resulting SSC emission (see Petropoulou et al. 2011).

The observation frequency corresponding to $\bar{\gamma}_{\rm min}$ (written in hertz, as it falls in the infrared band) is

$$\begin{aligned} \nu_{\rm min} &= \mathcal{D} h_1 B \bar{\gamma}_{\rm min}^2/(1 + z) \\ &\approx \epsilon_{B,-2}^{1/2} \epsilon_{\rm e\,,-1}^2 E_{54}^{1/2} t_{10}^{-3/2} \\ &\quad \times \sqrt{1 + z}\, \left(\tfrac{p-2}{p-1}\right)^2 \begin{cases} 22.7\ \text{THz} & \text{case (a)} \\ 45.7\ \text{THz} & \text{case (b)}, \end{cases} \end{aligned} \tag{13}$$

where we have again selected $\bar{\mu} = 1$ and ignored the correction in Equation (12) due to finite maximum energy.

Once injected, an accelerated electron loses energy primarily via inverse Compton and synchrotron radiation in the downstream plasma, and its Lorentz factor $\bar{\gamma}_e$ changes at the rate $\dot{\gamma}_{\rm rad}(\bar{\gamma}_e) = -(1 + x) h_0 \bar{\gamma}_e^2 B^2$, where $h_0 = 1.29 \times 10^{-9}$ s^{-1} G^{-2}. Provided $\bar{\gamma}_e/|\dot{\gamma}_{\rm rad}(\bar{\gamma}_e)|$ is shorter than the dynamical evolution time of the shell, $\bar{t}_{\rm dyn} \approx t/2\gamma_2$, i.e., provided $\bar{\gamma}_e > \bar{\gamma}_c = 2\gamma_2/[(1 + x) h_0 B^2 t]$, the particles lose essentially all of their energy to radiation, the synchrotron component of which is observed at frequencies greater than the "cooling frequency":

$$\nu_{\rm c} = \mathcal{D} h_1 B \bar{\gamma}_c^2/(1 + z) \approx \begin{cases} 48 \epsilon_{B,-2}^{-3/2} n_1^{-1} E_{54}^{-1/2} t_{10}^{-1/2} \frac{(1+z)^{-\frac{1}{2}}}{(1+x)^2}\ \text{THz} & \text{case (a)} \\ 9.7 \epsilon_{B,-2}^{-3/2} E_{54}^{1/2} A_{35}^{-2} t_{10}^{1/2} \frac{(1+z)^{-\frac{3}{2}}}{(1+x)^2}\ \text{PHz} & \text{case (b)}. \end{cases} \tag{14}$$

If the loss rate is such that $\nu_c > \nu_{\rm min}$ or, equivalently, $\bar{\gamma}_c > \bar{\gamma}_{\rm min}$, the emission is said to occur in the slow-cooling regime, since the bulk of the electrons lose only a fraction of their energy to radiative cooling.

3.2. Synchrotron Spectrum

Apart from very early times, immediately after the prompt phase, it is clear from Equations (13) and (14) that, for typical GRB parameters, $\nu_c > \nu_{\rm min}$; i.e., synchrotron emission occurs in the slow-cooling regime. It is common practice in this case to neglect the emission from electrons that were injected more than a dynamical time earlier, although this procedure is not always justified (see, for example, Granot et al. 1999). The emitting electrons are thus assumed to occupy a thin homogeneous shell immediately behind the shock front and produce a spectral power that we approximate as $F(\nu) \propto \nu^{1/3}$ for $\nu < \nu_{\rm min}$, $F(\nu) \propto \nu^{-(p-1)/2}$ for $\nu_{\rm min} < \nu < \nu_c$, and $F(\nu) \propto \nu^{-p/2} \exp(-\nu/\nu_{\rm max})$ for $\nu > \nu_c$.

Now consider an element of this shell of area dA, which, in the comoving frame, emits synchrotron radiation with spectral power

$$\frac{d\bar{F}(\bar{\nu})}{dA} = m_e c^2 |\dot{\gamma}_{\rm syn}| \frac{dn}{d\bar{\gamma}_e} \frac{d\bar{\gamma}_e}{d\bar{\nu}}, \tag{15}$$

where $\dot{\gamma}_{\rm syn} = \dot{\gamma}_{\rm rad}/(1 + x)$ is the cooling rate due to synchrotron losses only. For $\bar{\gamma}_e > \bar{\gamma}_c$, a steady-state electron distribution, dn/d$\bar{\gamma}_e$ (per unit area of the shock), is established such that the rate $\dot{n}_>(\bar{\gamma}_e)$ at which particles are injected with Lorentz factors greater than $\bar{\gamma}_e$ equals the rate at which they cool to lower Lorentz factors, $|\dot{\gamma}_{\rm rad}(\bar{\gamma}_e)|$ dn/d$\bar{\gamma}_e$. The spectral power in this range is, therefore,

$$\frac{\mathrm{d}\bar{F}(\bar{\nu} > \bar{\nu}_{\mathrm{c}})}{\mathrm{d}A} = \frac{m_{\mathrm{e}}c^2}{2h_1 B\bar{\gamma}_{\mathrm{e}}}\frac{\dot{n}_{>}(\bar{\gamma}_{\mathrm{e}})}{1+x}, \tag{16}$$

where it is understood that electrons at a given Lorentz factor emit at $\bar{\gamma}_{\mathrm{e}} = \sqrt{h_1 B/\bar{\nu}}$.

On the other hand, for $\bar{\gamma}_{\mathrm{e}} < \bar{\gamma}_{\mathrm{c}}$, a steady state is achieved because particles are assumed to cease radiating a certain time $\bar{t}_{\mathrm{esc}}$ after injection without having appreciably changed their Lorentz factor, i.e., $|\mathrm{d}\dot{n}_{>}/\mathrm{d}\bar{\gamma}_{\mathrm{e}}| = \bar{t}_{\mathrm{esc}}^{-1}\mathrm{d}n\big/\mathrm{d}\bar{\gamma}_{\mathrm{e}}$. In this case, the spectral power either vanishes (for fast cooling) or is given by

$$\frac{\mathrm{d}\bar{F}(\bar{\nu} < \bar{\nu}_{\mathrm{c}})}{\mathrm{d}A} = \frac{m_{\mathrm{e}}c^2}{2h_1 B\bar{\gamma}_{\mathrm{e}}}|\dot{\gamma}_{\mathrm{syn}}|\;\bar{t}_{\mathrm{esc}}\left|\frac{\mathrm{d}\dot{n}_{>}}{\mathrm{d}\bar{\gamma}_{\mathrm{e}}}\right|. \tag{17}$$

We exploit the freedom inherent in the single-zone model by choosing $\bar{t}_{\mathrm{esc}} = \bar{t}_{\mathrm{dyn}}/(p-1)$, which ensures that, in the slow-cooling case, the model flux is continuous at $\bar{\nu} = \bar{\nu}_{\mathrm{c}}$. The peak spectral power (i.e., the maximum of $\mathrm{d}\bar{F}(\bar{\nu})/\mathrm{d}A$) for this shell element is emitted at $\bar{\nu}_{\mathrm{peak}} = \min[\bar{\nu}_{\mathrm{c}}, \bar{\nu}_{\mathrm{min}}]$, at which point $\dot{n}_{>} = 4\gamma_2 n_1 c/3$ and, for slow cooling, $(p-1)^{-1}\bar{\gamma}_{\mathrm{e}}|\mathrm{d}\dot{n}_{>}/\mathrm{d}\bar{\gamma}_{\mathrm{e}}| = \dot{n}_{>}$. In each case,

$$\left.\frac{\mathrm{d}n}{\mathrm{d}\bar{\gamma}_{\mathrm{e}}}\right|_{\mathrm{peak}} = \frac{2n_1 R}{3\bar{\gamma}_{\mathrm{peak}}}. \tag{18}$$

To relate the above spectral power to observations, we first note that it is emitted isotropically in the comoving frame. Denoting the direction to the observer by the unit vector $\bar{\boldsymbol{\Omega}}$ in this frame, the spectral power per unit solid angle is $\mathrm{d}\bar{F}/\mathrm{d}\bar{\Omega} = \bar{F}/4\pi$. Then, in the observer's frame, the received spectral power per unit solid angle for a given area on the shock surface is $\mathrm{d}F/\mathrm{d}\boldsymbol{\Omega} = \mathcal{D}^3\mathrm{d}\bar{F}/\mathrm{d}\bar{\boldsymbol{\Omega}}$ (Rybicki & Lightman 1986, Equation (4.97)). We simplify the integration over the shock surface by replacing ν_{peak}, B, n_1, and R with their values at $\bar{\mu} = 1$ and noting that $\int \mathrm{d}\boldsymbol{A}\mathcal{D}^3 = 4\pi R^2\gamma_2$. With these simplifications, one finds the peak flux density at the observer

$$\mathcal{F}^{\mathrm{SYN}}(\nu_{\mathrm{peak}}) = \frac{1}{D_{\mathrm{L}}^2}\int\frac{\mathrm{d}F(\nu_{\mathrm{peak}})}{\mathrm{d}\boldsymbol{\Omega}}d\boldsymbol{\Omega}_{\mathrm{shell}} \tag{19}$$

$$= \frac{1}{D_{\mathrm{L}}^2}\frac{h_0 m_{\mathrm{e}}c^2}{3h_1}Bn_1R^3\gamma_2, \tag{20}$$

where D_{L} is the luminosity distance. For $x = 0$, this expression agrees to an order of magnitude with previous results (e.g., Sari et al. 1998).

3.3. Inverse Compton Emission

The effect of cutoffs in the maximum electron energy at modest values was previously demonstrated by Petropoulou et al. (2011), who explored the impact on both the light curves and spectra. Here we revisit this effect for the competing maximum-energy models discussed in Section 2.

We assume that the cooling break ν_{c} is determined by the combination of synchrotron and SSC losses in the Thomson regime. For consistency, this requires $\bar{\gamma} \ll \bar{\gamma}^* \equiv m_e c^2/h\bar{\nu}^*$, where $\bar{\nu}^* = \max[\bar{\nu}_{\mathrm{min}}, \bar{\nu}_{\mathrm{c}}]$. For typical GRB afterglow parameters, we find $\bar{\gamma}^* > \bar{\gamma}_{\mathrm{c}}$. Rather extreme conditions are required for Klein–Nishina (KN) effects to significantly modify the electron spectrum (see Abdalla et al. 2021, Supp. Mat.). However, as we show below, these effects have a strong impact on the high-energy photon spectrum.

To compute the SSC emission, we first need to model the specific energy density of synchrotron photons $\bar{U}(\bar{\nu})$ within the source. The specific intensity of radiation on the source surface is directly detectable, $\bar{I}_{\bar{\nu}} = \mathrm{d}\bar{F}(\bar{\nu})/\mathrm{d}A/\mathrm{d}\Omega$, but modeling this quantity in the interior of the source requires additional assumptions. Here we follow previous treatments and assume that $\bar{I}_{\bar{\nu}}$ within the source is homogeneous and isotropic, so that $\bar{U}(\bar{\nu}) = (\alpha/c)\mathrm{d}\bar{F}(\bar{\nu})/\mathrm{d}A$, and set the geometrical factor α to unity.[5] Inserting the synchrotron photon power given in Equations (16) and (17) then leads to an implicit expression for $x = \int\bar{U}(\bar{\nu})d\bar{\nu}\big/\bar{U}_B$, which, in the limit $\bar{\gamma}_{\mathrm{max}} \gg \bar{\gamma}_{\mathrm{min}}$, reduces to an expression similar to Sari & Esin (2001, Equation (3.1)). However, for a general $\bar{\gamma}_{\mathrm{max}}$, we solve the full expression for x numerically. For simplicity, we again restrict ourselves to the Thomson regime, although the method can, in principle, be extended to include KN effects (in which case, x is energy dependent). The resulting SSC flux density is (cf. Rybicki & Lightman 1986, Equation (7.28a))

$$\mathcal{F}^{\mathrm{SSC}}(\nu_{\mathrm{IC}}) = 3\sigma_{\mathrm{T}}\int_{\bar{\gamma}_1}^{\bar{\gamma}_{\mathrm{max}}}\mathrm{d}\bar{\gamma}_{\mathrm{e}}\frac{\mathrm{d}n}{\mathrm{d}\bar{\gamma}_{\mathrm{e}}}\left(1 - \frac{h\nu_{\mathrm{IC}}}{\mathcal{D}\bar{\gamma}mc^2}\right)$$
$$\times\int_{1/4\bar{\gamma}2}^{1}\mathrm{d}zg(z)\mathcal{F}^{\mathrm{SYN}}\left(\frac{\nu_{\mathrm{IC}}}{4\bar{\gamma}^2 z\left(1 - \frac{h\nu_{\mathrm{IC}}}{\mathcal{D}\bar{\gamma}mc^2}\right)}\right),$$

where $g(z) = 1 + z + 2z\ln(z) - 2z^2 + \frac{1-z}{2}\left[\frac{(h\nu_{\mathrm{IC}}\,/\,\mathcal{D}\bar{\gamma}mc^2)^2}{(1 - h\nu_{\mathrm{IC}}\,/\,\mathcal{D}\bar{\gamma}mc^2)}\right]$ (Jones 1968). The full KN expression should be used here, since an accurate picture at the highest photon energies is required. Adopting a step function cutoff in the synchrotron flux density above $\bar{\nu}_{\mathrm{max}}$, the integral over z can be performed analytically, leaving a single integration over the electron distribution, which is done numerically. The electron distribution follows from Equation (18) and the corresponding slopes of the synchrotron spectrum. In deriving the above, we have assumed isotropy of the electrons and photons in the fluid frame and exploited the fact that $\mathcal{F}^{\mathrm{SSC}}$ and $\mathcal{F}^{\mathrm{SYN}}$ transform in the same way (Sari & Esin 2001).

In Figure 2, we compare representative fits for the wind and constant-density scenarios to the afterglow emission of the nearest VHE-detected GRB (GRB 190829A), since it is the object least affected by uncertainties connected with intergalactic absorption that, nevertheless, has significant late-time detection (Abdalla et al. 2021). While several recent theoretical works on this have tried to match the observations in a standard SSC model, the maximum energy was either assumed to be at the Bohm limit (Lu-Lu et al. 2021) or left as a free parameter (Salafia et al. 2021). Here we attempt to quantify the extent to which observations are consistent with current maximum-energy predictions discussed in the previous sections.

For $\ell_{\mathrm{w}} = 10$, the maximum electron energy is fixed by the magnetized limit (see Figure 1) and is too low to match either the X-ray or γ-ray data (see Figure 3). In addition, $\bar{\gamma}_{\mathrm{damp}} < \bar{\gamma}_{\mathrm{mag}}$ for all ℓ_{w}. We conclude that damping of magnetic field

---

[5] The SSC expression that follows reduces in the Thomson limit to that of Sari & Esin (2001) if we take $\alpha = (p-1) \approx 1$, due to our definition of $\bar{t}_{\mathrm{esc}}$. Note that the R in their Equation (A2) corresponds to the postshocked radius in which the emitting electrons reside, which, following Blandford & McKee (1976), is $\approx R/\Gamma_{\mathrm{sh}}^2$ for an upstream observer in our notation.

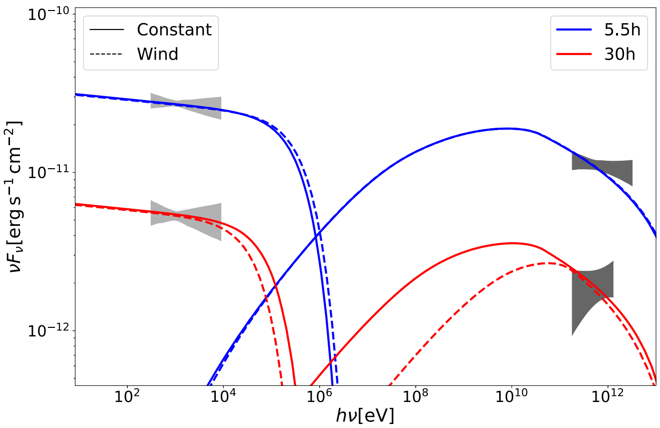

Figure 2. Model fit to GRB 190829A using the method described in the text (which rejects the potential damping limit). The luminosity distance is $D = 1 \times 10^{27}$ cm. For the wind density profile, $A_{35} = 2$, while for the constant profile, $n_1 = 1\ \mathrm{cm}^{-3}$. In both cases, the explosion energy is $E = 5 \times 10^{52}$ erg, electron injection index $p = 2.06$, $\sigma_u = 10^{-9}$, and $\ell_w = 100$. The values of ($\epsilon_{e,-2}$, $\epsilon_{B,-3}$, χ_{IC}, $\bar{\gamma}_{min}$) are (5.7, 1.3, 7.4, 93) and (4.3, 1.3, 4, 35) at $t = 5.5$ and 30 hr, respectively, in the constant-density case and (5.8, 1.2, 8.6, 111) and (4.7, 1.0, 5.3, 58) in the wind profile scenario. The X-ray data are automatically processed by the UK Swift Science Data Centre (Evans et al. 2007, 2009), and the gamma-ray butterflies are from Abdalla et al. (2021).

fluctuations is slow and plays no role. Allowing ℓ_w to increase permits one to fit the X-ray data. However, irrespective of the maximum energy, KN suppression causes the SSC γ-ray spectra to be unavoidably softer than the data suggest (Abdalla et al. 2021), with $\nu F_\nu \sim \nu^{-0.23}$ at early times, steepening to $\sim\nu^{-0.33}$ at later times. The dependence of the synchrotron and SSC spectrum on ℓ_w, and hence the maximum electron energy, is illustrated in Figure 3, where the spectrum is calculated for GRB 190829A at 5.5 hr after the prompt emission using a constant external density profile. We note that for $\ell_w = 10$, $\bar{\gamma}_{mag} \ll \bar{\gamma}_{loss}$; for $\ell_w = 100$, $\bar{\gamma}_{mag} \approx \bar{\gamma}_{loss}$; and for $\ell_w = 1000$, $\bar{\gamma}_{mag} \gg \bar{\gamma}_{loss}$. In the extreme $\ell_w = 10^4$ case, $a \approx a_{crit}$ and is very close the synchrotron burn-off limit. While the synchrotron cutoff is pushed to higher frequencies with increasing ℓ_w (cf. Equations (10) and (11)), the SSC spectrum above 100 GeV unavoidably softens due to Klein–Nishina suppression. Detection of a turnover, or its absence, in hard X-rays (see, for example, Kouveliotou et al. 2013) in future TeV-detected afterglows would clearly constrain the models further.

For fixed ϵ_e and ϵ_B, the TeV flux in our model decays with observed time as $\propto t_{obs}^{-s}$, with $s \approx 1.2$ in the uniform medium case and $s \approx 1.3$ in the wind case, both being slightly more rapid than the decay rate by the H.E.S.S. data. By admitting a temporal (or γ_2) dependence of ϵ_B and/or ϵ_e, it is not difficult to produce a light curve that matches both the X-ray and TeV data. However, such a dependence is, to our knowledge, not seen in simulations.

4. Discussion

The detection of several GRB afterglows in the TeV γ-ray domain provides a critical test not only of the standard external shock model of GRB afterglows, but of the particle acceleration theory at weakly magnetized ultrarelativistic shocks in general. Here we have focused on the constraints such measurements may place on the maximum electron energy within the external shock acceleration framework for GRB afterglows. The physical conditions implied by numerical simulations of weakly magnetized relativistic shocks generally indicate that acceleration will proceed with an efficiency significantly below the frequently adopted Bohm rate. The maximum synchrotron photon energy is thus predicted to fall short of the theoretical maximum synchrotron burn-off limit at $h\nu_{max} \approx 100\ \Gamma_{sh}$ MeV.

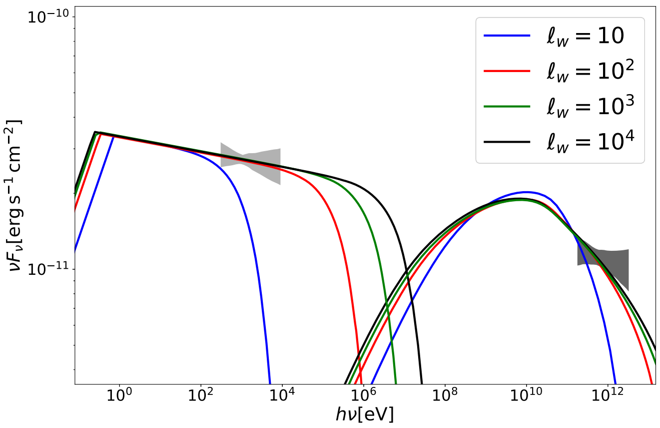

Figure 3. Comparison of predictions with varying ℓ_w for GRB 1908929A at $t = 5.5$ hr for the constant-density case. Environmental parameters are the same as used in Figure 2. Acceleration parameters are selected to match the low-energy synchrotron flux, with the SSC spectrum intersecting the H.E.S.S. butterfly at the upper leftmost point. The values of ($\epsilon_{e,-2}$, $\epsilon_{B,-3}$, χ_{IC}, $\bar{\gamma}_{min}$) are the same for $\ell_w = 100$ and (4, 1, 6, 78), (6.3, 1.4, 7.8, 98), and (7, 1.4, 8.4, 103) for $\ell_w = 10$, 10^3, and 10^4 respectively. See text for further details.

Following the approach of Kirk & Reville (2010), we consider different physical scenarios, motivated by the results of current kinetic simulations. Within the limitations of our assumptions, we conclude the following.

1. Scenarios in which the magnetic field damps rapidly downstream of the shock are clearly ruled out in the shock acceleration picture (see Figure 1). On the other hand, a plateau (or, equivalently, a very slow decay on a scale $\gg \sigma_u^{-1/2} c/\omega_p$) in the downstream field intensity (e.g., Vanthieghem et al. 2020) can be accommodated.
2. Adopting a characteristic scale of $\lambda = 10c/\omega_p$ for the scattering centers, we find that quenching by the large-scale magnetic field, the so-called magnetization limit, is operative, and this scenario is also ruled out by the data. Larger-scale structures are, therefore, required but not seen to develop in the currently available simulations. However, this may be a limitation of the spatial extent/short duration of these studies. Future simulations with a larger dynamical range, along with a deeper understanding of upstream wave excitation and the nature of preexisting ambient turbulence, will assist in clarifying this question (see Lemoine & Pelletier 2010; Reville & Bell 2014).
3. If we allow for $\ell_w > 10$, the magnetization limit increases, and quenching by radiation losses ultimately sets the upper limit. However, this scenario is also challenged by the data. The measurements by Abdalla et al. (2021) show that the VHE γ-ray spectrum is hard. However, Klein–Nishina suppression softens the spectrum in the VHE γ-ray band and presents a significant obstacle to simultaneously matching the X-ray and γ-ray data. Current observations thus appear to also be in conflict with the loss-limited scenario.

Taken together, these conclusions present a serious challenge to the external shock acceleration model for GRB afterglows.

However, they are based on data from a single GRB and also weakened by the numerous simplifying assumptions conventionally adopted in the single-zone external shock model. It is perhaps not surprising that the discovery of late-time VHE γ-ray emission presents a challenge to the simplest picture. Future detection with high-quality spectral and temporal data will be essential to resolve this issue.

Finally, we speculate on some requirements for alternative models. Given the many successes of the external shock framework in meeting GRB afterglow data, it is attractive to explore alternative scenarios that do not deviate drastically from the essential aspects of the model, in particular, the self-similar nature of the blast wave. One such possibility is to consider an external Compton scenario (Zhang et al. 2020, 2021). To avoid the same spectral softening that challenges the SSC model, the external target photons should be scattered in the Thomson regime. Motivating the required photon fields to reproduce the spectral and temporal features requires careful consideration. Looking beyond the standard external shock scenario, one could consider a model in which electrons are instead accelerated in the jet either via shear (Rieger & Duffy 2005) or inductive (Kirk et al. 2021) acceleration but nevertheless radiate in the postshock amplified fields. This two-zone picture is appealing, since the decoupling of the acceleration and emission processes avoids the synchrotron burn-off limit for maximum-energy synchrotron photons (e.g., Kirk & Giacinti 2017). Future γ-ray detection will be critical in terms of both motivating and distinguishing such alternative scenarios.

The authors thank Andrew Taylor for valuable discussions.

ORCID iDs

Zhi-Qiu Huang https://orcid.org/0000-0002-9239-323X
John G. Kirk https://orcid.org/0000-0002-9859-0496
Gwenael Giacinti https://orcid.org/0000-0001-9745-5738
Brian Reville https://orcid.org/0000-0002-3778-1432

References

Abdalla, H., Adam, R., Aharonian, F., et al. 2019, Natur, 575, 464
Abdalla, H., Aharonian, F., Ait Benkhali, F., et al. 2021, Sci, 372, 1081
Acciari, V. A., Ansoldi, S., Antonelli, L. A., et al. 2019, Natur, 575, 459
Achterberg, A., Gallant, Y. A., Kirk, J. G., & Guthmann, A. W. 2001, MNRAS, 328, 393
Ajello, M., Arimoto, M., Axelsson, M., et al. 2019, ApJ, 878, 52
Amano, T., & Kirk, J. G. 2013, ApJ, 770, 18
Asano, K., Murase, K., & Toma, K. 2020, ApJ, 905, 105
Blandford, R. D., & McKee, C. F. 1976, PhFl, 19, 1130
Chevalier, R. A., & Li, Z.-Y. 2000, ApJ, 536, 195
Derishev, E., & Piran, T. 2021, ApJ, 923, 135
Derishev, E. V. 2007, Ap&SS, 309, 157
Evans, P. A., Beardmore, A. P., Page, K. L., et al. 2007, A&A, 469, 379
Evans, P. A., Beardmore, A. P., Page, K. L., et al. 2009, MNRAS, 397, 1177
Fleishman, G. D. 2006, ApJ, 638, 348
Granot, J., Piran, T., & Sari, R. 1999, ApJ, 513, 679
Jones, F. C. 1968, PhRv, 167, 1159
Keshet, U., Katz, B., Spitkovsky, A., & Waxman, E. 2009, ApJL, 693, L127
Khangulyan, D., Aharonian, F., Romoli, C., & Taylor, A. 2021, ApJ, 914, 76
Kirk, J., Reville, B., & Giacinti, G. 2021, in 43rd COSPAR Scientific Assembly, ed. D. Castro & T. Temim (Athens: COSPAR), 1481
Kirk, J. G., & Giacinti, G. 2017, PhRvL, 119, 211101
Kirk, J. G., Guthmann, A. W., Gallant, Y. A., & Achterberg, A. 2000, ApJ, 542, 235
Kirk, J. G., & Reville, B. 2010, ApJL, 710, L16
Kouveliotou, C., Granot, J., Racusin, J. L., et al. 2013, ApJL, 779, L1
Kumar, P., Hernández, R. A., Bošnjak, Ž., & Barniol Duran, R. 2012, MNRAS, 427, L40
Kumar, P., & Zhang, B. 2015, PhR, 561, 1
Landau, L. D., & Lifshitz, E. M. 1971, The Classical Theory of Fields (3rd ed.; Oxford: Pergamon)
Lemoine, M. 2013, MNRAS, 428, 845
Lemoine, M., & Pelletier, G. 2010, MNRAS, 402, 321
Lu-Lu, Z., Jia, R., Xiao-Li, H., et al. 2021, ApJ, 917, 95
Mészáros, P. 2002, ARA&A, 40, 137
Niemiec, J., Ostrowski, M., & Pohl, M. 2006, ApJ, 650, 1020
Panaitescu, A., & Mészáros, P. 1998, ApJL, 493, L31
Petropoulou, M., Mastichiadis, A., & Piran, T. 2011, A&A, 531, A76
Piran, T. 2004, RvMP, 76, 1143
Reville, B., & Bell, A. R. 2014, MNRAS, 439, 2050
Reville, B., & Kirk, J. G. 2010, ApJ, 724, 1283
Rieger, F. M., & Duffy, P. 2005, ApJL, 632, L21
Rybicki, G. B., & Lightman, A. P. 1986, Radiative Processes in Astrophysics (New York: Wiley)
Salafia, O. S., Ravasio, M. E., Yang, J., et al. 2021, arXiv:2106.07169
Sari, R., & Esin, A. A. 2001, ApJ, 548, 787
Sari, R., Piran, T., & Narayan, R. 1998, ApJL, 497, L17
Sironi, L., Spitkovsky, A., & Arons, J. 2013, ApJ, 771, 54
Vanthieghem, A., Lemoine, M., Plotnikov, I., et al. 2020, Galax, 8, 33
Zhang, B. T., Murase, K., Veres, P., & Mészáros, P. 2021, ApJ, 920, 55
Zhang, H., Christie, I. M., Petropoulou, M., Rueda-Becerril, J. M., & Giannios, D. 2020, MNRAS, 496, 974

Chapter 5

Prospects for ultra-high-energy particle acceleration at relativistic shocks

A previous widely-held argument is that, relativistic shocks may not be efficient particle accelerators. The regular magnetic fields downstream are significantly compressed within the shock front and hence particles cannot be accelerated anymore if they become magnetized and are constrained to move along the magnetic lines. Such a mechanism provides an upper limit, known as the magnetized limit to the maximum achievable energy.

In the previous chapter we try to get some implications on the maximum electron energy accelerated at relativistic shocks by fitting the simultaneous observational data in X-ray and TeV bands. Adopting the characteristic GRB afterglow parameters and recent numerical simulations on relativistic shocks, the maximum electron energy is usually fixed by the magnetized limit. We demonstrate that there is a gap between the late-time observations and the maximum electron energy, motivating us to revisit the acceleration processes at ultra-relativistic shocks.

As a first step, we consider the case in which the uniform regular magnetic fields are perpendicular to the shock normal. Utilizing a Monto-Carlo test-particle code, we study the produced particle spectra. Particles can keep crossing the shock front if they are unmagnetized on either side of the shock. If the scattering upstream is strong, particles can still gain energy even their trajectories are dominant by gyro-motion downstream, and hence the achievable maximum energy can exceed the magnetized limit. Although this uniform field configuration is instructive, it is only feasible when the gyro-radius of the accelerated particles are much smaller compared to the scale of the system. For particles with highest energy, the detailed structure of the fields come into play.

Therefore, a regular magnetic field with cylindrical symmetry is taken into account. Due to the curvature of the field, there would be drift motions for charged particles along the shock normal. The direction of such a drift is charge/helicity dependent. For particles with favourable charges, such drift motions can enhance the acceleration efficiency and energize particles to the confinement limit of the system.

Monthly Notices
of the
ROYAL ASTRONOMICAL SOCIETY

MNRAS **522,** 4955–4962 (2023)
Advance Access publication 2023 May 04
https://doi.org/10.1093/mnras/stad1356

Prospects for ultra-high-energy particle acceleration at relativistic shocks

Zhi-Qiu Huang ,[1]★ Brian Reville ,[1]★ John G. Kirk [1]★ and Gwenael Giacinti[2,3,1]
[1]*Max-Planck-Institut für Kernphysik, Postfach 10 39 80, D-69029 Heidelberg, Germany*
[2]*Tsung-Dao Lee Institute, Shanghai Jiao Tong University, Shanghai 201210, China*
[3]*School of Physics and Astronomy, Shanghai Jiao Tong University, Shanghai 200240, China*

Accepted 2023 May 2. in original form 2023 April 12

ABSTRACT

We study the acceleration of charged particles by ultra-relativistic shocks using test-particle Monte Carlo simulations. Two field configurations are considered: (i) shocks with uniform upstream magnetic field in the plane of the shock, and (ii) shocks in which the upstream magnetic field has a cylindrical geometry. Particles are assumed to diffuse in angle due to frequent non-resonant scattering on small-scale fields. The steady-state distribution of particles' Lorentz factors is shown to approximately satisfy $\mathrm{d}N/\mathrm{d}\gamma \propto \gamma^{-2.2}$ provided the particle motion is scattering dominated on at least one side of the shock. For scattering dominated transport, the acceleration rate scales as $t_{\mathrm{acc}} \propto t^{1/2}$, though recovers Bohm scaling $t_{\mathrm{acc}} \propto t$ if particles become magnetized on one side of the shock. For uniform field configurations, a limiting energy is reached when particles are magnetized on both sides of the shock. For the cylindrical field configuration, this limit does not apply, and particles of one sign of charge will experience a curvature drift that redirects particles upstream. For the non-resonant scattering model considered, these particles preferentially escape only when they reach the confinement limit determined by the finite system size, and the distribution approaches the escapeless limit $\mathrm{d}N/\mathrm{d}\gamma \propto \gamma^{-1}$. The cylindrical field configuration resembles that expected for jets launched by the Blandford & Znajek mechanism, the luminous jets of active galactic nuclei and gamma-ray bursts thus provide favourable sites for the production of ultra-high-energy cosmic rays.

Key words: acceleration of particles – shock waves – cosmic rays.

1 INTRODUCTION

Relativistic shocks occur in many astrophysical sources of non-thermal emission such as pulsars, gamma-ray bursts (GRBs), micro-quasars, and active galactic nuclei (AGN) and there is a growing wealth of observational evidence indicating that these shocks efficiently convert a large fraction of the energy they process into extremely energetic particles. Acceleration by the first-order Fermi mechanism operating at shocks has been proposed and thoroughly investigated by numerical and analytical approaches for the case of parallel shocks. However, interpreting recent observations, in particular those at very high energy (Abdalla et al. 2019; MAGIC Collaboration 2019; H. E. S. S. Collaboration 2021), requires a clear understanding of, at the very least, the spectral index predicted and the maximum particle energy achievable under more realistic physical conditions. Even in the test-particle approximation, our knowledge of these quantities remains incomplete.

Our goal in this work is to use test-particle Monte Carlo simulations to predict these quantities in two relevant field configurations: that of a uniform magnetic field and that of a cylindrically symmetric field around a current carrying axis, such as can be expected in the jets that are either directly observed or inferred in all of the classes of object listed above. In each case we concentrate on a planar, perpendicular shock front – one in which the magnetic field and the shock lie in the same plane. This is the generic situation downstream of a highly relativistic shock front, since the component of the field in the shock plane is compressed by roughly the Lorentz factor of the shock, whereas the component along the shock normal is unchanged (Begelman & Kirk 1990).

The test-particle theory of particle acceleration at relativistic shocks was mostly developed in the decade following the original works outlining the non-relativistic theory (see e.g. Kirk & Duffy 1999, for a review) Two complementary approaches have been used: (i) Monte Carlo simulation in which particles move in a simple, prescribed magnetic field geometry whilst undergoing stochastic transport, either represented as a sequence of small-angle scattering events (e.g. Kirk & Schneider 1988; Ostrowski 1993; Summerlin & Baring 2012) or, more formally, treated using stochastic differential equations (Achterberg et al. 2001; Takamoto & Kirk 2015) and (ii) direct numerical integration of particle orbits in a synthetically constructed, turbulent magnetic field (e.g. Ballard & Heavens 1991; Lemoine & Revenu 2006; Niemiec, Ostrowski & Pohl 2006). Both methods have the drawback that they rely on a poorly constrained prescription for the turbulence. However, the former method, which we adopt here, has the advantages that it can be benchmarked against approximate analytic solutions, can model the energy dependent scattering expected to arise from self-excited fluctuations, and requires relatively modest computing resources.

Kinetic particle-in-cell (PIC) simulations do not have the fundamental limitations inherent in the test-particle approximation and have recently advanced towards a self-consistent study of relativistic shocks (Vanthieghem et al. 2020; Sironi et al. 2021;

★ E-mail: zhiqiu.huang@mpi-hd.mpg.de (Z-QH); brian.reville@mpi-hd.mpg.de (BR); john.kirk@mpi-hd.mpg.de (JGK)

Bresci, Lemoine & Gremillet 2023). In such simulations, Fermi acceleration is routinely observed as a consequence of shock formation, at least for those shocks in which the upstream medium is sufficiently weakly magnetized. These simulations provide valuable insights into the physical processes that initiate acceleration, and, although they are currently limited to a narrow range of energy and length-scales, nevertheless motivate the form of the scattering operator used in our analytical and Monte Carlo work.

In the light of GRB afterglow detections at TeV gamma-ray energies, Huang et al. (2022a) used these insights to place constraints on the maximum electron energy expected at an ultra-relativistic shock. This revealed tension between observations and the simple one-zone synchrotron self-Compton emission model. A partial resolution was proposed in a companion paper (Kirk, Reville & Huang 2023), which used both analytical and Monte Carlo methods to show that a strong, uniform downstream magnetic field does not necessarily inhibit acceleration, as had previously been supposed (Achterberg et al. 2001). Here, we extend these studies in Section 3.1, using the Monte Carlo method to quantify the maximum energy reached at a shock front in a uniform magnetic field scenario.

While the uniform field configuration is instructive and can be applied in many cases, it is inadequate when the length-scales associated with the highest energy particles become comparable to those of pre-existing structure in the magnetic field. One interesting example is that of the termination shock of a pulsar wind, since particles accelerated at latitudes within one gyroradius of the equatorial current sheet can experience a reversal of the magnetic field during their excursions both upstream and downstream. This situation was treated using the synthetic field method by Giacinti & Kirk (2018) and global PIC simulations were performed by Cerutti & Giacinti (2020). In each case, spectra harder than those predicted for relativistic shocks in a homogeneous magnetic field were observed (see also Cerutti et al. 2013; Contopoulos & Stefanou 2019).

Motivated by this finding, and by the fact that jets are a common feature in the sources of interest, we consider, in Section 3.2, the related configuration of a cylindrically symmetric magnetic field. This is a reasonable model of the field upstream of the termination shock of a current-carrying jet, or upstream of the forward shock of an explosion that propagates along the rotation axis of a progenitor star into its magnetized wind. We identify a spectral break from the standard result at lower energy to one with a harder index at higher energy. As in the case addressed by Giacinti & Kirk (2018), the new component consists of particles of only one sign of charge. We find that the harder spectral index is almost independent of the level of scattering and that this component can extend to extremely high energy, limited only by the transverse size of the jet.

The paper is organized as follows: In Section 2, we motivate the transport model that we implement in our Monte Carlo method. Numerical results for the uniform and cylindrical field cases are presented in Sections 3.1 and 3.2, respectively, and the implications and limitations of our results are discussed in Section 4.

2 TEST-PARTICLE TRANSPORT

The distribution function $f(t, \boldsymbol{x}, \boldsymbol{p})$ in phase space $(\boldsymbol{x}, \boldsymbol{p})$ of test particles that undergo small-angle, elastic scatterings satisfies the Fokker–Planck equation

$$\frac{\partial f}{\partial t} + \dot{\boldsymbol{x}} \cdot \frac{\partial f}{\partial \boldsymbol{x}} + \dot{\boldsymbol{p}} \cdot \frac{\partial f}{\partial \boldsymbol{p}} = \frac{\nu_\pm}{2} \Delta_{\boldsymbol{p}} f\,, \tag{1}$$

where $\Delta_{\boldsymbol{p}}$ is the angular part of the Laplacian in momentum space, $\nu_\pm$ the isotropic scattering rate (that can depend on $\boldsymbol{x}$ and p) and $(\dot{\boldsymbol{x}}, \dot{\boldsymbol{p}})$ are the time derivatives of an unscattered trajectory in phase space. Equation (1) applies in a reference frame, called the local fluid frame, in which the electric field vanishes. The unscattered trajectories of a particle of charge q and mass m are then determined by the large-scale, static magnetic field $\boldsymbol{B}$, i.e. $\dot{\boldsymbol{p}} = q(\dot{\boldsymbol{x}} \times \boldsymbol{B})/c$. In the presence of a shock front that lies in the plane $x = 0$ in cartesian coordinates, the two fluid frames of interest are the upstream $x > 0$, suffix '+' and downstream $x < 0$, suffix '−', frames, each with a corresponding scattering rate $\nu_\pm$. We will assume, for simplicity, that these frames are connected by a Lorentz boost in the x-direction. Length and time-scales in the local frame are conveniently normalized using the non-relativistic gyrofrequency $\omega_\pm = |qB_{0\,\pm}|/mc$ associated with an upstream/downstream fiducial field strength $B_{0\,\pm}$. When a trajectory reaches the shock front, it is assumed to emerge into the region on the other side without changing its momentum.

The nature of the particle transport and, hence, the spectrum and angular distribution of accelerated particles, depends on the relative importance of scattering and deflection in the large-scale field in each half-space. For sufficiently weakly magnetized shocks, the Weibel instability, which operates initially on the scale of the plasma skin-depth, drives the growth of highly non-linear magnetic field structures in the shock-transition region, extending both into the upstream and downstream regions (e.g. Sironi, Spitkovsky & Arons 2013; Vanthieghem et al. 2020). Assuming these structures remain small compared to the gyroradius of a test particle, they are responsible for non-resonant scattering. Then, following Kirk & Reville (2010), for a characteristic fluctuation length-scale λ of volume averaged root mean square amplitude δB, the mean scattering angle per fluctuation is $\Delta\theta \approx |q|\delta B\lambda/pc$. Taking the mean time between scatterings to be λ/c one finds a scattering rate proportional to p^{-2}, characteristic of non-resonant interactions:

$$\nu_\pm = \nu_{0\pm}\,(p/mc)^{-2}\ , \tag{2}$$

$$\text{where } \nu_{0\pm} = (\delta B/B_{0\pm})^2\,\omega_\pm^2 \lambda/c \tag{3}$$

is independent of particle energy.

Simulations are required to determine the properties of δB and λ. Filamentary structures driven by the Weibel instability typically develop on length-scales $\lambda = 10 - 100c/\omega_{\mathrm{pi}}$ where $\omega_{\mathrm{pi}} = \sqrt{4\pi n^2 e^2 c^2/w}$ is the relativistically corrected plasma frequency, with w the enthalpy density. The growth of longer wavelength fluctuations in the foreshock region was investigated for unmagnetized (Medvedev & Zakutnyaya 2009) and magnetized (Reville & Bell 2014) ambient plasma conditions (see also Milosavljević & Nakar 2006). However, a complete multiscale theory of turbulent field generation at ultra-relativistic shocks does not exist at present, and for simplicity, we therefore treat the scattering rate as a free parameter that can take different values upstream or downstream, but is otherwise homogeneous.

We employ a Monte Carlo code – see Appendix A – to construct time-dependent solutions of equation (1) upstream and downstream of a relativistic shock front, measuring f at the shock front and assuming an injection term that is zero for $t < 0$ and constant for $t > 0$.

3 RESULTS

3.1 Uniform magnetic field

3.1.1 Parallel shock

We first use our code to revisit the case in which the large-scale field can be neglected. This is equivalent to the case of an exactly parallel shock front, in which the strength of the magnetic field plays no

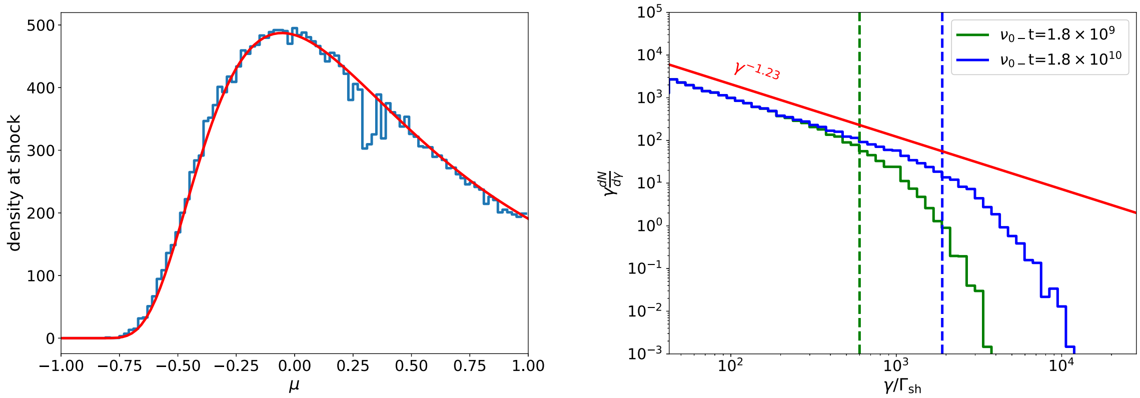

Figure 1. Results for the case of negligible large-scale magnetic field (equivalent to the parallel shock case), shown in the downstream frame. Left-hand panel: The dependence of the phase space density f at the shock front on the cosine μ of the angle between $\boldsymbol{p}$ and the shock normal (blue) compared to the analytic approximation. Right-hand panel: the dependence of $\gamma\mathrm{d}N/\mathrm{d}\gamma = \gamma^3 f$ at the shock front on the normalized particle Lorentz factor $\gamma/\Gamma_{\mathrm{sh}}$ at two different times, compared to the predicted power-law (red line) and the estimated maximum energy at the chosen times (green and blue vertical lines, see equation 5).

role. We adopt a constant Lorentz factor $\Gamma_{\mathrm{sh}} = 50\sqrt{2}$ for the shock, as seen by an upstream observer, and a downstream shock speed of $\beta_{\mathrm{d}} = 1/3$, as expected from the hydrodynamic jump conditions for an ultra-relativistic shock propagating in a cold gas. This case is not expected to differ significantly from the ultra-relativistic limit (Kirk et al. 2023), where an analytic approximation is known for the stationary (time-asymptotic) distribution function at $\gamma \gg \Gamma_{\mathrm{sh}}$ and estimates of the acceleration rate are available, thereby enabling the code to be benchmarked.

Fig. 1 shows the angular distribution of particles at the shock front (left) and the accelerated particle spectrum (right), both measured in the downstream frame. (In the angular distribution, we record only those particles with energy larger than 30 times that of injection, for which no memory of the injection conditions remains. In the spectrum we plot the number of these particles per logarithmic energy interval, $\gamma\mathrm{d}N/\mathrm{d}\gamma = \gamma^3 f$.) For comparison, we plot, in the left-hand panel, the angular dependence of the leading eigenfunction (Kirk et al. 2000), which shows close agreement with our simulation results. We note the feature associated with particles that graze the shock, here occurring at $\mu = 1/3$.

In the right-hand panel, we compare the expected time-asymptotic power-law spectrum with the simulation results at two different times. Below a cut-off, $\gamma_{\mathrm{c}}(t)$, that advances to higher energy with increasing time, the distribution is found to match closely the predicted stationary value $\gamma\mathrm{d}N/\mathrm{d}\gamma \propto \gamma^{-1.23}$ ($f \propto \gamma^{-4.23}$) for an ultrarelativistic shock. The time-dependent position of this cut-off, is predicted by equating the energy dependent acceleration time-scale with the time elapsed since injection started (see equation 43 in Achterberg et al. 2001). The acceleration time-scale is simply the sum of the average time spent upstream, Δt_+, and downstream, Δt_- – both measured in the downstream rest frame – during one cycle (which starts at the shock, crosses it once and then returns to it). When scattering dominates both up and downstream,

$$\begin{aligned}\Delta t_+ &= \gamma^2/(\Gamma_{\mathrm{sh}}\nu_{0+})\\ \Delta t_- &= \gamma^2/\nu_{0-}\,, \end{aligned}\tag{4}$$

therefore,

$$\gamma_{\mathrm{c}}(t) = t^{1/2}\left(\frac{1}{\nu_{0-}} + \frac{1}{\Gamma_{\mathrm{sh}}\nu_{0+}}\right)^{-1/2}.\tag{5}$$

In Fig. 1 we adopt $\nu_{0+} = \nu_{0-}$, in which case accelerating particles spend most of their time in the downstream region during one complete cycle. Since the shock does not decelerate and losses and boundary effects are neglected, the cut-off increases indefinitely. However, its rate of increase slows down because of the quadratic dependence of the scattering time on energy (cf. Stockem et al. 2012; Sironi et al. 2013; Plotnikov, Grassi & Grech 2018). The time-dependent spectrum softens significantly above the Lorentz factor given by equation (5), shown in the figure as green and blue vertical lines.

3.1.2 *Perpendicular shock*

We next consider the case where the regular magnetic field is perpendicular to the shock normal. This *perpendicular* shock is the generic configuration for relativistic shocks, because the velocity of the point of intersection of a magnetic field line and the shock surface exceeds c unless the shock normal happens to be aligned with the upstream magnetic field to within an angle of $1/\Gamma_{\mathrm{sh}}$. (Note that all such *superluminal shocks* can be transformed into perpendicular shocks by a Lorentz boost along the shock surface.) The downstream magnetic field is determined by the ideal magneto-hydrodynamic shock jump conditions for a weakly magnetized ultra-relativistic shock i.e. $B_- = 2\sqrt{2}\Gamma_{\mathrm{sh}}B_+$ (e.g. Kirk & Duffy 1999), where $B_\pm$ are measured in the corresponding rest frame of the plasma. Since the fields up and downstream are uniform, they can be taken to equal their fiducial values $B_\pm \equiv B_{0\,\pm}$. We again adopt $\Gamma_{\mathrm{sh}} = 50\sqrt{2}$ and set $\nu_{0\,-} = 3\times10^4\omega_-$.

The guiding centre of a magnetized particle downstream of a superluminal, relativistic shock recedes from the shock front at a substantial fraction of c, which led Achterberg et al. (2001) to the assertion that Fermi acceleration would be ineffective in the absence of strong cross-field transport (i.e., strong scattering) downstream. As a consequence, they presented results only for $\omega_- = 0$. The two limiting cases of strong and weak scattering upstream ($\omega_+ = 0$ and $\nu_+ = 0$, respectively) were investigated and yielded results which did not differ significantly from the analytic approximation for the parallel shock case ($\omega_+ = \omega_- = 0$) treated in Section 3.1.1.

Since we take account of the energy dependence of $\nu_\pm$, these different scattering regimes map into different ranges of Lorentz factors for the accelerated particles. Thus, strong and weak scattering downstream correspond to $\gamma \ll \gamma_{\max-}$ and $\gamma \gg \gamma_{\max-}$, respectively,

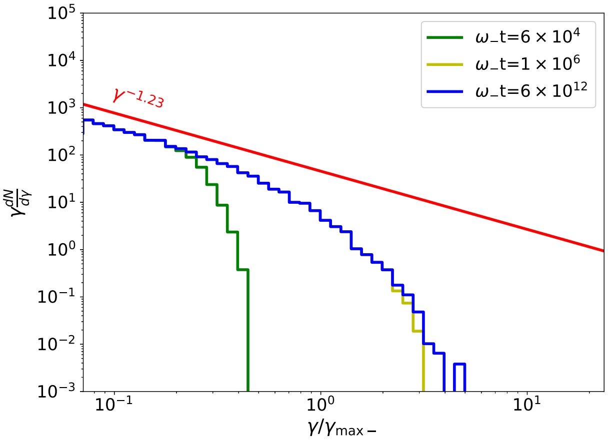

Figure 2. The particle spectra at a perpendicular shock in a uniform magnetic field with relatively weak scattering upstream $\nu_{0+} = 10^{-4}\nu_{0-}$, as a function of the ratio of the Lorentz factor to its predicted maximum, $\gamma_{\max -} = \nu_{0\,-}/\omega_{-} = 3\times 10^4$, see equation (6). The upstream magnetized limit, $\gamma_{\max +} \approx 600$, lies close to the injection energy and is not shown.

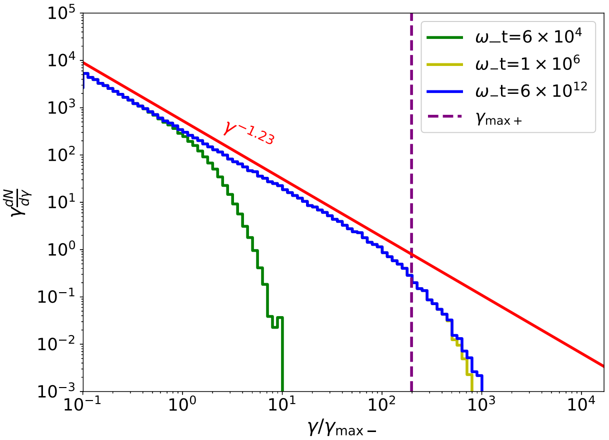

Figure 3. Particle spectra at a perpendicular shock in a uniform magnetic field, with relatively strong scattering upstream: $\nu_{0+} = \nu_{0-}$ and $\nu_{0\,-}/\omega_{-} = 3\times 10^4 = \gamma_{\max -}$, plotted as a function of $\gamma/\gamma_{\max -}$. The vertical dashed line shows the upstream magnetized limit, $\gamma_{\max +}$, see equation (7).

where

$$\gamma_{\max -} = \nu_{0-}/\omega_{-} \tag{6}$$

is the *downstream magnetized limit* to which we refer in Huang et al. (2022a). Similarly, it is possible to define a corresponding upstream limit, taking account of the fact that a particle is scattered or deflected through only a small angle $\sim 1/\Gamma_{\rm sh}$ whilst upstream, before being overtaken by the shock:

$$\gamma_{\max +} = 2\sqrt{2}\Gamma_{\rm sh}\nu_{0+}/\omega_{-}\, . \tag{7}$$

Simulations are shown in Fig. 2, for $\nu_{0+} = 10^{-4}\nu_{0-}$, implying $\gamma_{\max -} = 3\times 10^4$ and $\gamma_{\max +} \approx 600 \ll \gamma_{\max -}$. The stationary, power law part of the spectrum remains close to the analytic prediction, whereas the time-dependent cut off advances well beyond $\gamma_{\max +}$. In this case, particles in the range $\gamma_{\max +} \ll \gamma \ll \gamma_{\max -}$ suffer deflection rather than scattering whilst upstream and the average time they spend there is

$$\begin{aligned}\Delta t_{+} &= 2\sqrt{2}\gamma/\omega_{-}\\ &\approx (3\gamma_{\max -}/\gamma)\,\Delta t_{-}\, .\end{aligned} \tag{8}$$

Thus, they spend most of a cycle in the upstream, and the cut-off advances with time in this range according to $\gamma_{\rm c}(t) \approx \omega_{-}t/3$, i.e. essentially at the rate corresponding to *Bohm* scattering (see Section 4). Nevertheless, close to $\gamma_{\max -}$, equation (5) remains a good order of magnitude estimate, since here particles divide their time almost equally between the two regions. At $\omega_{-}t = 6\times 10^4$, $\gamma_{\rm c}(t)$ is roughly a factor of 3 less than $\gamma_{\max -}$, whereas at $\omega_{-}t > 10^6$ a stationary state is reached at essentially all energies to which particles can be accelerated, confirming that saturation occurs at roughly $\gamma_{\max -}$, in agreement with the findings of Achterberg et al. (2001).

If, however, $\gamma_{\max +} \gg \gamma_{\max -}$, the situation changes. In Fig. 3 we show results for $\nu_{0+} = \nu_{0-}$, implying $\gamma_{\max -} = 3\times 10^4$ and $\gamma_{\max +} = 6\times 10^6 \gg \gamma_{\max -}$. In this case the power-law spectrum does not cut off at the downstream magnetized limit, but extends up to $\gamma_{\max +}$. Particles in the range $\gamma_{\max -} \ll \gamma \ll \gamma_{\max +}$ now spend most of a cycle in the downstream region, from which they are ejected after a fraction of a gyration:

$$\begin{aligned}\Delta t_{-} &= \gamma/\omega_{-}\\ &\approx (\gamma_{\max +}/3\gamma)\,\Delta t_{+}\, .\end{aligned} \tag{9}$$

Once again, therefore, the cut-off advances linearly with time: $\gamma_{\rm c}(t) \approx \omega_{-}t$, corresponding to Bohm scattering.

The stationary spectra in the regime $\gamma_{\max -} \ll \gamma \ll \gamma_{\max +}$ were analysed by Kirk et al. (2023), using both our Monte Carlo code and an analytic approximation scheme. For $\Gamma_{\rm sh} > 50$ a power-law spectrum with index $f \propto \gamma^{-4.17}$ was found. However, the transition from a power law of index 1.23 to one of 1.17 is not discernible in Fig. 3, because of the relatively small range of Lorentz factors between $\gamma_{\max -}$ and $\gamma_{\max +}$.

We note that in the case of an oblique shock front, it is only the component of the magnetic field perpendicular to the shock normal in the upstream that causes particles to leave the narrow cone in which they can move ahead of the shock front. This implies that the *upstream* magnetized limit may depend on the shock obliquity for superluminal shocks, even though the regular magnetic field in the downstream remains almost perpendicular to the shock normal. Denoting by α the angle between the upstream magnetic field, as measured by an upstream observer, and the shock normal, we find

$$\gamma_{\max +} = 2\sqrt{2}\Gamma_{\rm sh}\nu_{0+}/\left(|\sin\alpha|\,\omega_{-}\right)\, ,\ \text{for } |\sin\alpha| > 1/\Gamma_{\rm sh}\, , \tag{10}$$

generalizing equation (7). We have performed additional simulations that confirm this increase.

3.2 Magnetic field with cylindrical symmetry

To model the situation of either a reverse shock in a magnetized jet, or the forward shock of a jet that propagates along the rotation axis into a medium whose magnetic structure mimics the *Parker wind*, we choose a simple geometry for the static magnetic field in the upstream region: one in which only azimuthal field components exist in cylindrical coordinates (ρ, θ, x). Satisfying the solenoidal field condition then requires that $\partial B_\theta/\partial\theta = 0$. To maintain a finite current in the jet, the field should approach zero on the symmetry axis. Therefore, we select a large-scale upstream field $\boldsymbol{B}_{+}$ that increases linearly with cylindrical radius ρ out to a distance ρ_0, outside of which it remains constant. As in the homogeneous case, we assume that it is compressed upon crossing the shock front, which remains

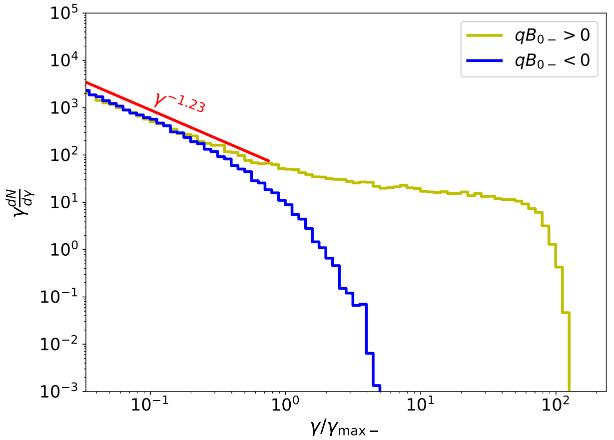

Figure 4. Particle spectra in a cylindrically symmetric magnetic field. Here we consider weak scattering in the upstream, $\nu_{0+} = 10^{-4}\nu_{0-}$. The yellow and blue histograms show results for $qB_{0-} > 0$ and $qB_{0-} < 0$, respectively, plotted as functions of $\gamma/\gamma_{\max -}$ ($\gamma_{\max -} = 3 \times 10^4$). The simulations were run until a steady state was reached. For $qB_{0-} > 0$ a cut off appears at roughly the confinement limit, $\gamma \approx \rho_{\max} = 10^7$.

in the plane $x = 0$ and is, therefore, also a perpendicular shock:

$$\boldsymbol{B}_\pm = B_{0\pm}\hat{\boldsymbol{\theta}} \times \begin{cases} (\rho/\rho_0)\,, & \rho \leqslant \rho_0 \\ 1, & \rho_0 < \rho \leqslant \rho_{\max}\,. \end{cases} \qquad (11)$$

This field corresponds to a constant axial current density within ρ_0, outside of which it falls off as $1/\rho$. We set a boundary at $\rho = \rho_{\max} \gg \rho_0$, and assume that all particles that reach it escape. In this way, ρ_0 models the thickness of the current carrying region around the axis, which is likely to be determined by microphysical processes, whereas $\rho_{\max}$ models the macroscopic geometry of the field, comparable, for example, to the distance of the shock from the central object/engine. Since times and distances are normalized to the non-relativistic gyro frequency and radius corresponding to B_{0-}, particles with $\gamma \gg \rho_0$ cross the axial region without significant deflection by the magnetic field, and particles with $\gamma > \rho_{\max}$ cannot be confined within the system, when downstream. When these particles enter the upstream region, their gyro radius increases by a factor $\sim \Gamma_{\rm sh}^2$. However, the constraints on sensitivity to the axial region and on confinement are unchanged, because their angular distribution is tightly beamed along the axis.

In the simulations presented here we set $\rho_0 = 10^5$ and $\rho_{\max} = 10^7$. As in Section 3.1, we select $\Gamma_{\rm sh} = 50\sqrt{2}$ and $\nu_{0-} = 3 \times 10^4\omega_-$, but note that ω_- is defined by the fiducial field B_{0-}, so that scattering is always dominant sufficiently close to the axis $\rho = 0$. Particles are initially injected at $\rho = 0$, with an isotropic angular distribution immediately downstream of the shock front.

The corresponding spectra for weak upstream scattering, $\nu_{0+} = 10^{-4}\nu_{0-}$, are shown in Fig. 4. The results shown in yellow are for test particles with the same sign of charge as the fiducial field, $qB_{0-} > 0$, whereas those in blue are for $qB_{0-} < 0$. These two spectra are essentially identical at low energy, but diverge above a Lorentz factor given roughly by the downstream magnetized limit $\gamma_{\max -}$. In the downstream region, the transport of particles of lower Lorentz factor is everywhere dominated by scattering, so that spectrum remains close to that expected in the parallel shock case, or, equivalently, in the perpendicular shock with $\gamma_{\max +} \ll \gamma_{\max -}$ (Fig. 2).

At Lorentz factors greater than $\gamma_{\max -}$, however, there is a dramatic difference: the blue spectrum cuts off, whereas the yellow spectrum hardens to higher energy until the confinement limit $\gamma \approx \rho_{\max}$ is reached.

In a uniform field, the only drift present is the $\boldsymbol{E} \times \boldsymbol{B}$ drift, that causes particles to be dragged along at the speed of the local plasma flow, independent of their charge. In the cylindrically symmetric field, however, a charge-dependent curvature drift is superposed on the $\boldsymbol{E} \times \boldsymbol{B}$ drift. For $qB_0 > 0$, this drift is directed in the positive x direction, i.e. in the direction of propagation of the shock front. The drift speed is slow far from the axis but is $\sim c$ when $\rho < \gamma$. As a consequence, particles with $qB_{0-} > 0$ that are located close to the axis in the downstream region and experience little scattering, are able to catch up and overtake the shock, whereas those with $qB_{0-} < 0$ are swept away from it. This behaviour is illustrated in the lower panels of Fig. 5, where we show a trajectory typical of a particle with $qB_{0-} > 0$ and a Lorentz factor $> \gamma_{\max -}$.

The situation is reversed in the upstream region, where particles with $qB_{0-} > 0$ tend to outrun the shock front – see the upper panel of Fig. 5. However, even a very low scattering rate there suffices eventually to deflect particles through an angle that allows them to be caught again by the shock front. Therefore, these particles can be accelerated beyond the limit $\gamma_{\max +}$ given in equation (7), provided the upstream region is sufficiently extended in the x-direction. This can be seen in Fig. 6, where we run the simulation without imposing a boundary on the radial extent of the magnetic field. In the presence of scattering, particles can then escape only by being swept far downstream. In this case, as in the case of a parallel shock in a uniform field, there is no intrinsic upper limit on the energy to which favourably charged particles located close to the axis can be accelerated, and the spectrum below the time-dependent upper cut-off approaches $f \propto \gamma^{-3}$, as expected for particles that are effectively confined to the vicinity of the shock front. Because the acceleration rate is now limited by the time spent upstream, the cut off advances according to $\gamma_{\rm c}(t) \approx \sqrt{\Gamma_{\rm sh}\nu_{0+}t}$.

Particles far from the axis do not benefit from the curvature drift. Hence, the positions at which particles are injected affects the accelerated spectrum. We demonstrate this effect in Fig. 7, where particles are injected at positions that are uniformly distributed in ρ between the axis and $\rho_{\max}$. Many of these particles remain far away from the axis and populate a spectrum with index $f \propto \gamma^{-4.23}$ and a cut off close to $\gamma_{\max -}$. Only a small fraction of them reaches this energy whilst sufficiently close to the axis – i.e. at $\rho < \gamma_{\max -}$ – to achieve a substantial drift velocity. These are then accelerated further into a hard spectrum that extends up to the confinement limit. In Fig. 7, $\rho_{\max}$ is reduced by a factor of 2 relative to that used in Fig. 4, and the maximum energy decreases by the same factor, thereby validating our assertion that particles are accelerated to the confinement limit.

4 DISCUSSION

The main results of this paper concern the energy spectrum of highly energetic charged particles that can be produced by a relativistic shock front. They fall into two parts, each of which addresses an idealized situation.

In the first, we consider a planar shock front that propagates into a medium containing a relatively weak, perfectly uniform magnetic field, upon which fluctuations are imposed. We assume that the uniform field lies in the plane of the shock front, i.e. the shock is *perpendicular*, since this is by far the most likely configuration for a relativistic shock front. The spectrum produced then depends on the strength and length-scale of the fluctuations. Assuming these are of short length-scale, as suggested by PIC simulations, we find that there is an intrinsic limit on the energy to which particles can

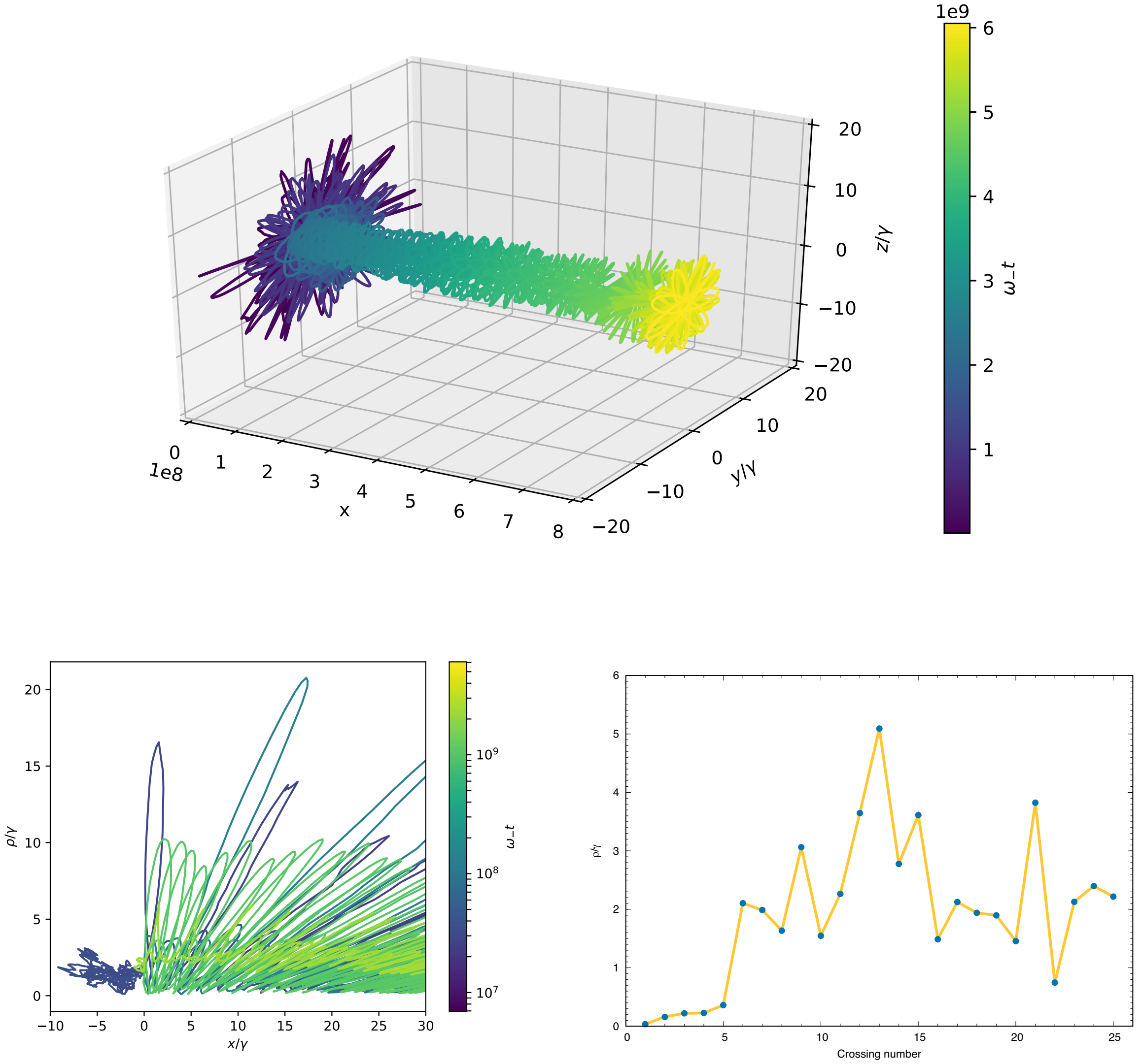

Figure 5. Trajectory in the shock rest frame of a particle with $qB_{0-} > 0$ and Lorentz factor above $\gamma_{\max-}$. Top panel: Particle trajectory in three-dimensional space before escaping from the boundary $\rho_{\max}$ in the upstream region. Bottom left-hand panel: the trajectory in the x–ρ-plane near the shock front, showing a total of 25 crossings. Bottom right-hand panel: The value of ρ/γ each time the trajectory crosses the shock front, showing that the trajectory is confined to a region close to the axis where the drift speed is $\sim c$.

be accelerated, even when other effects, such as radiative losses, or the finite size or finite lifetime of the system, can be neglected. This is in marked contrast to the (presumably less realistic) situation at a parallel shock front, which does not possess such an intrinsic limit. On the other hand, we find that the time-asymptotic particle spectrum below this limiting energy is essentially the same as that predicted for a parallel shock, and does not depend on the strength of the fluctuations.

The limit itself, however, does depend on the strength of the fluctuations in both the upstream and downstream plasma. If these are more effective in the downstream than the upstream, we confirm the maximum energy predicted by Huang et al. (2022a; the 'magnetized limit'), denoted here as $\gamma_{\max-}$ in equation (6). In the converse situation, we confirm the spectral index indeed remains close to that of a parallel shock, as predicted by Kirk et al. (2023), and find a new expression for the upper limit, $\gamma_{\max+}$, given in equation (7). In each case, we find that the spectrum evolves with an upper cut-off energy that increases linearly with time, as it approaches the limiting value, which is determined by the larger of the two quantities $\gamma_{\max\pm}$. This behaviour is the same as that predicted under the assumption of *Bohm* scattering, where the mean free path of a particle is assumed to equal its gyroradius. In contrast, a time-dependence $\gamma_{\mathrm{c}}(t) \propto t^{1/2}$ is expected when particle transport is dominated *everywhere* by non-resonant scattering (Kirk & Reville 2010).

The model described above is necessarily highly idealized. For example, the assumption of a perfectly uniform background field is reasonable only if there are no fluctuations on a length-scale comparable to the gyroradius of the highest energy particles. This fails if resonant interactions become important. But, more importantly it also places a strict lower limit R_{up} on the length-scale of structures that may pre-exist in the upstream medium. Although it is tempting to associate the length-scale R_{up} with the overall size R of the astrophysical system under consideration, there are several situations in which it is expected to be much smaller. For example, MHD models of pulsar wind nebulae and jets from accreting black holes (see Porth et al. 2017; Davis & Tchekhovskoy 2020, for reviews) show both narrow current sheets and axial current flows, where $R_{\mathrm{up}} \ll R$.

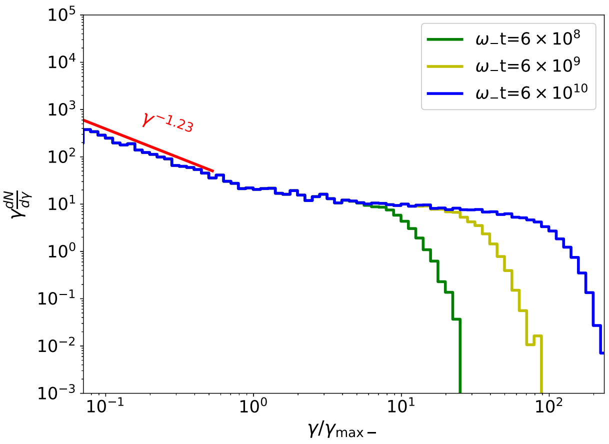

Figure 6. Spectra for particles with $qB_{0-} > 0$ and the same parameters as in Fig. 4, but without an upper limit on ρ. The cut-off on the hard component of the spectrum does not saturate, but increases monotonically with time according to $\gamma_{\rm c}(t) \propto t^{1/2}$.

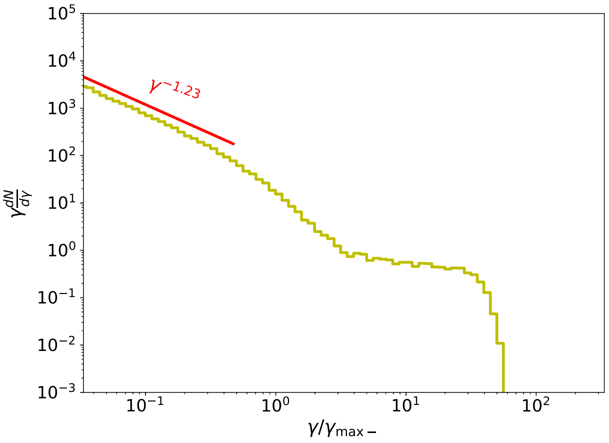

Figure 7. The spectrum for particles with $qB_{0-} > 0$ and the same parameters as in Fig. 4, but with an upper limit on the jet radius reduced by a factor of 2, i.e. $\rho_{\max} = 5 \times 10^{6}$. Also, particles are now injected with a uniform distribution in ρ between the axis $\rho = 0$ and $\rho_{\max}$. Only those that reach $\gamma \approx \gamma_{\max -}$ when close to the axis are accelerated further.

The second idealized situation we address is the latter: a relativistic shock propagating along the axis of a plasma containing a cylindrically symmetric field. In this situation, we find that the acceleration of particles with Lorentz factor $\gamma < \gamma_{\max -}$ proceeds in the same manner as in a uniform field, since their transport is dominated by scattering in the downstream region. At higher energy, however, there is a dramatic difference for those particles that are located within roughly one gyroradius of the axis downstream of the shock. There, unscattered trajectories undergo rapid curvature drifting, which enables charges of favourable sign to catch up with the shock, thereby reducing their probability of escaping the acceleration region. As a result, we find a hard $f \propto \gamma^{-3}$ spectrum (see Fig. 4) for the favoured particles, that can extend up to the confinement limit $\gamma \approx |qB_{0-}|R/mc^{2}$. This is reminiscent of the findings of Giacinti & Kirk (2018), who integrated particle orbits directly in synthetically constructed magnetic turbulence. They considered the equatorial region of a pulsar wind termination shock, which contains a plane current sheet rather than an axial current, and observed a turbulence-dependent hardening of the spectrum of one of the charged components, which they interpreted as due to *Speiser orbits* that cross the sheet. In our case, the sheet is essentially contracted into the axis of the cylinder, so that it is not possible for a particle orbit to cross it. Nevertheless, curvature drift takes over the role of the Speiser orbits and permits particles of one charge to decouple from the downstream fluid motion and recross into upstream.

In interpreting our results, it is important to remember the limitations not only of our assumed scattering model, but also of the test particle approximation. For example, the very hard spectrum we find will, if it extends to high energy, begin to exert a significant influence on the background plasma, which is not included. In principle, PIC simulations are capable of accounting for this and other physical effects, but they are currently challenged by the large range of spatial and temporal scales that separate the thermal particles from the most energetic. Thus, global PIC simulations of both the equatorial current sheet and the axial current case show tantalising hints of a hard spectral component (Cerutti & Giacinti 2020, 2023), but set the confinement limit of the simulation to a particle Lorentz factor $\sim 10^{3}$. Consequently, a distinct hard spectral component does not emerge and the maximum energy permitted in the simulation is well below that expected in astrophysical objects. Similarly, PIC simulations of acceleration in uniform fields report acceleration rates approximately proportional to $t^{1/2}$ (Stockem et al. 2012; Sironi et al. 2013; Plotnikov et al. 2018), but did not extend to energies above the lower of the two limits $\gamma_{\max\pm}$, above which we predict an unchanged spectral index and an acceleration rate $\propto t$.

Our principal findings on the maximum energy and spectral features have many potential applications for astrophysical sources which host relativistic shocks. Amongst the best known examples are GRBs, Pulsar wind termination shocks, and AGN/Blazars. All these source classes are well established gamma-ray emitters (e.g. Albert et al. 2021; H. E. S. S. Collaboration et al. 2021; Lhaaso Collaboration et al. 2021; Huang et al. 2022b) and/or hard X-ray synchrotron sources (e.g. Costamante et al. 2018; Thimmappa et al. 2022). We find that the steady-state spectrum in almost all cases where pitch-angle diffusion dominates on at least one side of the shock is almost indiscernible from the well-known result $\mathrm{d}N/\mathrm{d}\gamma \propto \gamma^{-2.2}$, originally derived for exactly parallel shocks. Although such spectra are typical of those inferred from GRB afterglow observations, harder spectra are not uncommon (see for example Ajello et al. 2018). Our results indicate that large scale field structures associated to the specific geometry of the source, can maintain the shock acceleration cycles through the drift motions induced by this geometry. This naturally leads to a maximum energy close to the confinement limit, in contrast with the findings of Bell et al. (2018), who considered only self-excited turbulence. It also suggests a hardening of the spectrum which may, in principle, be identified with a spectral break. The asymptotic ‘zero-escape’ limit presented here; $\mathrm{d}N/\mathrm{d}\gamma \propto \gamma^{-1}$ is a result of our simplified assumptions, and we anticipate a range of spectral shapes will be revealed in future environment-specific studies, in particular if feedback from the axial current on the upstream medium is included. Nevertheless, there are several clear examples where such hard spectra are favoured. It has been demonstrated, for example, that a hard source spectrum for ultra-high-energy cosmic rays (UHECR) alleviates the need to invoke problematic negative source evolution (Taylor, Ahlers & Hooper 2015). If relativistic jets, either those of GRBs or high power AGN, are the primary source of UHECRs, particles must be accelerated close to the confinement limit for these sources (see discussion in Blandford 2000; Matthews, Bell & Blundell 2020). Since these particles sample the full width of the jet, they naturally probe its large-scale underlying magnetic structure. In this regard, the origin of the highest energy cosmic rays in our local Universe is a natural consequence of the mechanism that efficiently extracts the power from the central engine (Blandford & Znajek 1977).

DATA AVAILABILITY STATEMENT

No new data were generated or analysed in support of this research.

REFERENCES

Abdalla H. et al., 2019, Nature, 575, 464

Achterberg A., Gallant Y. A., Kirk J. G., Guthmann A. W., 2001, MNRAS, 328, 393

Ajello M. et al., 2018, ApJ, 861, 85

Albert A. et al., 2021, ApJ, 911, 143

Ballard K. R., Heavens A. F., 1991, MNRAS, 251, 438

Begelman M. C., Kirk J. G., 1990, ApJ, 353, 66

Bell A. R., Araudo A. T., Matthews J. H., Blundell K. M., 2018, MNRAS, 473, 2364

Blandford R. D., 2000, Phys. Scr. T, T85, 191

Blandford R. D., Znajek R. L., 1977, MNRAS, 179, 433

Bresci V., Lemoine M., Gremillet L., 2023, preprint (arXiv:2303.11394)

Cerutti B., Giacinti G., 2020, A&A, 642, A123

Cerutti B., Giacinti G., 2023, preprint (arXiv:2303.12636)

Cerutti B., Werner G. R., Uzdensky D. A., Begelman M. C., 2013, ApJ, 770, 147

Contopoulos I., Stefanou P., 2019, MNRAS, 487, 952

Costamante L., Bonnoli G., Tavecchio F., Ghisellini G., Tagliaferri G., Khangulyan D., 2018, MNRAS, 477, 4257

Davis S. W., Tchekhovskoy A., 2020, ARA&A, 58, 407

Giacinti G., Kirk J. G., 2018, ApJ, 863, 18

H. E. S. S. Collaboration, 2021, Science, 372, 1081

Huang Z.-Q., Kirk J. G., Giacinti G., Reville B., 2022a, ApJ, 925, 182

Huang Y., Hu S., Chen S., Zha M., Liu C., Yao Z., Cao Z., Experiment T. L., 2022b, GCN Circ., 32677, 1

Kirk J. G., Duffy P., 1999, J. Phys. G: Nucl. Phys., 25, R163

Kirk J. G., Reville B., 2010, ApJ, 710, L16

Kirk J. G., Schneider P., 1988, A&A, 201, 177

Kirk J. G., Guthmann A. W., Gallant Y. A., Achterberg A., 2000, ApJ, 542, 235

Kirk J. G., Reville B., Huang Z.-Q., 2023, MNRAS, 519, 1022

Lemoine M., Revenu B., 2006, MNRAS, 366, 635

Lhaaso Collaboration, 2021, Science, 373, 425

MAGIC Collaboration, 2019, Nature, 575, 459

Matthews J. H., Bell A. R., Blundell K. M., 2020, New A Rev., 89, 101543

Medvedev M. V., Zakutnyaya O. V., 2009, ApJ, 696, 2269

Milosavljević M., Nakar E., 2006, ApJ, 651, 979

Niemiec J., Ostrowski M., Pohl M., 2006, ApJ, 650, 1020

Ostrowski M., 1993, MNRAS, 264, 248

Plotnikov I., Grassi A., Grech M., 2018, MNRAS, 477, 5238

Porth O., Buehler R., Olmi B., Komissarov S., Lamberts A., Amato E., Yuan Y., Rudy A., 2017, Space Sci. Rev., 207, 137

Press W. H., Teukolsky S. A., Vetterling W. T., Flannery B. P., 1992, Numerical recipes in FORTRAN. The art of scientific computing. Cambridge Univ. Press, Cambridge

Reville B., Bell A. R., 2014, MNRAS, 439, 2050

Sironi L., Spitkovsky A., Arons J., 2013, ApJ, 771, 54

Sironi L., Plotnikov I., Nättilä J., Beloborodov A. M., 2021, Phys. Rev. Lett., 127, 035101

Stockem A., Fiúza F., Fonseca R. A., Silva L. O., 2012, ApJ, 755, 68

Summerlin E. J., Baring M. G., 2012, ApJ, 745, 63

Takamoto M., Kirk J. G., 2015, ApJ, 809, 29

Taylor A. M., Ahlers M., Hooper D., 2015, Phys. Rev. D, 92, 063011

Thimmappa R., Stawarz Ł., Neilsen J., Ostrowski M., Reville B., 2022, ApJ, 941, 204

Vanthieghem A., Lemoine M., Plotnikov I., Grassi A., Grech M., Gremillet L., Pelletier G., 2020, Galaxies, 8, 33

APPENDIX A: MONTE CARLO CODE

In our Monte Carlo implementation, we update individual trajectories over a time Δt using a 5th order Runge–Kutta integrator (Press et al. 1992) with an adaptive time-step, and choose Δt such that the scattering is well resolved: Since the angular distribution function is concentrated in a cone of opening angle $1/\Gamma_{\rm sh}$ upstream, the condition we use there is $\Delta t = 10^{-3}/\left(\Gamma_{\rm sh}^2 \nu_+\right)$. Downstream, on the other hand, the distribution function is expected to be a smoothly varying function of angle, so that $\Delta t = 10^{-3}/\nu_-$. After each step Δt, the direction of the momentum vector changed to account for small angle scattering, following the method described by Kirk & Schneider (1988). If a particle crosses the shock front during Δt, a root finding algorithm is applied to truncate this step such that it ends precisely on the shock surface. A Lorentz transformation is then made to the new frame and a new step is taken in this frame before applying the next scattering. Since we consider relativistic shocks, where the probability of a particle returning to the shock front after entering the downstream region is relatively low ($\sim$ 50 per cent) a particle splitting method is adopted. Each particle is initially assigned a weight of unity. On every third shock crossing from upstream to downstream, eight daughter particles are created, with a weight adjusted accordingly, and are then followed along statistically independent paths. We set an upper limit of 10 on the number of generations of daughter particles.

At $t = 0$, particle trajectories are initiated isotropically immediately downstream of the shock with a Lorentz factor twice that of the shock. The energy spectrum and angular distribution are found by recording the momentum $\boldsymbol{p}$ each time a trajectory or one of its daughters crosses the shock front, until either the time elapsed, t (measured in the downstream), reaches a pre-determined value, or the particle moves sufficiently far from the shock downstream. We find the results are insensitive to this boundary provided it exceeds either 10 times the gyroradius $\gamma c/\omega_-$ or 100 times the scattering mean free path $c/\nu_{\rm d}$. In this way, a time-dependent solution of equation (1) is simulated with an injection term that is zero for $t < 0$ and constant for $t > 0$.

This paper has been typeset from a TEX/LATEX file prepared by the author.

Chapter 6

Particle acceleration at ultrarelativistic, perpendicular shock fronts

Utilizing the Monte-Carlo test-particle method, we study the properties of the accelerated particle spectra, both the spectral index and the maximum energy, in two magnetic field configurations. In both cases, particles can be accelerated to energy much higher than the predicted magnetized limit.

In this chapter we introduce an analytical method to study the same problem in the uniform perpendicular shock. We use the eigenfunction expansion, or so-called Q_j method the solve the particle transport equation at ultra-relativistic shocks. We prove that ultra-relativistic shocks can still accelerate particles effectively even when there is no significant turbulence downstream. A stationary power-law spectrum with an index $s = 4.17$ is generated under these conditions. Compared to the results from Monte-Carlo simulations, these two methods reach a consistence with each other, strongly supporting the new argument against the magnetized limit.

Monthly Notices
of the
ROYAL ASTRONOMICAL SOCIETY

MNRAS **519,** 1022–1029 (2023) https://doi.org/10.1093/mnras/stac3589
Advance Access publication 2022 December 9

Particle acceleration at ultrarelativistic, perpendicular shock fronts

John G. Kirk ,* Brian Reville and Zhi-Qiu Huang
Max-Planck-Institut für Kernphysik, Postfach 10 39 80, D-69029 Heidelberg, Germany

Accepted 2022 November 30. in original form 2022 October 25

ABSTRACT

Using an eigenfunction expansion to solve the transport equation, complemented by Monte Carlo simulations, we show that ultrarelativistic shocks can be effective particle accelerators even when they fail to produce large amplitude turbulence in the downstream plasma. This finding contradicts the widely held belief that a uniform downstream magnetic field perpendicular to the shock normal inhibits acceleration by the first-order Fermi process. In the ultrarelativistic limit, we find a stationary power-law particle spectrum of index $s = 4.17$ for these shocks, close to that predicted for a strictly parallel shock.

Key words: acceleration of particles – radiation mechanisms: non-thermal – transients: gamma-ray bursts.

1 INTRODUCTION

Discovered in the late 1970s, the theory of diffusive shock acceleration has established itself as the primary mechanism discussed in connection with the acceleration of cosmic rays, and has also found many other applications. The generalization of this mechanism to mildly relativistic shock fronts followed roughly a decade later, and, in the early 2000s, it was found that particles repeatedly crossing ultrarelativistic shocks can be accelerated into a power-law spectrum of index $s = 4.23$ (for recent reviews, see Bell 2014; Sironi, Keshet & Lemoine 2015).

However, in contrast to the non-relativistic case, an ultrarelativistic shock that overruns a region containing a uniform magnetic field is generically superluminal, in the sense that its speed, when projected on to a magnetic field line, exceeds that of light. At first sight, this poses a problem, since acceleration requires repeated crossings of the shock front, and a particle downstream of the shock cannot catch up with it by simply diffusing along a magnetic field line. Since cross-field diffusion is generally strongly suppressed, this suggests that the relativistic extension of the diffusive shock acceleration mechanism might be ineffective (Begelman & Kirk 1990).

This problem does not arise if the downstream field is effectively scrambled by strong fluctuations on the scale of a gyroradius (Achterberg et al. 2001). However, a mechanism for producing such fluctuations has so far not been identified. For the case of shock propagation into a weakly magnetized plasma, where the Weibel instability is thought responsible for the formation of the shock front, particle-in-cell simulations have shown that acceleration is facilitated by non-resonant scattering on the Weibel-induced filaments (e.g. Sironi & Spitkovsky 2009; Plotnikov, Grassi & Grech 2018; Vanthieghem et al. 2020). However, analytical considerations suggest that scattering exclusively mediated by such non-resonant interactions is not sufficient to provide the required cross-field transport in the downstream plasma above a critical particle energy (Lemoine & Pelletier 2010; Reville & Bell 2014; Huang et al. 2022). Furthermore, such short length-scale fluctuations are susceptible to damping in the hot downstream plasma, which further reduces the critical energy (Chang, Spitkovsky & Arons 2008; Keshet et al. 2009; Sironi, Spitkovsky & Arons 2013; Lemoine 2015).

In this paper, we reassess these arguments by solving a simple model of a relativistic, perpendicular shock, thereby demonstrating quantitatively that particles are accelerated into a power-law distribution, whose index lies very close to that predicted for the idealized, parallel shock case (Kirk et al. 2000). In our model, energetic particles are assumed to diffuse in angle, whilst being deflected by a uniform magnetic field that is *perpendicular* to the shock normal. We solve this model for the case in which transport upstream is scattering dominated, i.e. the particles there are *unmagnetized*, whereas particles are *magnetized* when downstream and follow essentially unscattered trajectories, gyrating about the regular, uniform magnetic field. Two complementary techniques are employed. First, we use a generalization of the eigenfunction approach (Kirk et al. 2000) that takes into account the full, two-dimensional anisotropy imposed on the particle distribution, including the drift induced by the downstream magnetic field. This technique is applied in the ultrarelativistic limit of large shock Lorentz factor, $\Gamma_s \to \infty$, which enables the eigenfunctions to be found in closed form. The second method of solution is a Monte Carlo simulation of many individual trajectories, using a code described more fully in a companion paper (Huang et al. 2023, henceforth 'ZH'). This is applied here to shocks ranging from mildly to highly relativistic and shows that, as Γ_s rises from 2 to 50, the power-law index approaches the asymptotic value of $s = 4.17$ found by the eigenfunction method. This value is close to, but slightly harder than the result obtained previously for the case, where scattering dominates both up and downstream.

In Section 2, we formulate the equations describing particle transport, and present details of the first method of solution. Results of both methods, consisting of the power-law index of accelerated particles and the angular dependence of their distribution function at the shock front, are presented and compared in Section 3. In Section 4, we discuss the physics underlying our assumptions and their range of applicability and speculate on the implications of the results for more realistic cases.

---

* E-mail: john.kirk@mpi-hd.mpg.de

2 METHOD

2.1 Transport equation

In the presence of isotropic scattering in angle and gyration about a uniform field, the transport equation governing the phase-space density f of relativistic particles is given by equation (1) of Takamoto & Kirk (2015, henceforth 'TK'). Mixed coordinates are used in this equation, with Cartesian coordinates in configuration space measured in a frame in which the shock is at rest in the plane $x = 0$. The upstream plasma occupies the region $x > 0$, the downstream $x < 0$. Momentum space coordinates, on the other hand, are expressed in spherical polar coordinates, measured in the local (upstream or downstream) rest frame of the plasma. In this paper, we depart from the notation of TK and use the shock normal as the axis for these coordinates. Then, the momentum of an ultrarelativistic particle, in units of $c \times$ the rest mass, is $\boldsymbol{p} = (\gamma, \mu, \phi)$, with γ the Lorentz factor, $\arccos\mu$ the polar angle to the shock normal, and ϕ the azimuthal angle about this axis. The direction of motion of the shock front in this reference frame is $\mu = 1$, and $\mu = 0$, $\phi = 0$ is the direction of the uniform magnetic field $\boldsymbol{B}$. Solutions are sought that are stationary as seen in the shock rest frame, and have no dependence on the spatial coordinates y and z. Equation (12) of TK is then

$$\frac{2\Gamma^2\eta c}{\omega_{\mathrm{g}}}(\mu-\beta)\frac{\partial f}{\partial x} = \frac{\partial}{\partial\mu}\left(1-\mu^2\right)\frac{\partial f}{\partial\mu} + \frac{1}{1-\mu^2}\frac{\partial^2 f}{\partial\phi^2} + \frac{2\Gamma\eta\mu\cos\phi}{\sqrt{1-\mu^2}}\frac{\partial f}{\partial\phi} - 2\Gamma\eta\sqrt{1-\mu^2}\sin\phi\frac{\partial f}{\partial\mu}, \tag{1}$$

where $c\beta$ is the shock velocity measured in the local rest frame of the plasma, $\Gamma = (1-\beta^2)^{-1/2}$ is the Lorentz factor of the shock front, and we have assumed $\gamma \gg \Gamma$. The quantity η in this equation is the ratio of the gyrofrequency of an accelerated particle in the uniform field, $\omega_{\mathrm{g}} = |eB/\gamma mc|$, to Γ times the scattering frequency. Following Reville & Bell (2014), it can be written in terms of the magnetization parameter σ_{turb} associated with the strength δB of the magnetic fluctuations responsible for scattering, their characteristic length-scale λ, the magnetization parameter σ_{reg} of the uniform or *regular* upstream field, and the ion plasma frequency ω_{i}:

$$\eta = \left(\frac{mc}{m_{\mathrm{p}}\langle\gamma\rangle\omega_{\mathrm{i}}\lambda}\right)\left(\frac{\sigma_{\mathrm{reg}}^{1/2}}{\sigma_{\mathrm{turb}}}\right)\left(\frac{\gamma}{\Gamma}\right), \tag{2}$$

where m and m_{p} are the rest masses of the accelerating particles and that of the species dominating the plasma inertia, respectively, and $\langle\gamma\rangle m_{\mathrm{p}}c^2$ is the mean energy per plasma particle. When $\eta \ll 1$, scattering dominates the transport process and deflections by the regular magnetic field are unimportant. We then refer to the particles as being unmagnetized. On the other hand, when $\eta \gg 1$, the particles are magnetized and follow essentially unscattered trajectories in the uniform or regular magnetic field. Equation (1) applies in both the upstream and the downstream regions, where the speeds of the relativistic shock are denoted by β_{s} and β_{d}, respectively, and the corresponding Lorentz factors are $\Gamma_{\mathrm{s}} \gg 1$ and $\Gamma_{\mathrm{d}} \sim 1$. Analogous notation, $\eta_{\mathrm{s,d}}$, is used for the magnetization parameter.

2.2 Transport upstream

As is the case for particles accelerated at a parallel, ultrarelativistic shock front, we expect the stationary particle distribution in the upstream medium to be concentrated in a narrow cone of opening angle $\sim 1/\Gamma_{\mathrm{s}}$ about the shock normal. Consequently, it is convenient to replace μ by the *stretched* variable

$$\begin{aligned}\xi &= (1-\mu)/(1-\beta_{\mathrm{s}})\\ &\approx 2\Gamma_{\mathrm{s}}^2(1-\mu)\end{aligned} \tag{3}$$

(Kirk & Schneider 1989), which is zero for particles moving directly along the shock normal and unity for those moving parallel to the shock front. The phase-space density is now to be regarded as a function of x and the momentum space variables (γ, ξ, ϕ) that lie in the domain $\gamma > 1$, $0 \le \xi < \infty$, $0 \le \phi < 2\pi$, which we denote by A. Then, inserting the definition (3) into (1), expanding in powers of the small parameter $1/\Gamma_{\mathrm{s}}$, and assuming the particles are unmagnetized:

$$\eta_{\mathrm{s}} \ll 1, \tag{4}$$

the transport equation upstream becomes

$$\frac{\partial^2 f}{\partial\xi^2} + \frac{1}{\xi}\frac{\partial f}{\partial\xi} + \frac{1}{4\xi^2}\frac{\partial^2 f}{\partial\phi^2} - \left(\frac{1}{\xi}-1\right)\frac{\partial f}{\partial\hat{x}} = 0, \tag{5}$$

where we have introduced the dimensionless coordinate $\hat{x} = x\left(4\Gamma_{\mathrm{s}}^2\omega_{\mathrm{g}}\right)/(\eta c)$.

Equation (5) is separable, resulting in an exponential dependence of f on $\hat{x}$ and two eigenvalue problems, one for the ξ-dependence and one for the ϕ-dependence. Taken together with the boundary conditions (i) $f \to 0$ as $x \to \infty$, (ii) f bounded at $\xi = 0$ and ∞, (iii) f periodic in ϕ with period 2π, and (iv) f invariant under a change of sign in the component of momentum parallel to the downstream magnetic field: $f(\gamma, \xi, \phi, x) = f(\gamma, \xi, \pi - \phi, x)$, each eigenvalue problem is self-adjoint. Therefore, the solution can be expanded in the two-dimensional eigenfunctions Q_i:

$$f(\gamma, \xi, \phi, x) = F(\gamma)\sum_{i=1}^{\infty} \mathrm{e}^{\Lambda_i\hat{x}} a_i Q_i(\xi, \phi), \tag{6}$$

where the a_i are constants and the eigenfunctions are orthogonal over the weighting function $\xi - 1$:

$$\iint_{p\in A} \mathrm{d}\xi\,\mathrm{d}\phi\, Q_i(\xi, \phi)(\xi-1)\, Q_j(\xi, \phi) = 0, \quad i \ne j. \tag{7}$$

In Appendix A, we give explicit expressions for the eigenvalues Λ_i and the eigenfunctions Q_i.

2.3 Transport downstream

Transport in the downstream plasma is potentially more complex, since the accelerated particles are not concentrated in a narrow beam when viewed from the frame in which the plasma is at rest. Here, we follow the arguments presented by Reville & Bell (2014), who conclude that deflection in the uniform magnetic field perpendicular to the shock normal dominates the transport process for particles with sufficiently large Lorentz factor, i.e.

$$\eta_{\mathrm{d}} \gg 1. \tag{8}$$

We concentrate on these high-energy particles, because those of lower energy can be scattered in the turbulence generated at the shock front, and there is general agreement that the dominance of scattering on both sides of a relativistic shock results in a power-law spectrum $f \propto \gamma^{-s}$ with index $s \approx 4.2$.

For $\eta = \eta_{\mathrm{d}} \gg 1$ and $\Gamma = \Gamma_{\mathrm{d}} \sim 1$, equation (1) reverts to Liouville's equation, albeit written in our unconventional mixed coordinate system. The distribution of particles that are too energetic to experience scattering downstream is therefore controlled by Liouville's theorem, which dictates that the phase-space density remains constant along particle trajectories. When viewed from a frame of reference in which

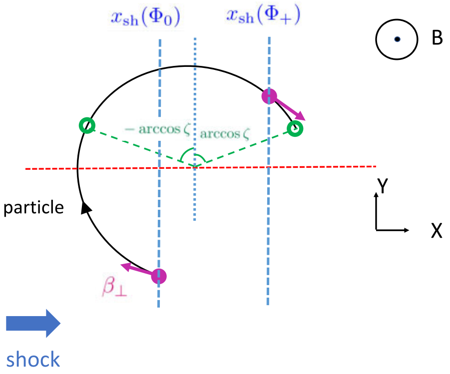

Figure 1. Sample trajectory for a positively charged particle with $\boldsymbol{p} \in R$ as seen in the downstream frame. The shock velocity and magnetic field are directed along the positive x- and z-axes, respectively. The magnitude of the particle's velocity $\beta_\perp$ in the x–y plane is a constant of motion, and its direction along the positive x-axis when the phase Φ is an integer multiple of 2π. The filled magenta circles denote example positions where the particle enters and exits the downstream, at phases Φ_0 and $\Phi_{+,}$ respectively. To overtake the shock, the x-component of the particle velocity must exceed that of the shock, requiring $-\arccos\zeta < \Phi_+ < \arccos\zeta$, where $\zeta = \beta_{\rm d}/\beta_\perp$. This range is delimited by the two green circles. For particles with $\boldsymbol{p} \in U$, we make the replacements $\Phi_0 \to \Phi_-$ and $\Phi_+ \to \Phi_0$. Further details are provided in Appendix B.

the downstream plasma is at rest, these trajectories are simply helices along which the Lorentz factor γ remains constant.

At the shock front, $x = 0$, the domain of momentum space A can be divided into three non-overlapping subdomains: (i) those trajectories crossing into downstream that subsequently return to the shock front, denoted by R (ii) those crossing into downstream that subsequently escape without re-encountering the shock, denoted by E, and (iii) those crossing into upstream (i.e. all trajectories with $0 < \xi < 1$), denoted by U. Given the coordinates in momentum space $\boldsymbol{p} = (\gamma, \xi, \phi)$ of a trajectory in R, it is straightforward to compute the mapping $\mathcal{M} : R \to U$ that relates the point $\boldsymbol{p}$ on a particle trajectory to the point $\boldsymbol{p}_+ = (\gamma_+, \xi_+, \phi_+) = \mathcal{M}\boldsymbol{p}$ at which this trajectory returns to the shock front. In Fig. 1, we provide a schematic sketch of a returning trajectory (for details, see Appendix B). Then, Liouville's theorem requires the distribution at the shock front, $x = 0$ to satisfy

$$f(\boldsymbol{p}, 0) = f(\mathcal{M}\boldsymbol{p}, 0) \qquad \boldsymbol{p} \in R. \tag{9}$$

Conversely, given the coordinates of a trajectory that crosses the shock from downstream to upstream, one can simply invert this mapping to find the coordinates $\boldsymbol{p}_- = (\gamma_-, \xi_-, \phi_-) = \mathcal{M}^{-1}\boldsymbol{p}$ with which it previously entered the downstream region, which implies

$$f(\boldsymbol{p}, 0) = f\left(\mathcal{M}^{-1}\boldsymbol{p}, 0\right) \qquad \boldsymbol{p} \in U\,. \tag{10}$$

Liouville's theorem does not provide a constraint on the points $\boldsymbol{p} \in E$ on trajectories that escape from the shock into the downstream plasma, but it is convenient to define the mapping $\mathcal{M}$ to be unity when operating on these: $\mathcal{M}\boldsymbol{p} = \boldsymbol{p}$, $\boldsymbol{p} \in E$.

2.4 Approximation scheme

Since the problem, as formulated here, does not contain a characteristic scale for the particle Lorentz factor γ, we look for solutions that are a power law in this quantity, $F(\gamma) = \gamma^{-s}$. The index s is then determined by matching the phase-space density across the shock front, i.e. by imposing the conditions (9) and (10) on the expression (6) for f in the upstream region, evaluated at the shock front $\hat{x} = 0$.

However, to find a numerical value for s, it is necessary to implement an approximation scheme. Here, we use a variant of the *Galerkin* method, similar to that used by Kirk & Schneider (1987), which essentially truncates the expansion (6) after the first $i_{\rm max}$ terms. Writing

$$f(\boldsymbol{p}, 0) = \gamma^{-s}\left[g_{i_{\rm max}}(\xi, \phi) + \mathcal{R}_{i_{\rm max}}(\xi, \phi)\right], \tag{11}$$

$$\text{where } g_{i_{\rm max}}(\xi, \phi) = \sum_{i=1}^{i_{\rm max}} a_i Q_i(\xi, \phi) \tag{12}$$

is the desired approximation to the angular part of the distribution function at the shock front, we demand that the residual $\mathcal{R}_{i_{\rm max}}$ be orthogonal to the first $i_{\rm max}$ eigenfunctions:

$$\iint_{\boldsymbol{p}\in A} {\rm d}\xi {\rm d}\phi Q_i(\xi - 1)\mathcal{R}_{i_{\rm max}}(\xi, \phi) = 0 \;\text{ for } i = 1, \dots i_{\rm max} \tag{13}$$

and, additionally, that the constraints (9) and (10) are satisfied not only by f, but also by its approximation, $\gamma^{-s} g_{i_{\rm max}}$. This scheme can be motivated physically if the terms in the summation in equation (6) are ordered by the eigenvalue Λ_i, such that

$$\Lambda_i \geq \Lambda_{i+1}, \qquad i \geq 1. \tag{14}$$

Since $\Lambda_1 < 0$, the higher order terms in the expansion decay ever more rapidly with increasing distance from the shock in the upstream region. The particles described by these terms move almost in the plane of the shock, and, as a consequence, receive only a small boost in energy in a cycle of crossing and recrossing. It is therefore to be expected that the index s is determined primarily by the first few terms in the summation.

Multiplying equation (11) by $\gamma^s Q_j$ and the weighting function, and integrating over $\boldsymbol{p} \in A$ leads to

$$\sum_{j=1}^{i_{\rm max}} \left[D_{ij} - M_{ij}(s)\right] a_j = 0 \qquad i = 1, \dots i_{\rm max}\,, \tag{15}$$

where the diagonal matrix D_{ij} results from substituting the expansion (6) into the left-hand side of (11):

$$D_{ij} = \iint_{\boldsymbol{p}\in A} {\rm d}\xi {\rm d}\phi\; Q_i(\xi, \phi)(\xi - 1)\, Q_j(\xi, \phi)\,. \tag{16}$$

Similarly, the matrix $M_{ij}(s)$ is obtained from the right-hand side by applying the constraints (9) and (10) to the function $g_{i_{\rm max}}$ and the constraint (13) to the function $\mathcal{R}_{i_{\rm max}}$:

$$\begin{aligned} M_{ij}(s) = {}& \gamma^s \iint_{\boldsymbol{p}\notin U} {\rm d}\xi {\rm d}\phi\, \gamma_+^{-s} Q_i(\xi, \phi)(\xi - 1)\, Q_j(\xi_+, \phi_+) \\ & + \gamma^s \iint_{\boldsymbol{p}\in U} {\rm d}\xi {\rm d}\phi\, \gamma_-^{-s} Q_i(\xi, \phi)(\xi - 1)\, Q_j(\xi_-, \phi_-)\,. \end{aligned} \tag{17}$$

Thus, equation (15) represents a system of homogeneous, linear algebraic equations for the a_j, which have a non-trivial solution only if

$$\text{Det}\left[D_{ij} - M_{ij}(s)\right] = 0\,. \tag{18}$$

Given a guess for s, it is straightforward to evaluate these matrices by numerical quadrature. Then, a root-finding algorithm applied to equation (18) yields s and the coefficients a_i are found from the null space of the corresponding matrix.

3 RESULTS

The usefulness of the approximation scheme described in Section 2.4 is confirmed by the rapid convergence as the number of

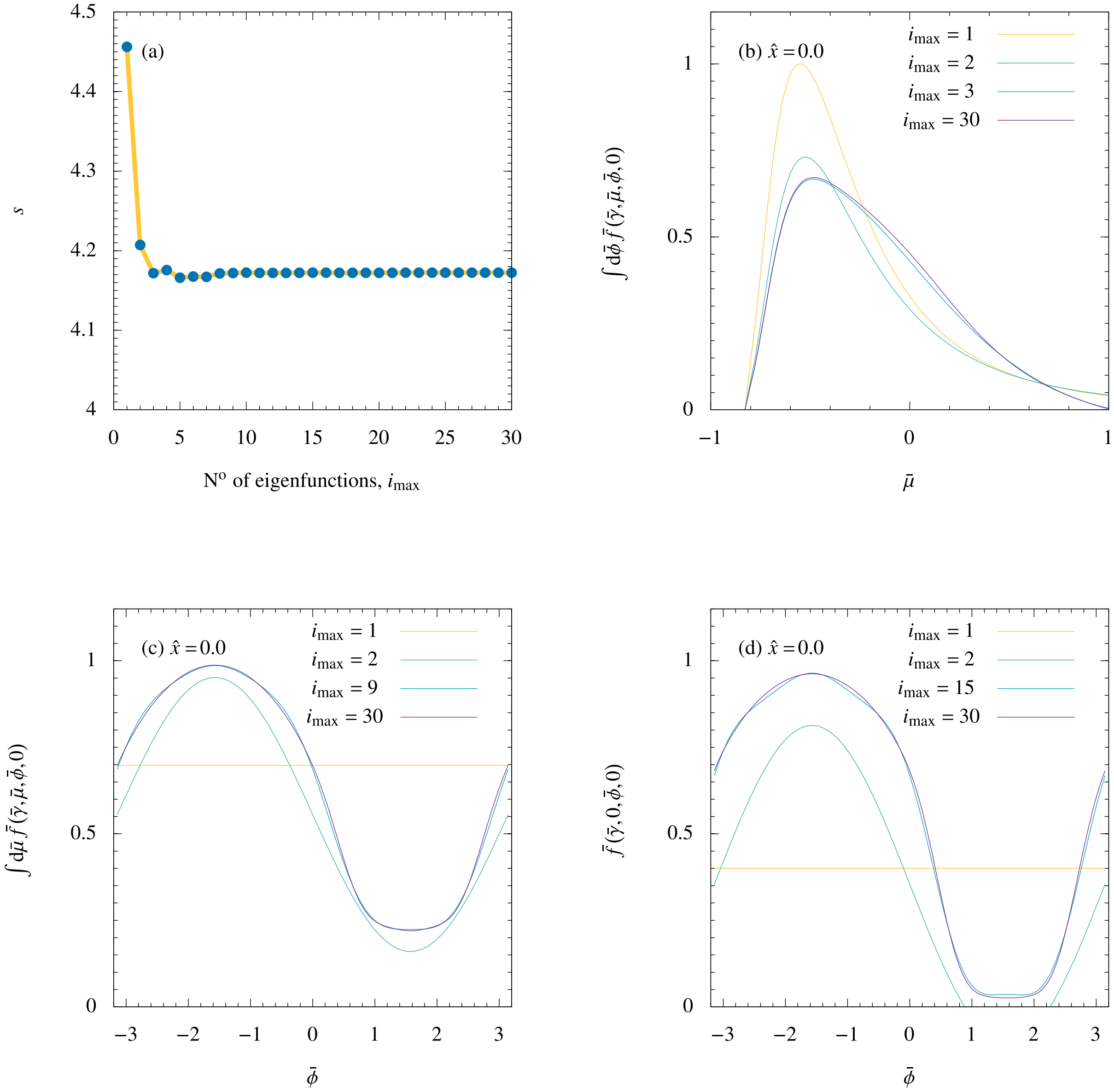

Figure 2. Convergence properties of the approximation scheme: (a) the power-law index s as a function of $i_{\rm max}$, the number of eigenfunctions used in equation (12), (b) and (c) the phase-space distribution $\bar{f}$ at the shock front ($\hat{x} = 0$) as seen in the frame in which the shock front is at rest, i.e. at constant particle Lorentz factor in this frame ($\bar{\gamma}$). $\bar{\mu}$ is the cosine of the angle between the particle momentum and the shock normal, and $\bar{\phi}$ is the azimuthal angle about this axis. Particles entering the upstream have $\bar{\mu} > 0$. (b) shows $\bar{f}$ averaged over phase, and (c) shows $\bar{f}$ averaged over $\bar{\mu}$. (d) shows a slice of $\bar{f}$ for particles that graze the shock, $\bar{\mu} = 0$. Results are plotted for $i_{\rm max} = 1$, 2 and the fully converged $i_{\rm max} = 30$, as well as for an intermediate value that indicates the rapidity of convergence. In all cases, the speed of the downstream plasma speed is $\beta_{\rm d} = 1/3$. In (b), (c), and (d), only the relative values of the functions plotted are physically significant.

eigenfunctions $i_{\rm max}$ is increased, as shown in Fig. 2. The converged value of s for an ultrarelativistic shock front in an ideal fluid, for which $\beta_{\rm d} = 1/3$, is 4.17, close to, but slightly harder than the result found when particle transport is dominated by scattering both upstream and downstream. This value depends only on $\beta_{\rm d}$, and is, in particular, independent of both the strength of the upstream scattering and the strength of the downstream magnetic field. As shown in panel (a) of Fig. 2, convergence to this result requires only a few (∼4) eigenfunctions. Because of the ordering of the eigenfunctions, equation (14), convergence of the angular dependence of the phase-space density is slowest at the shock front itself. Panels (b), (c), and (d) show this dependence as seen in the frame in which the shock is at rest, and the flow is directed along the shock normal. In this reference frame, the transformed spherical polar coordinates are denoted by $\bar{\gamma}$, $\bar{\mu}$, $\bar{\phi}$ where

$$\bar{\gamma} = \gamma\Gamma_{\rm s}\left(1 - \beta_{\rm s}\mu\right) \tag{19}$$

$$\bar{\mu} = \left(\mu - \beta_{\rm s}\right)/\left(1 - \mu\beta_{\rm s}\right) \tag{20}$$

$$\bar{\phi} = \phi \tag{21}$$

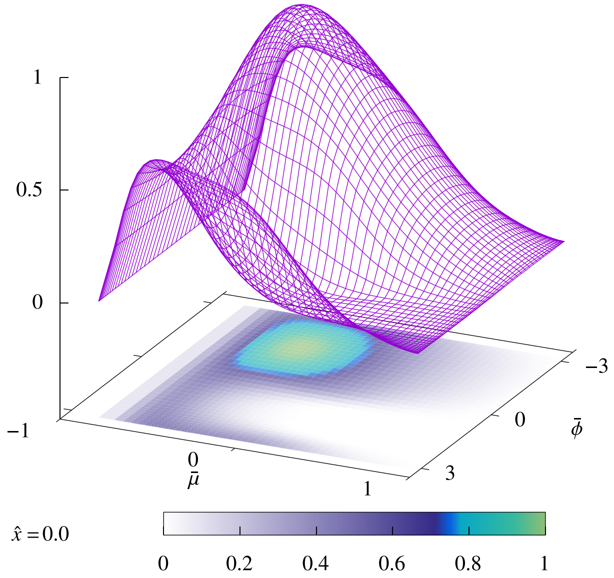

Figure 3. The full angular distribution of the phase-space density $\bar{f}\left(\bar{\gamma},\bar{\mu},\bar{\phi}\right)$ of accelerated particles at the shock front ($\hat{x}=0$), as seen in the frame in which the shock front is at rest. The downstream magnetic field is in the direction $\bar{\mu}=0$, $\bar{\phi}=0$, particles crossing into the upstream region have $\bar{\mu}>0$.

and, since the phase-space density, denoted in this frame by $\bar{f}$, is a Lorentz invariant quantity

$$\bar{f}\left(\bar{\gamma},\bar{\mu},\bar{\phi},x\right)=f\left(\gamma,\mu,\phi,x\right)\ . \tag{22}$$

Note that although the average over either $\bar{\phi}$ or $\bar{\mu}$ of the distribution converges with only ∼3 and ∼9 eigenfunctions, respectively, the phase distribution of those particles that move precisely along the shock front converges much more slowly, needing ∼15 eigenfunctions. This illustrates the fact that grazing particles have essentially no impact on the power-law index.

The angular distribution at the shock front is, as expected, anisotropic. In addition to the anisotropy with respect to the shock normal, which is well known from earlier studies of the scattering-dominated case and which arises because the relative velocity of the upstream and downstream plasmas is only slightly less than the particle velocity, a strong anisotropy in the azimuthal angle $\bar{\phi}$ is present because the downstream magnetic field imposes a drift along the shock front. This is clearly seen in the full 2D angular distribution at the shock front, as shown in Fig. 3. In terms of a right-handed system of coordinates with the magnetic field along the positive z-axis, the drift for a positively charged particle is in the positive y-direction ($\sin\bar{\phi}<0$), i.e. in the direction opposite to that of the electric field seen in the shock rest frame. Thus, as seen in the rest frame of the shock, particles gain energy during an excursion upstream, but lose some on their downstream loop.

Monte Carlo simulations, using the code described in ZH, provide an independent cross-check of these results, as well as extending them by lifting the restriction to the ultrarelativistic limit. In Fig. 4, we compare the angular distributions found by both methods. Shock grazing particles are problematic in the Monte Carlo approach when sampling the distribution precisely on the shock surface. Making the comparison a short distance upstream, here at the surface $\hat{x}=0.1$, mitigates the problem. Results for the eigenfunction method are shown in the ultrarelativistic limit, since using a finite value of $\Gamma_{\rm s}$ would necessitate a numerical evaluation of the eigenfunctions. The Monte Carlo simulations were performed with $\Gamma_{\rm s}=50$. Agreement is generally excellent, with small fluctuations visible only in the Monte Carlo results for the full 2D distribution.

The distribution of accelerated particles in energy for shock speeds ranging from mildly to highly relativistic is shown in Fig. 5. These are found using Monte Carlo simulations that inject 10^6 particles into the upstream with $\gamma=2\Gamma_{\rm s}^2$, and a uniform angular distribution within a cone about the shock normal of opening angle $1/\Gamma_{\rm s}$. The trajectories are then followed until they escape downstream, whilst registering the value of $\bar{\gamma}$ at each crossing of the shock. After several crossings, the distribution settles into a power law, that extends up to a point at which the statistical noise becomes significant. For simplicity, we choose in each case the jump conditions for a relativistic gas: $\beta_{\rm d}\beta_{\rm s}=1/3$. The figure shows the distribution weighted by the factor $\bar{\gamma}^{4.17}$ in order to highlight the departure of the finite $\Gamma_{\rm s}$ results from the ultrarelativistic result found by the eigenfunction method. It can be seen that the power-law index s is within a few per cent of its asymptotic value for $\Gamma_{\rm s}>5$.

4 DISCUSSION

Whether or not the mechanism of diffusive shock acceleration operates effectively at a perpendicular shock is a question that is still the subject of controversy, over four decades after the publication of the discovery papers, which implicitly addressed parallel shocks. In this context 'effectively' means either that the acceleration rate is comparable to or faster than that at a parallel shock, or that the power-law index of the stationary phase-space distribution of accelerated particles is close to or harder than that produced at a parallel shock. The main result of this paper concerns the power-law index produced by highly relativistic, and therefore generically perpendicular shocks. Assuming that particles can be treated as unmagnetized when upstream of the shock (4), but as magnetized when downstream (8), we demonstrate quantitatively that these shocks are just as effective accelerators as the possibly less realistic parallel shocks addressed by previous analytical work. This result has major implications also for the expected acceleration rate, and the related maximum energy to which particles can be accelerated at a shock in a given physical situation. These questions are addressed in ZH.

The persistence of turbulence in the *downstream* medium at a level sufficient to demagnetize particles is generally perceived to be a major problem for the theory of diffusive shock acceleration at relativistic shocks (e.g. Bykov et al. 2012). Our assumption that turbulence is completely negligible downstream is specifically designed to address this point. It is therefore not restrictive, in the sense that diffusive acceleration can be expected to proceed as previously predicted if this assumption is not justified in a particular application.

On the other hand, the assumption that particles diffuse in angle when *upstream* of the shock is important. Unless a degree of randomness enters into the trajectories that return to the shock from upstream, diffusive acceleration will cease and particles will receive only a single, finite boost in energy before being swept away downstream (Begelman & Kirk 1990; Pelletier, Lemoine & Marcowith 2009). We have adopted the simple prescription of isotropic diffusion to describe this randomness, since it renders the analytic approximations tractable; at least in the parallel shock case, this assumption does not appear to be crucial (Kirk et al. 2000). However, the validity of our approach does depend on the presence of turbulence of sufficient amplitude in the upstream medium. In the

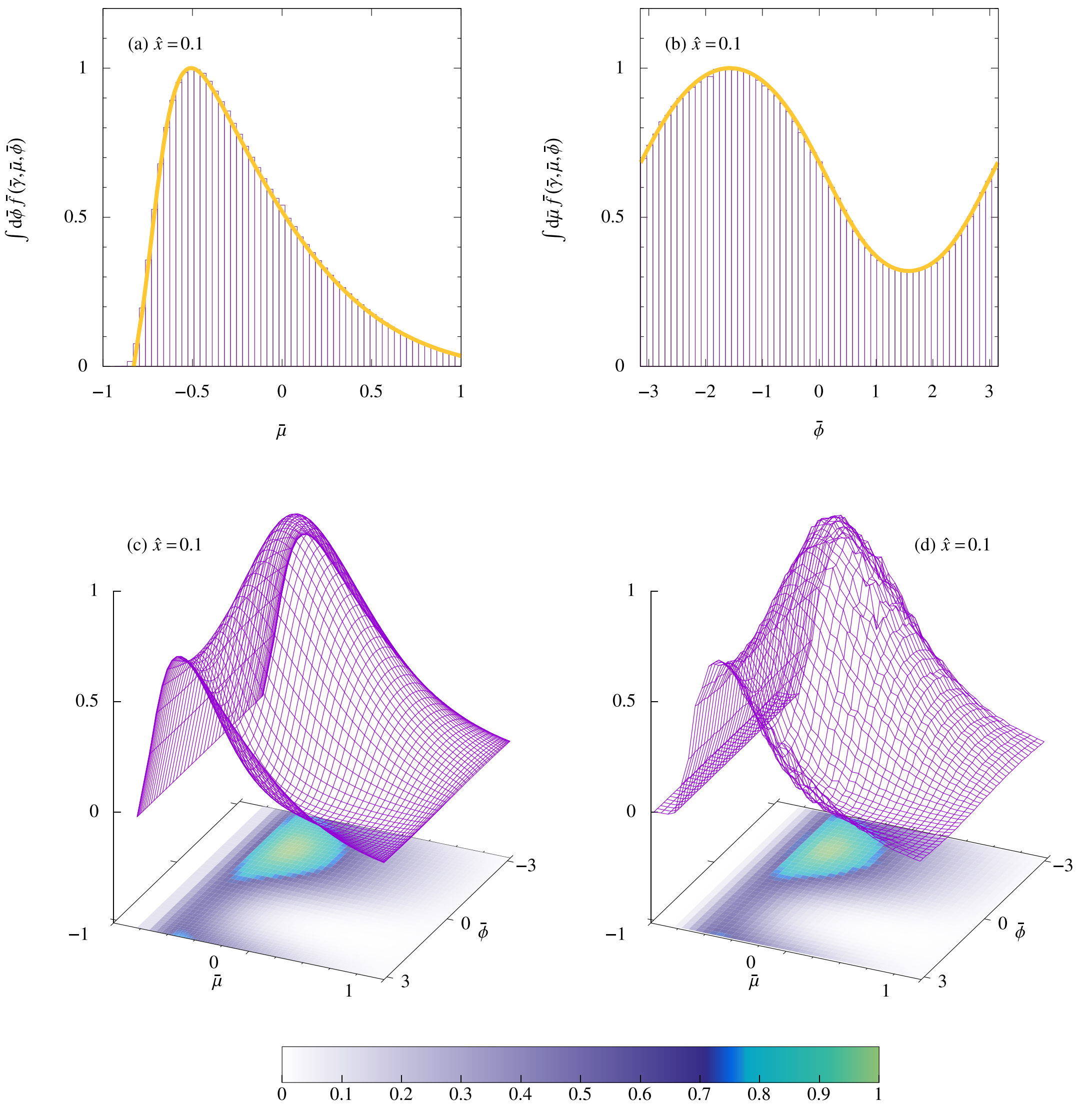

Figure 4. A comparison of the angular distributions just upstream of the shock front found by the eigenfunction method in the ultrarelativistic limit, and by Monte Carlo simulation for $\Gamma_{\rm s} = 50$. In (a), the distributions averaged over phase (about the shock normal), and in (b), over the angle to the shock normal are compared. In each case, the result for 30 eigenfunctions is shown as a yellow curve and that of the simulation as a purple histogram. In (c) and (d), the full distributions are shown for the eigenfunction and Monte Carlo methods, respectively.

case of a weakly magnetized plasma $\sigma_{\rm reg} < 10^{-3}$, such as might be encountered by the blast wave of a gamma-ray burst (GRB), a lower limit on the level of upstream turbulence is provided by shock-generated Weibel filaments, which, according to particle-in-cell simulations and analytical considerations, are amplified to $\sigma_{\rm turb} \approx 0.1$. According to (2), this is already sufficient to demagnetize particles with $\gamma < 0.1 \times \Gamma_{\rm s} \left(m_{\rm p}/m\right) \sigma_{\rm reg}^{-1/2}$, and therefore enable diffusive acceleration even if the filaments are strongly damped downstream. However, this limit is unduly restrictive if turbulence exists in the upstream that is not directly excited by the processes that form the shock. In the case of a GRB, for example, the ionization, heating, and pair-loading of the surrounding medium by the prompt emission (Beloborodov 2002; Grošelj, Sironi & Beloborodov 2022) seems unlikely to leave behind a quiescent environment. Furthermore, turbulence is known to be present in the winds of the progenitors of some supernovae of the type Ibc (Wellons, Soderberg & Chevalier 2012) that is associated with long duration GRBs. On the other hand, if the upstream medium is strongly magnetized, such as in the case of the termination shock of a pulsar wind, turbulence is embedded in the outflow by the pulsar and is thought to facilitate acceleration (Sironi & Spitkovsky 2011; Giacchè & Kirk 2017). Whereas previous discussions assumed this process to be confined to the equatorial region of the wind, where the regular field component vanishes, the results presented above suggest that it may persist to higher latitudes, with interesting implications for modelling the emission from pulsar wind nebulae (Olmi et al. 2015).

In summary, if sufficient turbulence is present in the upstream medium, our results demonstrate that the perpendicular magnetic field in the plasma downstream of a relativistic shock front does not inhibit acceleration. Rather than being swept away without returning to the shock front, particles indeed return, and populate a power-law distribution whose index is insensitive to the nature of the dominant transport mechanism downstream.

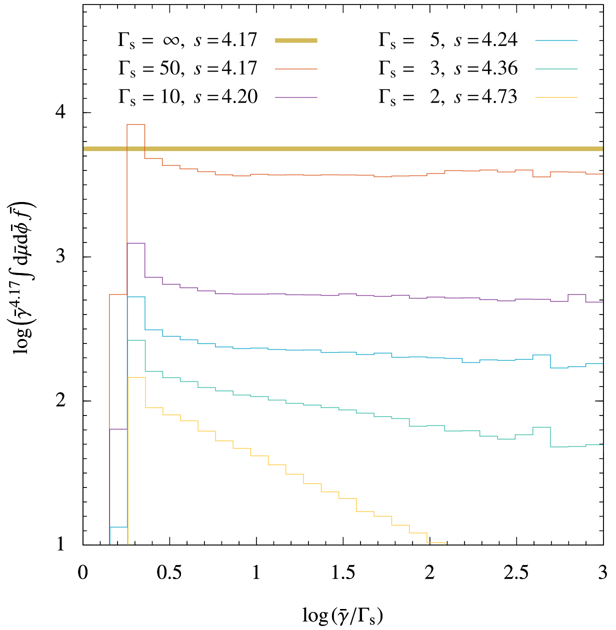

Figure 5. The angle-averaged distribution just upstream at $\hat{x} = 0.1$, as a function of the particle Lorentz factor $\bar{\gamma}$, measured in the rest frame of the shock. As the shock Lorentz factor Γ_s increases, the power-law section of the distribution converges towards the result found by the eigenfunction method in the ultrarelativistic limit, shown here as a horizontal line. For each Γ_s, the power-law index s, found from a least-squares fit to the data in the region $0.5 < \bar{\gamma}/\Gamma_s < 3$, is listed in the legend.

ACKNOWLEDGEMENTS

We thank Nils Schween, Gwenael Giacinti, Tony Bell, Martin Lemoine, and Daniel Grošelj for helpful discussions.

DATA AVAILABILITY

No data relevant to this paper are available.

REFERENCES

Achterberg A., Gallant Y. A., Kirk J. G., Guthmann A. W., 2001, MNRAS, 328, 393
Begelman M. C., Kirk J. G., 1990, ApJ, 353, 66
Bell A. R., 2014, Braz. J. Phys., 44, 415
Beloborodov A. M., ApJ, 565, 808
Bykov A., Gehrels N., Krawczynski H., Lemoine M., Pelletier G., Pohl M., 2012, Space Sci. Rev., 173, 309
Chang P., Spitkovsky A., Arons J., 2008, ApJ, 674, 378
Giacchè S., Kirk J. G., 2017, ApJ, 835, 235
Grošelj D., Sironi L., Beloborodov A. M., 2022, ApJ, 933, 74
Huang Z.-Q., Reville B., Kirk J.G., Giacinti G., 2022, ApJ, 925, 182
Huang Z.-Q., Giacinti G., Kirk J. G., Reville B. 2023, in preparation
Ince E. L., 1956, Ordinary Differential Equations. Dover Press, New York
Keshet U., Katz B., Spitkovsky A., Waxman E., 2009, ApJ, 693, L127
Kirk J. G., Schneider P., 1987, ApJ, 315, 425
Kirk J. G., Schneider P., 1989, A&A, 225, 559
Kirk J. G., Guthmann A. W., Gallant Y. A., Achterberg A., 2000, ApJ, 542, 235
Lemoine M., 2015, J. Plasma Phys., 81, 455810101
Lemoine M., Pelletier G., 2010, MNRAS, 402, 321
Olmi B., Del Zanna L., Amato E., Bucciantini N., 2015, MNRAS, 449, 3149
Pelletier G., Lemoine M., Marcowith A., 2009, MNRAS, 393, 587
Plotnikov I., Grassi A., Grech M., 2018, MNRAS, 477, 5238
Reville B., Bell A. R., 2014, MNRAS, 439, 2050
Sironi L., Spitkovsky A., 2009, ApJ, 698, 1523
Sironi L., Spitkovsky A., 2011, ApJ, 741, 39
Sironi L., Spitkovsky A., Arons J., 2013, ApJ, 771, 54
Sironi L., Keshet U., Lemoine M., 2015, Space Sci. Rev., 191, 519
Takamoto M., Kirk J. G., 2015, ApJ, 809, 29
Vanthieghem A., Lemoine M., Plotnikov I., Grassi A., Grech M., Gremillet L., Pelletier G., 2020, Galaxies, 8, 33
Wellons S., Soderberg A. M., Chevalier R. A., 2012, ApJ, 752, 17

APPENDIX A: 2D EIGENFUNCTIONS

Inserting the expansion (6) into (5) and separating the variables according to

$$Q_i(\xi,\phi) = T_i(\xi)\, S_i(\phi) \tag{A1}$$

one obtains for the ϕ-dependent function

$$S_i'' = -j^2 S_i\,, \tag{A2}$$

where j is a constant, which, since S is periodic with period 2π, is an integer. Without loss of generality, we can choose $j \geq 0$ and identify two families of solutions that satisfy the additional symmetry $S_i(\phi) = S_i(\pi - \phi)$:

$$S_i \propto \begin{cases} \cos(j\phi) & j \text{ even or zero} \\ \sin(j\phi) & j \text{ odd}\,. \end{cases} \tag{A3}$$

The equation determining the ξ-dependent eigenfunction is

$$\left(\xi T_i'\right)' - \left[\frac{j^2}{4\xi} + \Lambda_i\,(1-\xi)\right] T_i = 0\,. \tag{A4}$$

Following Kirk & Schneider (1989, appendix A; see also Ince 1956, section7.31), one looks for a solution of the form

$$T_i = \mathrm{e}^{\lambda\xi}\xi^{\alpha}\sum_{n=0}^{\infty} c_n\xi^n\,. \tag{A5}$$

Inserting this into equation (A4) shows that the choice $\lambda = -\sqrt{-\Lambda_i}$ is convenient, since it removes the highest power of ξ in the term proportional to T_i, leading to a two-term recurrence relation for the c_n. The indicial equation is $\alpha^2 = j^2/4$, so that there are two possible solutions

$$\begin{aligned} T_i^+ &= \mathrm{e}^{-\sqrt{-\Lambda_i}\xi}\sum_{n=0}^{\infty}\xi^n c_n^+ \qquad j \text{ even or zero} \\ T_i^- &= \mathrm{e}^{-\sqrt{-\Lambda_i}\xi}\sum_{n=0}^{\infty}\xi^{n+\frac{1}{2}} c_n^- \qquad j \text{ odd.} \end{aligned} \tag{A6}$$

Table A1. 2D eigenfunctions: i uniquely identifies the eigenfunction Q_i, j defines its ϕ-dependence according to equation (A3), k is the largest integer such that $c_k \neq 0$ in equation (A6), Λ_i is the eigenvalue determining the x-dependence associated with this eigenfunction in equation (6). The (arbitrary) normalization of the Q_i is $c_n = 1$, where $n = j/2$ (j even or zero), or $n = (j-1)/2$ (j odd) is the smallest integer for which $c_n \neq 0$.

i	j	k	Λ_i	Q_i
1	0	0	-1	$\mathrm{e}^{-\xi}$
2	1	0	-4	$\mathrm{e}^{-2\xi}\sqrt{\xi}\,\sin(\phi)$
3	0	1	-9	$\mathrm{e}^{-3\xi}(1-6\xi)$
4	2	1	-9	$\mathrm{e}^{-3\xi}\xi\cos(2\phi)$
5	1	1	-16	$\mathrm{e}^{-4\xi}\sqrt{\xi}\,(1-4\xi)\sin\phi$
6	3	1	-16	$\mathrm{e}^{-4\xi}\xi^{3/2}\sin(3\phi)$

Inserting (A6) into (A4) and equating coefficients gives $j^2 c_0^+ = 0$ and $\left(j^2-1\right) c_0^- = 0$ and, for $n \geq 0$, the recurrence relations

$$c_{n+1}^+ = \left(\frac{4\sqrt{-\Lambda_i}\left(2n+1-\sqrt{-\Lambda_i}\right)}{(2n+2)^2-j^2}\right) c_n^+$$
$$c_{n+1}^- = \left(\frac{4\sqrt{-\Lambda_i}\left(2n+2-\sqrt{-\Lambda_i}\right)}{(2n+3)^2-j^2}\right) c_n^- \, . \tag{A7}$$

Since $c_{n+1}^\pm / c_n^\pm \to 2\sqrt{-\Lambda_i}/n$, as $n \to \infty$ it follows that $T_i^\pm \to \mathrm{e}^{\sqrt{-\Lambda_i}\xi}$ as $\xi \to \infty$, unless the relevant series truncates at finite n. Therefore, the eigenvalues satisfying the boundary conditions of boundedness at $\xi = 0, \infty$ are found by requiring truncation for, say, $n > k \geq 0$. Then,

$$\Lambda_i = \begin{cases} -(2k+1)^2 & j \text{ even or zero, } 0 \leq j \leq 2k \\ -4(k+1)^2 & j \text{ odd, } 1 \leq j \leq 2k+1 \end{cases} , \tag{A8}$$

where k is a positive integer or zero. Thus, each index i corresponds to a pair of indices k and j. The eigenvalues Λ_i depend on k and only the parity of j. The corresponding eigenfunctions can be evaluated using the recurrence relations (A7). The first few are listed in Table A1.

APPENDIX B: MAPPING

For an ultrarelativistic particle ($\gamma \gg \Gamma_\mathrm{s}$), membership of the three subdomains of momentum space at the shock front – upstream (U), returning (R), and escaping (E) – of the particle phase space (A) is determined solely by the direction of motion, labelled by the stretched variable ξ, defined in (3), and the azimuthal phase (with respect to the shock normal) ϕ. Membership of U requires only $\xi < 1$, but the requirements for R and E are more complicated. First, define the auxiliary parameter ζ to be the ratio of the shock speed $c\,\beta_\mathrm{d}$ to the component $c\beta_\perp$ of the particle speed that is perpendicular to the magnetic field, both seen from the frame in which the downstream plasma is at rest. The computation of ζ from (ξ, ϕ) involves a Lorentz boost from the rest frame of the upstream plasma to that of the downstream plasma, followed by a change of axis of the polar coordinates from the shock normal to the magnetic field. To lowest order in $1/\Gamma_\mathrm{s}$, one finds

$$\zeta = \frac{\beta_\mathrm{d}\left[(1+\beta_\mathrm{d})+(1-\beta_\mathrm{d})\,\xi\right]}{\sqrt{\left[(1+\beta_\mathrm{d})+(1-\beta_\mathrm{d})\,\xi\right]^2 - 4\xi\left(1-\beta_\mathrm{d}^2\right)\cos^2\phi}} \geq \beta_\mathrm{d} \, . \tag{B1}$$

This quantity remains constant during the particle's residence downstream. Clearly, $\zeta > 1$ implies that the particle cannot recross the shock front ($\boldsymbol{p} \in E$) and the mapping $\mathcal{M}$ is unity:

$$\mathcal{M}\boldsymbol{p} = \boldsymbol{p}_+, \;\; \boldsymbol{p} \in E :$$
$$\gamma_+ = \gamma \qquad \xi_+ = \xi \qquad \phi_+ = \phi \, . \tag{B2}$$

However, although $\zeta > 1$ is sufficient for $\boldsymbol{p} \in E$, it is not a necessary condition. The distance d, in units of the particle's gyroradius, between the shock and a point on the trajectory depends on ζ, the particle's phase Φ (measured about the downstream magnetic field, such that it is an increasing function of time for a positively charged particle) and the phase Φ_0 at which the trajectory intersects the shock front:

$$\mathrm{d}\left(\zeta, \phi, \phi_0\right) = \zeta\left(\phi - \phi_0\right) - \left(\sin\phi - \sin\phi_0\right) \, . \tag{B3}$$

From the Lorentz boost and coordinate transformation, one finds, to lowest order in $1/\Gamma_\mathrm{s}$,

$$\phi_0 = \mathrm{atan2}\left[2\sin\phi\sqrt{\left(1-\beta_\mathrm{d}^2\right)\xi},\; (1+\beta_\mathrm{d}) - (1-\beta_\mathrm{d})\,\xi\right] + 2n\pi \, , \tag{B4}$$

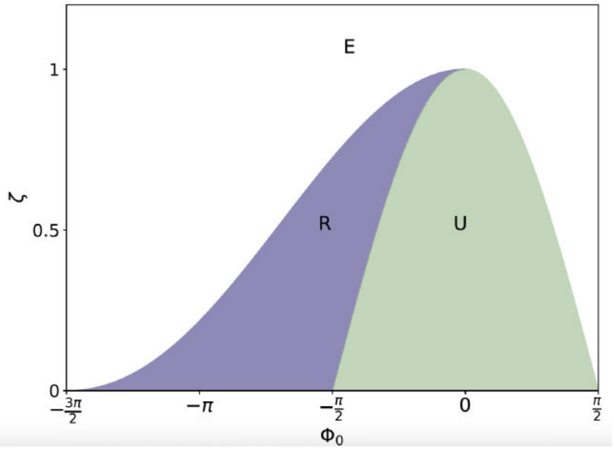

Figure B1. The three subdomains of particle phase space at the shock front in the Φ_0–ζ plane: purple for $\boldsymbol{p} \in R$, green for $\boldsymbol{p} \in U$, and the remaining unshaded area for $\boldsymbol{p} \in E$. Note that $\zeta > \beta_\mathrm{d}$.

where, to simplify the discussion, the integer n is to be chosen such that $-2\pi + \arccos\zeta \leq \Phi_0 < \arccos\zeta$. For $\boldsymbol{p} \notin U$, the distance d grows initially, implying $-2\pi + \arccos\zeta < \Phi_0 < -\arccos\zeta$, and subsequently goes through an alternating series of maxima and minima as the trajectory gyrates about the magnetic field. The first maximum is reached when $\Phi = -\arccos\zeta$ and the subsequent minimum when $\Phi = +\arccos\zeta$. Therefore, if $\zeta < 1$, a sufficient condition for the particle to escape is that $d > 0$ at this minimum, i.e.

$$\mathrm{d}\left(\zeta, \arccos\zeta, \phi_0\right) > 0 \, , \tag{B5}$$

in which case $\mathcal{M}$ is again the unit mapping (B2). If, on the other hand, $d < 0$ at this point, then $\boldsymbol{p} \in R$, and the phase Φ_+, with which the trajectory returns to the shock front, is given by the single solution of the equation

$$\mathrm{d}\left(\zeta, \phi_+, \phi_0\right) = 0 \, , \tag{B6}$$

with $-\arccos\zeta < \Phi_+ < \arccos\zeta$. Similarly, for $\boldsymbol{p} \in U$, which implies $-\arccos\zeta < \Phi_0 < \arccos\zeta$, the phase Φ_-, at which the trajectory previously entered the downstream region, is the single solution of the equation

$$\mathrm{d}\left(\zeta, \phi_0, \phi_-\right) = 0 \, , \tag{B7}$$

with $-2\pi + \arccos\zeta < \Phi_- < -\arccos\zeta$. Thus, the boundaries between the different subdomains for particles in R, E, and U are uniquely defined in the Φ_0–ζ plane, as summarized in Fig. B1.

To find $\mathcal{M}$, it remains to transform the coordinates and apply a Lorentz boost back to the upstream frame, which gives, to lowest order in $1/\Gamma_\mathrm{s}$, one finds

$$\mathcal{M}\boldsymbol{p} = \boldsymbol{p}_+, \;\; \boldsymbol{p} \in R \text{ and } \mathcal{M}^{-1}\boldsymbol{p} = \boldsymbol{p}_-, \;\; \boldsymbol{p} \in U :$$
$$\gamma_\pm = \gamma\left(\zeta + \beta_\mathrm{d}\cos\phi_\pm\right)\frac{(1-\beta_\mathrm{d})\,\xi + (1+\beta_\mathrm{d})}{2\,(1-\beta_\mathrm{d})\,\zeta}$$
$$\xi_\pm = \frac{(1+\beta_\mathrm{d})\left(\zeta - \beta_\mathrm{d}\cos\phi_\pm\right)}{(1-\beta_\mathrm{d})\left(\zeta + \beta_\mathrm{d}\cos\phi_\pm\right)}$$
$$\phi_\pm = \mathrm{atan2}\left(\beta_\mathrm{d}\sin\phi_\pm, \sqrt{\zeta^2 - \beta_\mathrm{d}^2}\right) \, . \tag{B8}$$

This paper has been typeset from a TEX/LATEX file prepared by the author.

Chapter 7

Discussions

After the first discovery of cosmic rays by Victor Hess, the origin of these high-energy particles has always been a heated topic in astrophysics. Shocks, as a typical case of first-order Fermi acceleration, are considered one of the promising acceleration mechanisms. Corresponding research has been conducted in numerous works since the theory of diffusive shock acceleration was first proposed in the late 1970s. A wealth of observational evidence indicates the existence of shocks in various astrophysical objects and their high efficiency in converting energy into very-high-energy particles. Despite significant efforts in this field, many open questions remain under debate. Among them, the effectiveness of relativistic shocks as particle accelerators has long been a subject of argument.

To gain energy, particles must continuously traverse the relativistic shock front. Neglecting the scale limit of the system, particles upstream can consistently return downstream through regular deflection or scattering. However, particles downstream have to chase the relativistic shock front. These particles face a higher probability of transporting far downstream and escaping. To return upstream, strong turbulence downstream on the scale of the gyro-radius is required to randomize particles [26]. Unfortunately, a mechanism to produce such fluctuations has not been discovered yet. Recent numerical simulations demonstrate that particle acceleration at relativistic shocks is facilitated by non-resonant scattering mediated by the Weibel instability [e.g. 31, 104, 105]. However, this mechanism is not efficient enough to provide cross-field transport for particles downstream above a threshold energy [37, 106, 107].

A prevalent belief suggests that, in the absence of efficient cross-field diffusion downstream, particles are constrained by downstream magnetic lines, which are almost perpendicular to the shock normal due to shock compression. Consequently, particles struggle to catch up to the shock front, leading to the quenching of the acceleration process. This scenario assumes that the non-resonant scattering frequency becomes smaller than the gyro-frequency induced by the regular field. As particle energy increases, both the scattering frequency and the gyro-frequency decrease, but the former shrinks much faster than the latter ($\nu_{\rm sc} \propto \gamma^{-2}$ while $\omega_{\rm g} \propto \gamma^{-1}$). Beyond a critical energy where $\nu_{\rm sc} < \omega_{\rm g}$, particles become magnetized and cannot move upstream, establishing an upper limit on the achievable energy accelerated by relativistic shocks, known as the magnetized limit. The primary scientific goal of this thesis is to demonstrate the limitations of the aforementioned argument concerning particle acceleration at relativistic shocks.

7.1 The Implications of TeV-detected GRB Afterglows for Acceleration at Relativistic Shocks

In our initial paper, we sought to derive implications for the maximum electron energy from late-time afterglow detections of GRB 190829A. At that point, we adhered to our existing understanding of relativistic shock acceleration, which is demonstrated to be

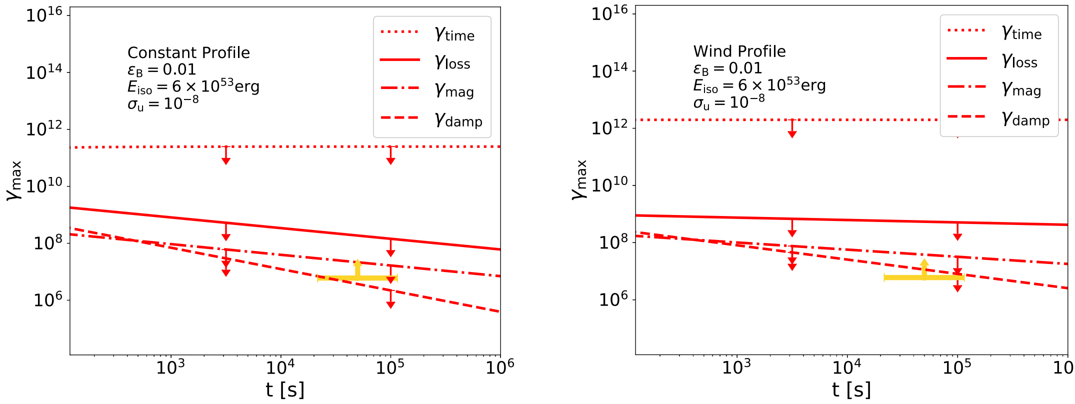

Figure 7.1: The maximum electron energy as a function of observer time for different external profiles. Left panel: constant density profile. Right panel: wind density profile. From bottom to top we identify four different limits: damping limited (dashed), magnetization limit (dashed-dotted), radiation loss limited (solid) and time limited (dotted). The maximum detected photon energy serves as a lower limit on the maximum electron energy in the source and is shown in yellow for the late-time VHE emission of GRB 190829A. The damping limit is shown for $L_{\rm damp} \approx \sigma_u^{-1/2} c/\omega_{\rm p}$, and the loss and magnetization limits for $\ell_{\rm w} = 10$. In the published version, there is a mistake on the line of damping limit. Here we use the modified version.

inaccurate in subsequent works. Utilizing GRB afterglow parameters obtained from spectrum fitting, we compared various models regarding the maximum electron energy. It is important to note that the published version contained an error in the expression used for the damping limit, and the correct expression is as follows:

$$\bar{\gamma}_{\rm damp} \approx (\ell_{\rm w}\epsilon_B)^{1/2}\,(m_{\rm p}/m_{\rm e})\Gamma_{\rm sh}\sigma_u^{-1/4} \tag{7.1}$$

Here we attach the corrected version of Fig. 1 in Chapter 4.

In the published version, the damping limit consistently falls below the observational constraints, leading us to reject this model. However, after the necessary modifications, this revised damping limit model is not as easily excluded. Given that this adjusted limit is now comparable to the magnetized limit, it does not significantly impact the primary conclusions drawn in our paper.

Recent simulations [34] propose a characteristic scale of $\lambda = 10c/\omega_{\rm p}$ for scattering driven by Weibel instability near the GRB shock front. However, the associated magnetization limit is contradicted by the data, as the maximum electron energy derived from this limit is too low to align with late-time X-ray detections. While we previously suggested the necessity of larger-scale turbulent structures, not evident in simulations due to spatial or temporal limitations, our subsequent studies on particle acceleration at relativistic shocks provide alternative solutions. The combined effects of strong scattering upstream and the drift motion induced by the curvature of the surrounding regular magnetic field, which we will discuss in the following sections, emerge as crucial factors enabling particle acceleration beyond the magnetized limit. This challenges and updates our existing understanding of relativistic shocks.

Relaxing constraints on the maximum electron energy, challenges persist in explaining the hard spectra observed in TeV bands. The single-zone SSC model faces difficulties due to the Klein-Nishina effect, resulting in calculated spectra softer than the observed ones. Although there is insufficient data to draw a definitive conclusion, alternative models have been proposed. One suggestion posits TeV afterglow photons originate from an external photon background [103, 108]. To produce a hard spectrum while avoiding the Klein-Nishina effect, scattering of these background photons should occur in the Thomson regime. Another proposed model is the two-zone model [109], which separates the acceleration and radiation of electrons into distinct regions, preventing the synchrotron burn-off limit for the maximum energy of synchrotron photons. Both models are intriguing and await testing through future gamma-ray detections.

7.2 Prospects for Ultra-high-energy Particle Acceleration at Relativistic Shocks

Fitting the multi-wavelength spectra of GRB 190829A, contradictions between observational data and our current understanding of shock acceleration emerge. Motivated by this, we employ the Monte-Carlo test-particle code to reexamine the acceleration process at relativistic shocks. Two configurations of the regular fields are taken into consideration.

7.2.1 Perpendicular Uniform Magnetic Field

Shocks with a uniform field in the plane of the shock are often considered as an instructive case for shock acceleration. In Chapter 5 and Chapter 6, we demonstrate, through numerical simulations and the analytical eigenfunction method, that particles can continue to be accelerated until they become magnetized on both sides of the shock. In this section, we provide some additional supplements to these two chapters.

7.2.1.1 Angular Distribution from Eigenfunction Method

As a first-step test for our test-particle code, we compare the angular distribution at the shock front obtained from the numerical code with that from the eigenfunction method introduced in Chapter 2 as well as Kirk *et al.* [30] and Kirk and Schneider [110].

In the shock rest frame the angular distribution at the shock front can be written as [30]

$$f_s \propto (1-\mu_s u_-)^{-s} \exp\left(-\frac{1+\mu_s}{1-u_-\mu_s}\right). \tag{7.2}$$

Transform to the downstream rest frame utilizing $p_d^{-s} f_d = p_s^{-s} f_s$, we derive

$$f_d \propto (1-\mu_s(\mu_d) u_-)^{-s} \exp\left(-\frac{1+\mu_s(\mu_d)}{1-u_-\mu_s(\mu_d)}\right)(1-u_-\mu_d)^{-s}. \tag{7.3}$$

The angular distribution from simulations fit well with this expression. We also compare the spectral indexes from the two methods. Without the constraints on the maximum accelerated energy, the predicted accelerated spectrum is a single power-law with $dN/d\gamma \propto \gamma^{-2.23}$ extending to infinity. This is consistent with the spectral index before the cutoff obtained from the numerical code.

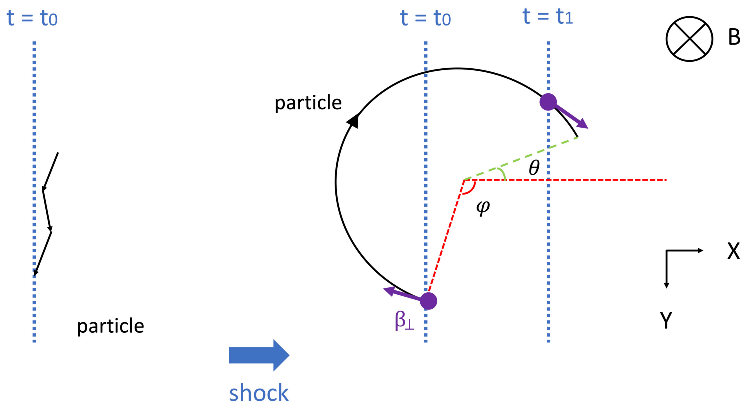

Figure 7.2: Schematic picture of the particle trajectory in the downstream rest frame. We consider an extreme case with pure scattering in upstream and only regular deflection in downstream. The shock moves along the x-axis and the regular magnetic field points toward the z-axis. A negatively-charged particle would rotate clockwise along the field. At $t = t_0$, the particle is caught by the shock and moves from upstream to downstream. At $t = t_1$, this particle catches the shock by regular deflection and moves from downstream to upstream. $\beta_\perp$ is the particle velocity perpendicular to the regular field, φ represents the initial phase when the particle moves to downstream, and θ represents the angle in which the particle velocity along the x-axis become smaller than the shock velocity.

7.2.1.2 Trajectory of the Particle with Energy beyond the Downstream Magnetized Limit

Based on the previous understanding, downstream magnetized particles were thought to be constrained to move along magnetic lines, being washed away far downstream and unable to cross the shock front. However, our recent findings indicate that particles can still be effectively accelerated under such conditions. To better comprehend the acceleration process, studying the trajectories of these high-energy particles downstream would be instructive.

Consider an extreme scenario where particles exclusively undergo gyro-motion downstream and experience pure scattering upstream. This aligns with our earlier discussion in Chapter 6 (see Fig. 7.2 as an illustration).

At time $t = t_0$, this particle is captured by the shock and moves from upstream to downstream, characterized by a phase angle φ. Here $\varphi = 0$ points towards the positive x-axis direction and increases clockwise. At $t = t_1$, this particle is deflected by the regular magnetic field and catches the shock again. Note the particle must catch the shock before its velocity along x-axis β_x becomes smaller than the shock velocity. Consequently, a critical angle $\theta = \arcsin\left(\frac{1}{3\beta_\perp}\right)$ exists, and particles need to catch the shock front before reaching this angle. For particles that can return back to upstream by regular deflection, the relation between $\beta_\perp$ and φ is written as:

$$\frac{(\cos\theta - \cos\varphi) r_{\rm g}}{c/3} > \frac{2\pi - \varphi - \theta}{\omega_{\rm g}}. \tag{7.4}$$

where $r_{\rm g} = \beta_\perp/\omega_{\rm g}$. Note $\varphi \leqslant 2\pi - \theta$.

Besides, when the particle moves from upstream to downstream at $t = t_0$, its velocity

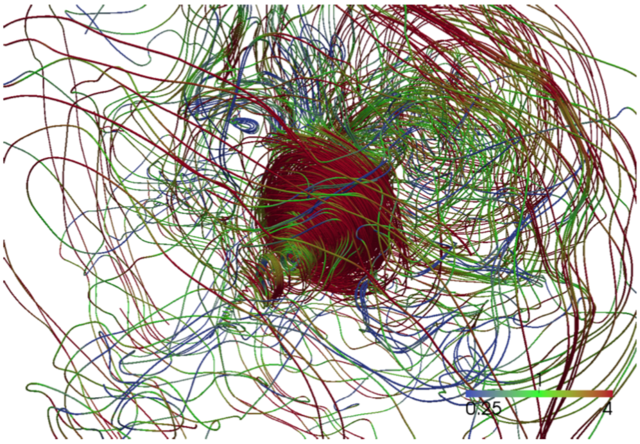

Figure 7.3: 3D simulations of magnetic fields in pulsar wind nebulae taken from Porth *et al.* [111]. Although quite chaotic, we can still see some cylindrical structures at the center.

along x-axis must be smaller than the shock velocity,

$$\beta_x < \frac{1}{3}. \tag{7.5}$$

In such a case, the maximum energy increases with time linearly, corresponding to the Bohm scattering.

7.2.2 Magnetic Field with Cylindrical Symmetry

In the case of a perpendicular shock, the outcomes from both the test-particle code and the eigenfunction method align, challenging the previous belief that perpendicular relativistic shocks are ineffective accelerators.

While the assumption of a uniform magnetic field configuration holds in certain scenarios, it becomes impractical when the gyro-radius of particles reaches a scale comparable to that of the system. Particularly for ultra-high-energy particles, which are heated topics in astrophysical research, the impact of pre-existing structures in the magnetic field can be substantial.

An enhanced configuration involves considering a magnetic field with cylindrical symmetry„ as predicted in pulsar wind nebulae [111] (see Fig. (7.3)), relativistic jets from active galactic nuclei [112, 113] (Fig. (7.4)), and the forward shock propagating into an ambient medium with Parker-wind-type magnetic structures.

Continuing our investigation with the Monte-Carlo test-particle code, we explore particle acceleration at relativistic shocks propagating into a medium with a simple cylindrical magnetic field. The curvature of the magnetic field induces drift motions along the shock normal for charged particles, as illustrated in Fig. (7.5). The orientation of this drift depends on the charge of the particle. For particles with favorable charges, such drift motions can improve the acceleration efficiency and energize particles up to the confinement limit of the system. In Fig. (7.6) the drift motion on the trajectory of a positively charged particle is clearly evident in our case.

Exploring particle acceleration at relativistic shocks propagating into a medium with toroidal field configurations has broad applicability. It is crucial to note that the drift motion direction depends on both the charge of the particle and the helicity of the

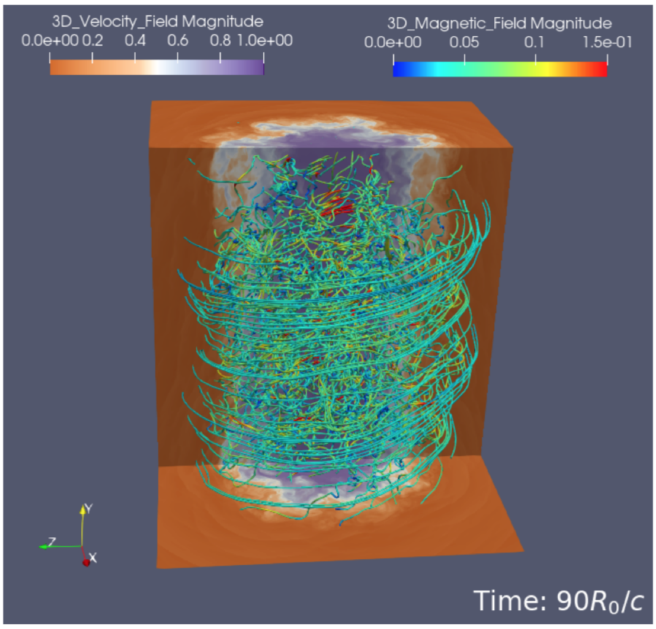

Figure 7.4: 3D simulations of magnetic fields in active galactic nuclei taken from Wang *et al.* [112].

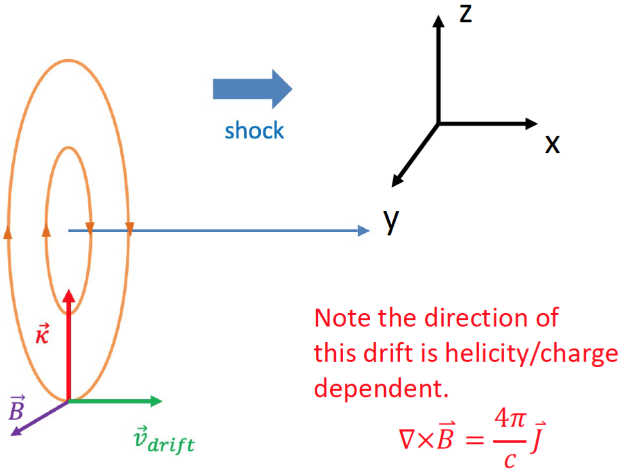

Figure 7.5: Schematic picture for the curvature drift.

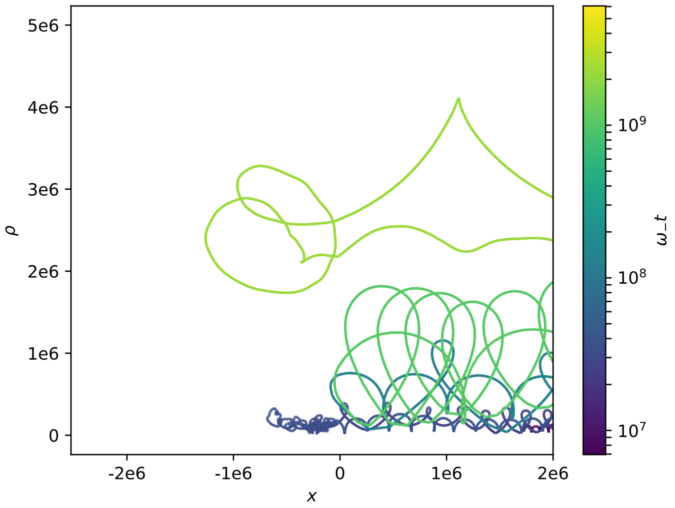

Figure 7.6: Trajectory of a positively charged particle in the x–ρ-plane near the shock front.

regular field. As a result, the acceleration efficiencies for particles with different charges show significant discrepancies, giving rise to distinct features in the accelerated spectra for negatively and positively charged particles.

Taking blazars as an example, recent observations have identified certain blazars emitting radiation in the very high-energy bands, exceeding 0.1 TeV. Notably, photons with an energy of around 10 TeV have been observed from sources like 1ES 0229+200 [114]. While both leptonic [e.g., 115, 116] and hadronic scenarios [e.g., 117–119] can explain these very-high-energy emissions, challenges persist in hadronic models. Consequently, scientists tend to favor leptonic models to explain the origins of TeV photons from blazars.

If TeV photons from blazars indeed originate from electrons, it implies a significantly high acceleration efficiency for electrons. However, the acceleration process for positively charged particles, such as protons and heavy nuclei, would be considerably less effective due to the opposite directions of drift motion in cylindrical fields. This discrepancy may preclude TeV blazars from being sources of ultra-high-energy cosmic rays. Conversely, our recent findings suggest that ultra-high-energy cosmic rays could originate from dark objects without radiation detections in the very high-energy range. Given the prevalence of helical field configurations in various astrophysical objects, these discoveries offer a new perspective on understanding the origin of high-energy cosmic rays.

Chapter 8

Conclusions

The origin of ultra-high-energy cosmic rays (UHECRs) is still under debate. Going back to 1949, Enrico Fermi proposed a potential mechanism to produce cosmic rays by scattering off moving clouds. Today we refer to all such mechanisms, where particles gain energy by sampling relative fluid motions, Fermi acceleration mechanisms. Diffusive shock acceleration, as a typical case of such a mechanism, has long been studied. Particles can gain energy by crossing the shock front until escaping from the system, or limited by some cooling process. In the case of a non-relativistic shock, as occurs in a supernova, the particle moves much faster than the shock, resulting in an almost isotropic angular distribution near the shock front. Therefore, we can solve the diffusive transport equation to get the accelerated spectrum. However, such a method becomes unfeasible for relativistic shocks, in which case the shock velocity is comparable to that of particles, and hence the angular distribution near the shock is highly anisotropic. In this thesis, analytical methods as well as numerical simulations are utilized to investigate acceleration processes at relativistic shocks.

Relativistic shocks triggered by catastrophic phenomena like GRBs are widely considered as possible sites for accelerating high-energy particles. Nowadays, thanks to the rapidly-increasing improvements and investments in experimental instruments, plenty of observational data have been accumulated, indicating an efficient energy conversion from shocks into energetic particles. Over the last several decades, significant efforts and progress have also been made in understanding particle acceleration at relativistic shocks, both through analytical and numerical methods. However, a fundamental understanding of all the competing processes is lacking.

Recent detections of TeV photons from GRB afterglows provide an opportunity to test our current understanding on particle acceleration at relativistic shocks. These TeV photons are most likely generated through the synchrotron self-Compton (SSC) process by high-energy electrons that are accelerated at relativistic shocks, carrying critical implications on the maximum electron energy and the acceleration process. The maximum electron energy is constrained by several mechanisms. Based on recent numerical simulations of relativistic shocks, we take several theoretical models for the maximum electron energy into consideration and compare them with observations. Adopting characteristic parameters for GRB afterglows, this maximum energy should be fixed by the so-called magnetized limit. **By fitting the late-time TeV detections of GRB190829A, we find a tension between our current knowledge on the maximum accelerated energy by relativistic shocks and the observational data. This incongruity prompts our further investigations into shock acceleration.** Additionally, due to the Klein-Nishina (KN) effect, the spectrum would be greatly suppressed in very-high-energy gamma-ray band, posing an obstacle to match the observational TeV data. These conclusions present a challenge to the standard external shock model for GRB afterglows [107].

Motivated by the discrepancy between predicted maximum electron energy and the observations in our first paper, we reexamine the claim that the particle acceleration ceases when downstream particles become magnetized. Utilizing a Monte-Carlo test-particle code, we explore shock acceleration in two configurations of regular magnetic fields. **In the scenario involving a uniform field perpendicular to the shock normal on both sides of the shock, we illustrate that particles can still undergo effective acceleration if they can be treated as unmagnetized on either side of the shock. The resulting spectrum has an index of approximately -2.2 [120]. These outcomes are further validated using the eigenfunction method [121].** For the field with a cylindrical geometry, which is prevalent in the magnetized jets from rotating black holes and in the ambient medium of long GRBs, the curvature of the regular field would produce a current line along the symmetric axis of the system, inducing drift motions for charged particles. The direction of such a drift depends on the charge of the particles as well as the helicity of the field, leading to significant discrepancies in the produced accelerated spectra. **This result clearly illustrates the significant role of particle drift, a non-diffusive behavior, in relativistic shocks (also explored in Giacinti and Kirk [122]),which hasn't been fully appreciated yet.** Multi-dimensional kinetic simulations will be essential for future self-consistent modeling of particle acceleration at relativistic shocks.

The work presented in this thesis have challenged the existing models of Fermi acceleration at relativistic shocks, and opened new possibilities for future studies. These findings have promising implications for high-energy astrophysics, particularly concerning scenarios for the production of ultra-high-energy cosmic rays. However, our work relies on certain simplifications that can be refined in future investigations. Notably, we neglect the cooling effects of particles, which are crucial especially for electrons. Additionally, our consideration of simple geometries for regular magnetic fields may not fully capture the complexity of real astrophysical scenarios. Obtaining information on these fields like MHD simulations of jets, and incorporating it into the Monte-Carlo test-particle code, can unveil more interesting features in the produced spectra. In the case of cylindrical regular fields, the spectra of particles with favorable charges could be quite hard at high energies. The interactions between these high-energy particles and the background plasma would be significant, which cannot be considered in the test-particle code. Therefore, PIC simulations are needed to explore this important effect and lead to a more comprehensive understanding of the acceleration mechanisms at relativistic shocks.

Appendices

Appendix A

Momentum transform in the Galilean limit

In this appendix we give the detailed deduction on momentum transform in the Galilean limit.

The four-vector momentum of a relativistic particle $p^{\mu} = (E/c, \vec{p})$. Doing the Lorentz transformation, the momentum $p^{\mu'}$ measured in another frame with a relative velocity $\beta = u/c$ and a Lorentz factor γ is

$$p^{\mu'} = (E/c, \vec{p}) \begin{pmatrix} \gamma & -\gamma\beta & 0 & 0 \\ -\gamma\beta & \gamma & 0 & 0 \\ 0 & 0 & 1 & 0 \\ 0 & 0 & 0 & 1 \end{pmatrix} \tag{A.1}$$

Hence wecan write down the space momentum $\vec{p}^{'} = (p_x^{'}, p_y^{'}, p_z^{'})$ as

$$\begin{aligned} p_x^{'} &= -\gamma\beta\frac{E}{c} + \gamma p_x \\ p_y^{'} &= p_y \\ p_z^{'} &= p_z \end{aligned} \tag{A.2}$$

And

$$\begin{aligned} p^{'} &= \sqrt{p_x^{'2} + p_y^{'2} + p_y^{'2}} \\ &= \sqrt{p_x^{'2} + p_{\perp}^{'2}} \\ &= \sqrt{\gamma^2\beta^2E^2/c^2 + \gamma^2p_x^2 - 2\gamma^2\beta E p_x/c + p_{\perp}^2} \end{aligned} \tag{A.3}$$

Consider the Galilean limit with $\beta \to 0$ and $\gamma \to 1$ and ignore the high order on β, Eq. A.4 can be simplified as

$$\begin{aligned} p^{'} &= \sqrt{p_x^2 + p_{\perp}^2 - 2\beta E p\mu/c} \\ &= \sqrt{p^2 - 2\beta\frac{\Gamma mc^2 p\mu v}{cv}} \\ &= \sqrt{p^2 - 2\beta\frac{p^2\mu c}{v}} \\ &\simeq p(1 - \frac{u}{v}\mu) \end{aligned} \tag{A.4}$$

Here we use $E = \Gamma mc^2$ and $p = \Gamma mv$ for the relativistic particle.

Appendix B

Detailed calculation on the recurrence relation

Here we give the detailed calculation for the recurrence relation in the eigenfunction method.

Recall

$$Q_i = \exp\left(-(1-u)\sqrt{\Lambda_i/dy}\right) \sum c_n y^n \tag{B.1}$$

Let $k = (1-u)\sqrt{\Lambda_i/d}$ and insert Eq B.1 into

$$y\frac{d^2Q_i}{dy^2} + \frac{dQ_i}{dy} = \Lambda_i \frac{(1-u)^2}{d}(y-1)Q_i. \tag{B.2}$$

Note

$$\begin{aligned} \frac{dQ_i}{dy} &= -k\exp(-ky)\sum c_n y^n + \exp(-ky)\sum n c_n y^{n-1} && \text{(B.3)} \\ y\frac{d^2Q_i}{dy^2} &= k^2\exp(-ky)\sum c_n y^{n+1} - 2k\exp(-ky)\sum n c_n y^n + && \text{(B.4)} \\ &\qquad \exp(-ky)\sum n(n-1)c_n y^{n-1} && \\ & && \text{(B.5)} \end{aligned}$$

and then we have

$$\begin{aligned} k^2\exp(-ky) \quad & \sum c_n y^{n+1} - k\exp(-ky)\sum(2n+1)c_n y^n + \exp(-ky)\sum n^2 c_n y^{n-1} && \text{(B.6)} \\ & = k^2(y-1)\exp(-ky)\sum c_n y^n && \\ & k^2\sum c_n y^n - k\sum(2n+1)c_n y^n + \sum n^2 c_n y^{n-1} = 0 && \text{(B.7)} \\ & k^2 c_n - k(2n+1)c_n + (n+1)^2 c_{n+1} = 0 && \text{(B.8)} \end{aligned}$$

Finally we get

$$c_{n+1} = \frac{k(2n+1-k)}{(n+1)^2} \tag{B.9}$$

Appendix C

Deduction for ultrarelativistic, perpendicular shock fronts

In this chapter we give deductions on the transport equation using the eigenfunction method.

Recall the transport equation given by Takamoto and Kirk [123]

$$\frac{2\Gamma^2\eta c}{\omega_{\mathrm{g}}}(\mu-\beta)\frac{\partial f}{\partial x} = \frac{\partial}{\partial\mu}\left(1-\mu^2\right)\frac{\partial f}{\partial\mu} + \frac{1}{1-\mu^2}\frac{\partial^2 f}{\partial\phi^2} \tag{C.1}$$

$$+\frac{2\Gamma\eta\mu\cos\phi}{\sqrt{1-\mu^2}}\frac{\partial f}{\partial\phi} - 2\Gamma\eta\sqrt{1-\mu^2}\sin\phi\frac{\partial f}{\partial\mu} \tag{C.2}$$

The particle distribution in the upstream fluid should be concentrated in a cone with an opening angle $\sim 1/\Gamma_{\mathrm{s}}$. Replace μ by another variable ξ which is defined as

$$\xi = (1-\mu)/(1-\beta_{\mathrm{s}}) \approx 2\Gamma_{\mathrm{s}}^2(1-\mu). \tag{C.3}$$

Here we consider the ultra-relativistic case, with $\Gamma_{\mathrm{s}} \gg 1$ and $\mu \to 1$.

Now we rewrite each term in Eq. C.2.

$$\frac{2\Gamma^2\eta c}{\omega_{\mathrm{g}}}(\mu-\beta)\frac{\partial f}{\partial x} = 4\Gamma^2(1-\xi)\frac{\partial f}{\partial\hat{x}} \tag{C.4}$$

$$\begin{aligned}\frac{\partial}{\partial\mu}\left(1-\mu^2\right)\frac{\partial f}{\partial\mu} &= 4\Gamma^4\frac{\partial}{\partial\xi}\left[\left(\frac{4\Gamma^2\xi-\xi^2}{4\Gamma^4}\right)\frac{\partial f}{\partial\xi}\right] \\ &= (4\Gamma^2-2\xi)\frac{\partial f}{\partial\xi} + (4\Gamma^2\xi-\xi^2)\frac{\partial^2 f}{\partial\xi^2} \\ &\approx 4\Gamma^2\frac{\partial f}{\partial\xi} + 4\Gamma^2\xi\frac{\partial^2 f}{\partial\xi^2}\end{aligned} \tag{C.5}$$

$$\begin{aligned}\frac{1}{1-\mu^2}\frac{\partial^2 f}{\partial\phi^2} &= \frac{4\Gamma^4}{4\Gamma^2\xi-\xi^2}\frac{\partial^2 f}{\partial\phi^2} \\ &\approx \frac{\Gamma^2}{\xi}\frac{\partial^2 f}{\partial\phi^2}\end{aligned} \tag{C.6}$$

$$\frac{2\Gamma\eta\mu\cos\phi}{\sqrt{1-\mu^2}}\frac{\partial f}{\partial\phi} = \frac{2\Gamma\eta\mu\cos\phi}{\sqrt{2\xi/2\Gamma^2}}\frac{\partial f}{\partial\phi} \tag{C.7}$$

$$= \frac{2\Gamma^2\eta\cos\phi}{\sqrt{\xi}}\frac{\partial f}{\partial\phi}$$

$$\begin{aligned} 2\Gamma\eta\sqrt{1-\mu^2}\sin\phi\frac{\partial f}{\partial\mu} &= 2\Gamma\eta\frac{\sqrt{4\Gamma^2\xi-\xi^2}}{2\Gamma^2}\sin\phi\frac{\partial f}{\partial\mu} \\ &\approx 2\eta\sqrt{\xi}\sin\phi\frac{\partial f}{\partial\mu} \end{aligned} \tag{C.8}$$

Divide each term by $4\Gamma^2\xi$, use $\eta \ll 1$ and remove the negligible terms, the transport equation upstream becomes

$$\frac{\partial^2 f}{\partial\xi^2} + \frac{1}{\xi}\frac{\partial f}{\partial\xi} + \frac{1}{4\xi^2}\frac{\partial^2 f}{\partial\phi^2} - \left(\frac{1}{\xi}-1\right)\frac{\partial f}{\partial\hat{x}} = 0 \tag{C.9}$$

Now we try to separate Eq. C.9. Assuming $f(\gamma,\xi,\phi,\hat{x}) = F(\gamma)\sum_i a_i X_i(\hat{x})Q_i(\xi,\phi)$, we get

$$\begin{aligned} &X_i\frac{\partial^2 Q_i}{\partial\xi^2} + \frac{1}{\xi}X_i\frac{\partial Q_i}{\partial\xi} + \frac{1}{4\xi^2}X_i\frac{\partial^2 Q_i}{\partial\phi^2} - \left(\frac{1}{\xi}-1\right)\frac{\partial X_i}{\partial\hat{x}}Q_i = 0 \\ &\left(\frac{1}{\xi}-1\right)\frac{1}{X_i}\frac{\partial X_i}{\partial\hat{x}} = \frac{1}{Q_i}\left(\frac{\partial^2 Q_i}{\partial\xi^2} + \frac{1}{\xi}\frac{\partial Q_i}{\partial\xi} + \frac{1}{4\xi^2}\frac{\partial^2 Q_i}{\partial\phi^2}\right) \\ &X_i = \exp(\Lambda_i\hat{x}) \end{aligned} \tag{C.10}$$

Bibliography

[1] C. L. Critchfield, E. P. Ney, and S. Oleksa, “The Electrons in Cosmic Rays,” Physical Review **79**, 402 (1950).

[2] J. A. Earl, “Cloud-Chamber Observations of Primary Cosmic-Ray Electrons,” Physical Review L **6**, 125 (1961).

[3] M. Amenomori, X. J. Bi, D. Chen, S. W. Cui, Danzengluobu, L. K. Ding, X. H. Ding, C. Fan, C. F. Feng, Z. Feng, Z. Y. Feng, X. Y. Gao, Q. X. Geng, H. W. Guo, H. H. He, M. He, K. Hibino, N. Hotta, H. Hu, H. B. Hu, J. Huang, Q. Huang, H. Y. Jia, F. Kajino, K. Kasahara, Y. Katayose, C. Kato, K. Kawata, Labaciren, G. M. Le, A. F. Li, J. Y. Li, Y. Q. Lou, H. Lu, S. L. Lu, X. R. Meng, K. Mizutani, J. Mu, K. Munakata, A. Nagai, H. Nanjo, M. Nishizawa, M. Ohnishi, I. Ohta, H. Onuma, T. Ouchi, S. Ozawa, J. R. Ren, T. Saito, T. Y. Saito, M. Sakata, T. K. Sako, M. Shibata, A. Shiomi, T. Shirai, H. Sugimoto, M. Takita, Y. H. Tan, N. Tateyama, S. Torii, H. Tsuchiya, S. Udo, B. Wang, H. Wang, X. Wang, Y. Wang, Y. G. Wang, H. R. Wu, L. Xue, Y. Yamamoto, C. T. Yan, X. C. Yang, S. Yasue, Z. H. Ye, G. C. Yu, A. F. Yuan, T. Yuda, H. M. Zhang, J. L. Zhang, N. J. Zhang, X. Y. Zhang, Y. Zhang, Y. Zhang, Zhaxisangzhu, X. X. Zhou, and Tibet ASγ Collaboration, “The All-Particle Spectrum of Primary Cosmic Rays in the Wide Energy Range from 10^{14} to 10^{17} eV Observed with the Tibet-III Air-Shower Array,” The Astrophysical Journal **678**, 1165 (2008), arXiv:0801.1803 [hep-ex] .

[4] V. Verzi, “Measurement of the energy spectrum of ultra-high energy cosmic rays using the Pierre Auger Observatory,” in *36th International Cosmic Ray Conference (ICRC2019)*, International Cosmic Ray Conference, Vol. 36 (2019) p. 450.

[5] P. Abreu, M. Aglietta, J. M. Albury, I. Allekotte, A. Almela, J. Alvarez-Muñiz, R. Alves Batista, G. A. Anastasi, L. Anchordoqui, B. Andrada, S. Andringa, C. Aramo, P. R. Araújo Ferreira, J. C. Arteaga Velázquez, H. Asorey, P. Assis, G. Avila, A. M. Badescu, A. Bakalova, A. Balaceanu, F. Barbato, R. J. Barreira Luz, K. H. Becker, J. A. Bellido, C. Berat, M. E. Bertaina, X. Bertou, P. L. Biermann, P. Billoir, V. Binet, K. Bismark, T. Bister, J. Biteau, J. Blazek, C. Bleve, M. Boháčová, D. Boncioli, C. Bonifazi, L. Bonneau Arbeletche, N. Borodai, A. M. Botti, J. Brack, T. Bretz, P. G. Brichetto Orchera, F. L. Briechle, P. Buchholz, A. Bueno, S. Buitink, M. Buscemi, M. Büsken, K. S. Caballero-Mora, L. Caccianiga, F. Canfora, I. Caracas, J. M. Carceller, R. Caruso, A. Castellina, F. Catalani, G. Cataldi, L. Cazon, M. Cerda, J. A. Chinellato, J. Chudoba, L. Chytka, R. W. Clay, A. C. Cobos Cerutti, R. Colalillo, A. Coleman, M. R. Coluccia, R. Conceição, A. Condorelli, G. Consolati, F. Contreras, F. Convenga, D. Correia dos Santos, C. E. Covault, S. Dasso, K. Daumiller, B. R. Dawson, J. A. Day, R. M. de Almeida, J. de Jesús, S. J. de Jong, G. De Mauro, J. R. T. de Mello Neto, I. De Mitri, J. de Oliveira, D. de Oliveira Franco, F. de Palma, V. de Souza, E. De Vito, M. del Río, O. Deligny, A. Di Matteo, C. Dobrigkeit, J. C. D’Olivo, L. M. Domingues Mendes, R. C. dos Anjos, D. dos Santos, M. T. Dova, J. Ebr, R. Engel, I. Epicoco, M. Erdmann, C. O. Escobar, A. Etchegoyen, H. Falcke, J. Farmer,

G. Farrar, A. C. Fauth, N. Fazzini, F. Feldbusch, F. Fenu, B. Fick, J. M. Figueira, A. Filipčič, T. Fitoussi, T. Fodran, M. M. Freire, T. Fujii, A. Fuster, C. Galea, C. Galelli, B. García, A. L. Garcia Vegas, H. Gemmeke, F. Gesualdi, A. Gherghel-Lascu, P. L. Ghia, U. Giaccari, M. Giammarchi, J. Glombitza, F. Gobbi, F. Gollan, G. Golup, M. Gómez Berisso, P. F. Gómez Vitale, J. P. Gongora, J. M. González, N. González, I. Goos, D. Góra, A. Gorgi, M. Gottowik, T. D. Grubb, F. Guarino, G. P. Guedes, E. Guido, S. Hahn, P. Hamal, M. R. Hampel, P. Hansen, D. Harari, V. M. Harvey, A. Haungs, T. Hebbeker, D. Heck, G. C. Hill, C. Hojvat, J. R. Hörandel, P. Horvath, M. Hrabovský, T. Huege, A. Insolia, P. G. Isar, P. Janecek, J. A. Johnsen, J. Jurysek, A. Kääpä, K. H. Kampert, N. Karastathis, B. Keilhauer, J. Kemp, A. Khakurdikar, V. V. Kizakke Covilakam, H. O. Klages, M. Kleifges, J. Kleinfeller, M. Köpke, N. Kunka, B. L. Lago, R. G. Lang, N. Langner, M. A. Leigui de Oliveira, V. Lenok, A. Letessier-Selvon, I. Lhenry-Yvon, D. Lo Presti, L. Lopes, R. López, L. Lu, Q. Luce, J. P. Lundquist, A. Machado Payeras, G. Mancarella, D. Mandat, B. C. Manning, J. Manshanden, P. Mantsch, S. Marafico, A. G. Mariazzi, I. C. Mariş, G. Marsella, D. Martello, S. Martinelli, H. Martinez, O. Martínez Bravo, M. Mastrodicasa, H. J. Mathes, J. Matthews, G. Matthiae, E. Mayotte, P. O. Mazur, G. Medina-Tanco, D. Melo, A. Menshikov, K. D. Merenda, S. Michal, M. I. Micheletti, L. Miramonti, D. Mockler, S. Mollerach, F. Montanet, C. Morello, M. Mostafá, A. L. Müller, M. A. Muller, K. Mulrey, R. Mussa, M. Muzio, W. M. Namasaka, A. Nasr-Esfahani, L. Nellen, M. Niculescu-Oglinzanu, M. Niechciol, D. Nitz, D. Nosek, V. Novotny, L. Nožka, A. Nucita, L. A. Núñez, M. Palatka, J. Pallotta, P. Papenbreer, G. Parente, A. Parra, J. Pawlowsky, M. Pech, F. Pedreira, J. PÈ©kala, R. Pelayo, J. Peña-Rodriguez, E. E. Pereira Martins, J. Perez Armand, C. Pérez Bertolli, M. Perlin, L. Perrone, S. Petrera, T. Pierog, M. Pimenta, V. Pirronello, M. Platino, B. Pont, M. Pothast, P. Privitera, M. Prouza, A. Puyleart, S. Querchfeld, J. Rautenberg, D. Ravignani, M. Reininghaus, J. Ridky, F. Riehn, M. Risse, V. Rizi, W. Rodrigues de Carvalho, J. Rodriguez Rojo, M. J. Roncoroni, M. Roth, E. Roulet, A. C. Rovero, P. Ruehl, S. J. Saffi, A. Saftoiu, F. Salamida, H. Salazar, G. Salina, J. D. Sanabria Gomez, F. Sánchez, E. M. Santos, E. Santos, F. Sarazin, R. Sarmento, C. Sarmiento-Cano, R. Sato, P. Savina, C. M. Schäfer, V. Scherini, H. Schieler, M. Schimassek, M. Schimp, F. Schlüter, D. Schmidt, O. Scholten, P. Schovánek, F. G. Schröder, S. Schröder, J. Schulte, A. Schulz, S. J. Sciutto, M. Scornavacche, A. Segreto, S. Sehgal, R. C. Shellard, G. Sigl, G. Silli, O. Sima, R. Šmída, P. Sommers, J. F. Soriano, J. Souchard, R. Squartini, M. Stadelmaier, D. Stanca, S. Stanič, J. Stasielak, P. Stassi, A. Streich, M. Suárez-Durán, T. Sudholz, T. Suomijärvi, A. D. Supanitsky, Z. Szadkowski, A. Tapia, C. Taricco, C. Timmermans, O. Tkachenko, P. Tobiska, C. J. Todero Peixoto, B. Tomé, Z. Torrès, A. Travaini, P. Travnicek, C. Trimarelli, M. Tueros, R. Ulrich, M. Unger, L. Vaclavek, M. Vacula, J. F. Valdés Galicia, L. Valore, E. Varela, A. Vásquez-Ramírez, D. Veberič, C. Ventura, I. D. Vergara Quispe, V. Verzi, J. Vicha, J. Vink, S. Vorobiov, H. Wahlberg, C. Watanabe, A. A. Watson, M. Weber, A. Weindl, L. Wiencke, H. Wilczyński, M. Wirtz, D. Wittkowski, B. Wundheiler, A. Yushkov, O. Zapparrata, E. Zas, D. Zavrtanik, M. Zavrtanik, L. Zehrer, and Pierre Auger Collaboration, "The energy spectrum of cosmic rays beyond the turn-down around 10^{17} eV as measured with the surface detector of the Pierre Auger Observatory," European Physical Journal C **81**, 966 (2021), arXiv:2109.13400 [astro-ph.HE] .

[6] J. W. Cronin, T. K. Gaisser, and S. P. Swordy, "Cosmic Rays at the Energy

Frontier," Scientific American **276**, 44 (1997).

[7] J. Blümer, R. Engel, and J. R. Hörandel, "Cosmic rays from the knee to the highest energies," Progress in Particle and Nuclear Physics **63**, 293 (2009), arXiv:0904.0725 [astro-ph.HE] .

[8] E. Cappellaro and M. Turatto, "Supernova Types and Rates," in *The Influence of Binaries on Stellar Population Studies*, Astrophysics and Space Science Library, Vol. 264, edited by D. Vanbeveren (2001) p. 199, arXiv:astro-ph/0012455 [astro-ph] .

[9] M. Turatto, "Classification of Supernovae," in *Supernovae and Gamma-Ray Bursters*, Vol. 598, edited by K. Weiler (2003) pp. 21–36.

[10] R. Antonucci, "Unified models for active galactic nuclei and quasars." Annu. Rev. Astron. Astrophys **31**, 473 (1993).

[11] C. M. Urry and P. Padovani, "Unified Schemes for Radio-Loud Active Galactic Nuclei," Publications of the Astronomical Society of the Pacific **107**, 803 (1995), arXiv:astro-ph/9506063 [astro-ph] .

[12] B. Zhang, *The physics of gamma-ray bursts* (2019).

[13] E. Costa, F. Frontera, J. Heise, M. Feroci, J. in't Zand, F. Fiore, M. N. Cinti, D. Dal Fiume, L. Nicastro, M. Orlandini, E. Palazzi, M. Rapisarda#, G. Zavattini, R. Jager, A. Parmar, A. Owens, S. Molendi, G. Cusumano, M. C. Maccarone, S. Giarrusso, A. Coletta, L. A. Antonelli, P. Giommi, J. M. Muller, L. Piro, and R. C. Butler, "Discovery of an X-ray afterglow associated with the γ-ray burst of 28 February 1997," Nature **387**, 783 (1997), arXiv:astro-ph/9706065 [astro-ph] .

[14] E. Ruiz Velasco, *Search and first detection of very-high-energy photons in gamma-ray bursts: an analysis with HAWC and H.E.S.S.*, Ph.D. thesis, Ruprecht-Karls University of Heidelberg, Germany (2021).

[15] S. Ohm, *Development of an Advanced gamma/hadron separation technique and application to particular gamma-ray sources with H.E.S.S.*, Ph.D. thesis, Ruprecht-Karls University of Heidelberg, Germany (2010).

[16] A. Jardin-Blicq, *The TeV gamma-ray emission of the Galactic Plane. HAWC and H.E.S.S. observations of the Galactic Plane and detailed study of the region surrounding 2HWC J1928+177*, Ph.D. thesis, Ruprecht-Karls University of Heidelberg, Germany (2019).

[17] A. Mignone, T. Plewa, and G. Bodo, "The Piecewise Parabolic Method for Multidimensional Relativistic Fluid Dynamics," The Astrophysical Journal Supplement **160**, 199 (2005), arXiv:astro-ph/0505200 [astro-ph] .

[18] E. Fermi, "On the Origin of the Cosmic Radiation," Physical Review **75**, 1169 (1949).

[19] J. G. Kirk, "Particle Acceleration (With 26 figures)," in *Saas-Fee Advanced Course 24: Plasma Astrophysics* (1994) p. 225.

[20] A. R. Bell, "The acceleration of cosmic rays in shock fronts - II." Mon. Not. R. Astron. Soc. **182**, 443 (1978).

[21] A. R. Bell, “The acceleration of cosmic rays in shock fronts - I.” Mon. Not. R. Astron. Soc. **182**, 147 (1978).

[22] G. F. Krymskii, “A regular mechanism for the acceleration of charged particles on the front of a shock wave,” Akademiia Nauk SSSR Doklady **234**, 1306 (1977).

[23] W. I. Axford, E. Leer, and G. Skadron, “The Acceleration of Cosmic Rays by Shock Waves,” in *International Cosmic Ray Conference*, International Cosmic Ray Conference, Vol. 11 (1977) p. 132.

[24] R. D. Blandford and J. P. Ostriker, “Particle acceleration by astrophysical shocks.” The Astrophysical Journal Letter **221**, L29 (1978).

[25] R. M. Kulsrud, *Plasma Physics for Astrophysics* (2004).

[26] A. Achterberg, Y. A. Gallant, J. G. Kirk, and A. W. Guthmann, “Particle acceleration by ultrarelativistic shocks: theory and simulations,” Mon. Not. R. Astron. Soc. **328**, 393 (2001), arXiv:astro-ph/0107530 [astro-ph] .

[27] Y. A. Gallant and A. Achterberg, “Ultra-high-energy cosmic ray acceleration by relativistic blast waves,” Mon. Not. R. Astron. Soc. **305**, L6 (1999), arXiv:astro-ph/9812316 [astro-ph] .

[28] J. G. Kirk, R. Schlickeiser, and P. Schneider, “Cosmic-Ray Transport in Accelerating Flows,” The Astrophysical Journal **328**, 269 (1988).

[29] J. G. Kirk and P. Schneider, “Particle acceleration at modified shock fronts. II - The problem of injection,” Astronomy and Astrophysics **225**, 559 (1989).

[30] J. G. Kirk, A. W. Guthmann, Y. A. Gallant, and A. Achterberg, “Particle Acceleration at Ultrarelativistic Shocks: An Eigenfunction Method,” The Astrophysical Journal **542**, 235 (2000), arXiv:astro-ph/0005222 [astro-ph] .

[31] A. Vanthieghem, M. Lemoine, I. Plotnikov, A. Grassi, M. Grech, L. Gremillet, and G. Pelletier, “Physics and Phenomenology of Weakly Magnetized, Relativistic Astrophysical Shock Waves,” Galaxies **8**, 33 (2020), arXiv:2002.01141 [astro-ph.HE] .

[32] L. Sironi, I. Plotnikov, J. Nättilä, and A. M. Beloborodov, “Coherent Electromagnetic Emission from Relativistic Magnetized Shocks,” Physical Review L **127**, 035101 (2021), arXiv:2107.01211 [astro-ph.HE] .

[33] V. Bresci, M. Lemoine, and L. Gremillet, “Particle acceleration at magnetized, relativistic turbulent shock fronts,” arXiv e-prints , arXiv:2303.11394 (2023), arXiv:2303.11394 [astro-ph.HE] .

[34] L. Sironi, A. Spitkovsky, and J. Arons, “The Maximum Energy of Accelerated Particles in Relativistic Collisionless Shocks,” The Astrophysical Journal **771**, 54 (2013), arXiv:1301.5333 [astro-ph.HE] .

[35] A. M. Hillas, “The Origin of Ultra-High-Energy Cosmic Rays,” Annu. Rev. Astron. Astrophys **22**, 425 (1984).

[36] K. Kotera and A. V. Olinto, “The Astrophysics of Ultrahigh-Energy Cosmic Rays,” Annu. Rev. Astron. Astrophys **49**, 119 (2011), arXiv:1101.4256 [astro-ph.HE] .

[37] M. Lemoine and G. Pelletier, "On electromagnetic instabilities at ultra-relativistic shock waves," Mon. Not. R. Astron. Soc. **402**, 321 (2010), arXiv:0904.2657 [astro-ph.HE] .

[38] J. G. Kirk and B. Reville, "Radiative Signatures of Relativistic Shocks," The Astrophysical Journal Letter **710**, L16 (2010), arXiv:1001.0687 [astro-ph.HE] .

[39] G. B. Rybicki and A. P. Lightman, *Radiative processes in astrophysics* (1979).

[40] F. C. Jones, "Calculated Spectrum of Inverse-Compton-Scattered Photons," Physical Review **167**, 1159 (1968).

[41] G. R. Blumenthal and R. J. Gould, "Bremsstrahlung, Synchrotron Radiation, and Compton Scattering of High-Energy Electrons Traversing Dilute Gases," Reviews of Modern Physics **42**, 237 (1970).

[42] J. Goodman, "Are gamma-ray bursts optically thick?" The Astrophysical Journal Letter **308**, L47 (1986).

[43] B. Paczynski, "Gamma-ray bursters at cosmological distances," The Astrophysical Journal Letter **308**, L43 (1986).

[44] G. Cavallo and M. J. Rees, "A qualitative study of cosmic fireballs and gamma -ray bursts." Mon. Not. R. Astron. Soc. **183**, 359 (1978).

[45] M. S. Briggs, W. S. Paciesas, G. N. Pendleton, C. A. Meegan, G. J. Fishman, J. M. Horack, M. N. Brock, C. Kouveliotou, D. H. Hartmann, and J. Hakkila, "BATSE Observations of the Large-Scale Isotropy of Gamma-Ray Bursts," The Astrophysical Journal **459**, 40 (1996), arXiv:astro-ph/9509078 [astro-ph] .

[46] C. A. Meegan, G. J. Fishman, R. B. Wilson, W. S. Paciesas, G. N. Pendleton, J. M. Horack, M. N. Brock, and C. Kouveliotou, "Spatial distribution of γ-ray bursts observed by BATSE," Nature **355**, 143 (1992).

[47] C. Kouveliotou, C. A. Meegan, G. J. Fishman, N. P. Bhat, M. S. Briggs, T. M. Koshut, W. S. Paciesas, and G. N. Pendleton, "Identification of Two Classes of Gamma-Ray Bursts," The Astrophysical Journal Letter **413**, L101 (1993).

[48] J. van Paradijs, P. J. Groot, T. Galama, C. Kouveliotou, R. G. Strom, J. Telting, R. G. M. Rutten, G. J. Fishman, C. A. Meegan, M. Pettini, N. Tanvir, J. Bloom, H. Pedersen, H. U. Nørdgaard-Nielsen, M. Linden-Vørnle, J. Melnick, G. Van der Steene, M. Bremer, R. Naber, J. Heise, J. in't Zand, E. Costa, M. Feroci, L. Piro, F. Frontera, G. Zavattini, L. Nicastro, E. Palazzi, K. Bennett, L. Hanlon, and A. Parmar, "Transient optical emission from the error box of the γ-ray burst of 28 February 1997," Nature **386**, 686 (1997).

[49] D. A. Frail, S. R. Kulkarni, L. Nicastro, M. Feroci, and G. B. Taylor, "The radio afterglow from the γ-ray burst of 8 May 1997," Nature **389**, 261 (1997).

[50] M. R. Metzger, S. G. Djorgovski, S. R. Kulkarni, C. C. Steidel, K. L. Adelberger, D. A. Frail, E. Costa, and F. Frontera, "Spectral constraints on the redshift of the optical counterpart to the γ-ray burst of 8 May 1997," Nature **387**, 878 (1997).

[51] T. J. Galama, P. M. Vreeswijk, J. van Paradijs, C. Kouveliotou, T. Augusteijn, H. Böhnhardt, J. P. Brewer, V. Doublier, J. F. Gonzalez, B. Leibundgut, C. Lidman, O. R. Hainaut, F. Patat, J. Heise, J. in't Zand, K. Hurley, P. J. Groot, R. G. Strom, P. A. Mazzali, K. Iwamoto, K. Nomoto, H. Umeda, T. Nakamura, T. R. Young, T. Suzuki, T. Shigeyama, T. Koshut, M. Kippen, C. Robinson, P. de Wildt, R. A. M. J. Wijers, N. Tanvir, J. Greiner, E. Pian, E. Palazzi, F. Frontera, N. Masetti, L. Nicastro, M. Feroci, E. Costa, L. Piro, B. A. Peterson, C. Tinney, B. Boyle, R. Cannon, R. Stathakis, E. Sadler, M. C. Begam, and P. Ianna, "An unusual supernova in the error box of the γ-ray burst of 25 April 1998," Nature **395**, 670 (1998), arXiv:astro-ph/9806175 [astro-ph] .

[52] S. R. Kulkarni, D. A. Frail, M. H. Wieringa, R. D. Ekers, E. M. Sadler, R. M. Wark, J. L. Higdon, E. S. Phinney, and J. S. Bloom, "Radio emission from the unusual supernova 1998bw and its association with the γ-ray burst of 25 April 1998," Nature **395**, 663 (1998).

[53] K. Z. Stanek, T. Matheson, P. M. Garnavich, P. Martini, P. Berlind, N. Caldwell, P. Challis, W. R. Brown, R. Schild, K. Krisciunas, M. L. Calkins, J. C. Lee, N. Hathi, R. A. Jansen, R. Windhorst, L. Echevarria, D. J. Eisenstein, B. Pindor, E. W. Olszewski, P. Harding, S. T. Holland, and D. Bersier, "Spectroscopic Discovery of the Supernova 2003dh Associated with GRB 030329," The Astrophysical Journal Letter **591**, L17 (2003), arXiv:astro-ph/0304173 [astro-ph] .

[54] J. Hjorth, J. Sollerman, P. Møller, J. P. U. Fynbo, S. E. Woosley, C. Kouveliotou, N. R. Tanvir, J. Greiner, M. I. Andersen, A. J. Castro-Tirado, J. M. Castro Cerón, A. S. Fruchter, J. Gorosabel, P. Jakobsson, L. Kaper, S. Klose, N. Masetti, H. Pedersen, K. Pedersen, E. Pian, E. Palazzi, J. E. Rhoads, E. Rol, E. P. J. van den Heuvel, P. M. Vreeswijk, D. Watson, and R. A. M. J. Wijers, "A very energetic supernova associated with the γ-ray burst of 29 March 2003," Nature **423**, 847 (2003), arXiv:astro-ph/0306347 [astro-ph] .

[55] A. I. MacFadyen and S. E. Woosley, "Collapsars: Gamma-Ray Bursts and Explosions in "Failed Supernovae"," The Astrophysical Journal **524**, 262 (1999), arXiv:astro-ph/9810274 [astro-ph] .

[56] P. Mészáros, "γ-ray bursts: The supernova connection," Nature **423**, 809 (2003).

[57] S. D. Barthelmy, L. M. Barbier, J. R. Cummings, E. E. Fenimore, N. Gehrels, D. Hullinger, H. A. Krimm, C. B. Markwardt, D. M. Palmer, A. Parsons, G. Sato, M. Suzuki, T. Takahashi, M. Tashiro, and J. Tueller, "The Burst Alert Telescope (BAT) on the SWIFT Midex Mission," Space Science Reviews **120**, 143 (2005), arXiv:astro-ph/0507410 [astro-ph] .

[58] D. N. Burrows, J. E. Hill, J. A. Nousek, J. A. Kennea, A. Wells, J. P. Osborne, A. F. Abbey, A. Beardmore, K. Mukerjee, A. D. T. Short, G. Chincarini, S. Campana, O. Citterio, A. Moretti, C. Pagani, G. Tagliaferri, P. Giommi, M. Capalbi, F. Tamburelli, L. Angelini, G. Cusumano, H. W. Bräuninger, W. Burkert, and G. D. Hartner, "The Swift X-Ray Telescope," Space Science Reviews **120**, 165 (2005), arXiv:astro-ph/0508071 [astro-ph] .

[59] P. W. A. Roming, T. E. Kennedy, K. O. Mason, J. A. Nousek, L. Ahr, R. E. Bingham, P. S. Broos, M. J. Carter, B. K. Hancock, H. E. Huckle, S. D. Hunsberger,

H. Kawakami, R. Killough, T. S. Koch, M. K. McLelland, K. Smith, P. J. Smith, J. C. Soto, P. T. Boyd, A. A. Breeveld, S. T. Holland, M. Ivanushkina, M. S. Pryzby, M. D. Still, and J. Stock, "The Swift Ultra-Violet/Optical Telescope," Space Science Reviews **120**, 95 (2005), arXiv:astro-ph/0507413 [astro-ph] .

[60] N. Gehrels, C. L. Sarazin, P. T. O'Brien, B. Zhang, L. Barbier, S. D. Barthelmy, A. Blustin, D. N. Burrows, J. Cannizzo, J. R. Cummings, M. Goad, S. T. Holland, C. P. Hurkett, J. A. Kennea, A. Levan, C. B. Markwardt, K. O. Mason, P. Meszaros, M. Page, D. M. Palmer, E. Rol, T. Sakamoto, R. Willingale, L. Angelini, A. Beardmore, P. T. Boyd, A. Breeveld, S. Campana, M. M. Chester, G. Chincarini, L. R. Cominsky, G. Cusumano, M. de Pasquale, E. E. Fenimore, P. Giommi, C. Gronwall, D. Grupe, J. E. Hill, D. Hinshaw, J. Hjorth, D. Hullinger, K. C. Hurley, S. Klose, S. Kobayashi, C. Kouveliotou, H. A. Krimm, V. Mangano, F. E. Marshall, K. McGowan, A. Moretti, R. F. Mushotzky, K. Nakazawa, J. P. Norris, J. A. Nousek, J. P. Osborne, K. Page, A. M. Parsons, S. Patel, M. Perri, T. Poole, P. Romano, P. W. A. Roming, S. Rosen, G. Sato, P. Schady, A. P. Smale, J. Sollerman, R. Starling, M. Still, M. Suzuki, G. Tagliaferri, T. Takahashi, M. Tashiro, J. Tueller, A. A. Wells, N. E. White, and R. A. M. J. Wijers, "A short γ-ray burst apparently associated with an elliptical galaxy at redshift z = 0.225," Nature **437**, 851 (2005), arXiv:astro-ph/0505630 [astro-ph] .

[61] J. S. Bloom, J. X. Prochaska, D. Pooley, C. H. Blake, R. J. Foley, S. Jha, E. Ramirez-Ruiz, J. Granot, A. V. Filippenko, S. Sigurdsson, A. J. Barth, H. W. Chen, M. C. Cooper, E. E. Falco, R. R. Gal, B. F. Gerke, M. D. Gladders, J. E. Greene, J. Hennanwi, L. C. Ho, K. Hurley, B. P. Koester, W. Li, L. Lubin, J. Newman, D. A. Perley, G. K. Squires, and W. M. Wood-Vasey, "Closing in on a Short-Hard Burst Progenitor: Constraints from Early-Time Optical Imaging and Spectroscopy of a Possible Host Galaxy of GRB 050509b," The Astrophysical Journal **638**, 354 (2006), arXiv:astro-ph/0505480 [astro-ph] .

[62] Z. Cao, "An ultra-high-energy γ-ray telescope at 4,410 m," Nature Astronomy **5**, 849 (2021).

[63] J. Pretz, "Highlights from the High Altitude Water Cherenkov Observatory," in *34th International Cosmic Ray Conference (ICRC2015)*, International Cosmic Ray Conference, Vol. 34 (2015) p. 25, arXiv:1509.07851 [astro-ph.HE] .

[64] A. S. Fruchter, A. J. Levan, L. Strolger, P. M. Vreeswijk, S. E. Thorsett, D. Bersier, I. Burud, J. M. Castro Cerón, A. J. Castro-Tirado, C. Conselice, T. Dahlen, H. C. Ferguson, J. P. U. Fynbo, P. M. Garnavich, R. A. Gibbons, J. Gorosabel, T. R. Gull, J. Hjorth, S. T. Holland, C. Kouveliotou, Z. Levay, M. Livio, M. R. Metzger, P. E. Nugent, L. Petro, E. Pian, J. E. Rhoads, A. G. Riess, K. C. Sahu, A. Smette, N. R. Tanvir, R. A. M. J. Wijers, and S. E. Woosley, "Long γ-ray bursts and core-collapse supernovae have different environments," Nature **441**, 463 (2006), arXiv:astro-ph/0603537 [astro-ph] .

[65] J. P. U. Fynbo, P. Jakobsson, P. Møller, J. Hjorth, B. Thomsen, M. I. Andersen, A. S. Fruchter, J. Gorosabel, S. T. Holland, C. Ledoux, H. Pedersen, J. Rhoads, M. Weidinger, and R. A. M. J. Wijers, "On the Lyalpha emission from gamma-ray burst host galaxies: Evidence for low metallicities," Astronomy and Astrophysics **406**, L63 (2003), arXiv:astro-ph/0306403 [astro-ph] .

[66] J. X. Prochaska, J. S. Bloom, H.-W. Chen, K. C. Hurley, J. Melbourne, A. Dressler, J. R. Graham, D. J. Osip, and W. D. Vacca, "The Host Galaxy of GRB 031203: Implications of Its Low Metallicity, Low Redshift, and Starburst Nature," The Astrophysical Journal **611**, 200 (2004), arXiv:astro-ph/0402085 [astro-ph] .

[67] Y. Niino, K. Nagamine, and B. Zhang, "Metallicity measurements of gamma-ray burst and supernova explosion sites: lessons from H II regions in M31," Mon. Not. R. Astron. Soc. **449**, 2706 (2015), arXiv:1408.7059 [astro-ph.HE] .

[68] L.-X. Li and B. Paczyński, "Transient Events from Neutron Star Mergers," The Astrophysical Journal Letter **507**, L59 (1998), arXiv:astro-ph/9807272 [astro-ph] .

[69] B. D. Metzger, G. Martínez-Pinedo, S. Darbha, E. Quataert, A. Arcones, D. Kasen, R. Thomas, P. Nugent, I. V. Panov, and N. T. Zinner, "Electromagnetic counterparts of compact object mergers powered by the radioactive decay of r-process nuclei," Mon. Not. R. Astron. Soc. **406**, 2650 (2010), arXiv:1001.5029 [astro-ph.HE] .

[70] S. R. Kulkarni, "Modeling Supernova-like Explosions Associated with Gamma-ray Bursts with Short Durations," arXiv e-prints , astro-ph/0510256 (2005), arXiv:astro-ph/0510256 [astro-ph] .

[71] J. Barnes and D. Kasen, "Effect of a High Opacity on the Light Curves of Radioactively Powered Transients from Compact Object Mergers," The Astrophysical Journal **775**, 18 (2013), arXiv:1303.5787 [astro-ph.HE] .

[72] M. Tanaka and K. Hotokezaka, "Radiative Transfer Simulations of Neutron Star Merger Ejecta," The Astrophysical Journal **775**, 113 (2013), arXiv:1306.3742 [astro-ph.HE] .

[73] C. N. Leibler and E. Berger, "The Stellar Ages and Masses of Short Gamma-ray Burst Host Galaxies: Investigating the Progenitor Delay Time Distribution and the Role of Mass and Star Formation in the Short Gamma-ray Burst Rate," The Astrophysical Journal **725**, 1202 (2010), arXiv:1009.1147 [astro-ph.HE] .

[74] E. Berger, "Short-Duration Gamma-Ray Bursts," Annu. Rev. Astron. Astrophys **52**, 43 (2014), arXiv:1311.2603 [astro-ph.HE] .

[75] S. D. Barthelmy, G. Chincarini, D. N. Burrows, N. Gehrels, S. Covino, A. Moretti, P. Romano, P. T. O'Brien, C. L. Sarazin, C. Kouveliotou, M. Goad, S. Vaughan, G. Tagliaferri, B. Zhang, L. A. Antonelli, S. Campana, J. R. Cummings, P. D'Avanzo, M. B. Davies, P. Giommi, D. Grupe, Y. Kaneko, J. A. Kennea, A. King, S. Kobayashi, A. Melandri, P. Meszaros, J. A. Nousek, S. Patel, T. Sakamoto, and R. A. M. J. Wijers, "An origin for short γ-ray bursts unassociated with current star formation," Nature **438**, 994 (2005), arXiv:astro-ph/0511579 [astro-ph] .

[76] biB. P. Abbott, R. Abbott, T. D. Abbott, F. Acernese, K. Ackley, C. Adams, T. Adams, P. Addesso, R. X. Adhikari, V. B. Adya, C. Affeldt, M. Afrough, B. Agarwal, M. Agathos, K. Agatsuma, N. Aggarwal, O. D. Aguiar, L. Aiello, A. Ain, P. Ajith, B. Allen, G. Allen, A. Allocca, P. A. Altin, A. Amato,

A. Ananyeva, S. B. Anderson, W. G. Anderson, S. V. Angelova, S. Antier, S. Appert, K. Arai, M. C. Araya, J. S. Areeda, N. Arnaud, K. G. Arun, S. Ascenzi, G. Ashton, M. Ast, S. M. Aston, P. Astone, D. V. Atallah, P. Aufmuth, C. Aulbert, K. AultONeal, C. Austin, A. Avila-Alvarez, S. Babak, P. Bacon, M. K. M. Bader, S. Bae, M. Bailes, P. T. Baker, F. Baldaccini, G. Ballardin, S. W. Ballmer, S. Banagiri, J. C. Barayoga, S. E. Barclay, B. C. Barish, D. Barker, K. Barkett, F. Barone, B. Barr, L. Barsotti, M. Barsuglia, D. Barta, S. D. Barthelmy, J. Bartlett, I. Bartos, R. Bassiri, A. Basti, J. C. Batch, M. Bawaj, J. C. Bayley, M. Bazzan, B. Bécsy, C. Beer, M. Bejger, I. Belahcene, A. S. Bell, B. K. Berger, G. Bergmann, S. Bernuzzi, J. J. Bero, C. P. L. Berry, D. Bersanetti, A. Bertolini, J. Betzwieser, S. Bhagwat, R. Bhandare, I. A. Bilenko, G. Billingsley, C. R. Billman, J. Birch, R. Birney, O. Birnholtz, S. Biscans, S. Biscoveanu, A. Bisht, M. Bitossi, C. Biwer, M. A. Bizouard, J. K. Blackburn, J. Blackman, C. D. Blair, D. G. Blair, R. M. Blair, S. Bloemen, O. Bock, N. Bode, M. Boer, G. Bogaert, A. Bohe, F. Bondu, E. Bonilla, R. Bonnand, B. A. Boom, R. Bork, V. Boschi, S. Bose, K. Bossie, Y. Bouffanais, A. Bozzi, C. Bradaschia, P. R. Brady, M. Branchesi, J. E. Brau, T. Briant, A. Brillet, M. Brinkmann, V. Brisson, P. Brockill, J. E. Broida, A. F. Brooks, D. A. Brown, D. D. Brown, S. Brunett, C. C. Buchanan, A. Buikema, T. Bulik, H. J. Bulten, A. Buonanno, D. Buskulic, C. Buy, R. L. Byer, M. Cabero, L. Cadonati, G. Cagnoli, C. Cahillane, J. Calderón Bustillo, T. A. Callister, E. Calloni, J. B. Camp, M. Canepa, P. Canizares, K. C. Cannon, H. Cao, J. Cao, C. D. Capano, E. Capocasa, F. Carbognani, S. Caride, M. F. Carney, G. Carullo, J. Casanueva Diaz, C. Casentini, S. Caudill, M. Cavaglià, F. Cavalier, R. Cavalieri, G. Cella, C. B. Cepeda, P. Cerdá-Durán, G. Cerretani, E. Cesarini, S. J. Chamberlin, M. Chan, S. Chao, P. Charlton, E. Chase, E. Chassande-Mottin, D. Chatterjee, K. Chatziioannou, B. D. Cheeseboro, H. Y. Chen, X. Chen, Y. Chen, H. P. Cheng, H. Chia, A. Chincarini, A. Chiummo, T. Chmiel, H. S. Cho, M. Cho, J. H. Chow, N. Christensen, Q. Chu, A. J. K. Chua, S. Chua, A. K. W. Chung, S. Chung, G. Ciani, R. Ciolfi, C. E. Cirelli, A. Cirone, F. Clara, J. A. Clark, P. Clearwater, F. Cleva, C. Cocchieri, E. Coccia, P. F. Cohadon, D. Cohen, A. Colla, C. G. Collette, L. R. Cominsky, M. Constancio, L. Conti, S. J. Cooper, P. Corban, T. R. Corbitt, I. Cordero-Carrión, K. R. Corley, N. Cornish, A. Corsi, S. Cortese, C. A. Costa, M. W. Coughlin, S. B. Coughlin, J. P. Coulon, S. T. Countryman, P. Couvares, P. B. Covas, E. E. Cowan, D. M. Coward, M. J. Cowart, D. C. Coyne, R. Coyne, J. D. E. Creighton, T. D. Creighton, J. Cripe, S. G. Crowder, T. J. Cullen, A. Cumming, L. Cunningham, E. Cuoco, T. Dal Canton, G. Dálya, S. L. Danilishin, S. D'Antonio, K. Danzmann, A. Dasgupta, C. F. Da Silva Costa, V. Dattilo, I. Dave, M. Davier, D. Davis, E. J. Daw, B. Day, S. De, D. DeBra, J. Degallaix, M. De Laurentis, S. Deléglise, W. Del Pozzo, N. Demos, T. Denker, T. Dent, R. De Pietri, V. Dergachev, R. De Rosa, R. T. DeRosa, C. De Rossi, R. DeSalvo, O. de Varona, J. Devenson, S. Dhurandhar, M. C. Díaz, T. Dietrich, L. Di Fiore, M. Di Giovanni, T. Di Girolamo, A. Di Lieto, S. Di Pace, I. Di Palma, F. Di Renzo, Z. Doctor, V. Dolique, F. Donovan, K. L. Dooley, S. Doravari, I. Dorrington, R. Douglas, M. Dovale Álvarez, T. P. Downes, M. Drago, C. Dreissigacker, J. C. Driggers, Z. Du, M. Ducrot, R. Dudi, P. Dupej, S. E. Dwyer, T. B. Edo, M. C. Edwards, A. Effler, H. B. Eggenstein, P. Ehrens, J. Eichholz, S. S. Eikenberry, R. A. Eisenstein, R. C. Essick, D. Estevez, Z. B. Etienne, T. Etzel, M. Evans, T. M. Evans, M. Factourovich, V. Fafone, H. Fair, S. Fairhurst, X. Fan, S. Farinon, B. Farr, W. M. Farr, E. J. Fauchon-Jones, M. Favata, M. Fays,

C. Fee, H. Fehrmann, J. Feicht, M. M. Fejer, A. Fernandez-Galiana, I. Ferrante, E. C. Ferreira, F. Ferrini, F. Fidecaro, D. Finstad, I. Fiori, D. Fiorucci, M. Fishbach, R. P. Fisher, M. Fitz-Axen, R. Flaminio, M. Fletcher, H. Fong, J. A. Font, P. W. F. Forsyth, S. S. Forsyth, J. D. Fournier, S. Frasca, F. Frasconi, Z. Frei, A. Freise, R. Frey, V. Frey, E. M. Fries, P. Fritschel, V. V. Frolov, P. Fulda, M. Fyffe, H. Gabbard, B. U. Gadre, S. M. Gaebel, J. R. Gair, L. Gammaitoni, M. R. Ganija, S. G. Gaonkar, C. Garcia-Quiros, F. Garufi, B. Gateley, S. Gaudio, G. Gaur, V. Gayathri, N. Gehrels, G. Gemme, E. Genin, A. Gennai, D. George, J. George, L. Gergely, V. Germain, S. Ghonge, A. Ghosh, A. Ghosh, S. Ghosh, J. A. Giaime, K. D. Giardina, A. Giazotto, K. Gill, L. Glover, E. Goetz, R. Goetz, S. Gomes, B. Goncharov, G. González, J. M. Gonzalez Castro, A. Gopakumar, M. L. Gorodetsky, S. E. Gossan, M. Gosselin, R. Gouaty, A. Grado, C. Graef, M. Granata, A. Grant, S. Gras, C. Gray, G. Greco, A. C. Green, E. M. Gretarsson, P. Groot, H. Grote, S. Grunewald, P. Gruning, G. M. Guidi, X. Guo, A. Gupta, M. K. Gupta, K. E. Gushwa, E. K. Gustafson, R. Gustafson, O. Halim, B. R. Hall, E. D. Hall, E. Z. Hamilton, G. Hammond, M. Haney, M. M. Hanke, J. Hanks, C. Hanna, M. D. Hannam, O. A. Hannuksela, J. Hanson, T. Hardwick, J. Harms, G. M. Harry, I. W. Harry, M. J. Hart, C. J. Haster, K. Haughian, J. Healy, A. Heidmann, M. C. Heintze, H. Heitmann, P. Hello, G. Hemming, M. Hendry, I. S. Heng, J. Hennig, A. W. Heptonstall, M. Heurs, S. Hild, T. Hinderer, W. C. G. Ho, D. Hoak, D. Hofman, K. Holt, D. E. Holz, P. Hopkins, C. Horst, J. Hough, E. A. Houston, E. J. Howell, A. Hreibi, Y. M. Hu, E. A. Huerta, D. Huet, B. Hughey, S. Husa, S. H. Huttner, T. Huynh-Dinh, N. Indik, R. Inta, G. Intini, H. N. Isa, J. M. Isac, M. Isi, B. R. Iyer, K. Izumi, T. Jacqmin, K. Jani, P. Jaranowski, S. Jawahar, F. Jiménez-Forteza, W. W. Johnson, N. K. Johnson-McDaniel, D. I. Jones, R. Jones, R. J. G. Jonker, L. Ju, J. Junker, C. V. Kalaghatgi, V. Kalogera, B. Kamai, S. Kandhasamy, G. Kang, J. B. Kanner, S. J. Kapadia, S. Karki, K. S. Karvinen, M. Kasprzack, W. Kastaun, M. Katolik, E. Katsavounidis, W. Katzman, S. Kaufer, K. Kawabe, F. Kéfélian, D. Keitel, A. J. Kemball, R. Kennedy, C. Kent, J. S. Key, F. Y. Khalili, I. Khan, S. Khan, Z. Khan, E. A. Khazanov, N. Kijbunchoo, C. Kim, J. C. Kim, K. Kim, W. Kim, W. S. Kim, Y. M. Kim, S. J. Kimbrell, E. J. King, P. J. King, M. Kinley-Hanlon, R. Kirchhoff, J. S. Kissel, L. Kleybolte, S. Klimenko, T. D. Knowles, P. Koch, S. M. Koehlenbeck, S. Koley, V. Kondrashov, A. Kontos, M. Korobko, W. Z. Korth, I. Kowalska, D. B. Kozak, C. Krämer, V. Kringel, B. Krishnan, A. Królak, G. Kuehn, P. Kumar, R. Kumar, S. Kumar, L. Kuo, A. Kutynia, S. Kwang, B. D. Lackey, K. H. Lai, M. Landry, R. N. Lang, J. Lange, B. Lantz, R. K. Lanza, S. L. Larson, A. Lartaux-Vollard, P. D. Lasky, M. Laxen, A. Lazzarini, C. Lazzaro, P. Leaci, S. Leavey, C. H. Lee, H. K. Lee, H. M. Lee, H. W. Lee, K. Lee, J. Lehmann, A. Lenon, E. Leon, M. Leonardi, N. Leroy, N. Letendre, Y. Levin, T. G. F. Li, S. D. Linker, T. B. Littenberg, J. Liu, X. Liu, R. K. L. Lo, N. A. Lockerbie, L. T. London, J. E. Lord, M. Lorenzini, V. Loriette, M. Lormand, G. Losurdo, J. D. Lough, C. O. Lousto, G. Lovelace, H. Lück, D. Lumaca, A. P. Lundgren, R. Lynch, Y. Ma, R. Macas, S. Macfoy, B. Machenschalk, M. MacInnis, D. M. Macleod, I. Magaña Hernandez, F. Magaña-Sandoval, L. Magaña Zertuche, R. M. Magee, E. Majorana, I. Maksimovic, N. Man, V. Mandic, V. Mangano, G. L. Mansell, M. Manske, M. Mantovani, F. Marchesoni, F. Marion, S. Márka, Z. Márka, C. Markakis, A. S. Markosyan, A. Markowitz, E. Maros, A. Marquina, P. Marsh, F. Martelli, L. Martellini, I. W. Martin, R. M. Martin, D. V. Martynov, J. N. Marx, K. Mason, E. Massera, A. Masserot, T. J.

Massinger, M. Masso-Reid, S. Mastrogiovanni, A. Matas, F. Matichard, L. Matone, N. Mavalvala, N. Mazumder, R. McCarthy, D. E. McClelland, S. McCormick, L. McCuller, S. C. McGuire, G. McIntyre, J. McIver, D. J. McManus, L. McNeill, T. McRae, S. T. McWilliams, D. Meacher, G. D. Meadors, M. Mehmet, J. Meidam, E. Mejuto-Villa, A. Melatos, G. Mendell, R. A. Mercer, E. L. Merilh, M. Merzougui, S. Meshkov, C. Messenger, C. Messick, R. Metzdorff, P. M. Meyers, H. Miao, C. Michel, H. Middleton, E. E. Mikhailov, L. Milano, A. L. Miller, B. B. Miller, J. Miller, M. Millhouse, M. C. Milovich-Goff, O. Minazzoli, Y. Minenkov, J. Ming, C. Mishra, S. Mitra, V. P. Mitrofanov, G. Mitselmakher, R. Mittleman, D. Moffa, A. Moggi, K. Mogushi, M. Mohan, S. R. P. Mohapatra, I. Molina, M. Montani, C. J. Moore, D. Moraru, G. Moreno, S. Morisaki, S. R. Morriss, B. Mours, C. M. Mow-Lowry, G. Mueller, A. W. Muir, A. Mukherjee, D. Mukherjee, S. Mukherjee, N. Mukund, A. Mullavey, J. Munch, E. A. Muñiz, M. Muratore, P. G. Murray, A. Nagar, K. Napier, I. Nardecchia, L. Naticchioni, R. K. Nayak, J. Neilson, G. Nelemans, T. J. N. Nelson, M. Nery, A. Neunzert, L. Nevin, J. M. Newport, G. Newton, K. K. Y. Ng, P. Nguyen, T. T. Nguyen, D. Nichols, A. B. Nielsen, S. Nissanke, A. Nitz, A. Noack, F. Nocera, D. Nolting, C. North, L. K. Nuttall, J. Oberling, G. D. O'Dea, G. H. Ogin, J. J. Oh, S. H. Oh, F. Ohme, M. A. Okada, M. Oliver, P. Oppermann, R. J. Oram, B. O'Reilly, R. Ormiston, L. F. Ortega, R. O'Shaughnessy, S. Ossokine, D. J. Ottaway, H. Overmier, B. J. Owen, A. E. Pace, J. Page, M. A. Page, A. Pai, S. A. Pai, J. R. Palamos, O. Palashov, C. Palomba, A. Pal-Singh, H. Pan, H.-W. Pan, B. Pang, P. T. H. Pang, C. Pankow, F. Pannarale, B. C. Pant, F. Paoletti, A. Paoli, M. A. Papa, A. Parida, W. Parker, D. Pascucci, A. Pasqualetti, R. Passaquieti, D. Passuello, M. Patil, B. Patricelli, B. L. Pearlstone, M. Pedraza, R. Pedurand, L. Pekowsky, A. Pele, S. Penn, C. J. Perez, A. Perreca, L. M. Perri, H. P. Pfeiffer, M. Phelps, O. J. Piccinni, M. Pichot, F. Piergiovanni, V. Pierro, G. Pillant, L. Pinard, I. M. Pinto, M. Pirello, M. Pitkin, M. Poe, R. Poggiani, P. Popolizio, E. K. Porter, A. Post, J. Powell, J. Prasad, J. W. W. Pratt, G. Pratten, V. Predoi, T. Prestegard, M. Prijatelj, M. Principe, S. Privitera, R. Prix, G. A. Prodi, L. G. Prokhorov, O. Puncken, M. Punturo, P. Puppo, M. Pürrer, H. Qi, V. Quetschke, E. A. Quintero, R. Quitzow-James, F. J. Raab, D. S. Rabeling, H. Radkins, P. Raffai, S. Raja, C. Rajan, B. Rajbhandari, M. Rakhmanov, K. E. Ramirez, A. Ramos-Buades, P. Rapagnani, V. Raymond, M. Razzano, J. Read, T. Regimbau, L. Rei, S. Reid, D. H. Reitze, W. Ren, S. D. Reyes, F. Ricci, P. M. Ricker, S. Rieger, K. Riles, M. Rizzo, N. A. Robertson, R. Robie, F. Robinet, A. Rocchi, L. Rolland, J. G. Rollins, V. J. Roma, J. D. Romano, R. Romano, C. L. Romel, J. H. Romie, D. Rosińska, M. P. Ross, S. Rowan, A. Rüdiger, P. Ruggi, G. Rutins, K. Ryan, S. Sachdev, T. Sadecki, L. Sadeghian, M. Sakellariadou, L. Salconi, M. Saleem, F. Salemi, A. Samajdar, L. Sammut, L. M. Sampson, E. J. Sanchez, L. E. Sanchez, N. Sanchis-Gual, V. Sandberg, J. R. Sanders, B. Sassolas, B. S. Sathyaprakash, P. R. Saulson, O. Sauter, R. L. Savage, A. Sawadsky, P. Schale, M. Scheel, J. Scheuer, J. Schmidt, P. Schmidt, R. Schnabel, R. M. S. Schofield, A. Schönbeck, E. Schreiber, D. Schuette, B. W. Schulte, B. F. Schutz, S. G. Schwalbe, J. Scott, S. M. Scott, E. Seidel, D. Sellers, A. S. Sengupta, D. Sentenac, V. Sequino, A. Sergeev, D. A. Shaddock, T. J. Shaffer, A. A. Shah, M. S. Shahriar, M. B. Shaner, L. Shao, B. Shapiro, P. Shawhan, A. Sheperd, D. H. Shoemaker, D. M. Shoemaker, K. Siellez, X. Siemens, M. Sieniawska, D. Sigg, A. D. Silva, L. P. Singer, A. Singh, A. Singhal, A. M. Sintes, B. J. J. Slagmolen, B. Smith, J. R. Smith, R. J. E. Smith, S. Somala, E. J.

Son, J. A. Sonnenberg, B. Sorazu, F. Sorrentino, T. Souradeep, A. P. Spencer, A. K. Srivastava, K. Staats, A. Staley, M. Steinke, J. Steinlechner, S. Steinlechner, D. Steinmeyer, S. P. Stevenson, R. Stone, D. J. Stops, K. A. Strain, G. Stratta, S. E. Strigin, A. Strunk, R. Sturani, A. L. Stuver, T. Z. Summerscales, L. Sun, S. Sunil, J. Suresh, P. J. Sutton, B. L. Swinkels, M. J. Szczepańczyk, M. Tacca, S. C. Tait, C. Talbot, D. Talukder, D. B. Tanner, M. Tápai, A. Taracchini, J. D. Tasson, J. A. Taylor, R. Taylor, S. V. Tewari, T. Theeg, F. Thies, E. G. Thomas, M. Thomas, P. Thomas, K. A. Thorne, K. S. Thorne, E. Thrane, S. Tiwari, V. Tiwari, K. V. Tokmakov, K. Toland, M. Tonelli, Z. Tornasi, A. Torres-Forné, C. I. Torrie, D. Töyrä, F. Travasso, G. Traylor, J. Trinastic, M. C. Tringali, L. Trozzo, K. W. Tsang, M. Tse, R. Tso, L. Tsukada, D. Tsuna, D. Tuyenbayev, K. Ueno, D. Ugolini, C. S. Unnikrishnan, A. L. Urban, S. A. Usman, H. Vahlbruch, G. Vajente, G. Valdes, M. Vallisneri, N. van Bakel, M. van Beuzekom, J. F. J. van den Brand, C. Van Den Broeck, D. C. Vander-Hyde, L. van der Schaaf, J. V. van Heijningen, A. A. van Veggel, M. Vardaro, V. Varma, S. Vass, M. Vasúth, A. Vecchio, G. Vedovato, J. Veitch, P. J. Veitch, K. Venkateswara, G. Venugopalan, D. Verkindt, F. Vetrano, A. Viceré, A. D. Viets, S. Vinciguerra, D. J. Vine, J. Y. Vinet, S. Vitale, T. Vo, H. Vocca, C. Vorvick, S. P. Vyatchanin, A. R. Wade, L. E. Wade, M. Wade, R. Walet, M. Walker, L. Wallace, S. Walsh, G. Wang, H. Wang, J. Z. Wang, W. H. Wang, Y. F. Wang, R. L. Ward, J. Warner, M. Was, J. Watchi, B. Weaver, L. W. Wei, M. Weinert, A. J. Weinstein, R. Weiss, L. Wen, E. K. Wessel, P. Weßels, J. Westerweck, T. Westphal, K. Wette, J. T. Whelan, S. E. Whitcomb, B. F. Whiting, C. Whittle, D. Wilken, D. Williams, R. D. Williams, A. R. Williamson, J. L. Willis, B. Willke, M. H. Wimmer, W. Winkler, C. C. Wipf, H. Wittel, G. Woan, J. Woehler, J. Wofford, K. W. K. Wong, J. Worden, J. L. Wright, D. S. Wu, D. M. Wysocki, S. Xiao, H. Yamamoto, C. C. Yancey, L. Yang, M. J. Yap, M. Yazback, H. Yu, H. Yu, M. Yvert, A. ZadroŻny, M. Zanolin, T. Zelenova, J. P. Zendri, M. Zevin, L. Zhang, M. Zhang, T. Zhang, Y. H. Zhang, C. Zhao, M. Zhou, Z. Zhou, S. J. Zhu, X. J. Zhu, A. B. Zimmerman, M. E. Zucker, J. Zweizig, LIGO Scientific Collaboration, and Virgo Collaboration, "GW170817: Observation of Gravitational Waves from a Binary Neutron Star Inspiral," Physical Review L **119**, 161101 (2017), arXiv:1710.05832 [gr-qc] .

[77] B. P. Abbott, R. Abbott, T. D. Abbott, F. Acernese, K. Ackley, C. Adams, T. Adams, P. Addesso, R. X. Adhikari, V. B. Adya, C. Affeldt, M. Afrough, B. Agarwal, M. Agathos, K. Agatsuma, N. Aggarwal, O. D. Aguiar, L. Aiello, A. Ain, P. Ajith, B. Allen, G. Allen, A. Allocca, M. A. Aloy, P. A. Altin, A. Amato, A. Ananyeva, S. B. Anderson, W. G. Anderson, S. V. Angelova, S. Antier, S. Appert, K. Arai, M. C. Araya, J. S. Areeda, N. Arnaud, K. G. Arun, S. Ascenzi, G. Ashton, M. Ast, S. M. Aston, P. Astone, D. V. Atallah, P. Aufmuth, C. Aulbert, K. AultONeal, C. Austin, A. Avila-Alvarez, S. Babak, P. Bacon, M. K. M. Bader, S. Bae, P. T. Baker, F. Baldaccini, G. Ballardin, S. W. Ballmer, S. Banagiri, J. C. Barayoga, S. E. Barclay, B. C. Barish, D. Barker, K. Barkett, F. Barone, B. Barr, L. Barsotti, M. Barsuglia, D. Barta, J. Bartlett, I. Bartos, R. Bassiri, A. Basti, J. C. Batch, M. Bawaj, J. C. Bayley, M. Bazzan, B. Bécsy, C. Beer, M. Bejger, I. Belahcene, A. S. Bell, B. K. Berger, G. Bergmann, J. J. Bero, C. P. L. Berry, D. Bersanetti, A. Bertolini, J. Betzwieser, S. Bhagwat, R. Bhandare, I. A. Bilenko, G. Billingsley, C. R. Billman, J. Birch, R. Birney, O. Birnholtz, S. Biscans, S. Biscoveanu, A. Bisht, M. Bitossi, C. Biwer, M. A. Bizouard, J. K. Blackburn, J. Blackman, C. D. Blair, D. G. Blair, R. M. Blair, S. Bloemen, O. Bock, N. Bode, M. Boer,

G. Bogaert, A. Bohe, F. Bondu, E. Bonilla, R. Bonnand, B. A. Boom, R. Bork, V. Boschi, S. Bose, K. Bossie, Y. Bouffanais, A. Bozzi, C. Bradaschia, P. R. Brady, M. Branchesi, J. E. Brau, T. Briant, A. Brillet, M. Brinkmann, V. Brisson, P. Brockill, J. E. Broida, A. F. Brooks, D. A. Brown, D. D. Brown, S. Brunett, C. C. Buchanan, A. Buikema, T. Bulik, H. J. Bulten, A. Buonanno, D. Buskulic, C. Buy, R. L. Byer, M. Cabero, L. Cadonati, G. Cagnoli, C. Cahillane, J. Calderón Bustillo, T. A. Callister, E. Calloni, J. B. Camp, M. Canepa, P. Canizares, K. C. Cannon, H. Cao, J. Cao, C. D. Capano, E. Capocasa, F. Carbognani, S. Caride, M. F. Carney, J. Casanueva Diaz, C. Casentini, S. Caudill, M. Cavaglià, F. Cavalier, R. Cavalieri, G. Cella, C. B. Cepeda, P. Cerdá-Durán, G. Cerretani, E. Cesarini, S. J. Chamberlin, M. Chan, S. Chao, P. Charlton, E. Chase, E. Chassande-Mottin, D. Chatterjee, K. Chatziioannou, B. D. Cheeseboro, H. Y. Chen, X. Chen, Y. Chen, H. P. Cheng, H. Chia, A. Chincarini, A. Chiummo, T. Chmiel, H. S. Cho, M. Cho, J. H. Chow, N. Christensen, Q. Chu, A. J. K. Chua, S. Chua, A. K. W. Chung, S. Chung, G. Ciani, R. Ciolfi, C. E. Cirelli, A. Cirone, F. Clara, J. A. Clark, P. Clearwater, F. Cleva, C. Cocchieri, E. Coccia, P. F. Cohadon, D. Cohen, A. Colla, C. G. Collette, L. R. Cominsky, J. Constancio, M., L. Conti, S. J. Cooper, P. Corban, T. R. Corbitt, I. Cordero-Carrión, K. R. Corley, N. Cornish, A. Corsi, S. Cortese, C. A. Costa, M. W. Coughlin, S. B. Coughlin, J. P. Coulon, S. T. Countryman, P. Couvares, P. B. Covas, E. E. Cowan, D. M. Coward, M. J. Cowart, D. C. Coyne, R. Coyne, J. D. E. Creighton, T. D. Creighton, J. Cripe, S. G. Crowder, T. J. Cullen, A. Cumming, L. Cunningham, E. Cuoco, T. Dal Canton, G. Dálya, S. L. Danilishin, S. D'Antonio, K. Danzmann, A. Dasgupta, C. F. Da Silva Costa, V. Dattilo, I. Dave, M. Davier, D. Davis, E. J. Daw, B. Day, S. De, D. DeBra, J. Degallaix, M. De Laurentis, S. Deléglise, W. Del Pozzo, N. Demos, T. Denker, T. Dent, R. De Pietri, V. Dergachev, R. De Rosa, R. T. DeRosa, C. De Rossi, R. DeSalvo, O. de Varona, J. Devenson, S. Dhurandhar, M. C. Díaz, L. Di Fiore, M. Di Giovanni, T. Di Girolamo, A. Di Lieto, S. Di Pace, I. Di Palma, F. Di Renzo, Z. Doctor, V. Dolique, F. Donovan, K. L. Dooley, S. Doravari, I. Dorrington, R. Douglas, M. Dovale Álvarez, T. P. Downes, M. Drago, C. Dreissigacker, J. C. Driggers, Z. Du, M. Ducrot, P. Dupej, S. E. Dwyer, T. B. Edo, M. C. Edwards, A. Effler, H. B. Eggenstein, P. Ehrens, J. Eichholz, S. S. Eikenberry, R. A. Eisenstein, R. C. Essick, D. Estevez, Z. B. Etienne, T. Etzel, M. Evans, T. M. Evans, M. Factourovich, V. Fafone, H. Fair, S. Fairhurst, X. Fan, S. Farinon, B. Farr, W. M. Farr, E. J. Fauchon-Jones, M. Favata, M. Fays, C. Fee, H. Fehrmann, J. Feicht, M. M. Fejer, A. Fernandez-Galiana, I. Ferrante, E. C. Ferreira, F. Ferrini, F. Fidecaro, D. Finstad, I. Fiori, D. Fiorucci, M. Fishbach, R. P. Fisher, M. Fitz-Axen, R. Flaminio, M. Fletcher, H. Fong, J. A. Font, P. W. F. Forsyth, S. S. Forsyth, J. D. Fournier, S. Frasca, F. Frasconi, Z. Frei, A. Freise, R. Frey, V. Frey, E. M. Fries, P. Fritschel, V. V. Frolov, P. Fulda, M. Fyffe, H. Gabbard, B. U. Gadre, S. M. Gaebel, J. R. Gair, L. Gammaitoni, M. R. Ganija, S. G. Gaonkar, C. Garcia-Quiros, F. Garufi, B. Gateley, S. Gaudio, G. Gaur, V. Gayathri, N. Gehrels, G. Gemme, E. Genin, A. Gennai, D. George, J. George, L. Gergely, V. Germain, S. Ghonge, A. Ghosh, A. Ghosh, S. Ghosh, J. A. Giaime, K. D. Giardina, A. Giazotto, K. Gill, L. Glover, E. Goetz, R. Goetz, S. Gomes, B. Goncharov, G. González, J. M. Gonzalez Castro, A. Gopakumar, M. L. Gorodetsky, S. E. Gossan, M. Gosselin, R. Gouaty, A. Grado, C. Graef, M. Granata, A. Grant, S. Gras, C. Gray, G. Greco, A. C. Green, E. M. Gretarsson, P. Groot, H. Grote, S. Grunewald, P. Gruning, G. M. Guidi, X. Guo, A. Gupta,

M. K. Gupta, K. E. Gushwa, E. K. Gustafson, R. Gustafson, O. Halim, B. R. Hall, E. D. Hall, E. Z. Hamilton, G. Hammond, M. Haney, M. M. Hanke, J. Hanks, C. Hanna, M. D. Hannam, O. A. Hannuksela, J. Hanson, T. Hardwick, J. Harms, G. M. Harry, I. W. Harry, M. J. Hart, C. J. Haster, K. Haughian, J. Healy, A. Heidmann, M. C. Heintze, H. Heitmann, P. Hello, G. Hemming, M. Hendry, I. S. Heng, J. Hennig, A. W. Heptonstall, M. Heurs, S. Hild, T. Hinderer, D. Hoak, D. Hofman, K. Holt, D. E. Holz, P. Hopkins, C. Horst, J. Hough, E. A. Houston, E. J. Howell, A. Hreibi, Y. M. Hu, E. A. Huerta, D. Huet, B. Hughey, S. Husa, S. H. Huttner, T. Huynh-Dinh, N. Indik, R. Inta, G. Intini, H. N. Isa, J. M. Isac, M. Isi, B. R. Iyer, K. Izumi, T. Jacqmin, K. Jani, P. Jaranowski, S. Jawahar, F. Jiménez-Forteza, W. W. Johnson, N. K. Johnson-McDaniel, D. I. Jones, R. Jones, R. J. G. Jonker, L. Ju, J. Junker, C. V. Kalaghatgi, V. Kalogera, B. Kamai, S. Kandhasamy, G. Kang, J. B. Kanner, S. J. Kapadia, S. Karki, K. S. Karvinen, M. Kasprzack, W. Kastaun, M. Katolik, E. Katsavounidis, W. Katzman, S. Kaufer, K. Kawabe, F. Kéfélian, D. Keitel, A. J. Kemball, R. Kennedy, C. Kent, J. S. Key, F. Y. Khalili, I. Khan, S. Khan, Z. Khan, E. A. Khazanov, N. Kijbunchoo, C. Kim, J. C. Kim, K. Kim, W. Kim, W. S. Kim, Y. M. Kim, S. J. Kimbrell, E. J. King, P. J. King, M. Kinley-Hanlon, R. Kirchhoff, J. S. Kissel, L. Kleybolte, S. Klimenko, T. D. Knowles, P. Koch, S. M. Koehlenbeck, S. Koley, V. Kondrashov, A. Kontos, M. Korobko, W. Z. Korth, I. Kowalska, D. B. Kozak, C. Krämer, V. Kringel, B. Krishnan, A. Królak, G. Kuehn, P. Kumar, R. Kumar, S. Kumar, L. Kuo, A. Kutynia, S. Kwang, B. D. Lackey, K. H. Lai, M. Landry, R. N. Lang, J. Lange, B. Lantz, R. K. Lanza, A. Lartaux-Vollard, P. D. Lasky, M. Laxen, A. Lazzarini, C. Lazzaro, P. Leaci, S. Leavey, C. H. Lee, H. K. Lee, H. M. Lee, H. W. Lee, K. Lee, J. Lehmann, A. Lenon, M. Leonardi, N. Leroy, N. Letendre, Y. Levin, T. G. F. Li, S. D. Linker, T. B. Littenberg, J. Liu, R. K. L. Lo, N. A. Lockerbie, L. T. London, J. E. Lord, M. Lorenzini, V. Loriette, M. Lormand, G. Losurdo, J. D. Lough, C. O. Lousto, G. Lovelace, H. Lück, D. Lumaca, A. P. Lundgren, R. Lynch, Y. Ma, R. Macas, S. Macfoy, B. Machenschalk, M. MacInnis, D. M. Macleod, I. Magaña Hernandez, F. Magaña-Sandoval, L. Magaña Zertuche, R. M. Magee, E. Majorana, I. Maksimovic, N. Man, V. Mandic, V. Mangano, G. L. Mansell, M. Manske, M. Mantovani, F. Marchesoni, F. Marion, S. Márka, Z. Márka, C. Markakis, A. S. Markosyan, A. Markowitz, E. Maros, A. Marquina, F. Martelli, L. Martellini, I. W. Martin, R. M. Martin, D. V. Martynov, K. Mason, E. Massera, A. Masserot, T. J. Massinger, M. Masso-Reid, S. Mastrogiovanni, A. Matas, F. Matichard, L. Matone, N. Mavalvala, N. Mazumder, R. McCarthy, D. E. McClelland, S. McCormick, L. McCuller, S. C. McGuire, G. McIntyre, J. McIver, D. J. McManus, L. McNeill, T. McRae, S. T. McWilliams, D. Meacher, G. D. Meadors, M. Mehmet, J. Meidam, E. Mejuto-Villa, A. Melatos, G. Mendell, R. A. Mercer, E. L. Merilh, M. Merzougui, S. Meshkov, C. Messenger, C. Messick, R. Metzdorff, P. M. Meyers, H. Miao, C. Michel, H. Middleton, E. E. Mikhailov, L. Milano, A. L. Miller, B. B. Miller, J. Miller, M. Millhouse, M. C. Milovich-Goff, O. Minazzoli, Y. Minenkov, J. Ming, C. Mishra, S. Mitra, V. P. Mitrofanov, G. Mitselmakher, R. Mittleman, D. Moffa, A. Moggi, K. Mogushi, M. Mohan, S. R. P. Mohapatra, M. Montani, C. J. Moore, D. Moraru, G. Moreno, S. R. Morriss, B. Mours, C. M. Mow-Lowry, G. Mueller, A. W. Muir, A. Mukherjee, D. Mukherjee, S. Mukherjee, N. Mukund, A. Mullavey, J. Munch, E. A. Muñiz, M. Muratore, P. G. Murray, K. Napier, I. Nardecchia, L. Naticchioni, R. K. Nayak, J. Neilson, G. Nelemans, T. J. N. Nelson, M. Nery, A. Neunzert, L. Nevin, J. M.

Newport, G. Newton, K. K. Y. Ng, T. T. Nguyen, D. Nichols, A. B. Nielsen, S. Nissanke, A. Nitz, A. Noack, F. Nocera, D. Nolting, C. North, L. K. Nuttall, J. Oberling, G. D. O'Dea, G. H. Ogin, J. J. Oh, S. H. Oh, F. Ohme, M. A. Okada, M. Oliver, P. Oppermann, R. J. Oram, B. O'Reilly, R. Ormiston, L. F. Ortega, R. O'Shaughnessy, S. Ossokine, D. J. Ottaway, H. Overmier, B. J. Owen, A. E. Pace, J. Page, M. A. Page, A. Pai, S. A. Pai, J. R. Palamos, O. Palashov, C. Palomba, A. Pal-Singh, H. Pan, H.-W. Pan, B. Pang, P. T. H. Pang, C. Pankow, F. Pannarale, B. C. Pant, F. Paoletti, A. Paoli, M. A. Papa, A. Parida, W. Parker, D. Pascucci, A. Pasqualetti, R. Passaquieti, D. Passuello, M. Patil, B. Patricelli, B. L. Pearlstone, M. Pedraza, R. Pedurand, L. Pekowsky, A. Pele, S. Penn, C. J. Perez, A. Perreca, L. M. Perri, H. P. Pfeiffer, M. Phelps, O. J. Piccinni, M. Pichot, F. Piergiovanni, V. Pierro, G. Pillant, L. Pinard, I. M. Pinto, M. Pirello, M. Pitkin, M. Poe, R. Poggiani, P. Popolizio, E. K. Porter, A. Post, J. Powell, J. Prasad, J. W. W. Pratt, G. Pratten, V. Predoi, T. Prestegard, M. Prijatelj, M. Principe, S. Privitera, G. A. Prodi, L. G. Prokhorov, O. Puncken, M. Punturo, P. Puppo, M. Pürrer, H. Qi, V. Quetschke, E. A. Quintero, R. Quitzow-James, F. J. Raab, D. S. Rabeling, H. Radkins, P. Raffai, S. Raja, C. Rajan, B. Rajbhandari, M. Rakhmanov, K. E. Ramirez, A. Ramos-Buades, P. Rapagnani, V. Raymond, M. Razzano, J. Read, T. Regimbau, L. Rei, S. Reid, D. H. Reitze, W. Ren, S. D. Reyes, F. Ricci, P. M. Ricker, S. Rieger, K. Riles, M. Rizzo, N. A. Robertson, R. Robie, F. Robinet, A. Rocchi, L. Rolland, J. G. Rollins, V. J. Roma, R. Romano, C. L. Romel, J. H. Romie, D. Rosińska, M. P. Ross, S. Rowan, A. Rüdiger, P. Ruggi, G. Rutins, K. Ryan, S. Sachdev, T. Sadecki, L. Sadeghian, M. Sakellariadou, L. Salconi, M. Saleem, F. Salemi, A. Samajdar, L. Sammut, L. M. Sampson, E. J. Sanchez, L. E. Sanchez, N. Sanchis-Gual, V. Sandberg, J. R. Sanders, B. Sassolas, B. S. Sathyaprakash, P. R. Saulson, O. Sauter, R. L. Savage, A. Sawadsky, P. Schale, M. Scheel, J. Scheuer, J. Schmidt, P. Schmidt, R. Schnabel, R. M. S. Schofield, A. Schönbeck, E. Schreiber, D. Schuette, B. W. Schulte, B. F. Schutz, S. G. Schwalbe, J. Scott, S. M. Scott, E. Seidel, D. Sellers, A. S. Sengupta, D. Sentenac, V. Sequino, A. Sergeev, D. A. Shaddock, T. J. Shaffer, A. A. Shah, M. S. Shahriar, M. B. Shaner, L. Shao, B. Shapiro, P. Shawhan, A. Sheperd, D. H. Shoemaker, D. M. Shoemaker, K. Siellez, X. Siemens, M. Sieniawska, D. Sigg, A. D. Silva, L. P. Singer, A. Singh, A. Singhal, A. M. Sintes, B. J. J. Slagmolen, B. Smith, J. R. Smith, R. J. E. Smith, S. Somala, E. J. Son, J. A. Sonnenberg, B. Sorazu, F. Sorrentino, T. Souradeep, A. P. Spencer, A. K. Srivastava, K. Staats, A. Staley, M. Steinke, J. Steinlechner, S. Steinlechner, D. Steinmeyer, S. P. Stevenson, R. Stone, D. J. Stops, K. A. Strain, G. Stratta, S. E. Strigin, A. Strunk, R. Sturani, A. L. Stuver, T. Z. Summerscales, L. Sun, S. Sunil, J. Suresh, P. J. Sutton, B. L. Swinkels, M. J. Szczepańczyk, M. Tacca, S. C. Tait, C. Talbot, D. Talukder, D. B. Tanner, M. Tápai, A. Taracchini, J. D. Tasson, J. A. Taylor, R. Taylor, S. V. Tewari, T. Theeg, F. Thies, E. G. Thomas, M. Thomas, P. Thomas, K. A. Thorne, K. S. Thorne, E. Thrane, S. Tiwari, V. Tiwari, K. V. Tokmakov, K. Toland, M. Tonelli, Z. Tornasi, A. Torres-Forné, C. I. Torrie, D. Töyrä, F. Travasso, G. Traylor, J. Trinastic, M. C. Tringali, L. Trozzo, K. W. Tsang, M. Tse, R. Tso, L. Tsukada, D. Tsuna, D. Tuyenbayev, K. Ueno, D. Ugolini, C. S. Unnikrishnan, A. L. Urban, S. A. Usman, H. Vahlbruch, G. Vajente, G. Valdes, N. van Bakel, M. van Beuzekom, J. F. J. van den Brand, C. Van Den Broeck, D. C. Vander-Hyde, L. van der Schaaf, J. V. van Heijningen, A. A. van Veggel, M. Vardaro, V. Varma, S. Vass, M. Vasúth, A. Vecchio, G. Vedovato,

J. Veitch, P. J. Veitch, K. Venkateswara, G. Venugopalan, D. Verkindt, F. Vetrano, A. Viceré, A. D. Viets, S. Vinciguerra, D. J. Vine, J. Y. Vinet, S. Vitale, T. Vo, H. Vocca, C. Vorvick, S. P. Vyatchanin, A. R. Wade, L. E. Wade, M. Wade, R. Walet, M. Walker, L. Wallace, S. Walsh, G. Wang, H. Wang, J. Z. Wang, W. H. Wang, Y. F. Wang, R. L. Ward, J. Warner, M. Was, J. Watchi, B. Weaver, L. W. Wei, M. Weinert, A. J. Weinstein, R. Weiss, L. Wen, E. K. Wessel, P. Weßels, J. Westerweck, T. Westphal, K. Wette, J. T. Whelan, S. E. Whitcomb, B. F. Whiting, C. Whittle, D. Wilken, D. Williams, R. D. Williams, A. R. Williamson, J. L. Willis, B. Willke, M. H. Wimmer, W. Winkler, C. C. Wipf, H. Wittel, G. Woan, J. Woehler, J. Wofford, K. W. K. Wong, J. Worden, J. L. Wright, D. S. Wu, D. M. Wysocki, S. Xiao, H. Yamamoto, C. C. Yancey, L. Yang, M. J. Yap, M. Yazback, H. Yu, H. Yu, M. Yvert, A. Zadrożny, M. Zanolin, T. Zelenova, J. P. Zendri, M. Zevin, L. Zhang, M. Zhang, T. Zhang, Y. H. Zhang, C. Zhao, M. Zhou, Z. Zhou, S. J. Zhu, X. J. Zhu, A. B. Zimmerman, M. E. Zucker, J. Zweizig, (LIGO Scientific Collaboration, Virgo Collaboration, E. Burns, P. Veres, D. Kocevski, J. Racusin, A. Goldstein, V. Connaughton, M. S. Briggs, L. Blackburn, R. Hamburg, C. M. Hui, A. von Kienlin, J. McEnery, R. D. Preece, C. A. Wilson-Hodge, E. Bissaldi, W. H. Cleveland, M. H. Gibby, M. M. Giles, R. M. Kippen, S. McBreen, C. A. Meegan, W. S. Paciesas, S. Poolakkil, O. J. Roberts, M. Stanbro, F. Gamma-ray Burst Monitor, V. Savchenko, C. Ferrigno, E. Kuulkers, A. Bazzano, E. Bozzo, S. Brandt, J. Chenevez, T. J. L. Courvoisier, R. Diehl, A. Domingo, L. Hanlon, E. Jourdain, P. Laurent, F. Lebrun, A. Lutovinov, S. Mereghetti, L. Natalucci, J. Rodi, J. P. Roques, R. Sunyaev, P. Ubertini, and (INTEGRAL, "Gravitational Waves and Gamma-Rays from a Binary Neutron Star Merger: GW170817 and GRB 170817A," The Astrophysical Journal Letter **848**, L13 (2017), arXiv:1710.05834 [astro-ph.HE] .

[78] A. Goldstein, P. Veres, E. Burns, M. S. Briggs, R. Hamburg, D. Kocevski, C. A. Wilson-Hodge, R. D. Preece, S. Poolakkil, O. J. Roberts, C. M. Hui, V. Connaughton, J. Racusin, A. von Kienlin, T. Dal Canton, N. Christensen, T. Littenberg, K. Siellez, L. Blackburn, J. Broida, E. Bissaldi, W. H. Cleveland, M. H. Gibby, M. M. Giles, R. M. Kippen, S. McBreen, J. McEnery, C. A. Meegan, W. S. Paciesas, and M. Stanbro, "An Ordinary Short Gamma-Ray Burst with Extraordinary Implications: Fermi-GBM Detection of GRB 170817A," The Astrophysical Journal Letter **848**, L14 (2017), arXiv:1710.05446 [astro-ph.HE] .

[79] V. Savchenko, C. Ferrigno, E. Kuulkers, A. Bazzano, E. Bozzo, S. Brandt, J. Chenevez, T. J. L. Courvoisier, R. Diehl, A. Domingo, L. Hanlon, E. Jourdain, A. von Kienlin, P. Laurent, F. Lebrun, A. Lutovinov, A. Martin-Carrillo, S. Mereghetti, L. Natalucci, J. Rodi, J. P. Roques, R. Sunyaev, and P. Ubertini, "INTEGRAL Detection of the First Prompt Gamma-Ray Signal Coincident with the Gravitational-wave Event GW170817," The Astrophysical Journal Letter **848**, L15 (2017), arXiv:1710.05449 [astro-ph.HE] .

[80] I. Andreoni, K. Ackley, J. Cooke, A. Acharyya, J. R. Allison, G. E. Anderson, M. C. B. Ashley, D. Baade, M. Bailes, K. Bannister, A. Beardsley, M. S. Bessell, F. Bian, P. A. Bland, M. Boer, T. Booler, A. Brandeker, I. S. Brown, D. A. H. Buckley, S. W. Chang, D. M. Coward, S. Crawford, H. Crisp, B. Crosse, A. Cucchiara, M. Cupák, J. S. de Gois, A. Deller, H. A. R. Devillepoix, D. Dobie, E. Elmer, D. Emrich, W. Farah, T. J. Farrell, T. Franzen, B. M. Gaensler, D. K. Galloway, B. Gendre, T. Giblin, A. Goobar, J. Green, P. J. Hancock, B. A. D.

Hartig, E. J. Howell, L. Horsley, A. Hotan, R. M. Howie, L. Hu, Y. Hu, C. W. James, S. Johnston, M. Johnston-Hollitt, D. L. Kaplan, M. Kasliwal, E. F. Keane, D. Kenney, A. Klotz, R. Lau, R. Laugier, E. Lenc, X. Li, E. Liang, C. Lidman, L. C. Luvaul, C. Lynch, B. Ma, D. Macpherson, J. Mao, D. E. McClelland, C. McCully, A. Möller, M. F. Morales, D. Morris, T. Murphy, K. Noysena, C. A. Onken, N. B. Orange, S. Osłowski, D. Pallot, J. Paxman, S. B. Potter, T. Pritchard, W. Raja, R. Ridden-Harper, E. Romero-Colmenero, E. M. Sadler, E. K. Sansom, R. A. Scalzo, B. P. Schmidt, S. M. Scott, N. Seghouani, Z. Shang, R. M. Shannon, L. Shao, M. M. Shara, R. Sharp, M. Sokolowski, J. Sollerman, J. Staff, K. Steele, T. Sun, N. B. Suntzeff, C. Tao, S. Tingay, M. C. Towner, P. Thierry, C. Trott, B. E. Tucker, P. Väisänen, V. V. Krishnan, M. Walker, L. Wang, X. Wang, R. Wayth, M. Whiting, A. Williams, T. Williams, C. Wolf, C. Wu, X. Wu, J. Yang, X. Yuan, H. Zhang, J. Zhou, and H. Zovaro, "Follow Up of GW170817 and Its Electromagnetic Counterpart by Australian-Led Observing Programmes," Publications of the Astronomical Society of Australia **34**, e069 (2017), arXiv:1710.05846 [astro-ph.HE] .

[81] D. A. Coulter, R. J. Foley, C. D. Kilpatrick, M. R. Drout, A. L. Piro, B. J. Shappee, M. R. Siebert, J. D. Simon, N. Ulloa, D. Kasen, B. F. Madore, A. Murguia-Berthier, Y. C. Pan, J. X. Prochaska, E. Ramirez-Ruiz, A. Rest, and C. Rojas-Bravo, "Swope Supernova Survey 2017a (SSS17a), the optical counterpart to a gravitational wave source," Science **358**, 1556 (2017), arXiv:1710.05452 [astro-ph.HE] .

[82] P. A. Evans, S. B. Cenko, J. A. Kennea, S. W. K. Emery, N. P. M. Kuin, O. Korobkin, R. T. Wollaeger, C. L. Fryer, K. K. Madsen, F. A. Harrison, Y. Xu, E. Nakar, K. Hotokezaka, A. Lien, S. Campana, S. R. Oates, E. Troja, A. A. Breeveld, F. E. Marshall, S. D. Barthelmy, A. P. Beardmore, D. N. Burrows, G. Cusumano, A. D'Aì, P. D'Avanzo, V. D'Elia, M. de Pasquale, W. P. Even, C. J. Fontes, K. Forster, J. Garcia, P. Giommi, B. Grefenstette, C. Gronwall, D. H. Hartmann, M. Heida, A. L. Hungerford, M. M. Kasliwal, H. A. Krimm, A. J. Levan, D. Malesani, A. Melandri, H. Miyasaka, J. A. Nousek, P. T. O'Brien, J. P. Osborne, C. Pagani, K. L. Page, D. M. Palmer, M. Perri, S. Pike, J. L. Racusin, S. Rosswog, M. H. Siegel, T. Sakamoto, B. Sbarufatti, G. Tagliaferri, N. R. Tanvir, and A. Tohuvavohu, "Swift and NuSTAR observations of GW170817: Detection of a blue kilonova," Science **358**, 1565 (2017), arXiv:1710.05437 [astro-ph.HE] .

[83] M. Nicholl, E. Berger, D. Kasen, B. D. Metzger, J. Elias, C. Briceño, K. D. Alexander, P. K. Blanchard, R. Chornock, P. S. Cowperthwaite, T. Eftekhari, W. Fong, R. Margutti, V. A. Villar, P. K. G. Williams, W. Brown, J. Annis, A. Bahramian, D. Brout, D. A. Brown, H. Y. Chen, J. C. Clemens, E. Dennihy, B. Dunlap, D. E. Holz, E. Marchesini, F. Massaro, N. Moskowitz, I. Pelisoli, A. Rest, F. Ricci, M. Sako, M. Soares-Santos, and J. Strader, "The Electromagnetic Counterpart of the Binary Neutron Star Merger LIGO/Virgo GW170817. III. Optical and UV Spectra of a Blue Kilonova from Fast Polar Ejecta," The Astrophysical Journal Letter **848**, L18 (2017), arXiv:1710.05456 [astro-ph.HE] .

[84] N. R. Tanvir, A. J. Levan, C. González-Fernández, O. Korobkin, I. Mandel, S. Rosswog, J. Hjorth, P. D'Avanzo, A. S. Fruchter, C. L. Fryer, T. Kangas, B. Milvang-Jensen, S. Rosetti, D. Steeghs, R. T. Wollaeger, Z. Cano, C. M. Copperwheat, S. Covino, V. D'Elia, A. de Ugarte Postigo, P. A. Evans, W. P. Even,

S. Fairhurst, R. Figuera Jaimes, C. J. Fontes, Y. I. Fujii, J. P. U. Fynbo, B. P. Gompertz, J. Greiner, G. Hodosan, M. J. Irwin, P. Jakobsson, U. G. Jørgensen, D. A. Kann, J. D. Lyman, D. Malesani, R. G. McMahon, A. Melandri, P. T. O'Brien, J. P. Osborne, E. Palazzi, D. A. Perley, E. Pian, S. Piranomonte, M. Rabus, E. Rol, A. Rowlinson, S. Schulze, P. Sutton, C. C. Thöne, K. Ulaczyk, D. Watson, K. Wiersema, and R. A. M. J. Wijers, "The Emergence of a Lanthanide-rich Kilonova Following the Merger of Two Neutron Stars," The Astrophysical Journal Letter **848**, L27 (2017), arXiv:1710.05455 [astro-ph.HE] .

[85] A. von Kienlin, C. A. Meegan, W. S. Paciesas, P. N. Bhat, E. Bissaldi, M. S. Briggs, J. M. Burgess, D. Byrne, V. Chaplin, W. Cleveland, V. Connaughton, A. C. Collazzi, G. Fitzpatrick, S. Foley, M. Gibby, M. Giles, A. Goldstein, J. Greiner, D. Gruber, S. Guiriec, A. J. van der Horst, C. Kouveliotou, E. Layden, S. McBreen, S. McGlynn, V. Pelassa, R. D. Preece, A. Rau, D. Tierney, C. A. Wilson-Hodge, S. Xiong, G. Younes, and H.-F. Yu, "The Second Fermi GBM Gamma-Ray Burst Catalog: The First Four Years," The Astrophysical Journal Supplement **211**, 13 (2014), arXiv:1401.5080 [astro-ph.HE] .

[86] B. Paczynski and J. E. Rhoads, "Radio Transients from Gamma-Ray Bursters," The Astrophysical Journal Letter **418**, L5 (1993), arXiv:astro-ph/9307024 [astro-ph] .

[87] P. Mészáros and M. J. Rees, "Optical and Long-Wavelength Afterglow from Gamma-Ray Bursts," The Astrophysical Journal **476**, 232 (1997), arXiv:astro-ph/9606043 [astro-ph] .

[88] B. Zhang, Y. Z. Fan, J. Dyks, S. Kobayashi, P. Mészáros, D. N. Burrows, J. A. Nousek, and N. Gehrels, "Physical Processes Shaping Gamma-Ray Burst X-Ray Afterglow Light Curves: Theoretical Implications from the Swift X-Ray Telescope Observations," The Astrophysical Journal **642**, 354 (2006), arXiv:astro-ph/0508321 [astro-ph] .

[89] S. D. Barthelmy, J. K. Cannizzo, N. Gehrels, G. Cusumano, V. Mangano, P. T. O'Brien, S. Vaughan, B. Zhang, D. N. Burrows, S. Campana, G. Chincarini, M. R. Goad, C. Kouveliotou, P. Kumar, P. Mészáros, J. A. Nousek, J. P. Osborne, A. Panaitescu, J. N. Reeves, T. Sakamoto, G. Tagliaferri, and R. A. M. J. Wijers, "Discovery of an Afterglow Extension of the Prompt Phase of Two Gamma-Ray Bursts Observed by Swift," The Astrophysical Journal Letter **635**, L133 (2005), arXiv:astro-ph/0511576 [astro-ph] .

[90] L. Li, E.-W. Liang, Q.-W. Tang, J.-M. Chen, S.-Q. Xi, H.-J. Lü, H. Gao, B. Zhang, J. Zhang, S.-X. Yi, R.-J. Lu, L.-Z. Lü, and J.-Y. Wei, "A Comprehensive Study of Gamma-Ray Burst Optical Emission. I. Flares and Early Shallow-decay Component," The Astrophysical Journal **758**, 27 (2012), arXiv:1203.2332 [astro-ph.HE] .

[91] A. J. van der Horst, Z. Paragi, A. G. de Bruyn, J. Granot, C. Kouveliotou, K. Wiersema, R. L. C. Starling, P. A. Curran, R. A. M. J. Wijers, A. Rowlinson, G. A. Anderson, R. P. Fender, J. Yang, and R. G. Strom, "A comprehensive radio view of the extremely bright gamma-ray burst 130427A," Mon. Not. R. Astron. Soc. **444**, 3151 (2014), arXiv:1404.1945 [astro-ph.HE] .

[92] MAGIC Collaboration, V. A. Acciari, S. Ansoldi, L. A. Antonelli, A. A. Engels, D. Baack, A. Babić, B. Banerjee, U. Barres de Almeida, J. A. Barrio, J. Becerra González, W. Bednarek, L. Bellizzi, E. Bernardini, A. Berti, J. Besenrieder, W. Bhattacharyya, C. Bigongiari, A. Biland, O. Blanch, G. Bonnoli, Ž. Bošnjak, G. Busetto, R. Carosi, G. Ceribella, Y. Chai, A. Chilingaryan, S. Cikota, S. M. Colak, U. Colin, E. Colombo, J. L. Contreras, J. Cortina, S. Covino, V. D'Elia, P. da Vela, F. Dazzi, A. de Angelis, B. de Lotto, M. Delfino, J. Delgado, D. Depaoli, F. di Pierro, L. di Venere, E. Do Souto Espiñeira, D. Dominis Prester, A. Donini, D. Dorner, M. Doro, D. Elsaesser, V. Fallah Ramazani, A. Fattorini, G. Ferrara, D. Fidalgo, L. Foffano, M. V. Fonseca, L. Font, C. Fruck, S. Fukami, R. J. García López, M. Garczarczyk, S. Gasparyan, M. Gaug, N. Giglietto, F. Giordano, N. Godinović, D. Green, D. Guberman, D. Hadasch, A. Hahn, J. Herrera, J. Hoang, D. Hrupec, M. Hütten, T. Inada, S. Inoue, K. Ishio, Y. Iwamura, L. Jouvin, D. Kerszberg, H. Kubo, J. Kushida, A. Lamastra, D. Lelas, F. Leone, E. Lindfors, S. Lombardi, F. Longo, M. López, R. López-Coto, A. López-Oramas, S. Loporchio, B. Machado de Oliveira Fraga, C. Maggio, P. Majumdar, M. Makariev, M. Mallamaci, G. Maneva, M. Manganaro, K. Mannheim, L. Maraschi, M. Mariotti, M. Martínez, D. Mazin, S. Mićanović, D. Miceli, M. Minev, J. M. Miranda, R. Mirzoyan, E. Molina, A. Moralejo, D. Morcuende, V. Moreno, E. Moretti, P. Munar-Adrover, V. Neustroev, C. Nigro, K. Nilsson, D. Ninci, K. Nishijima, K. Noda, L. Nogués, S. Nozaki, S. Paiano, M. Palatiello, D. Paneque, R. Paoletti, J. M. Paredes, P. Peñil, M. Peresano, M. Persic, P. G. P. Moroni, E. Prandini, I. Puljak, W. Rhode, M. Ribó, J. Rico, C. Righi, A. Rugliancich, L. Saha, N. Sahakyan, T. Saito, S. Sakurai, K. Satalecka, K. Schmidt, T. Schweizer, J. Sitarek, I. Šnidarić, D. Sobczynska, A. Somero, A. Stamerra, D. Strom, M. Strzys, Y. Suda, T. Surić, M. Takahashi, F. Tavecchio, P. Temnikov, T. Terzić, M. Teshima, N. Torres-Albà, L. Tosti, V. Vagelli, J. van Scherpenberg, G. Vanzo, M. Vazquez Acosta, C. F. Vigorito, V. Vitale, I. Vovk, M. Will, D. Zarić, L. Nava, P. Veres, P. N. Bhat, M. S. Briggs, W. H. Cleveland, R. Hamburg, C. M. Hui, B. Mailyan, R. D. Preece, O. J. Roberts, A. von Kienlin, C. A. Wilson-Hodge, D. Kocevski, M. Arimoto, D. Tak, K. Asano, M. Axelsson, G. Barbiellini, E. Bissaldi, F. F. Dirirsa, R. Gill, J. Granot, J. McEnery, N. Omodei, S. Razzaque, F. Piron, J. L. Racusin, D. J. Thompson, S. Campana, M. G. Bernardini, N. P. M. Kuin, M. H. Siegel, S. B. Cenko, P. O'Brien, M. Capalbi, A. Daı, M. de Pasquale, J. Gropp, N. Klingler, J. P. Osborne, M. Perri, R. L. C. Starling, G. Tagliaferri, A. Tohuvavohu, A. Ursi, M. Tavani, M. Cardillo, C. Casentini, G. Piano, Y. Evangelista, F. Verrecchia, C. Pittori, F. Lucarelli, A. Bulgarelli, N. Parmiggiani, G. E. Anderson, J. P. Anderson, G. Bernardi, J. Bolmer, M. D. Caballero-García, I. M. Carrasco, A. Castellón, N. Castro Segura, A. J. Castro-Tirado, S. V. Cherukuri, A. M. Cockeram, P. D'Avanzo, A. di Dato, R. Diretse, R. P. Fender, E. Fernández-García, J. P. U. Fynbo, A. S. Fruchter, J. Greiner, M. Gromadzki, K. E. Heintz, I. Heywood, A. J. van der Horst, Y. D. Hu, C. Inserra, L. Izzo, V. Jaiswal, P. Jakobsson, J. Japelj, E. Kankare, D. A. Kann, C. Kouveliotou, S. Klose, A. J. Levan, X. Y. Li, S. Lotti, K. Maguire, D. B. Malesani, I. Manulis, M. Marongiu, S. Martin, A. Melandri, M. J. Michałowski, J. C. A. Miller-Jones, K. Misra, A. Moin, K. P. Mooley, S. Nasri, M. Nicholl, A. Noschese, G. Novara, S. B. Pandey, E. Peretti, C. J. Pérez Del Pulgar, M. A. Pérez-Torres, D. A. Perley, L. Piro, F. Ragosta, L. Resmi, R. Ricci, A. Rossi, R. Sánchez-Ramírez, J. Selsing, S. Schulze, S. J. Smartt, I. A. Smith, V. V. Sokolov, J. Stevens, N. R. Tanvir, C. C. Thöne,

A. Tiengo, E. Tremou, E. Troja, A. de Ugarte Postigo, A. F. Valeev, S. D. Vergani, M. Wieringa, P. A. Woudt, D. Xu, O. Yaron, and D. R. Young, "Observation of inverse Compton emission from a long γ-ray burst," Nature **575**, 459 (2019), arXiv:2006.07251 [astro-ph.HE] .

[93] H. Abdalla, R. Adam, F. Aharonian, F. Ait Benkhali, E. O. Angüner, M. Arakawa, C. Arcaro, C. Armand, H. Ashkar, M. Backes, V. Barbosa Martins, M. Barnard, Y. Becherini, D. Berge, K. Bernlöhr, E. Bissaldi, R. Blackwell, M. Böttcher, C. Boisson, J. Bolmont, S. Bonnefoy, J. Bregeon, M. Breuhaus, F. Brun, P. Brun, M. Bryan, M. Büchele, T. Bulik, T. Bylund, M. Capasso, S. Caroff, A. Carosi, S. Casanova, M. Cerruti, T. Chand, S. Chandra, A. Chen, S. Colafrancesco, M. Curyło, I. D. Davids, C. Deil, J. Devin, P. deWilt, L. Dirson, A. Djannati-Ataï, A. Dmytriiev, A. Donath, V. Doroshenko, J. Dyks, K. Egberts, G. Emery, J. P. Ernenwein, S. Eschbach, K. Feijen, S. Fegan, A. Fiasson, G. Fontaine, S. Funk, M. Füßling, S. Gabici, Y. A. Gallant, F. Gaté, G. Giavitto, L. Giunti, D. Glawion, J. F. Glicenstein, D. Gottschall, M. H. Grondin, J. Hahn, M. Haupt, G. Heinzelmann, G. Henri, G. Hermann, J. A. Hinton, W. Hofmann, C. Hoischen, T. L. Holch, M. Holler, D. Horns, D. Huber, H. Iwasaki, M. Jamrozy, D. Jankowsky, F. Jankowsky, A. Jardin-Blicq, I. Jung-Richardt, M. A. Kastendieck, K. Katarzyński, M. Katsuragawa, U. Katz, D. Khangulyan, B. Khélifi, J. King, S. Klepser, W. Kluźniak, N. Komin, K. Kosack, D. Kostunin, M. Kreter, G. Lamanna, A. Lemière, M. Lemoine-Goumard, J. P. Lenain, E. Leser, C. Levy, T. Lohse, I. Lypova, J. Mackey, J. Majumdar, D. Malyshev, V. Marandon, A. Marcowith, A. Mares, C. Mariaud, G. Martí-Devesa, R. Marx, G. Maurin, P. J. Meintjes, A. M. W. Mitchell, R. Moderski, M. Mohamed, L. Mohrmann, C. Moore, E. Moulin, J. Muller, T. Murach, S. Nakashima, M. de Naurois, H. Ndiyavala, F. Niederwanger, J. Niemiec, L. Oakes, P. O'Brien, H. Odaka, S. Ohm, E. de Ona Wilhelmi, M. Ostrowski, I. Oya, M. Panter, R. D. Parsons, C. Perennes, P. O. Petrucci, B. Peyaud, Q. Piel, S. Pita, V. Poireau, A. Priyana Noel, D. A. Prokhorov, H. Prokoph, G. Pühlhofer, M. Punch, A. Quirrenbach, S. Raab, R. Rauth, A. Reimer, O. Reimer, Q. Remy, M. Renaud, F. Rieger, L. Rinchiuso, C. Romoli, G. Rowell, B. Rudak, E. Ruiz-Velasco, V. Sahakian, S. Sailer, S. Saito, D. A. Sanchez, A. Santangelo, M. Sasaki, R. Schlickeiser, F. Schüssler, A. Schulz, H. M. Schutte, U. Schwanke, S. Schwemmer, M. Seglar-Arroyo, M. Senniappan, A. S. Seyffert, N. Shafi, K. Shiningayamwe, R. Simoni, A. Sinha, H. Sol, A. Specovius, M. Spir-Jacob, Ł. Stawarz, R. Steenkamp, C. Stegmann, C. Steppa, T. Takahashi, T. Tavernier, A. M. Taylor, R. Terrier, D. Tiziani, M. Tluczykont, C. Trichard, M. Tsirou, N. Tsuji, R. Tuffs, Y. Uchiyama, D. J. van der Walt, C. van Eldik, C. van Rensburg, B. van Soelen, G. Vasileiadis, J. Veh, C. Venter, P. Vincent, J. Vink, H. J. Völk, T. Vuillaume, Z. Wadiasingh, S. J. Wagner, R. White, A. Wierzcholska, R. Yang, H. Yoneda, M. Zacharias, R. Zanin, A. A. Zdziarski, A. Zech, A. Ziegler, J. Zorn, N. Żywucka, F. de Palma, M. Axelsson, and O. J. Roberts, "A very-high-energy component deep in the γ-ray burst afterglow," Nature **575**, 464 (2019), arXiv:1911.08961 [astro-ph.HE] .

[94] H. E. S. S. Collaboration, H. Abdalla, F. Aharonian, F. Ait Benkhali, E. O. Angüner, C. Arcaro, C. Armand, T. Armstrong, H. Ashkar, M. Backes, V. Baghmanyan, V. Barbosa Martins, A. Barnacka, M. Barnard, Y. Becherini, D. Berge, K. Bernlöhr, B. Bi, E. Bissaldi, M. Böttcher, C. Boisson, J. Bolmont, M. de Bony de Lavergne, M. Breuhaus, F. Brun, P. Brun, M. Bryan, M. Büchele, T. Bulik, T. By-

lund, S. Caroff, A. Carosi, S. Casanova, T. Chand, S. Chandra, A. Chen, G. Cotter, M. Curyło, J. Damascene Mbarubucyeye, I. D. Davids, J. Davies, C. Deil, J. Devin, L. Dirson, A. Djannati-Ataï, A. Dmytriiev, A. Donath, V. Doroshenko, L. Dreyer, C. Duffy, J. Dyks, K. Egberts, F. Eichhorn, S. Einecke, G. Emery, J. P. Ernenwein, K. Feijen, S. Fegan, A. Fiasson, G. Fichet de Clairfontaine, G. Fontaine, S. Funk, M. Füßling, S. Gabici, Y. A. Gallant, G. Giavitto, L. Giunti, D. Glawion, J. F. Glicenstein, M. H. Grondin, J. Hahn, M. Haupt, G. Hermann, J. A. Hinton, W. Hofmann, C. Hoischen, T. L. Holch, M. Holler, M. Hörbe, D. Horns, D. Huber, M. Jamrozy, D. Jankowsky, F. Jankowsky, A. Jardin-Blicq, V. Joshi, I. Jung-Richardt, E. Kasai, M. A. Kastendieck, K. Katarzyński, U. Katz, D. Khangulyan, B. Khélifi, S. Klepser, W. Kluźniak, N. Komin, R. Konno, K. Kosack, D. Kostunin, M. Kreter, G. Lamanna, A. Lemière, M. Lemoine-Goumard, J. P. Lenain, F. Leuschner, C. Levy, T. Lohse, I. Lypova, J. Mackey, J. Majumdar, D. Malyshev, D. Malyshev, V. Marandon, P. Marchegiani, A. Marcowith, A. Mares, G. Martí-Devesa, R. Marx, G. Maurin, P. J. Meintjes, M. Meyer, A. Mitchell, R. Moderski, L. Mohrmann, A. Montanari, C. Moore, P. Morris, E. Moulin, J. Muller, T. Murach, K. Nakashima, A. Nayerhoda, M. de Naurois, H. Ndiyavala, J. Niemiec, L. Oakes, P. O'Brien, H. Odaka, S. Ohm, L. Olivera-Nieto, E. de Ona Wilhelmi, M. Ostrowski, S. Panny, M. Panter, R. D. Parsons, G. Peron, B. Peyaud, Q. Piel, S. Pita, V. Poireau, A. Priyana Noel, D. A. Prokhorov, H. Prokoph, G. Pühlhofer, M. Punch, A. Quirrenbach, S. Raab, R. Rauth, P. Reichherzer, A. Reimer, O. Reimer, Q. Remy, M. Renaud, F. Rieger, L. Rinchiuso, C. Romoli, G. Rowell, B. Rudak, E. Ruiz-Velasco, V. Sahakian, S. Sailer, H. Salzmann, D. A. Sanchez, A. Santangelo, M. Sasaki, M. Scalici, J. Schäfer, F. Schüssler, H. M. Schutte, U. Schwanke, M. Seglar-Arroyo, M. Senniappan, A. S. Seyffert, N. Shafi, J. N. S. Shapopi, K. Shiningayamwe, R. Simoni, A. Sinha, H. Sol, A. Specovius, S. Spencer, M. Spir-Jacob, Ł. Stawarz, L. Sun, R. Steenkamp, C. Stegmann, S. Steinmassl, C. Steppa, T. Takahashi, T. Tam, T. Tavernier, A. M. Taylor, R. Terrier, J. H. E. Thiersen, D. Tiziani, M. Tluczykont, L. Tomankova, M. Tsirou, R. Tuffs, Y. Uchiyama, D. J. van der Walt, C. van Eldik, C. van Rensburg, B. van Soelen, G. Vasileiadis, J. Veh, C. Venter, P. Vincent, J. Vink, H. J. Völk, Z. Wadiasingh, S. J. Wagner, J. Watson, F. Werner, R. White, A. Wierzcholska, Y. W. Wong, A. Yusafzai, M. Zacharias, R. Zanin, D. Zargaryan, A. A. Zdziarski, A. Zech, S. J. Zhu, J. Zorn, S. Zouari, N. Żywucka, P. Evans, and K. Page, "Revealing x-ray and gamma ray temporal and spectral similarities in the GRB 190829A afterglow," Science **372**, 1081 (2021), arXiv:2106.02510 [astro-ph.HE] .

[95] Z. Cao, F. Aharonian, Q. An, Axikegu, Y. X. Bai, Y. W. Bao, D. Bastieri, X. J. Bi, Y. J. Bi, J. T. Cai, Q. Cao, W. Y. Cao, Z. Cao, J. Chang, J. F. Chang, A. M. Chen, E. S. Chen, L. Chen, L. Chen, L. Chen, M. J. Chen, M. L. Chen, Q. H. Chen, S. H. Chen, S. Z. Chen, T. L. Chen, Y. Chen, N. Cheng, Y. D. Cheng, M. Y. Cui, S. W. Cui, X. H. Cui, Y. D. Cui, B. Z. Dai, H. L. Dai, Z. G. Dai, Danzengluobu, D. della Volpe, X. Q. Dong, K. K. Duan, J. H. Fan, Y. Z. Fan, J. Fang, K. Fang, C. F. Feng, L. Feng, S. H. Feng, X. T. Feng, Y. L. Feng, S. Gabici, B. Gao, C. D. Gao, L. Q. Gao, Q. Gao, W. Gao, W. K. Gao, M. M. Ge, L. S. Geng, G. Giacinti, G. H. Gong, Q. B. Gou, M. H. Gu, F. L. Guo, X. L. Guo, Y. Q. Guo, Y. Y. Guo, Y. A. Han, H. H. He, H. N. He, J. Y. He, X. B. He, Y. He, M. Heller, Y. K. Hor, B. W. Hou, C. Hou, X. Hou, H. B. Hu, Q. Hu, S. C. Hu, D. H. Huang, T. Q. Huang, W. J. Huang, X. T. Huang, X. Y. Huang, Y. Huang, Z. C. Huang, X. L. Ji, H. Y. Jia, K. Jia, K. Jiang, X. W. Jiang, Z. J. Jiang, M. Jin, M. M. Kang,

T. Ke, D. Kuleshov, K. Kurinov, B. B. Li, C. Li, C. Li, D. Li, F. Li, H. B. Li, H. C. Li, H. Y. Li, J. Li, J. Li, J. Li, K. Li, W. L. Li, W. L. Li, X. R. Li, X. Li, Y. Z. Li, Z. Li, Z. Li, E. W. Liang, Y. F. Liang, S. J. Lin, B. Liu, C. Liu, D. Liu, H. Liu, H. D. Liu, J. Liu, J. L. Liu, J. Y. Liu, M. Y. Liu, R. Y. Liu, S. M. Liu, W. Liu, Y. Liu, Y. N. Liu, R. Lu, Q. Luo, H. K. Lv, B. Q. Ma, L. L. Ma, X. H. Ma, J. R. Mao, Z. Min, W. Mitthumsiri, H. J. Mu, Y. C. Nan, A. Neronov, Z. W. Ou, B. Y. Pang, P. Pattarakijwanich, Z. Y. Pei, M. Y. Qi, Y. Q. Qi, B. Q. Qiao, J. J. Qin, D. Ruffolo, A. Sáiz, D. Semikoz, C. Y. Shao, L. Shao, O. Shchegolev, X. D. Sheng, F. W. Shu, H. C. Song, Y. V. Stenkin, V. Stepanov, Y. Su, Q. N. Sun, X. N. Sun, Z. B. Sun, P. H. T. Tam, Q. W. Tang, Z. B. Tang, W. W. Tian, C. Wang, C. B. Wang, G. W. Wang, H. G. Wang, H. H. Wang, J. C. Wang, K. Wang, L. P. Wang, L. Y. Wang, P. H. Wang, R. Wang, W. Wang, X. G. Wang, X. Y. Wang, Y. Wang, Y. D. Wang, Y. J. Wang, Z. H. Wang, Z. X. Wang, Z. Wang, Z. Wang, D. M. Wei, J. J. Wei, Y. J. Wei, T. Wen, C. Y. Wu, H. R. Wu, S. Wu, X. F. Wu, Y. S. Wu, S. Q. Xi, J. Xia, J. J. Xia, G. M. Xiang, D. X. Xiao, G. Xiao, G. G. Xin, Y. L. Xin, Y. Xing, Z. Xiong, D. L. Xu, R. F. Xu, R. X. Xu, W. L. Xu, L. Xue, D. H. Yan, J. Z. Yan, T. Yan, C. W. Yang, F. Yang, F. F. Yang, H. W. Yang, J. Y. Yang, L. L. Yang, M. J. Yang, R. Z. Yang, S. B. Yang, Y. H. Yao, Z. G. Yao, Y. M. Ye, L. Q. Yin, N. Yin, X. H. You, Z. Y. You, Y. H. Yu, Q. Yuan, H. Yue, H. D. Zeng, T. X. Zeng, W. Zeng, M. Zha, B. B. Zhang, F. Zhang, H. M. Zhang, H. Y. Zhang, J. L. Zhang, L. X. Zhang, L. Zhang, P. F. Zhang, P. P. Zhang, R. Zhang, S. B. Zhang, S. R. Zhang, S. S. Zhang, X. Zhang, X. P. Zhang, Y. F. Zhang, Y. Zhang, Y. Zhang, B. Zhao, J. Zhao, L. Zhao, L. Z. Zhao, S. P. Zhao, F. Zheng, B. Zhou, H. Zhou, J. N. Zhou, M. Zhou, P. Zhou, R. Zhou, X. X. Zhou, C. G. Zhu, F. R. Zhu, H. Zhu, K. J. Zhu, and X. Zuo, "Very high-energy gamma-ray emission beyond 10 TeV from GRB 221009A," Science Advances **9**, eadj2778 (2023), arXiv:2310.08845 [astro-ph.HE] .

[96] L.-Q. Gao, X.-J. Bi, J. Li, R.-M. Yao, and P.-F. Yin, "Constraints on axion-like particles from the observation of GRB 221009A by LHAASO," JCAP **2024**, 026 (2024), arXiv:2310.11391 [astro-ph.HE] .

[97] S. Troitsky, "Towards a model of photon-axion conversion in the host galaxy of GRB 221009A," JCAP **2024**, 016 (2024), arXiv:2307.08313 [astro-ph.HE] .

[98] S. Nakagawa, F. Takahashi, M. Yamada, and W. Yin, "Axion dark matter from first-order phase transition, and very high energy photons from GRB 221009A," Physics Letters B **839**, 137824 (2023), arXiv:2210.10022 [hep-ph] .

[99] R. Sari and A. A. Esin, "On the Synchrotron Self-Compton Emission from Relativistic Shocks and Its Implications for Gamma-Ray Burst Afterglows," The Astrophysical Journal **548**, 787 (2001), arXiv:astro-ph/0005253 [astro-ph] .

[100] R. Sari, T. Piran, and R. Narayan, "Spectra and Light Curves of Gamma-Ray Burst Afterglows," The Astrophysical Journal Letter **497**, L17 (1998), arXiv:astro-ph/9712005 [astro-ph] .

[101] R. D. Blandford and C. F. McKee, "Fluid dynamics of relativistic blast waves," Physics of Fluids **19**, 1130 (1976).

[102] R. Sari, "Hydrodynamics of Gamma-Ray Burst Afterglow," The Astrophysical Journal Letter **489**, L37 (1997).

[103] H. Zhang, I. M. Christie, M. Petropoulou, J. M. Rueda-Becerril, and D. Giannios, “Inverse Compton signatures of gamma-ray burst afterglows,” Mon. Not. R. Astron. Soc. **496**, 974 (2020), arXiv:1910.14049 [astro-ph.HE] .

[104] L. Sironi and A. Spitkovsky, “Particle Acceleration in Relativistic Magnetized Collisionless Pair Shocks: Dependence of Shock Acceleration on Magnetic Obliquity,” The Astrophysical Journal **698**, 1523 (2009), arXiv:0901.2578 [astro-ph.HE] .

[105] I. Plotnikov, A. Grassi, and M. Grech, “Perpendicular relativistic shocks in magnetized pair plasma,” Mon. Not. R. Astron. Soc. **477**, 5238 (2018), arXiv:1712.02883 [astro-ph.HE] .

[106] B. Reville and A. R. Bell, “On the maximum energy of shock-accelerated cosmic rays at ultra-relativistic shocks,” Mon. Not. R. Astron. Soc. **439**, 2050 (2014), arXiv:1401.2803 [astro-ph.HE] .

[107] Z.-Q. Huang, J. G. Kirk, G. Giacinti, and B. Reville, “The Implications of TeV-detected GRB Afterglows for Acceleration at Relativistic Shocks,” The Astrophysical Journal **925**, 182 (2022), arXiv:2112.00111 [astro-ph.HE] .

[108] B. T. Zhang, K. Murase, P. Veres, and P. Mészáros, “External Inverse-Compton Emission from Low-luminosity Gamma-Ray Bursts: Application to GRB 190829A,” The Astrophysical Journal **920**, 55 (2021), arXiv:2012.07796 [astro-ph.HE] .

[109] D. Khangulyan, A. M. Taylor, and F. Aharonian, “The Formation of Hard Very High Energy Spectra from Gamma-ray Burst Afterglows via Two-zone Synchrotron Self-Compton Emission,” The Astrophysical Journal **947**, 87 (2023), arXiv:2301.08578 [astro-ph.HE] .

[110] J. G. Kirk and P. Schneider, “The influence of large-angle scattering on Fermi acceleration at shocks,” Astronomy and Astrophysics **201**, 177 (1988).

[111] O. Porth, R. Buehler, B. Olmi, S. Komissarov, A. Lamberts, E. Amato, Y. Yuan, and A. Rudy, “Modelling Jets, Tori and Flares in Pulsar Wind Nebulae,” Space Science Reviews **207**, 137 (2017), arXiv:1703.05184 [astro-ph.HE] .

[112] J.-S. Wang, B. Reville, Y. Mizuno, F. M. Rieger, and F. A. Aharonian, “Particle acceleration in shearing flows: the self-generation of turbulent spine-sheath structures in relativistic magnetohydrodynamic jet simulations,” Mon. Not. R. Astron. Soc. **519**, 1872 (2023), arXiv:2212.03226 [astro-ph.HE] .

[113] S. W. Davis and A. Tchekhovskoy, “Magnetohydrodynamics Simulations of Active Galactic Nucleus Disks and Jets,” Annu. Rev. Astron. Astrophys **58**, 407 (2020), arXiv:2101.08839 [astro-ph.HE] .

[114] F. Aharonian, A. G. Akhperjanian, U. Barres de Almeida, A. R. Bazer-Bachi, B. Behera, M. Beilicke, W. Benbow, K. Bernlöhr, C. Boisson, O. Bolz, V. Borrel, I. Braun, E. Brion, A. M. Brown, R. Bühler, T. Bulik, I. Büsching, T. Boutelier, S. Carrigan, P. M. Chadwick, L. M. Chounet, A. C. Clapson, G. Coignet, R. Cornils, L. Costamante, M. Dalton, B. Degrange, H. J. Dickinson, A. Djannati-Ataï, W. Domainko, L. O’C. Drury, F. Dubois, G. Dubus, J. Dyks, K. Egberts, D. Emmanoulopoulos, P. Espigat, C. Farnier, F. Feinstein, A. Fiasson, A. Förster,

G. Fontaine, S. Funk, M. Füßling, Y. A. Gallant, B. Giebels, J. F. Glicenstein, B. Glück, P. Goret, C. Hadjichristidis, D. Hauser, M. Hauser, G. Heinzelmann, G. Henri, G. Hermann, J. A. Hinton, A. Hoffmann, W. Hofmann, M. Holleran, S. Hoppe, D. Horns, A. Jacholkowska, O. C. de Jager, I. Jung, K. Katarzyński, E. Kendziorra, M. Kerschhaggl, B. Khélifi, D. Keogh, N. Komin, K. Kosack, G. Lamanna, I. J. Latham, A. Lemière, M. Lemoine-Goumard, J. P. Lenain, T. Lohse, J. M. Martin, O. Martineau-Huynh, A. Marcowith, C. Masterson, D. Maurin, G. Maurin, T. J. L. McComb, R. Moderski, E. Moulin, M. de Naurois, D. Nedbal, S. J. Nolan, S. Ohm, J. P. Olive, E. de Oña Wilhelmi, K. J. Orford, J. L. Osborne, M. Ostrowski, M. Panter, G. Pedaletti, G. Pelletier, P. O. Petrucci, S. Pita, G. Pühlhofer, M. Punch, S. Ranchon, B. C. Raubenheimer, M. Raue, S. M. Rayner, M. Renaud, J. Ripken, L. Rob, L. Rolland, S. Rosier-Lees, G. Rowell, B. Rudak, J. Ruppel, V. Sahakian, A. Santangelo, R. Schlickeiser, F. Schöck, R. Schröder, U. Schwanke, S. Schwarzburg, S. Schwemmer, A. Shalchi, H. Sol, D. Spangler, Ł. Stawarz, R. Steenkamp, C. Stegmann, G. Superina, P. H. Tam, J. P. Tavernet, R. Terrier, C. van Eldik, G. Vasileiadis, C. Venter, J. P. Vialle, P. Vincent, M. Vivier, H. J. Völk, F. Volpe, S. J. Wagner, M. Ward, A. A. Zdziarski, and A. Zech, "New constraints on the mid-IR EBL from the HESS discovery of VHE γ-rays from 1ES 0229+200," Astronomy and Astrophysics **475**, L9 (2007), arXiv:0709.4584 [astro-ph] .

[115] A. Konigl, "Relativistic jets as X-ray and gamma-ray sources." The Astrophysical Journal **243**, 700 (1981).

[116] M. Sikora, M. C. Begelman, and M. J. Rees, "Comptonization of Diffuse Ambient Radiation by a Relativistic Jet: The Source of Gamma Rays from Blazars?" The Astrophysical Journal **421**, 153 (1994).

[117] F. A. Aharonian, "TeV gamma rays from BL Lac objects due to synchrotron radiation of extremely high energy protons," New Astronomy **5**, 377 (2000), arXiv:astro-ph/0003159 [astro-ph] .

[118] M. Böttcher, A. Reimer, K. Sweeney, and A. Prakash, "Leptonic and Hadronic Modeling of Fermi-detected Blazars," The Astrophysical Journal **768**, 54 (2013), arXiv:1304.0605 [astro-ph.HE] .

[119] M. Cerruti, A. Zech, C. Boisson, and S. Inoue, "A hadronic origin for ultra-high-frequency-peaked BL Lac objects," Mon. Not. R. Astron. Soc. **448**, 910 (2015), arXiv:1411.5968 [astro-ph.HE] .

[120] Z.-Q. Huang, B. Reville, J. G. Kirk, and G. Giacinti, "Prospects for ultra-high-energy particle acceleration at relativistic shocks," Mon. Not. R. Astron. Soc. **522**, 4955 (2023), arXiv:2304.08132 [astro-ph.HE] .

[121] J. G. Kirk, B. Reville, and Z.-Q. Huang, "Particle acceleration at ultrarelativistic, perpendicular shock fronts," Mon. Not. R. Astron. Soc. **519**, 1022 (2023), arXiv:2212.02349 [physics.plasm-ph] .

[122] G. Giacinti and J. G. Kirk, "Acceleration of X-Ray Emitting Electrons in the Crab Nebula," The Astrophysical Journal **863**, 18 (2018), arXiv:1804.05056 [astro-ph.HE] .

[123] M. Takamoto and J. G. Kirk, “Rapid Cosmic-ray Acceleration at Perpendicular Shocks in Supernova Remnants,” The Astrophysical Journal **809**, 29 (2015), arXiv:1506.04354 [astro-ph.HE] .

Acknowledgements

Almost ten years ago, when I was still an undergraduate in Nanjing University, I spent all of my time and energy in the basketball and volleyball teams of my department. Consequently, my scores in each subjects were quite awful. During the summer vacation, there were some exchange programs between my university and Max-Planck Institute. I tried to submit an application, but obviously I was not qualified enough to get a chance. At that time, I would never imagine that I could become a PhD student in Max-Planck Institute in the future.

I am never a quite clever student, not to say an excellent student. Hence, I am really grateful to my supervisor Dr. Brian Reville. Without his supervision during my PhD career, I could never reach any achievement that I obtain nowadays.

I would say thank you to John Kirk, who is the one of the cleverest people I have ever met. He is always humble, and willing to answer my questions and give me useful suggestions.

I spent a happy time with my colleagues in the APT group: Jieshuang Wang, Nils Schween, Thibault Vieu, Lucia Härer, Florian Schulze, Cormac Larkin, and my previous colleagues who have already left our group: Gwenael Giacinti, Michelle Tsirou Christian Heppe, and Naveen Kumar. I really prefer to talk with them on various topics, including philosophy and politics. Although we often stand on different viewpoints and cultures, our conversations were always instructive and insightful, which helps me to understand opinions that are distinct or even opposite to my original ones.

I also thank Jim Hinton, Simon Steinmassl, Makarim Bouyahiaoui, Lars Mohrmann, Francesco Conte, Edna Ruiz, Laura Olivera Nieto, Georg Schwefer, Hazal Göksu, Mischa Breuhaus, Giada Peron, Richard Tuffs, Johannes Schaefer, Tim Lukas Holch, Jean Damascene Mbarubucyeye, Ruth Crespo, Natascha Bruch and other colleagues in the H.E.S.S group and MPIK. Their company enriches my experience in Heidelberg.

I share unforgettable memories with my Chinese friends I met in Heidelberg: Jieshuang Wang and his wife Xiaoling Zhou, Xiayi Helena Ren and her boyfriend Chao Chen, Chunhai Lyu, Li Han, Zheng Gong, Weiyu Zhang, Jianshun Gao, Shuyuan Hu, Yu Fung Wong, Peilun He, Yu He, Liangjun Zhang, Jing Li, Zean Peng, Guoyuan Huang Qingzheng Lyu, Zhangliang Xie, Wuji Wang and his wife Qing Xia. Most of them belong to the physics department in MPIK, ARI and MPIA. We usually gather together to celebrate Chinese and western festivals.

I joined a basketball club and played with my Chinese teammates. They are: Kaiqing Zhang, Hao Wang, Zhaozhi George Meng, Zibo Meng, Shangce Du, Boyang Chen, Miao Han, Zheng Gan, Xiaoyuan Xu, Xiang Li, Tingyi Yang, Tianhao Pang, Weiming Lai, Yugeng Gao, Xiao Tan, Sheng Liu, Zhenhua Li, Hao Li, Hao Xu, Jiayu Yang, Muyuan Liu, Chen Hong and Jingyi Zhang. We fought together and won games, especially kicking Ladenburg's ass, in which there were several racists against Chinese.

I am thankful to Christian Fendt to be the member of my IMPRS thesis committee, also to Matthias Bartelmann and Andreas Quirrenbach to be my thesis examiners.

I started to raise my first cat Nova. He is really cute and a little wild, but sometimes timid. He accompanied me during one of my most desperate time because of the breakup with my ex girlfriend. I still remember the first time when Nova came to my house. He was just two-month old at that time, and was quite tiny. Now he is almost 5.8 kg weight. Sometimes I just treat him as my own son.

Finally, I would like to say thank you to my father, my mother, my grandmother, and other family members. Without your support, I cannot insist on my dream to do scientific research.